Three-Dimensional Propagation and Scattering around a Conical Seamount

by

Wenyu Luo

Submitted to the Department of Mechanical Engineering
in partial fulfillment of the requirements for the degree of

Doctor of Philosophy in Oceanographic Engineering

at the

MASSACHUSETTS INSTITUTE OF TECHNOLOGY

and the

WOODS HOLE OCEANOGRAPHIC INSTITUTION

June 2007

Author . . . .
Department of Mechanical Engineering
June 14, 2007

Certified by . . . .
Henrik Schmidt
Professor
Thesis Supervisor

Accepted by . . . .
Lallit Anand
Chairman, Department Committee on Graduate Students

Accepted by . . . .
Henrik Schmidt
Chair, Joint Committee of Applied Ocean Science and Engineering
MIT/WHOI

Three-Dimensional Propagation and Scattering around a Conical Seamount

by

Wenyu Luo

Submitted to the Department of Mechanical Engineering
on June 14, 2007, in partial fulfillment of the
requirements for the degree of
Doctor of Philosophy in Oceanographic Engineering

Abstract

In this thesis, a numerically efficient three-dimensional propagation and scattering model is developed based on the three-dimensional coupled mode theory for axisymmetric bathymetry. The three-dimensional coupled mode approach applied in this thesis is fundamentally identical to the one applied in earlier models, such as the one presented by Taroudakis [20]. Thus, it is based on a Fourier expansion of the acoustic field around a seamount, with each azimuthal expansion coefficient being represented by a two-way coupled mode formulation. However, earlier formulations were severely limited in terms of frequency, size and geometry of the seamount, the seabed composition, and the distance between the source and the seamount, and are totally inadequate for modeling high-frequency, large-scale seamount problems. By introducing a number of changes in the numerical formulation and using a standard normal mode model (C-SNAP) for determining the fundamental modal solutions and coupling coefficients, orders of magnitude improvement in efficiency and fidelity has been achieved, allowing for realistic propagation and scattering scenarios to be modeled, including effects of seamount roughness and realistic sedimentary structure. Also, by the simple superposition principle, the computational requirements are made independent of the distance between the seamount and the source and receivers, and dependent only on the geometry of the seamount and the frequency of the source.

First, this thesis investigates the scattering from a cylindrical island, which is the simplest case of a conical seamount problem. Our model, using the superposition method, can solve the cylindrical problem in Athanassoulis and Prospathopoulos's paper [3] with the same accuracy while saving about 4/5 computational effort.

Second, this thesis demonstrates the spectral coupled mode approach, which includes a two-way coupled mode model and a superposition representation of the field.

Third, this thesis applies the three-dimensional model to investigate some physics issues of three-dimensional seamount scattering. As a result of the investigation, we learn that the $N\times 2$D model is a poor approximation of the true three-dimensional model when the three-dimensional effects are significant, though it is a good approximation of the three-dimensional model otherwise. The convergence of the model in terms of the seamount discretization is also discussed and demonstrated.

Finally, our three-dimensional spectral coupled mode model is tested by the application of the Kermit Seamount problem with realistic ocean environmental data from the 2004 BASSEX experiment.

Thesis Supervisor: Henrik Schmidt
Title: Professor

Acknowledgments

First, I thank my mother, Guilan Meng, and father, Shifu Luo, for supporting and loving me. I especially thank my brother, Wenlai Luo, for his kindness. For their support and encouragement, special thanks go to my wife, Qi Feng, and my sweet son, Fengjun Luo.

Second, thanks go to my advisor, Prof. Henrik Schmidt, who gave me the opportunity to make some contribution to acoustic research. Whenever I have encountered a problem in my research, Prof. Schmidt has helped me solve it with great patience. I am fortunate to work under the supervision of such a knowledgable, gentle advisor.

Third, thanks are due to Prof. Arthur B. Baggeroer and Dr. James Lynch for their valuable questions and suggestions.

Also, I am grateful to all the students and staff of MIT Ocean Acoustic Group. Thanks to Hyun Joe Kim and Joseph Sikora for discussion about sound propagation around underwater seamounts, and sharing the experimental data with me. Thanks to Geoffrey Fox for arranging so many appointments with Prof. Schmidt and the committee meetings.

Finally, a note of thanks goes to my friends, Jinshan Xu, Yan Wang, Liling Ren, Weichang Li, Qiao Hu, and Xiongjiu Liao.

Contents

5 Physics of Three-Dimensional Seamount Scattering 119

6 Sound Propagation around Kermit-Roosevelt Seamount in 2004 BASSEX Experiment 165

List of Figures

List of Tables

Chapter 1

Introduction

1.1 Motivation

During the last decades, a large number of numerical models have been developed dealing with the solutions of acoustic propagation in the ocean. Most of these models are aimed at providing solutions for two-dimensional (range and depth) problems, and they provide satisfactory solutions when the dependence on the third dimension, azimuth, is negligible.

However, the nature of the ocean itself is three dimensional. For example, the presence of a seamount, or an eddy, etc, will introduce an azimuthal inhomogeneity. In situations in which the three-dimensional effects can not be neglected, the two-dimensional models, or $N\times$2D models, fail to provide accurate solutions. In such situations, we need a model that can give accurate calculation of the field not only on range and depth, but also on azimuth, i.e., a three-dimensional model.

Solving three-dimensional propagation problems is difficult because the ocean must be modeled by a large number of parameters. In addition, even if a three-dimensional problem is formulated elegantly by means of mathematical and physical theory, the realistic implementation of such a solution requires huge computational effort.

My research is supported by the US Office of Naval Research (ONR). The goal of my research is to develop a numerically efficient three-dimensional propagation and scattering model.

1.2 Previous Work

The simulation of acoustic propagation in a range-dependent waveguide remains an area of active research. Among such problems, the problem of modeling three-dimensional sound propagation has drawn the attention of many scientists and engineers.

Three-dimensional models based on the parabolic equation (PE) method have been introduced by several researchers [4, 13, 19]. As is well known, parabolic equation models are suitable for treating underwater acoustic propagation problems in cases only where no significant backscattered field is expected because of the parabolic approximations introduced in reducing the full elliptic wave equation (Helmholtz equation) to the parabolic equation. In addition, the work by McDaniel [15] shows that the parabolic approximations have inherent phase errors, which limit their applicability to a certain range of angles around the main propagation direction.

The normal mode method is intended to solve the full-wave equation (Helmholtz equation), so it is valid for the cases where backscattering is important (e.g., steep obstacles, seamounts, or islands). In addition, the spectral coupled mode method is useful for physics interpretation because of the decomposition of the field into vertical modes and azimuthal modes.

In a paper by Athanassoulis and Propathopoulous [3], an analytic solution is presented for the three-dimensional problem of acoustic scattering from a nonpenetrable cylindrical island in shallow water. Although that solution is valid only for a rigid or soft cylindrical island, it can serve as a three-dimensional benchmark solution in the appropriate frequency range.

In 1996, a coupled-mode formulation for the solution of the Helmholtz equation in water in the presence of a conical seamount was developed by Taroudakis [20]. In his work, the conical seamount is divided into a number of rings, in each of which a series expansion of the acoustic pressure in terms of normal modes and cosine functions is considered. The coefficients of the various expansions are obtained by solving linear systems of equations resulting from the application of continuity conditions at the artificial interfaces of the rings. But there are several disadvantages in this model. First, since Hankel functions of high orders are involved in the expansions, numerical problems arise in the numerical implementation of the scheme in the case of the low convergence rate. Second, when the source is very far from the seamount, the number of azimuthal modes leading to convergence is too large to make this method applicable. Finally, this formulation may yield instable solutions since the linear systems to be solved in this formulation are not unconditionally stable.

In order to obtain a stable system from Taroudakis's model, Eskenazi used the Direct Global Matrix (DGM) approach in his master's thesis [6]. Eskenazi's model successfully solves only the problem of instability in Taroudakis's model. Because the dimensions of the linear systems are too large to be solved by regular software, such as MATLAB, Eskenazi used a special tool, LAPACK (Linear Algebra Package) [2], to solve these linear systems. In addition, the low efficiency of Eskenazi's model makes it not applicable to large-scale ocean acoustic problems due to the limitation of computational capabilities.

1.3 My Contribution

A new three-dimensional spectral coupled mode model is developed in this thesis, which extends the application of Taroudakis's formulation. This model has the following advantages:

1) $J_m(k_{rn}r)$ and $H_m^{(1)}(k_{rn}r)$ are used as the two linearly independent solutions of the Bessel equation in this model, instead of $H_m^{(1)}(k_{rn}r)$ and $H_m^{(2)}(k_{rn}r)$ in Taroudakis's approach. The advantage is that $J_m(k_{rn}r)$ and $H_m^{(1)}(k_{rn}r)$ remain linearly independent for both large and small arguments in numerical implementation.

2) Normalized Bessel and Hankel functions are used to avoid overflow and underflow problems; in addition, the asymptotic forms of normalized Bessel and Hankel func-

tions for small and large arguments are used. As a result, there is no numerical problem in evaluating high-order normalized Bessel and Hankel functions. Moreover, the recurrence relations of Bessel and Hankel functions are used in evaluating these functions of different orders, which improves efficiency.

3) The two-way coupled mode approach used in this model has low requirements for computer memory. For each azimuthal mode, instead of solving one linear system of a large dimension as in the DGM approach, this model solves multiple linear systems of small dimensions. This makes it possible to solve linear systems without using special tools such as LAPACK.

4) The coupling matrixes are independent of azimuthal orders, so they can be pre-calculated only once and stored. In our model, codes are added to C-SNAP to compute and store the coupling matrixes.

5) The efficiency is improved dramatically by introducing the superposition representation of the external field with respect to the seamount. In this model, the number of azimuthal modes required for convergence depends only on the product of the wavenumber and the radius of the base of the conical seamount/cylindrical island. In Athanassoulis and Propathopoulous's model, Taroudakis's model, and Eskenazi's model, this value depends on the product of the wavenumber and the distance between the source and the axle of the conical seamount/cylindrical island.

6) This model can be run in parallel on separate computers; therefore, it is applicable to large-scale three-dimensional problems.

In short, this new three-dimensional spectral coupled mode model is stable and efficient. For example, to solve the numerical example in Eskenazi's master's thesis [6], Eskenazi's model was run in parallel on 7 computers among which were six PCs (one 333 MHz Pentium II, two 400 MHz Pentium II, two 600 MHz Pentium III, and one 600 MHz K7 microprocessors), and one Alpha workstation (with a 667 MHz EV67 microprocessor), with a runtime of between one week and ten days. However, by running our model on a single PC (1.7 GHz P4), the runtime is only several hours.

Chapter 2

The Normal Mode Solution to the Helmholtz Equation

Underwater sound propagation is mathematically described by the wave equation, and the frequency-domain wave equation is known as the Helmholtz equation. There are essentially five types of models to solve it: Fast Field Program (FFP); normal mode (NM); ray; parabolic equation (PE) models; and direct finite-difference (FD), or finite-element (FE) solutions. This chapter is mainly concerned with the normal mode solution to the Helmholtz equation.

2.1 The General Helmholtz Equation

In a horizontally stratified medium, the general homogeneous wave equation takes the form [12, p.69]

$$\rho(z)\nabla\cdot\left(\frac{1}{\rho(z)}\nabla\tilde{p}\right)-\frac{1}{c^2(z)}\frac{\partial^2\tilde{p}}{\partial t^2}=0, \tag{2.1}$$

with harmonic representation $\tilde{p}(\vec{r},t)=p(\vec{r})e^{-i\omega t}$ and $\partial^2/\partial t^2=-\omega^2$, Eq. (2.1) gives rise to the general homogeneous Helmholtz equation,

$$\rho(z)\nabla\cdot\left(\frac{1}{\rho(z)}\nabla p\right)+\frac{\omega^2}{c^2(z)}p=0. \tag{2.2}$$

The general inhomogeneous Helmholtz equation takes the form

$$\rho(z)\nabla\cdot\left(\frac{1}{\rho(z)}\nabla p\right)+\frac{\omega^2}{c^2(z)}p=-\delta\left(\vec{r}-\vec{r}_s\right), \tag{2.3}$$

where $\vec{r}=\vec{r}_s$ is the location of the source. The impulse term $\delta\left(\vec{r}-\vec{r}_s\right)$ is chosen to take advantage of Green's theorem for general inhomogeneous problems. To obtain the solution to the Helmholtz equation with a general source term $f(\vec{r})$, which is like (assume density is constant)

$$\left[\nabla^2+\frac{\omega^2}{c^2(z)}\right]p\left(\vec{r}\right)=f\left(\vec{r}\right), \tag{2.4}$$

we may first find the general Green's function $G_\omega\left(\vec{r},\vec{r}_s\right)$, which satisfies the inhomogeneous Helmholtz equation

$$\left[\nabla^2+\frac{\omega^2}{c^2(z)}\right]G_\omega\left(\vec{r},\vec{r}_s\right)=-\delta\left(\vec{r}-\vec{r}_s\right), \tag{2.5}$$

with Green's theorem, $p(\vec{r})$ is obtained by (refer to Eq. (2.61) of [12, p. 81])

$$p(\vec{r})=\int_S\left[G_\omega(\vec{r},\vec{r}_s)\frac{\partial p(\vec{r}_s)}{\partial\vec{n}_0}-p(\vec{r}_s)\frac{\partial G_\omega(\vec{r},\vec{r}_s)}{\partial\vec{n}_0}\right]\mathrm{d}S_0-\int_V f(\vec{r}_s)G_\omega(\vec{r},\vec{r}_s)\mathrm{d}V_0, \tag{2.6}$$

where $\vec{n}_0$ is the outward-pointing normal on the surface. Eq. (2.6) is *Green's theorem* for sources in a bounded medium.

Next, we will give the different forms of the general Helmholtz equation (2.3) for two-dimensional problems, either with a point source in cylindrical geometry or with a line source in plane geometry, and for three-dimensional problems in cylindrical geometry.

2.1.1 The Two-Dimensional Helmholtz Equation with a Line Source in Plane Geometry

The two-dimensional model with a line source in plane geometry can be extended to the three-dimensional model involving a point source as well as a two-dimensional waveguide with a ridge-like bathymetry [14]. Moreover, working with a line source in plane geometry is useful for inter-model comparisons.

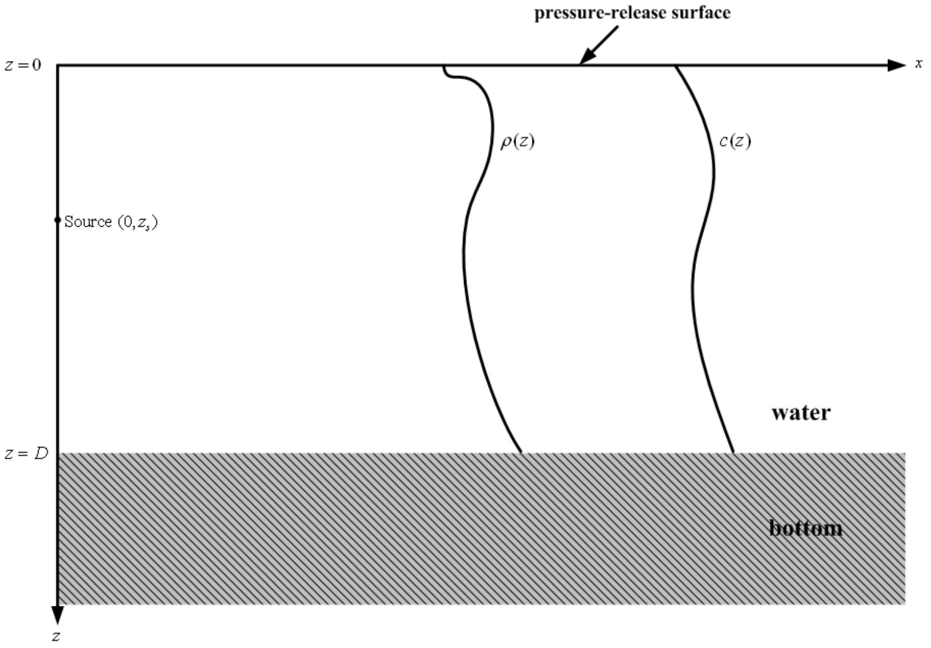

Figure 2-1: A line source in a horizontally stratified fluid medium.

As illustrated in Fig. 2-1, an infinitely long line source is located parallel to the y-axis, at depth $z = z_s$ in a horizontally stratified medium with density $\rho(z)$ and sound speed $c(z)$. This is a two-dimensional problem in Cartisian coordinates (x, z).

In Cartisian coordinates, the left-hand-side (LHS) of Eq. (2.3) may be simplified by

$$\begin{aligned}
\rho(z)\nabla\cdot\left(\frac{1}{\rho(z)}\nabla p\right)+\frac{\omega^2}{c^2(z)}p &= \rho\left(\frac{\partial}{\partial x},\frac{\partial}{\partial y},\frac{\partial}{\partial z}\right)\cdot\left(\frac{1}{\rho}\frac{\partial p}{\partial x},\frac{1}{\rho}\frac{\partial p}{\partial y},\frac{1}{\rho}\frac{\partial p}{\partial z}\right)+\frac{\omega^2}{c^2(z)}p \\
&= \rho\left[\frac{1}{\rho}\frac{\partial^2 p}{\partial x^2}+\cancelto{0}{\frac{1}{\rho}\frac{\partial^2 p}{\partial y^2}}+\frac{\partial}{\partial z}\left(\frac{1}{\rho}\frac{\partial p}{\partial z}\right)\right]+\frac{\omega^2}{c^2(z)}p \\
&= \frac{\partial^2 p}{\partial x^2}+\rho(z)\frac{\partial}{\partial z}\left(\frac{1}{\rho(z)}\frac{\partial p}{\partial z}\right)+\frac{\omega^2}{c^2(z)}p. \qquad (2.7)
\end{aligned}$$

In Cartisian coordinates (x, z), the impulse term in Eq. (2.3) takes the form $-\delta(x)\delta(z - z_s)$. Thus, with a line source in a horizontally stratified fluid medium, the

Helmholtz equation takes the form

$$\frac{\partial^2 p}{\partial x^2} + \rho(z)\frac{\partial}{\partial z}\left(\frac{1}{\rho(z)}\frac{\partial p}{\partial z}\right) + \frac{\omega^2}{c^2(z)}p = -\delta(x)\delta(z - z_s). \tag{2.8}$$

2.1.2 The Two-Dimensional Helmholtz Equation with a Point Source in Cylindrical Geometry

A point source is appropriate for practical problems in underwater acoustics. To take advantage of the cylindrical symmetry in such two-dimensional problems, we use cylindrical coordinates (r, z).

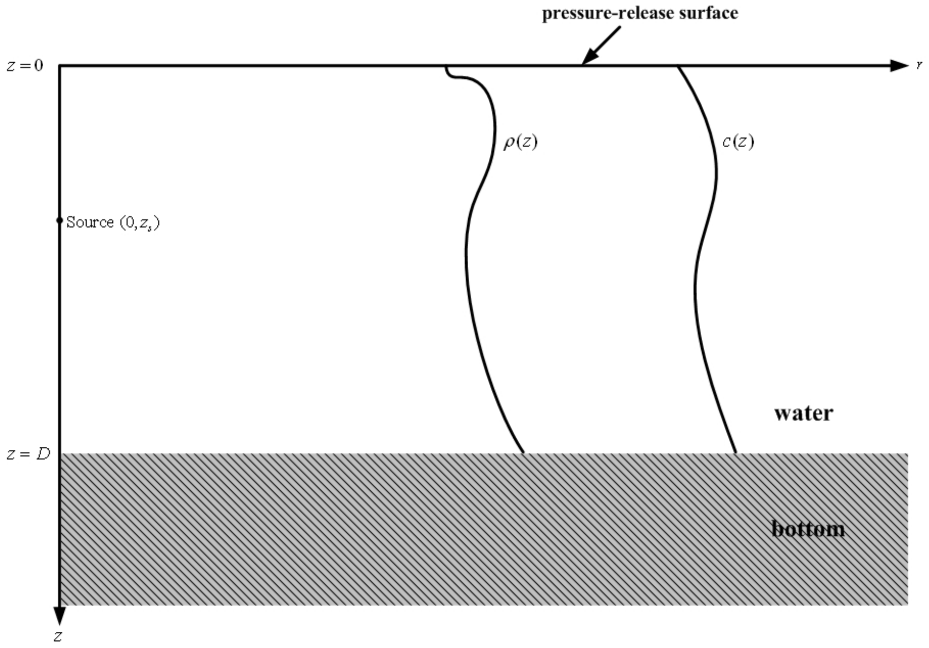

Figure 2-2: A point source in a horizontally stratified fluid medium (The field is axis-symmetric around that source).

As shown in Fig. 2-2, we consider a point source with cylindrical coordinates $(r, z) = (0, z_s)$ in a horizontally stratified medium with density $\rho(z)$ and sound speed $c(z)$. This is a two-dimensional problem in cylindrical coordinates (r, z).

To represent the general Helmholtz equation (2.3) in cylindrical coordinates with axis-symmetry, we first write out the LHS of Eq. (2.3) as following. Since (refer to

Appendix A)

$$\begin{aligned}\nabla p &= \left(\frac{\partial p}{\partial r}, \frac{1}{r}\frac{\partial p}{\partial \phi}, \frac{\partial p}{\partial z}\right), \\ \nabla \cdot (\vec{v}) &= \frac{1}{r}\frac{\partial}{\partial r}(r v_r) + \frac{1}{r}\frac{\partial v_\phi}{\partial \phi} + \frac{\partial v_z}{\partial z},\end{aligned}$$

then we obtain

$$\begin{aligned}\rho(z)\nabla \cdot \left(\frac{1}{\rho(z)}\nabla p\right) &= \rho(z)\left[\frac{1}{r}\frac{\partial}{\partial r}\left(\frac{1}{\rho(z)} r \frac{\partial p}{\partial r}\right) + \frac{1}{r}\frac{\partial}{\partial \phi}\left(\frac{1}{\rho(z)}\frac{1}{r}\frac{\partial p}{\partial \phi}\right) + \frac{\partial}{\partial z}\left(\frac{1}{\rho(z)}\frac{\partial p}{\partial z}\right)\right] \\ &= \frac{1}{r}\frac{\partial}{\partial r}\left(r\frac{\partial p}{\partial r}\right) + \frac{1}{r^2}\frac{\partial^2 p}{\partial \phi^2} + \rho(z)\frac{\partial}{\partial z}\left(\frac{1}{\rho(z)}\frac{\partial p}{\partial z}\right), \qquad (2.9)\end{aligned}$$

therefore the LHS of Eq. (2.3) becomes

$$\rho(z)\nabla \cdot \left(\frac{1}{\rho(z)}\nabla p\right) + \frac{\omega^2}{c^2(z)}p = \frac{1}{r}\frac{\partial}{\partial r}\left(r\frac{\partial p}{\partial r}\right) + \frac{1}{r^2}\frac{\partial^2 p}{\partial \phi^2} + \rho(z)\frac{\partial}{\partial z}\left(\frac{1}{\rho(z)}\frac{\partial p}{\partial z}\right) + \frac{\omega^2}{c^2(z)}p \qquad (2.10)$$

$$\begin{aligned}&\text{axis-symmetric, } \frac{\partial^2}{\partial \phi^2} = 0 \\ &= \frac{1}{r}\frac{\partial}{\partial r}\left(r\frac{\partial p}{\partial r}\right) + \rho(z)\frac{\partial}{\partial z}\left(\frac{1}{\rho(z)}\frac{\partial p}{\partial z}\right) + \frac{\omega^2}{c^2(z)}p. \qquad (2.11)\end{aligned}$$

The impulse term in Eq. (2.3) may be represented in cylindrical coordinates with axis-symmetry as below. Let

$$\delta(\vec{r} - \vec{r}_s) = A\frac{\delta(r)}{r}\delta(z - z_s),$$

where A is a constant. Since

$$\begin{aligned}\int_V \delta(\vec{r} - \vec{r}_s)\mathrm{d}V &= \int_V A\frac{\delta r}{\cancel{r}}\delta(z - z_s)\cancel{r}\mathrm{d}r\mathrm{d}\phi\mathrm{d}z \\ &= A\int \delta r \mathrm{d}r \int \delta(z - z_s)\mathrm{d}z \int_0^{2\pi} \mathrm{d}\phi \\ &= 2\pi A \\ &= 1,\end{aligned}$$

we obtain $A = \frac{1}{2\pi}$, and thus $\delta(\vec{r} - \vec{r}_s)$ in cylindrical coordinates (r, z) takes the form

$$\delta(\vec{r} - \vec{r}_s) = \frac{1}{2\pi}\frac{\delta r}{r}\delta(z - z_s). \tag{2.12}$$

With Eqs. (2.11) and (2.12), the Helmholtz equation in cylindrical coordinates (r, z) takes the form

$$\frac{1}{r}\frac{\partial}{\partial r}\left(r\frac{\partial p}{\partial r}\right) + \rho(z)\frac{\partial}{\partial z}\left(\frac{1}{\rho(z)}\frac{\partial p}{\partial z}\right) + \frac{\omega^2}{c^2(z)}p = -\frac{1}{2\pi}\frac{\delta r}{r}\delta(z - z_s). \tag{2.13}$$

2.1.3 The Three-Dimensional Helmholtz Equation with a Point Source in Cylindrical Geometry

If we consider a problem involving a point source and the field is not axis-symmetric around that source, as illustrated in Fig. 2-3, then it is a three-dimensional problem in which the field depends not only on range and depth, but also on azimuth. In such a three-dimensional problem, we use cylindrical polar coordinates (r, z, ϕ), where ϕ is the azimuthal angle.

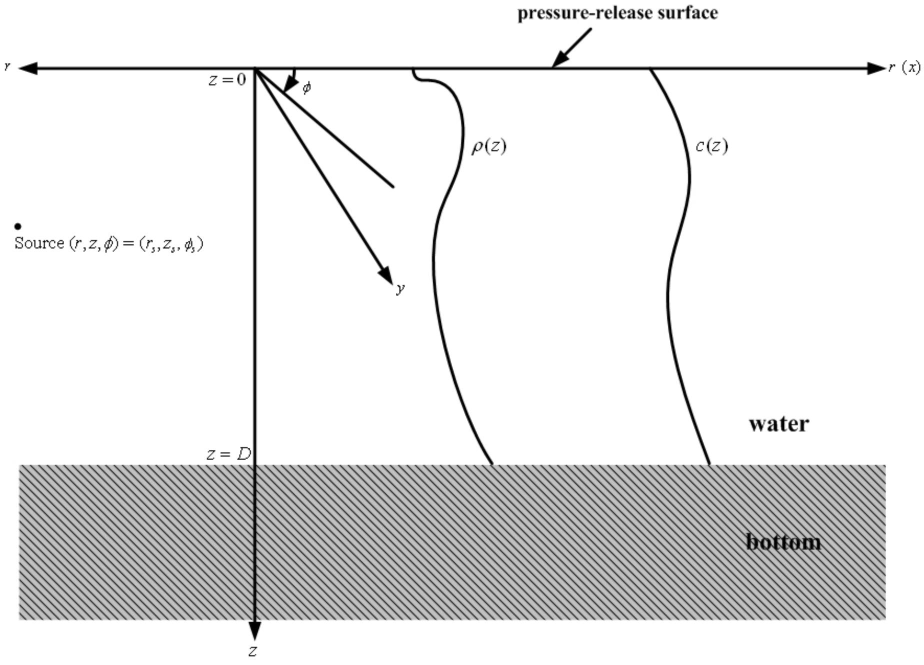

Figure 2-3: A point source in a horizontally stratified fluid medium (The field is not axis-symmetric around that source).

From Eq. (2.10), in cylindrical polar coordinates (r, z, ϕ), the LHS of the general Helmholtz equation (2.3) takes the form

$$\rho(z)\nabla\cdot\left(\frac{1}{\rho(z)}\nabla p\right)+\frac{\omega^2}{c^2(z)}p=\frac{1}{r}\frac{\partial}{\partial r}\left(r\frac{\partial p}{\partial r}\right)+\frac{1}{r^2}\frac{\partial^2 p}{\partial\phi^2}+\rho(z)\frac{\partial}{\partial z}\left(\frac{1}{\rho(z)}\frac{\partial p}{\partial z}\right)+\frac{\omega^2}{c^2(z)}p, \tag{2.14}$$

while the impulse term $\delta(\vec{r}-\vec{r}_s)$ takes a different form from that in Eq. (2.12). Let

$$\delta(\vec{r}-\vec{r}_s)=B\frac{\delta(r-r_s)}{r}\delta(z-z_s)\delta(\phi-\phi_s),$$

where B is a constant, then by

$$\begin{aligned}\int_V\delta(\vec{r}-\vec{r}_s)\mathrm{d}V &= \int B\frac{\delta(r-r_s)}{\cancel{r}}\delta(z-z_s)\delta(\phi-\phi_s)\cancel{r}\mathrm{d}r\mathrm{d}\phi\mathrm{d}z\\ &= B\int\delta(r-r_s)\mathrm{d}r\int\delta(z-z_s)\mathrm{d}z\int_0^{2\pi}\delta(\phi-\phi_s)\mathrm{d}\phi\\ &= B\\ &= 1,\end{aligned}$$

we obtain $B=1$ and

$$\delta(\vec{r}-\vec{r}_s)=\frac{\delta(r-r_s)}{r}\delta(z-z_s)\delta(\phi-\phi_s). \tag{2.15}$$

Thus, with Eqs. (2.14) and (2.15), in cylindrical polar coordinates (r, z, ϕ), the three-dimensional Helmholtz equation takes the form

$$\frac{1}{r}\frac{\partial}{\partial r}\left(r\frac{\partial p}{\partial r}\right)+\frac{1}{r^2}\frac{\partial^2 p}{\partial\phi^2}+\rho(z)\frac{\partial}{\partial z}\left(\frac{1}{\rho(z)}\frac{\partial p}{\partial z}\right)+\frac{\omega^2}{c^2(z)}p=-\frac{\delta(r-r_s)}{r}\delta(z-z_s)\delta(\phi-\phi_s). \tag{2.16}$$

2.2 The Spectral Normal Mode Solution to the Three-Dimensional Helmholtz Equation

In Section 2.1, different forms of Helmholtz equations are given to describe two-dimensional and three-dimensional sound propagation problems. In this section, we will solve the Helmholtz equation by means of the normal mode method. For the first two kinds of problems in Section 2.1, i.e., the two-dimensional Helmholtz equation with a line source as shown in Eq. (2.8), and the two-dimensional Helmholtz equation with a point source as shown in Eq. (2.13), both of which are two-dimensional problems, the solutions are relatively simple. Refer to Appendix B for solutions to the two-dimensional Helmholtz equations. Below we show how to obtain spectral normal mode solutions to the three-dimensional Helmholtz equation with a point source in cylindrical polar coordinates (r, z, ϕ) [20, 3].

From Section 2.1.3, the three-dimensional Helmholtz equation in cylindrical polar coordinates takes the form

$$\frac{1}{r}\frac{\partial}{\partial r}\left(r\frac{\partial p}{\partial r}\right)+\frac{1}{r^2}\frac{\partial^2 p}{\partial \phi^2}+\rho(z)\frac{\partial}{\partial z}\left(\frac{1}{\rho(z)}\frac{\partial p}{\partial z}\right)+\frac{\omega^2}{c^2(z)}p=-\frac{\delta(r-r_s)}{r}\delta(z-z_s)\delta(\phi-\phi_s), \tag{2.17}$$

where (r_s, z_s, ϕ_s) is the location of the point source.

2.2.1 The Spectral Normal Mode Solution to the Homogeneous Three-Dimensional Helmholtz Equation

The homogeneous three-dimensional Helmholtz equation in cylindrical-polar coordinates takes the form

$$\frac{1}{r}\frac{\partial}{\partial r}\left(r\frac{\partial p}{\partial r}\right)+\frac{1}{r^2}\frac{\partial^2 p}{\partial \phi^2}+\rho(z)\frac{\partial}{\partial z}\left(\frac{1}{\rho(z)}\frac{\partial p}{\partial z}\right)+\frac{\omega^2}{c^2(z)}p=0. \tag{2.18}$$

With separation of variables, let

$$p(r,z,\phi)=R(r)\Psi(z)\Phi(\phi), \tag{2.19}$$

and substitute Eq. (2.19) into Eq. (2.18) to obtain

$$\frac{1}{r}\frac{\mathrm{d}}{\mathrm{d}r}\left(r\frac{\mathrm{d}R}{\mathrm{d}r}\right)\Psi\Phi + \frac{1}{r^2}\frac{\mathrm{d}^2\Phi}{\mathrm{d}\phi^2}R\Psi + \rho\frac{\mathrm{d}}{\mathrm{d}z}\left(\frac{1}{\rho}\frac{\mathrm{d}\Psi}{\mathrm{d}z}\right)R\Phi + \frac{\omega^2}{c^2}R\Psi\Phi = 0,$$

divided by $R\Psi\Phi$, we obtain

$$\frac{1}{R}\frac{1}{r}\frac{\mathrm{d}}{\mathrm{d}r}\left(r\frac{\mathrm{d}R}{\mathrm{d}r}\right) + \frac{1}{\Phi}\frac{1}{r^2}\frac{\mathrm{d}^2\Phi}{\mathrm{d}\phi^2} + \frac{1}{\Psi}\rho\frac{\mathrm{d}}{\mathrm{d}z}\left(\frac{1}{\rho}\frac{\mathrm{d}\Psi}{\mathrm{d}z}\right) + \frac{\omega^2}{c^2} = 0. \tag{2.20}$$

To obtain the depth-dependent equation for $\Psi(z)$, let

$$\frac{1}{\Psi_n}\rho\frac{\mathrm{d}}{\mathrm{d}z}\left(\frac{1}{\rho}\frac{\mathrm{d}\Psi_n}{\mathrm{d}z}\right) + \frac{\omega^2}{c^2} = k_{rn}^2, \tag{2.21}$$

or,

$$\rho\frac{\mathrm{d}}{\mathrm{d}z}\left(\frac{1}{\rho}\frac{\mathrm{d}\Psi_n}{\mathrm{d}z}\right) + \left(\frac{\omega^2}{c^2} - k_{rn}^2\right)\Psi_n = 0, \tag{2.22}$$

and by substituting the depth-dependent equation (2.22) into Eq. (2.20), we obtain the equation for $R(r)$ and $\Phi(\phi)$,

$$\frac{r^2}{R}\frac{1}{r}\frac{\mathrm{d}}{\mathrm{d}r}\left(r\frac{\mathrm{d}R}{\mathrm{d}r}\right) + \frac{1}{\Phi}\frac{\mathrm{d}^2\Phi}{\mathrm{d}\phi^2} + k_{rn}^2 r^2 = 0. \tag{2.23}$$

Apply separation of variables again, and let

$$\frac{1}{\Phi_m}\frac{\mathrm{d}^2\Phi_m}{\mathrm{d}\phi^2} = -m^2,\ m = 0, 1, 2, \ldots, \tag{2.24}$$

which leads to solutions

$$\Phi_m(\phi) = e_m \cos m\phi,\ m = 0, 1, 2, \ldots \tag{2.25}$$

If we use the orthonormal relation

$$\int_{-\pi}^{\pi} \Phi_m(\phi)\Phi_n(\phi)\mathrm{d}\phi = \delta_{mn}, \tag{2.26}$$

then we have

$$e_m = \begin{cases} \frac{1}{\sqrt{2\pi}}, & m = 0, \\ \frac{1}{\sqrt{\pi}}, & m \neq 0. \end{cases} \tag{2.27}$$

Substitute Eq. (2.24) into Eq. (2.23), then we obtain the equation for $R(r)$,

$$\frac{r^2}{R_{mn}} \frac{1}{r} \frac{\mathrm{d}}{\mathrm{d}r} \left(r \frac{\mathrm{d}R_{mn}}{\mathrm{d}r} \right) + \left(k_{rn}^2 - \frac{m^2}{r^2} \right) r^2 = 0,$$

or,

$$\frac{1}{r} \frac{\mathrm{d}}{\mathrm{d}r} \left(r \frac{\mathrm{d}R_{mn}}{\mathrm{d}r} \right) + \left(k_{rn}^2 - \frac{m^2}{r^2} \right) R_{mn} = 0. \tag{2.28}$$

Eq. (2.28) is an mth-order Bessel equation, and its solution, $R_{mn}(r)$, is any pair of $H_m^{(1)}(k_{rn}r)$, $H_m^{(2)}(k_{rn}r)$, $J_m(k_{rn}r)$ and $Y_m(k_{rn}r)$.

Thus, the solution to the homogeneous three-dimensional Helmholtz equation, i.e. Eq. (2.18), is

$$p(r, z, \phi) = \sum_{m=0}^{\infty} \sum_{n=1}^{\infty} R_{mn}(r) \Psi_n(z) \Phi_m(\phi). \tag{2.29}$$

2.2.2 The Spectral Normal Mode Solution to the Inhomogeneous Three-Dimensional Helmholtz Equation

The inhomogeneous three-dimensional Helmholtz equation with a point source takes the form

$$\frac{1}{r} \frac{\partial}{\partial r} \left(r \frac{\partial p}{\partial r} \right) + \frac{1}{r^2} \frac{\partial^2 p}{\partial \phi^2} + \rho(z) \frac{\partial}{\partial z} \left(\frac{1}{\rho(z)} \frac{\partial p}{\partial z} \right) + \frac{\omega^2}{c^2(z)} p = -\frac{\delta(r - r_s)}{r} \delta(z - z_s) \delta(\phi - \phi_s). \tag{2.30}$$

From Section 2.2.1, we may represent the solution to Eq. (2.30) in the form

$$p(r, z, \phi) = \sum_{m=0}^{\infty} \sum_{n=1}^{\infty} R_{mn}(r) \Psi_n(z) \Phi_m(\phi), \tag{2.31}$$

where $\Psi_n(z)$ are the depth-dependent eigenfunctions satisfying Eq. (2.22), i.e.

$$\rho \frac{\mathrm{d}}{\mathrm{d}z} \left(\frac{1}{\rho} \frac{\mathrm{d}\Psi_n}{\mathrm{d}z} \right) + \left(\frac{\omega^2}{c^2} - k_{rn}^2 \right) \Psi_n = 0, \tag{2.32}$$

and $\Phi_m(\phi)$ are the azimuthal eigenfunctions satisfying Eq. (2.24), i.e.

$$\frac{\mathrm{d}^2\Phi_m}{\mathrm{d}\phi^2} + m^2\Phi_m = 0,\ m = 0, 1, 2, \ldots, \tag{2.33}$$

and $\Phi_m(\phi)$ are in the form

$$\Phi_m(\phi) = e_m \cos m(\phi - \phi_s),\ m = 0, 1, 2, \ldots, \tag{2.34}$$

where ϕ_s is the azimuthal angle of the point source.

By substituting Eq. (2.31) into Eq. (2.30), together with Eqs. (2.32) and (2.33), we obtain

$$\begin{aligned}
& \sum_m \sum_n \left[\frac{1}{r}\frac{\mathrm{d}}{\mathrm{d}r}\left(r\frac{\mathrm{d}R_{mn}}{\mathrm{d}r}\right)\Psi_n\Phi_m + \frac{1}{r^2}\frac{\mathrm{d}^2\Phi_m}{\mathrm{d}\phi^2}R_{mn}\Psi_n + \rho\frac{\mathrm{d}}{\mathrm{d}z}\left(\frac{1}{\rho}\frac{\mathrm{d}\Psi_n}{\mathrm{d}z}\right)R_{mn}\Phi_m + \frac{\omega^2}{c^2}R_{mn}\Psi_n\Phi_m\right] \\
= & \sum_m \sum_n \left[\frac{1}{r}\frac{\mathrm{d}}{\mathrm{d}r}\left(r\frac{\mathrm{d}R_{mn}}{\mathrm{d}r}\right)\Psi_n\Phi_m + \frac{1}{r^2}\left(-m^2\Phi_m\right)R_{mn}\Psi_n + k_{rn}^2 R_{mn}\Psi_n\Phi_m\right] \\
= & \sum_m \sum_n \left[\frac{1}{r}\frac{\mathrm{d}}{\mathrm{d}r}\left(r\frac{\mathrm{d}R_{mn}}{\mathrm{d}r}\right) + \left(k_{rn}^2 - \frac{m^2}{r^2}\right)R_{mn}\right]\Psi_n\Phi_m \\
= & -\frac{\delta(r - r_s)}{r}\delta(z - z_s)\delta(\phi - \phi_s).
\end{aligned} \tag{2.35}$$

We may eliminate $\Psi_n(z)$ and $\Phi_m(\phi)$ from Eq. (2.35) by applying the orthonormal relations of $\Psi_n(z)$ and $\Phi_m(\phi)$, and we can see that, as shown below, different orthonormal relations of $\Phi_m(\phi)$ lead to different equations for $R_{mn}(r)$. For example, below are two choices:

1) The orthonormal relation used in Taroudarkis's work [20] and in Eskenazi's work [6]:

$$\int_{-\pi}^{\pi} \Phi_m(\phi)\Phi_n(\phi)\mathrm{d}\phi = \delta_{mn}, \tag{2.36}$$

together with corresponding expansion coefficients e_m as

$$e_m = \begin{cases} \frac{1}{\sqrt{2\pi}}, & m = 0, \\ \frac{1}{\sqrt{\pi}}, & m \neq 0. \end{cases} \tag{2.37}$$

The above orthonormal relation is adopted in my work.

2) The orthonormal relation used in Athanassoulis and Propathopoulos's work [3]:

$$\delta(\phi) = \frac{1}{\pi}\sum_{m=0}^{\infty} e_m \cos m\phi, \tag{2.38}$$

together with corresponding expansion coefficients e_m as

$$e_m = \begin{cases} \frac{1}{2}, & m = 0, \\ 1, & m \neq 0. \end{cases} \tag{2.39}$$

Besides different expansion coefficients e_m, these two kinds of orthonormal relations lead to different range-dependent equations for $R_{mn}(r)$, as shown below:

1) The equation for $R_{mn}(r)$ using the orthonormal relation $\int_{-\pi}^{\pi} \Phi_m(\phi)\Phi_n(\phi)\mathrm{d}\phi = \delta_{mn}$

First, we apply the operator $\int_{-\pi}^{\pi} \Phi_\mu(\phi)(\cdot)\mathrm{d}\phi$ to Eq. (2.35) and obtain

$$\sum_n \left[\frac{1}{r}\frac{\mathrm{d}}{\mathrm{d}r}\left(r\frac{\mathrm{d}R_{\mu n}}{\mathrm{d}r}\right) + \left(k_{rn}^2 - \frac{\mu^2}{r^2}\right) R_{\mu n}\right]\Psi_n = -\frac{\delta(r-r_s)}{r}\delta(z-z_s)\Phi_\mu(\phi_s). \tag{2.40}$$

Next, we apply the operator $\int_0^\infty \frac{1}{\rho(z)}\Psi_\nu(z)(\cdot)\mathrm{d}z$ to Eq. (2.40) and obtain

$$\frac{1}{r}\frac{\mathrm{d}}{\mathrm{d}r}\left(r\frac{\mathrm{d}R_{\mu\nu}}{\mathrm{d}r}\right) + \left(k_{r\nu}^2 - \frac{\mu^2}{r^2}\right) R_{\mu\nu} = -\frac{\delta(r-r_s)}{r}\frac{\Psi_\nu(z_s)}{\rho(z_s)}\Phi_\mu(\phi_s), \tag{2.41}$$

or, rewritten in m and n,

$$\frac{1}{r}\frac{\mathrm{d}}{\mathrm{d}r}\left(r\frac{\mathrm{d}R_{mn}}{\mathrm{d}r}\right) + \left(k_{rn}^2 - \frac{m^2}{r^2}\right) R_{mn} = -\frac{\delta(r-r_s)}{r}\frac{\Psi_n(z_s)}{\rho(z_s)}\Phi_m(\phi_s). \tag{2.42}$$

Eq. (2.42) is the equation for $R_{mn}(r)$ with the orthonormal relation of $\Phi_m(\phi)$ as $\int_{-\pi}^{\pi} \Phi_m(\phi)\Phi_n(\phi)\mathrm{d}\phi = \delta_{mn}$.

2) The equation for $R_{mn}(r)$ using the orthonormal relation $\delta(\phi) = \frac{1}{\pi}\sum_{m=0}^{\infty} e_m \cos m\phi$

We still begin with Eq. (2.35). Now we have

$$\delta(\phi-\phi_s)=\frac{1}{\pi}\sum_{m=0}^{\infty}e_m\cos m(\phi-\phi_s)=\frac{1}{\pi}\sum_{m=0}^{\infty}\Phi_m(\phi). \tag{2.43}$$

By substituting Eq. (2.43) into Eq. (2.35), we obtain

$$\begin{aligned}&\sum_{m=0}^{\infty}\sum_{n=1}^{\infty}\left[\frac{1}{r}\frac{\mathrm{d}}{\mathrm{d}r}\left(r\frac{\mathrm{d}R_{mn}}{\mathrm{d}r}\right)+\left(k_{rn}^2-\frac{m^2}{r^2}\right)R_{mn}\right]\Psi_n(z)\Phi_m(\phi)\\ &=-\frac{\delta(r-r_s)}{r}\delta(z-z_s)\frac{1}{\pi}\sum_{m=0}^{\infty}\Phi_m(\phi),\end{aligned} \tag{2.44}$$

which leads to

$$\sum_{n=1}^{\infty}\left[\frac{1}{r}\frac{\mathrm{d}}{\mathrm{d}r}\left(r\frac{\mathrm{d}R_{mn}}{\mathrm{d}r}\right)+\left(k_{rn}^2-\frac{m^2}{r^2}\right)R_{mn}\right]\Psi_n(z)=-\frac{1}{\pi}\frac{\delta(r-r_s)}{r}\delta(z-z_s). \tag{2.45}$$

Apply $\int_0^\infty \frac{1}{\rho(z)}\Psi_\nu(z)(\cdot)\mathrm{d}z$ to Eq. (2.45) and obtain

$$\frac{1}{r}\frac{\mathrm{d}}{\mathrm{d}r}\left(r\frac{\mathrm{d}R_{m\nu}}{\mathrm{d}r}\right)+\left(k_{r\nu}^2-\frac{m^2}{r^2}\right)R_{m\nu}=-\frac{1}{\pi}\frac{\delta(r-r_s)}{r}\frac{\Psi_\nu(z_s)}{\rho(z_s)}, \tag{2.46}$$

or rewritten in m and n,

$$\frac{1}{r}\frac{\mathrm{d}}{\mathrm{d}r}\left(r\frac{\mathrm{d}R_{mn}}{\mathrm{d}r}\right)+\left(k_{rn}^2-\frac{m^2}{r^2}\right)R_{mn}=-\frac{1}{\pi}\frac{\delta(r-r_s)}{r}\frac{\Psi_n(z_s)}{\rho(z_s)}. \tag{2.47}$$

Eq. (2.47) is the equation for $R_{mn}(r)$ with the orthonormal relation of $\Phi_m(\phi)$ as $\delta(\phi)=\frac{1}{\pi}\sum_{m=0}^{\infty}e_m\cos m\phi$.

By comparing Eq. (2.42) and Eq. (2.47), we can see that different orthonormal relations of azimuthal eigenfunctions $\Phi_m(\phi)$ lead to different range-dependent equations for $R_{mn}(r)$. But both Eq. (2.42) and Eq. (2.47) are mth-order Bessel equations, so we may uniformly represent their solutions as

$$R_{mn}(r)=A_{mn}H_m^{(1)}(k_{rn}r)+B_{mn}H_m^{(2)}(k_{rn}r). \tag{2.48}$$

As illustrated in later chapters and in Appendix E, we prefer to choose $H_m^{(1)}(k_{rn}r)$ and $J_m(k_{rn}r)$, instead of $H_m^{(1)}(k_{rn}r)$ and $H_m^{(2)}(k_{rn}r)$, as the two linearly independent solutions to Eq. (2.42) and Eq. (2.47).

2.2.3 Source Conditions of the Inhomogeneous Three-Dimensional Helmholtz Equation

Source conditions are important in developing the three-dimensional spectral normal mode model, which gives the analytical forms of the incident coefficients. Fig. 2-4 illustrates a range-dependent waveguide with an arbitrary deformation and a point source in the water column.

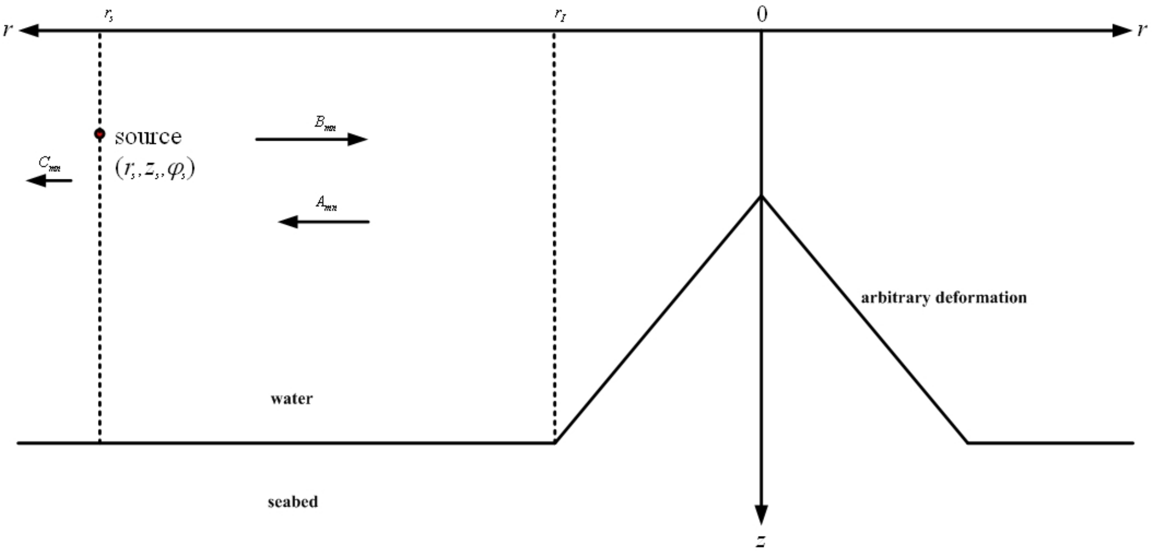

Figure 2-4: To obtain B_{mn} with source conditions.

From Section 2.2.2, the field is represented as

$$p(r, z, \phi) = \sum_{m=0}^{\infty} \sum_{n=1}^{\infty} R_{mn}(r)\Psi_n(z)\Phi_m(\phi), \tag{2.49}$$

with $\Psi_n(z)$ satisfying Eq. (2.22) and $\Phi_m(\phi)$ satisfying Eq. (2.24), and

$$\Phi_m(\phi) = e_m \cos m(\phi - \phi_s), \; m = 0, 1, 2, \ldots \tag{2.50}$$

$R_{mn}(r)$ is represented as

1) $r_I \le r < r_s$,

$$R_{mn}(r) = A_{mn}H_m^{(1)}(k_{rn}r) + B_{mn}H_m^{(2)}(k_{rn}r);\ \text{and} \tag{2.51}$$

2) $r \ge r_s$,

$$R_{mn}(r) = C_{mn}H_m^{(1)}(k_{rn}r). \tag{2.52}$$

With boundary conditions at $r = r_s$, we may obtain B_{mn} and C_{mn} in terms of A_{mn}. From Section 2.2.2 we know that two different orthonormal relations of $\Phi_m(\phi)$ may be applied, leading to different expansion coefficients e_m and different equations for $R_{mn}(r)$. Besides, from below we can see that they also lead to different source conditions. Denote the field in the region $r_I \le r < r_s$ by $p^-(r,z,\phi)$ and the field in the region $r \ge r_s$ by $p^+(r,z,\phi)$. We omit the argument $k_{rn}r_s$ for simplicity.

1) **Source conditions with the orthonormal relation $\int_{-\pi}^{\pi}\Phi_m(\phi)\Phi_n(\phi)\mathrm{d}\phi = \delta_{mn}$**

   (a) Pressure continuity at $r = r_s$ gives

$$p^-(r_s,z,\phi) = p^+(r_s,z,\phi). \tag{2.53}$$

By substituting Eqs. (2.51) and (2.52) into Eq. (2.53) we obtain

$$\sum_m\sum_n \left[B_{mn}H_m^{(2)} + A_{mn}H_m^{(1)}\right]\Psi_n(z)\Phi_m(\phi) = \sum_m\sum_n C_{mn}H_m^{(1)}\Psi_n(z)\Phi_m(\phi), \tag{2.54}$$

which leads to

$$B_{mn}H_m^{(2)} + A_{mn}H_m^{(1)} = C_{mn}H_m^{(1)}. \tag{2.55}$$

   (b) Normal particle velocity jumps at $r = r_s$.

From Eq. (2.42), now the equation for $R_{mn}(r)$ is

$$\frac{\mathrm{d}^2R_{mn}}{\mathrm{d}r^2} + \frac{1}{r}\frac{\mathrm{d}R_{mn}}{\mathrm{d}r} + \left(k_{rn}^2 - \frac{m^2}{r^2}\right)R_{mn} = -\frac{\delta(r-r_s)}{r}\frac{\Psi_n(z_s)}{\rho(z_s)}\Phi_m(\phi_s), \tag{2.56}$$

by integrating Eq. (2.56) over $[r_s^-, r_s^+]$, we obtain

$$\left.\frac{\mathrm{d}R_{mn}}{\mathrm{d}r}\right|_{r_s^-}^{r_s^+} = -\frac{1}{r_s}\frac{\Psi_n(z_s)}{\rho(z_s)}\Phi_m(\phi_s). \tag{2.57}$$

By substituting Eqs. (2.51) and (2.52) into Eq. (2.57), with notation

$$S \triangleq \frac{1}{r_s}\frac{\Psi_n(z_s)}{\rho(z_s)}\Phi_m(\phi_s), \tag{2.58}$$

we obtain

$$C_{mn}\frac{\mathrm{d}H_m^{(1)}}{\mathrm{d}r} - B_{mn}\frac{\mathrm{d}H_m^{(2)}}{\mathrm{d}r} - A_{mn}\frac{\mathrm{d}H_m^{(1)}}{\mathrm{d}r} = -S. \tag{2.59}$$

To solve B_{mn} and C_{mn} in terms of A_{mn}, rewrite Eqs. (2.55) and (2.59) as

$$B_{mn}H_m^{(2)} - C_{mn}H_m^{(1)} = -A_{mn}H_m^{(1)}, \text{ and} \tag{2.60}$$

$$B_{mn}\frac{\mathrm{d}H_m^{(2)}}{\mathrm{d}r} - C_{mn}\frac{\mathrm{d}H_m^{(1)}}{\mathrm{d}r} = -A_{mn}\frac{\mathrm{d}H_m^{(1)}}{\mathrm{d}r} + S. \tag{2.61}$$

To use Cramer's rule to obtain B_{mn}, first we find the determinants

$$\begin{aligned}
D &= \begin{vmatrix} H_m^{(2)} & -H_m^{(1)} \\ \frac{\mathrm{d}H_m^{(2)}}{\mathrm{d}r} & -\frac{\mathrm{d}H_m^{(1)}}{\mathrm{d}r} \end{vmatrix} \\
&= -\frac{\mathrm{d}H_m^{(1)}}{\mathrm{d}r}H_m^{(2)} + H_m^{(1)}\frac{\mathrm{d}H_m^{(2)}}{\mathrm{d}r} \\
&= H_m^{(1)}k_{rn}\frac{\mathrm{d}H_m^{(2)}}{\mathrm{d}(k_{rn}r)} - k_{rn}\frac{\mathrm{d}H_m^{(1)}}{\mathrm{d}(k_{rn}r)}H_m^{(2)} \\
&= k_{rn}W\left[H_m^{(1)}, H_m^{(2)}\right] \\
&= k_{rn}\left(-\frac{4i}{\pi k_{rn}r_s}\right) \\
&= -\frac{4i}{\pi r_s},
\end{aligned} \tag{2.62}$$

and

$$\begin{aligned}
N_B &= \begin{vmatrix} -A_{mn}H_m^{(1)} & -H_m^{(1)} \\ -A_{mn}\frac{\mathrm{d}H_m^{(1)}}{\mathrm{d}r} + S & -\frac{\mathrm{d}H_m^{(1)}}{\mathrm{d}r} \end{vmatrix} \\
&= A_{mn}H_m^{(1)}\frac{\mathrm{d}H_m^{(1)}}{\mathrm{d}r} - A_{mn}H_m^{(1)}\frac{\mathrm{d}H_m^{(1)}}{\mathrm{d}r} + SH_m^{(1)} \\
&= SH_m^{(1)}. \qquad (2.63)
\end{aligned}$$

Note that the Wronskian relation

$$W\left[H_m^{(1)}(z), H_m^{(2)}(z)\right] = -\frac{4i}{\pi z}, \qquad (2.64)$$

is used in obtaining Eq. (2.62). The Wronskian relations of Bessel and Hankel functions are listed in Appendix D.

Now we may solve B_{mn},

$$\begin{aligned}
B_{mn} &= \frac{N_B}{D} \\
&= \frac{i}{4}\pi r_s S H_m^{(1)}(k_{rn}r_s) \\
&= \frac{i}{4}\pi r_s \frac{1}{r_s}\frac{\Psi_n(z_s)}{\rho(z_s)}\Phi_m(\phi_s)H_m^{(1)}(k_{rn}r_s) \\
&= \frac{i}{4}\pi \frac{\Psi_n(z_s)}{\rho(z_s)}\Phi_m(\phi_s)H_m^{(1)}(k_{rn}r_s). \qquad (2.65)
\end{aligned}$$

By substituting Eq. (2.65) into Eq. (2.60), we obtain C_{mn},

$$C_{mn} = A_{mn} + B_{mn}\frac{H_m^{(2)}(k_{rn}r_s)}{H_m^{(1)}(k_{rn}r_s)} = A_{mn} + \frac{i}{4}\pi\frac{\Psi_n(z_s)}{\rho(z_s)}\Phi_m(\phi_s)H_m^{(2)}(k_{rn}r_s). \qquad (2.66)$$

2) **Source conditions with the orthonormal relation $\delta(\phi) = \frac{1}{\pi}\sum_{m=0}^{\infty} e_m \cos m\phi$**

Follow the same derivation as before, noticing that from Eq. (2.47), now the term S takes the form

$$S = \frac{1}{\pi}\frac{1}{r_s}\frac{\Psi_n(z_s)}{\rho(z_s)}, \qquad (2.67)$$

which leads to

$$B_{mn} = \frac{N_B}{D} = \frac{i}{4}\frac{\Psi_n(z_s)}{\rho(z_s)} H_m^{(1)}(k_{rn} r_s), \tag{2.68}$$

and

$$\begin{aligned} C_{mn} &= A_{mn} + B_{mn}\frac{H_m^{(2)}(k_{rn} r_s)}{H_m^{(1)}(k_{rn} r_s)} \\ &= A_{mn} + \frac{i}{4}\frac{\Psi_n(z_s)}{\rho(z_s)} H_m^{(2)}(k_{rn} r_s). \end{aligned} \tag{2.69}$$

Equivalence of Different Orthonormal Relations of $\Phi_m(\phi)$ in Representing the Field

From the previous section, we see that different orthonormal relations of $\Phi_m(\phi)$ lead to different source conditions, especially the expressions of the coefficients of incident wave, B_{mn}. However, as shown below, these two kinds of orthonormal relations are equivalent in representing the field. Below we demonstrate their equivalence in representing the incident field.

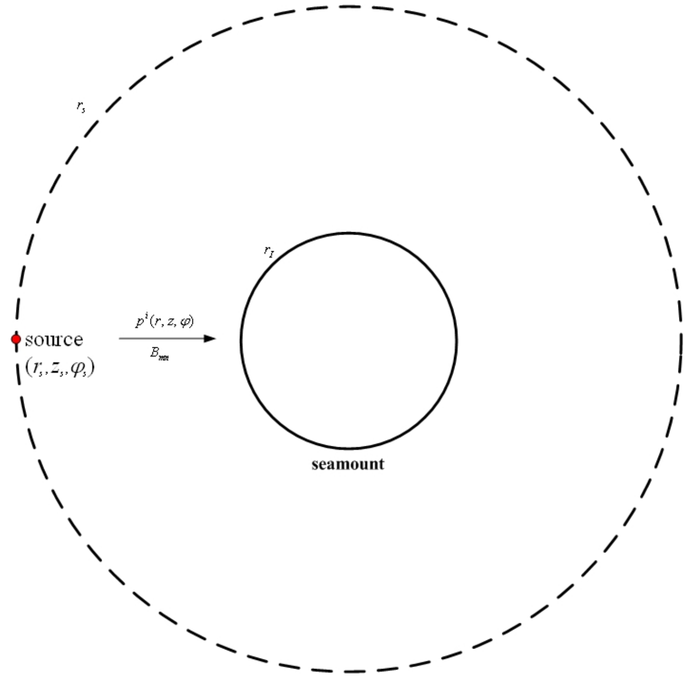

Figure 2-5: The incident field and incident coefficients B_{mn}.

As illustrated in Fig. 2-5, the incident field is

$$p^{(i)}(r,z,\phi)=\sum_{m=0}^{\infty}\sum_{n=1}^{\infty}B_{mn}H_m^{(2)}(k_{rn}r)\Psi_n(z)\Phi_m(\phi). \tag{2.70}$$

1) The incident field with the orthonormal relation $\int_{-\pi}^{\pi}\Phi_m(\phi)\Phi_n(\phi)\mathrm{d}\phi=\delta_{mn}$

From Eq. (2.65), in this case the incident coefficients are

$$B_{mn}=\frac{i}{4}\pi\frac{\Psi_n(z_s)}{\rho(z_s)}\Phi_m(\phi_s)H_m^{(1)}(k_{rn}r_s). \tag{2.71}$$

By substituting Eq. (2.71) into Eq. (2.70) we obtain

$$\begin{aligned}
p^{(i)}(r,z,\phi) &= \frac{i}{4\rho(z_s)}\pi\sum_{m=0}^{\infty}\sum_{n=1}^{\infty}H_m^{(1)}(k_{rn}r_s)H_m^{(2)}(k_{rn}r)\Psi_n(z_s)\Psi_n(z)\Phi_m(\phi_s)\Phi_m(\phi)\\
&= \frac{i}{4\rho(z_s)}\pi\left[\sum_{n=1}^{\infty}H_0^{(1)}(k_{rn}r_s)H_0^{(2)}(k_{rn}r)\Psi_n(z_s)\Psi_n(z)e_0^2\right.\\
&+ \left.\sum_{m=1}^{\infty}\sum_{n=1}^{\infty}H_m^{(1)}(k_{rn}r_s)H_m^{(2)}(k_{rn}r)\Psi_n(z_s)\Psi_n(z)e_m^2\cos m(\phi_s-\phi_s)\cos m(\phi-\phi_s)\right]\\
& \quad e_0=1/\sqrt{2\pi};\ e_m=1/\sqrt{\pi},\ m\neq 0\\
&= \frac{i}{4\rho(z_s)}\left[\frac{1}{2}\sum_{n=1}^{\infty}H_0^{(1)}(k_{rn}r_s)H_0^{(2)}(k_{rn}r)\Psi_n(z_s)\Psi_n(z)\right.\\
& \quad \left.+\sum_{m=1}^{\infty}\sum_{n=1}^{\infty}H_m^{(1)}(k_{rn}r_s)H_m^{(2)}(k_{rn}r)\Psi_n(z_s)\Psi_n(z)\cos m(\phi-\phi_s)\right].
\end{aligned} \tag{2.72}$$

2) The incident field with the orthonormal relation $\delta(\phi)=\frac{1}{\pi}\sum_{m=0}^{\infty}e_m\cos m\phi$

From Eq. (2.68), in this case the incident coefficients are

$$B_{mn}=\frac{i}{4}\frac{\Psi_n(z_s)}{\rho(z_s)}H_m^{(1)}(k_{rn}r_s). \tag{2.73}$$

By substituting Eq. (2.73) into Eq. (2.70) we obtain

$$\begin{aligned}
p^{(i)}(r,z,\phi) &= \frac{i}{4\rho(z_s)}\sum_{m=0}^{\infty}\sum_{n=1}^{\infty} H_m^{(1)}(k_{rn}r_s)H_m^{(2)}(k_{rn}r)\Psi_n(z_s)\Psi_n(z)\Phi_m(\phi) \\
&= \frac{i}{4\rho(z_s)}\left[\sum_{n=1}^{\infty} H_0^{(1)}(k_{rn}r_s)H_0^{(2)}(k_{rn}r)\Psi_n(z_s)\Psi_n(z)e_0\right. \\
&\quad \left. + \sum_{m=1}^{\infty}\sum_{n=1}^{\infty} H_m^{(1)}(k_{rn}r_s)H_m^{(2)}(k_{rn}r)\Psi_n(z_s)\Psi_n(z)e_m\cos m(\phi-\phi_s)\right] \\
&\quad e_0 = \frac{1}{2};\ e_m = 1,\ m \neq 0 \\
&= \frac{i}{4\rho(z_s)}\left[\frac{1}{2}\sum_{n=1}^{\infty} H_0^{(1)}(k_{rn}r_s)H_0^{(2)}(k_{rn}r)\Psi_n(z_s)\Psi_n(z)\right. \\
&\quad \left. + \sum_{m=1}^{\infty}\sum_{n=1}^{\infty} H_m^{(1)}(k_{rn}r_s)H_m^{(2)}(k_{rn}r)\Psi_n(z_s)\Psi_n(z)\cos m(\phi-\phi_s)\right].
\end{aligned} \tag{2.74}$$

By comparing Eq. (2.72) and Eq. (2.74) we can see that we obtain an identical expression for the incident field using these two kinds of orthonormal relations of $\Phi_m(\phi)$, which means they are equivalent in representing the field.

Source Conditions with Normalized Bessel and Hankel Functions, together with the Orthonormal Relation $\int_{-\pi}^{\pi}\Phi_m(\phi)\Phi_n(\phi)d\phi = \delta_{mn}$

In the above, we give the source conditions with $R_{mn}(r)$ represented as a combination of unnormalized Hankel functions, $H_m^{(1)}(k_{rn}r)$ and $H_m^{(2)}(k_{rn}r)$. Next we will give the source conditions corresponding to $R_{mn}(r)$ being represented in the form as below:

1) $r_I \le r < r_s$,

$$R_{mn}(r) = a_{mn}\frac{H_m^{(1)}(k_{rn}r)}{H_m^{(1)}(k_{rn}r_I)} + b_{mn}J_m(k_{rn}r)H_m^{(1)}(k_{rn}r_s);\ \text{and} \tag{2.75}$$

2) $r \ge r_s$,

$$R_{mn}(r) = c_{mn}\frac{H_m^{(1)}(k_{rn}r)}{H_m^{(1)}(k_{rn}r_s)}. \tag{2.76}$$

With the orthonormal relation $\int_{-\pi}^{\pi}\Phi_m(\phi)\Phi_n(\phi)\mathrm{d}\phi = \delta_{mn}$, instead of solving b_{mn} and c_{mn} as before, we may change $R_{mn}(r)$ in Eqs. (2.75) and (2.76) into the forms in Eqs. (2.51) and (2.52), then make use of the results in Eq. (2.65) and Eq. (2.66).

Since

$$J_m(k_{rn}r) = \frac{1}{2}\left[H_m^{(1)}(k_{rn}r) + H_m^{(2)}(k_{rn}r)\right], \tag{2.77}$$

we may rewrite Eq. (2.75) as

$$\begin{aligned} R_{mn}(r) &= a_{mn}\frac{H_m^{(1)}(k_{rn}r)}{H_m^{(1)}(k_{rn}r_I)} + b_{mn}\frac{1}{2}\left[H_m^{(1)}(k_{rn}r) + H_m^{(2)}(k_{rn}r)\right]H_m^{(1)}(k_{rn}r_s) \\ &= \left[\frac{a_{mn}}{H_m^{(1)}(k_{rn}r_I)} + \frac{1}{2}b_{mn}H_m^{(1)}(k_{rn}r_s)\right]H_m^{(1)}(k_{rn}r) + \frac{1}{2}b_{mn}H_m^{(1)}(k_{rn}r_s)H_m^{(2)}(k_{rn}r) \\ &= A_{mn}H_m^{(1)}(k_{rn}r) + B_{mn}H_m^{(2)}(k_{rn}r), \end{aligned} \tag{2.78}$$

from which we obtain

$$\frac{a_{mn}}{H_m^{(1)}(k_{rn}r_I)} + \frac{1}{2}b_{mn}H_m^{(1)}(k_{rn}r_s) = A_{mn}, \tag{2.79}$$

and

$$\frac{1}{2}b_{mn}H_m^{(1)}(k_{rn}r_s) = B_{mn}. \tag{2.80}$$

By substituting Eq. (2.65) into Eq. (2.80) we also obtain

$$\begin{aligned} b_{mn} &= \frac{2B_{mn}}{H_m^{(1)}(k_{rn}r_s)} \\ &= \frac{2}{H_m^{(1)}(k_{rn}r_s)}\frac{i}{4}\pi\frac{\Psi_n(z_s)}{\rho(z_s)}\Phi_m(\phi_s)H_m^{(1)}(k_{rn}r_s) \\ &= \frac{i}{2}\pi\frac{\Psi_n(z_s)}{\rho(z_s)}\Phi_m(\phi_s). \end{aligned} \tag{2.81}$$

To obtain c_{mn}, since in the region $r \geq r_s$,

$$R_{mn}(r) = c_{mn}\frac{H_m^{(1)}(k_{rn}r)}{H_m^{(1)}(k_{rn}r_s)} = C_{mn}H_m^{(1)}(k_{rn}r), \tag{2.82}$$

we obtain

$$
\begin{aligned}
c_{mn} &= C_{mn} H_m^{(1)}(k_{rn} r_s) \\
&= \left[A_{mn} + B_{mn} \frac{H_m^{(2)}(k_{rn} r_s)}{H_m^{(1)}(k_{rn} r_s)} \right] H_m^{(1)}(k_{rn} r_s) \\
&= \left[\frac{a_{mn}}{H_m^{(1)}(k_{rn} r_I)} + \frac{1}{2} b_{mn} H_m^{(1)}(k_{rn} r_s) + \frac{1}{2} b_{mn} H_m^{(1)}(k_{rn} r_s) \frac{H_m^{(2)}(k_{rn} r_s)}{H_m^{(1)}(k_{rn} r_s)} \right] H_m^{(1)}(k_{rn} r_s) \\
&= \left[\frac{a_{mn}}{H_m^{(1)}(k_{rn} r_I)} + \frac{1}{2} b_{mn} \left(H_m^{(1)}(k_{rn} r_s) + H_m^{(2)}(k_{rn} r_s) \right) \right] H_m^{(1)}(k_{rn} r_s) \\
&= a_{mn} \frac{H_m^{(1)}(k_{rn} r_s)}{H_m^{(1)}(k_{rn} r_I)} + b_{mn} J_m(k_{rn} r_s) H_m^{(1)}(k_{rn} r_s) \qquad (2.83) \\
&= a_{mn} \frac{H_m^{(1)}(k_{rn} r_s)}{H_m^{(1)}(k_{rn} r_I)} + \frac{i}{2} \pi \frac{\Psi_n(z_s)}{\rho(z_s)} \Phi_m(\phi_s) J_m(k_{rn} r_s) H_m^{(1)}(k_{rn} r_s). \qquad (2.84)
\end{aligned}
$$

2.2.4 Equivalence of the Two-Dimensional Normal Mode Solution and the Three-Dimensional Spectral Normal Mode Solution

In this section we will show the equivalence of the two-dimensional normal mode solution and the three-dimensional spectral normal mode solution to range-independent problems. This equivalence allows us to use the superposition method to obtain the solution outside the seamount (or cylinder) region for range-dependent problems, by means of replacing the incident part of the three-dimensional spectral normal mode solution by the two-dimensional normal mode solution.

The Two-Dimensional Normal Mode Solution and the Three-Dimensional Spectral Normal Mode Solution to a Range-Independent Waveguide Propagation Problem

We can solve a range-independent problem by either the two-dimensional normal mode solution or the three-dimensional spectral normal mode solution. Below we will show the equivalence of these two kinds of solutions.

Fig. 2-6 illustrates a range-independent waveguide propagation problem. The

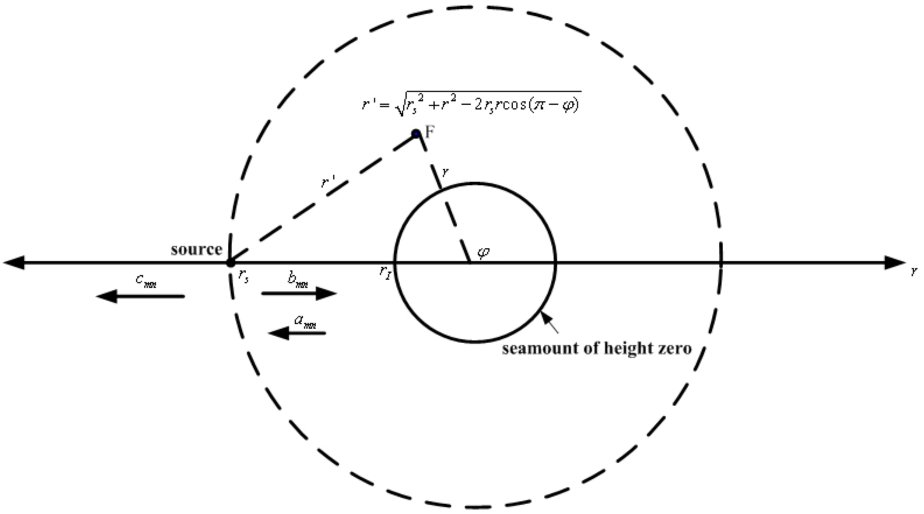

Figure 2-6: A range-independent waveguide (top view).

two-dimensional normal mode solution to this problem is well-known [12],

$$p(r', z) = \frac{i}{4\rho(z_s)} \sum_{n=1}^{\infty} \Psi_n(z_s)\Psi_n(z)H_0^{(1)}(k_{rn}r'), \tag{2.85}$$

where r' is the range of a field point F with respect to the source, and as $\phi_s = \pi$, r' is expressed as

$$r' = \sqrt{r^2 + r_s^2 - 2rr_s\cos(\phi - \phi_s)} = \sqrt{r^2 + r_s^2 - 2rr_s\cos(\pi - \phi)}. \tag{2.86}$$

Next we will seek the equivalent three-dimensional spectral normal mode solution to this range-independent problem. From Section 2.2.3 we know that the spectral normal mode solution is in the following form,

$$p(r, z, \phi) = \sum_{m=0}^{\infty} \sum_{n=1}^{\infty} R_{mn}(r)\Psi_n(z)\Phi_m(\phi), \tag{2.87}$$

where $R_{mn}(r)$ takes different forms in regions $r_s > r \geq r_I$ and $r \geq r_s$:

1) for $r_s > r \geq r_I$,

$$R_{mn}(r) = a_{mn}\frac{H_m^{(1)}(k_{rn}r)}{H_m^{(1)}(k_{rn}r_I)} + b_{mn}J_m(k_{rn}r)H_m^{(1)}(k_{rn}r_s);\text{ and} \tag{2.88}$$

2) for $r \geq r_s$,

$$\begin{aligned} R_{mn}(r) &= c_{mn}\frac{H_m^{(1)}(k_{rn}r)}{H_m^{(1)}(k_{rn}r_s)} \\ &= \left[a_{mn}\frac{H_m^{(1)}(k_{rn}r_s)}{H_m^{(1)}(k_{rn}r_I)} + b_{mn}J_m(k_{rn}r_s)H_m^{(1)}(k_{rn}r_s)\right]\frac{H_m^{(1)}(k_{rn}r)}{H_m^{(1)}(k_{rn}r_s)} \\ &= a_{mn}\frac{H_m^{(1)}(k_{rn}r)}{H_m^{(1)}(k_{rn}r_I)} + b_{mn}J_m(k_{rn}r_s)H_m^{(1)}(k_{rn}r). \end{aligned} \tag{2.89}$$

In Eqs. (2.88) and (2.89),

$$b_{mn} = \frac{i}{2}\frac{\pi}{\rho(z_s)}\Psi_n(z_s)\Phi_m(\phi_s). \tag{2.90}$$

For range-independent problems, we have $a_{mn} = 0$ and thus $R_{mn}(r)$ reduces to:

1) for $r_s > r \geq r_I$,

$$\begin{aligned} R_{mn}(r) &= b_{mn}J_m(k_{rn}r)H_m^{(1)}(k_{rn}r_s) \\ &= \frac{i}{2}\frac{\pi}{\rho(z_s)}\Psi_n(z_s)\Phi_m(\phi_s)J_m(k_{rn}r)H_m^{(1)}(k_{rn}r_s); \text{ and} \end{aligned} \tag{2.91}$$

2) for $r \geq r_s$,

$$\begin{aligned} R_{mn}(r) &= b_{mn}J_m(k_{rn}r_s)H_m^{(1)}(k_{rn}r) \\ &= \frac{i}{2}\frac{\pi}{\rho(z_s)}\Psi_n(z_s)\Phi_m(\phi_s)J_m(k_{rn}r_s)H_m^{(1)}(k_{rn}r). \end{aligned} \tag{2.92}$$

From the above, we find the relation between the two-dimensional normal mode solution and the three-dimensional spectral normal mode solution:

$$p(r', z) = \frac{i}{4\rho(z_s)} \sum_{n=1}^{\infty} \Psi_n(z_s)\Psi_n(z) H_0^{(1)}(k_{rn} r') \tag{2.93}$$

$$= \begin{cases} \frac{i}{2}\frac{\pi}{\rho(z_s)} \sum_{m=0}^{\infty}\sum_{n=1}^{\infty} \Psi_n(z_s)\Psi_n(z) J_m(k_{rn} r) H_m^{(1)}(k_{rn} r_s)\Phi_m(\phi_s)\Phi_m(\phi), & r_s > r \geq r_I; \\ \frac{i}{2}\frac{\pi}{\rho(z_s)} \sum_{m=0}^{\infty}\sum_{n=1}^{\infty} \Psi_n(z_s)\Psi_n(z) J_m(k_{rn} r_s) H_m^{(1)}(k_{rn} r)\Phi_m(\phi_s)\Phi_m(\phi), & r \geq r_s \end{cases}$$

$$= \frac{i}{2}\frac{\pi}{\rho(z_s)} \sum_{m=0}^{\infty}\sum_{n=1}^{\infty} \Psi_n(z_s)\Psi_n(z) J_m(k_{rn} r_<) H_m^{(1)}(k_{rn} r_>)\Phi_m(\phi_s)\Phi_m(\phi), \tag{2.94}$$

where $r_< = \min(r, r_s)$ and $r_> = \max(r, r_s)$.

The relation between the expression in Eq. (2.93) and that in Eq. (2.94) can also be reached mathematically. From [9, p.930] we have the so-called "summation theorem" for Bessel functions:

> Suppose that $r > 0$, $\rho > 0$, $\phi > 0$, and $R = \sqrt{r^2 + \rho^2 - 2r\rho\cos\phi}$; that is, suppose that r, ρ, and R are the sides of a triangle such that the angle between the sides r and ρ is equal to ϕ. Suppose also that $\rho < r$. When these conditions are satisfied, we have
>
> $$H_0^{(1,2)}(kR) = J_0(k\rho)H_0^{(1,2)}(kr) + 2\sum_{m=1}^{\infty} J_m(k\rho)H_m^{(1,2)}(kr)\cos m\phi, \tag{2.95}$$
>
> where k is an arbitrary complex number.

To prove the equity of the expressions in Eq. (2.93) and that in Eq. (2.94), we only need to prove

$$H_0^{(1)}(k_{rn} r') = 2\pi \sum_{m=0}^{\infty} J_m(k_{rn} r_<) H_m^{(1)}(k_{rn} r_>)\Phi_m(\phi_s)\Phi_m(\phi). \tag{2.96}$$

Since

$$
\begin{aligned}
\Phi_m(\phi_s)\Phi_m(\phi) &= e_m \cos m(\phi_s - \phi_s) e_m \cos m(\phi - \phi_s) \\
&= e_m^2 \cos m(\phi - \phi_s) \\
&= \begin{cases} \frac{1}{2\pi}, & m = 0; \\ \frac{1}{\pi}\cos m(\phi - \phi_s), & m \neq 0, \end{cases}
\end{aligned}
\tag{2.97}
$$

and as shown in Fig. 2-7, $|\phi - \phi_s|$ is the angle between the sides r_s and r, and $r_< = \min(r, r_s)$, $r_> = \max(r, r_s)$, by substituting Eq. (2.97) into right-hand-side (RHS) of Eq. (2.96), we obtain

$$
\begin{aligned}
&\text{RHS of Eq. (2.96)} \\
=&2\pi \left[J_0(k_{rn}r_<)H_0^{(1)}(k_{rn}r_>)\frac{1}{2\pi} + \sum_{m=1}^{\infty} J_m(k_{rn}r_<)H_m^{(1)}(k_{rn}r_>)\frac{1}{\pi}\cos m(\phi - \phi_s) \right] \\
=&J_0(k_{rn}r_<)H_0^{(1)}(k_{rn}r_>) + 2\sum_{m=1}^{\infty} J_m(k_{rn}r_<)H_m^{(1)}(k_{rn}r_>)\cos m(\phi - \phi_s),
\end{aligned}
\tag{2.98}
$$

and with the summation theorem in Eq. (2.95), the expression in Eq. (2.98) is equal to $H_0^{(1)}(k_{rn}r')$. Thus, the equity of the expressions in Eq. (2.93) and Eq. (2.94) is proved.

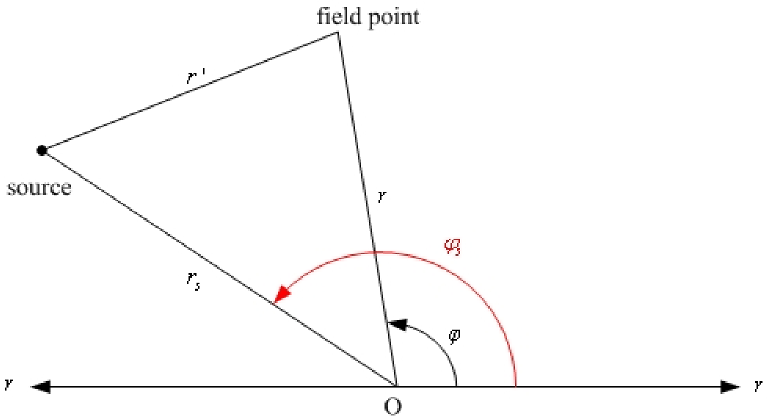

Figure 2-7: The triangle with sides r, r_s and r', with $|\phi_s - \phi|$ as the angle between the sides r_s and r.

The equivalence of the two-dimensional normal mode solution in Eq. (2.93) and the three-dimensional spectral normal mode solution in Eq. (2.94) can be illustrated by a numerical example with a schematic shown in Fig. 2-8. While the range-independent waveguide consists of a 250 m water column bounded above by a pressure-release surface and below by a rigid bottom, the water column is isovelocity with $c_w = 1500$ m/s. A point source is located at 100 m depth below the surface. The results of the two-dimensional normal mode solution in Eq. (2.93) and of the three-dimensional spectral normal mode solution in Eq. (2.94) are shown in Fig. 2-9, from which we can see clearly the equivalence of these two solutions. In addition, we see that in the three-dimensional spectral normal mode method, the number of azimuthal modes leading to convergence is at least $[kr_s]$, where k is the wavenumber in water and $[x]$ rounds x to the nearest integer towards infinity.

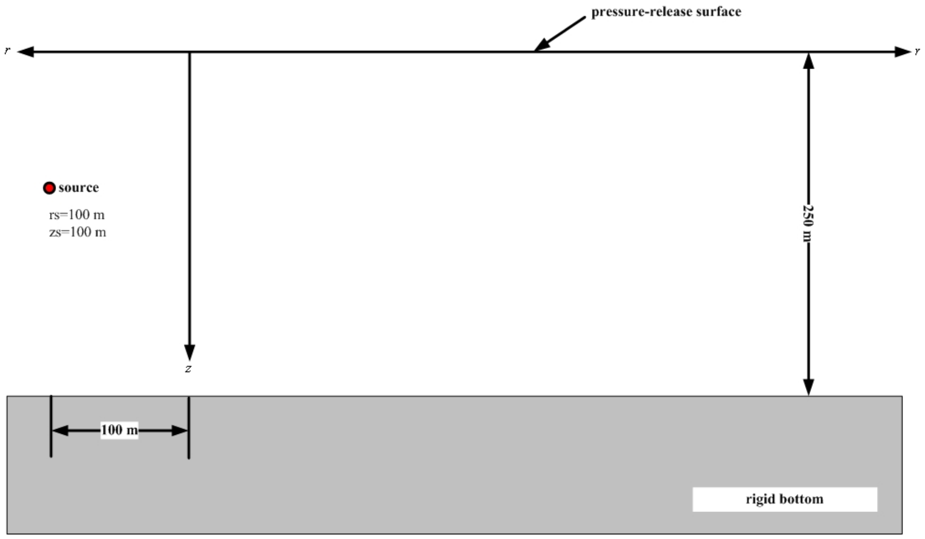

Figure 2-8: The schematic of a range-independent waveguide with a point source.

For a range-independent problem, the 2D normal mode solution is preferable to the 3D spectral normal mode solution in that the 2D normal mode solution consists of only one summation over normal modes, while the 3D spectral normal mode solution consists of two summations, one over normal modes, the other over azimuthal modes. So, for range-dependent problems, with the equivalence of these two solutions, we may apply the superposition method to obtain the field outside the seamount (or cylinder) region to improve efficiency, as illustrated below.

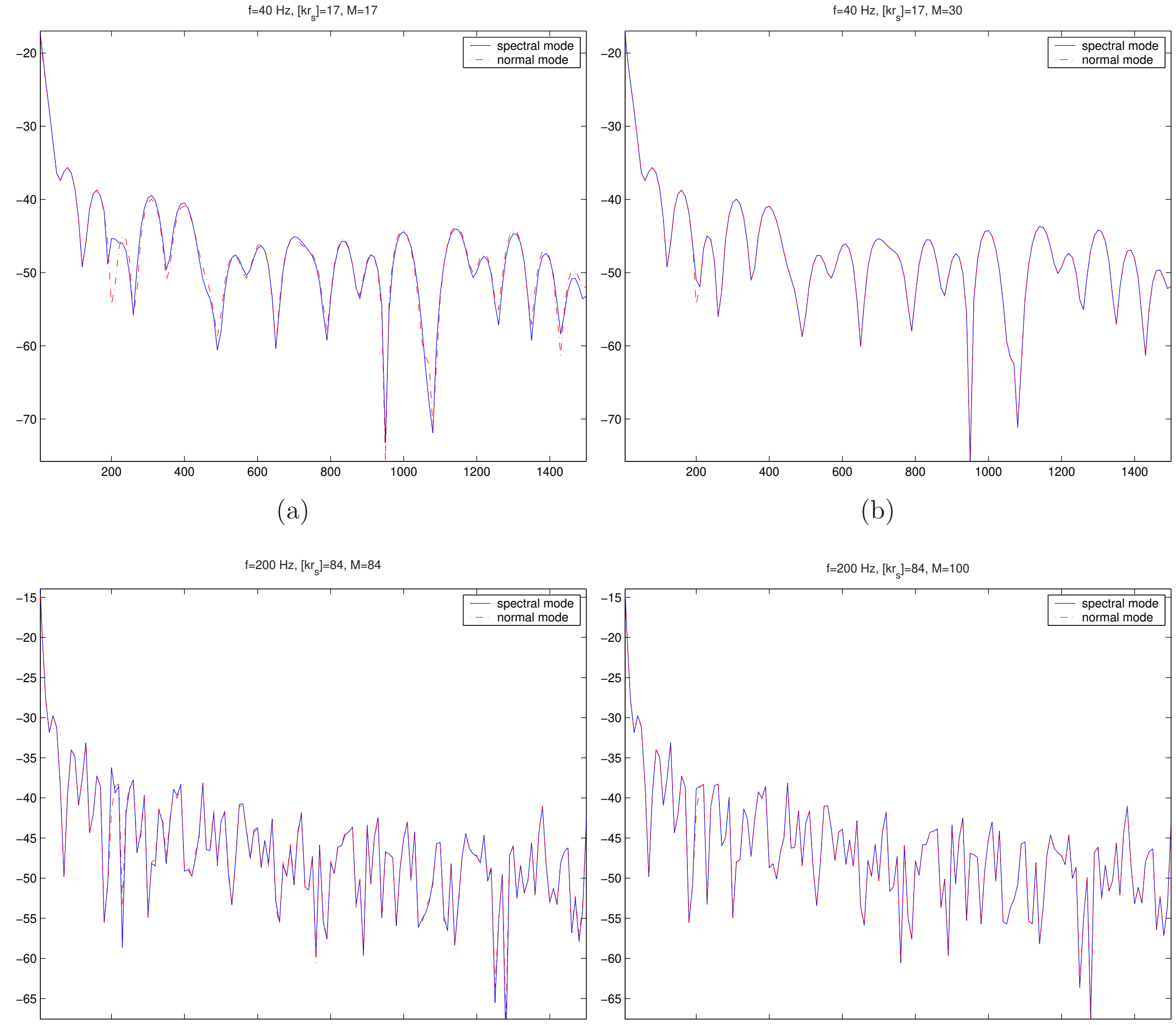

(a) (b)

(c) (d)

Figure 2-9: Transmission loss at depth 100 m, computed by the spectral normal mode method and the normal mode method. (a) $f = 40$ Hz, M=17, almost convergent, (b) $f = 40$ Hz, M=30, convergent; (c) $f = 200$ Hz, M=84, almost convergent, (d) $f = 200$ Hz, M=100, convergent.

Apply the Superposition Method to Obtain the Solution outside the Seamount (or Cylinder) Region

For range-dependent problems involving a seamount (or cylinder) in the waveguide, in the region outside the seamount (or cylinder), $R_{mn}(r)$ takes the form in Eq. (2.88) or Eq. (2.89), with $a_{mn} \neq 0$ (refer to Fig. 2-6). By taking advantage of the equivalence of the 3D spectral normal mode solution and the 2D normal mode solution, we may obtain the acoustic field outside the seamount (or cylinder) region as:

1) for $r_s > r \geq r_I$,

$$\begin{aligned}
&p(r,z,\phi) \\
=&\sum_{m=0}^{\infty}\sum_{n=1}^{\infty}\left[a_{mn}\frac{H_m^{(1)}(k_{rn}r)}{H_m^{(1)}(k_{rn}r_I)}+b_{mn}J_m(k_{rn}r)H_m^{(1)}(k_{rn}r_s)\right]\Psi_n(z)\Phi_m(\phi) \qquad (2.99)\\
=&\sum_{m=0}^{\infty}\sum_{n=1}^{\infty}b_{mn}J_m(k_{rn}r)H_m^{(1)}(k_{rn}r_s)\Psi_n(z)\Phi_m(\phi)+\sum_{m=0}^{\infty}\sum_{n=1}^{\infty}a_{mn}\frac{H_m^{(1)}(k_{rn}r)}{H_m^{(1)}(k_{rn}r_I)}\Psi_n(z)\Phi_m(\phi)\\
=&\frac{i}{4\rho(z_s)}\sum_{n=1}^{\infty}\Psi_n(z_s)\Psi_n(z)H_0^{(1)}(k_{rn}r')+\sum_{m=0}^{\infty}\sum_{n=1}^{\infty}a_{mn}\frac{H_m^{(1)}(k_{rn}r)}{H_m^{(1)}(k_{rn}r_I)}\Psi_n(z)\Phi_m(\phi); \text{ and}
\end{aligned}$$

(2.100)

2) for $r \geq r_s$,

$$\begin{aligned}
&p(r,z,\phi) \\
=&\sum_{m=0}^{\infty}\sum_{n=1}^{\infty}c_{mn}\frac{H_m^{(1)}(k_{rn}r)}{H_m^{(1)}(k_{rn}r_s)}\Psi_n(z)\Phi_m(\phi) \qquad (2.101)\\
=&\sum_{m=0}^{\infty}\sum_{n=1}^{\infty}\left[a_{mn}\frac{H_m^{(1)}(k_{rn}r_s)}{H_m^{(1)}(k_{rn}r_I)}+b_{mn}J_m(k_{rn}r_s)H_m^{(1)}(k_{rn}r_s)\right]\frac{H_m^{(1)}(k_{rn}r)}{H_m^{(1)}(k_{rn}r_s)}\Psi_n(z)\Phi_m(\phi)\\
=&\sum_{m=0}^{\infty}\sum_{n=1}^{\infty}b_{mn}J_m(k_{rn}r_s)H_m^{(1)}(k_{rn}r)\Psi_n(z)\Phi_m(\phi)+\sum_{m=0}^{\infty}\sum_{n=1}^{\infty}a_{mn}\frac{H_m^{(1)}(k_{rn}r)}{H_m^{(1)}(k_{rn}r_I)}\Psi_n(z)\Phi_m(\phi)\\
=&\frac{i}{4\rho(z_s)}\sum_{n=1}^{\infty}\Psi_n(z_s)\Psi_n(z)H_0^{(1)}(k_{rn}r')+\sum_{m=0}^{\infty}\sum_{n=1}^{\infty}a_{mn}\frac{H_m^{(1)}(k_{rn}r)}{H_m^{(1)}(k_{rn}r_I)}\Psi_n(z)\Phi_m(\phi),
\end{aligned}$$

(2.102)

where r' is the range of a field point with respect to the source, which is expressed as

$$r' = \sqrt{r^2 + r_s^2 - 2rr_s \cos(\phi_s - \phi)}. \tag{2.103}$$

From the above, we see that we have a uniform formula for $p(r, z, \phi)$ in the region outside the seamount (or cylinder), i.e. for $r \geq r_I$:

$$p(r, z, \phi) = p_i(r', z) + \sum_{m=0}^{\infty} \sum_{n=1}^{\infty} a_{mn} \frac{H_m^{(1)}(k_{rn} r)}{H_m^{(1)}(k_{rn} r_I)} \Psi_n(z) \Phi_m(\phi), \tag{2.104}$$

where

$$p_i(r', z) = \frac{i}{4\rho(z_s)} \sum_{n=1}^{\infty} \Psi_n(z_s) \Psi_n(z) H_0^{(1)}(k_{rn} r'). \tag{2.105}$$

The advantage of applying the superposition method in Eq. (2.104), instead of applying Eqs. (2.99) and (2.101), is that there is no dependence on r_s in the normalized Hankel functions in Eq. (2.104), and thus the number of azimuthal modes leading to convergence reduces from $[kr_s]$ to $[kr_I]$, where $[x]$ rounds x to the nearest integer towards infinity.

Chapter 3

The Spectral Normal Mode Approach to Three-Dimensional Propagation around a Cylindrical Island

Before the demonstration of the three-dimensional seamount model, we show how to solve the problem of three-dimensional propagation around a cylindrical island, which is a simple case of the problem involving a conical seamount because we need not consider mode coupling in the cylindrical island problem. Compared with Athanassoulis and Propathopoulos's model [3], by introducing modifications such as using normalized Bessel and Hankel functions as the two linearly independent solutions to the range-dependent equation, which is a Bessel equation, and applying the superposition method to obtain the acoustic field outside the cylinder region, and so on, both stability and efficiency can be improved dramatically. In this chapter, first we make a review of Athanassoulis and Propathopoulos's work; then we provide our approach, which is applicable not only for the cylindrical island problems, but also for more general problems such as problems involving a conical seamount; finally, comparison between Athanassoulis and Propathopoulos's approach and our approach will be given by solving a numerical example.

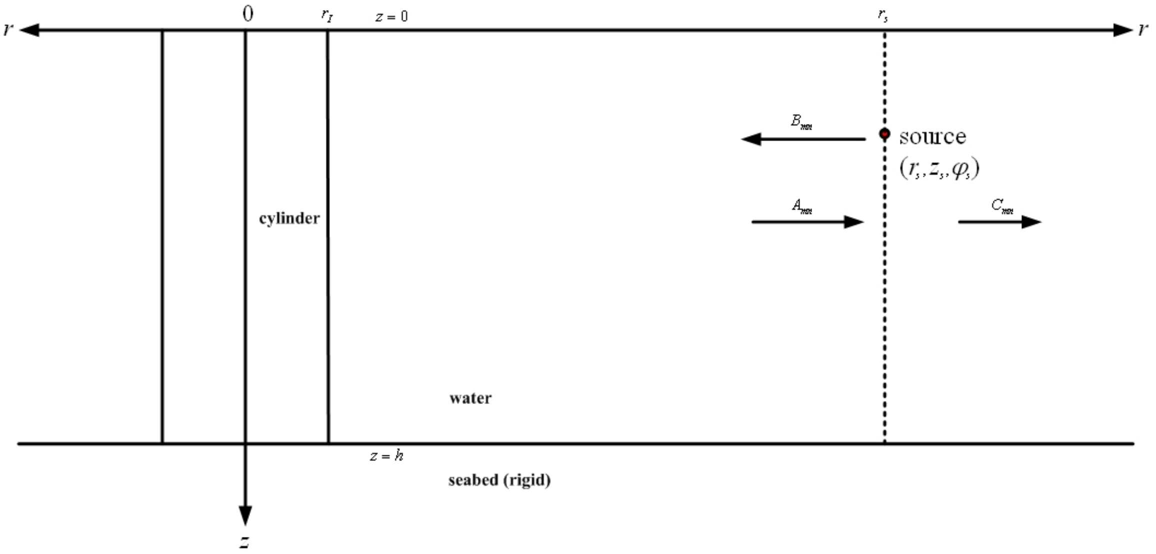

Figure 3-1: A waveguide involving a cylindrical island.

The geometrical configuration is illustrated in Fig. 3-1, in which the seabed is rigid. We consider two types of cylinders: hard and soft cylinders. Because this is a three-dimensional problem involving a point source, from Chapter 2 we know that the inhomogeneous three-dimensional Helmhotz equation takes the form

$$\frac{1}{r}\frac{\partial}{\partial r}\left(r\frac{\partial p}{\partial r}\right)+\frac{1}{r^2}\frac{\partial^2 p}{\partial \phi^2}+\rho(z)\frac{\partial}{\partial z}\left(\frac{1}{\rho(z)}\frac{\partial p}{\partial z}\right)+\frac{\omega^2}{c^2(z)}p=-\frac{\delta(r-r_s)}{r}\delta(z-z_s)\delta(\phi-\phi_s), \tag{3.1}$$

and the solution to Eq. (3.1) is in the form

$$p(r,z,\phi)=\sum_{m=0}^{\infty}\sum_{n=1}^{\infty}R_{mn}(r)\Psi_n(z)\Phi_m(\phi), \tag{3.2}$$

where $R_{mn}(r)$ are solutions to the range-dependent equation, which is an mth-order Bessel equation, $\Psi_n(z)$ are depth-dependent eigenfunctions, and $\Phi_m(\phi)$ are azimuthal eigenfunctions.

3.1 Review of Athanassoulis and Propathopoulos's Work

In Athanassoulis and Propathopoulos's work [3], the field is represented as

$$p(r, z, \phi) = \sum_{m=0}^{\infty} \sum_{n=1}^{\infty} R_{mn}(r) g_n(z) \Phi_m(\phi), \tag{3.3}$$

where $g_n(z)$ are the eigenfunctions of the vertical eigenvalue problem corresponding to range independent axis-symmetric environment outside the cylinder, which satisfy the orthonormal relation

$$\int_0^h g_n(z) g_\nu(z) \mathrm{d}z = \begin{cases} 1, & n = \nu; \\ 0, & n \neq \nu, \end{cases} \tag{3.4}$$

and $\Phi_m(\phi)$ are the azimuthal eigenfunctions, which take the form (as $\phi_s = 0$)

$$\Phi_m(\phi) = e_m \cos(m\phi), \tag{3.5}$$

where

$$e_m = \begin{cases} \frac{1}{2}, & m = 0; \\ 1, & m \neq 0. \end{cases} \tag{3.6}$$

Note that in Athanassoulis and Propathopoulos's work, the orthonormal relation of $\Phi_m(\phi)$ used is $\delta(\phi) = \frac{1}{\pi} \sum_{m=0}^{\infty} e_m \cos m\phi$, which leads to the coefficients e_m as shown in Eq. (3.6).

In Eq. (3.3), $R_{mn}(r)$ takes different forms in regions $r_s > r \geq r_I$ and $r \geq r_s$ as:

1) for $r_s > r \geq r_I$

$$R_{mn}(r) = B_{mn} H_m^{(2)}(k_{rn} r) + A_{mn} H_m^{(1)}(k_{rn} r); \text{ and} \tag{3.7}$$

2) for $r \geq r_s$

$$R_{mn}(r) = C_{mn} H_m^{(1)}(k_{rn} r). \tag{3.8}$$

The coefficients B_{mn}, A_{mn} and C_{mn} are determined by source conditions at $r = r_s$ as well as the boundary conditions at $r = r_I$, and the results are as following (refer to Section 2.2.3):

1) **a hard cylinder**

$$B_{mn} = \frac{i}{4} H_m^{(1)}(k_{rn} r_s) g_n(z_s), \tag{3.9}$$

$$A_{mn} = -\frac{i}{4} \frac{\Phi_m^{(2)}(k_{rn} r_I)}{\Phi_m^{(1)}(k_{rn} r_I)} H_m^{(1)}(k_{rn} r_s) g_n(z_s), \tag{3.10}$$

$$C_{mn} = A_{mn} + \frac{i}{4} H_m^{(2)}(k_{rn} r_s) g_n(z_s), \tag{3.11}$$

where

$$\Phi_m^{(p)}(x) = \frac{\mathrm{d} H_m^{(p)}(x)}{\mathrm{d} x}, \ p = 1, 2. \tag{3.12}$$

2) **a soft cylinder**

$$B_{mn} = \frac{i}{4} H_m^{(1)}(k_{rn} r_s) g_n(z_s), \tag{3.13}$$

$$A_{mn} = -\frac{i}{4} \frac{H_m^{(2)}(k_{rn} r_I)}{H_m^{(1)}(k_{rn} r_I)} H_m^{(1)}(k_{rn} r_s) g_n(z_s), \tag{3.14}$$

$$C_{mn} = A_{mn} + \frac{i}{4} H_m^{(2)}(k_{rn} r_s) g_n(z_s). \tag{3.15}$$

From the above, we notice that the incident coefficients B_{mn} are independent of the property of a cylinder because they are determined only by source conditions; however, they depend on the choice of the orthonormalization of azimuthal eigenfunctions. With $\rho(z_s) = 1$ g/cm^3, Eq. (3.9) and Eq. (3.13) are the same as Eq. (2.68) in Section 2.2.3.

Finally, the field for hard and soft cylinder cases are represented as below:

1) **a hard cylinder**

(a) for $r_s > r \geq r_I$,

$$p(r,z,\phi) = \frac{i}{4}\sum_{m=0}^{\infty}\sum_{n=1}^{\infty} H_m^{(1)}(k_{rn}r_s)\left[H_m^{(2)}(k_{rn}r) - \frac{\Phi_m^{(2)}(k_{rn}r_I)}{\Phi_m^{(1)}(k_{rn}r_I)}H_m^{(1)}(k_{rn}r)\right] \times g_n(z_s)g_n(z)\Phi_m(\phi), \tag{3.16}$$

(b) for $r \geq r_s$,

$$p(r,z,\phi) = \frac{i}{4}\sum_{m=0}^{\infty}\sum_{n=1}^{\infty} H_m^{(1)}(k_{rn}r)\left[H_m^{(2)}(k_{rn}r_s) - \frac{\Phi_m^{(2)}(k_{rn}r_I)}{\Phi_m^{(1)}(k_{rn}r_I)}H_m^{(1)}(k_{rn}r_s)\right] \times g_n(z_s)g_n(z)\Phi_m(\phi). \tag{3.17}$$

We may also rewrite the solutions in Eqs. (3.16) and (3.17) uniformly. For a hard cylinder, in the region $r \geq r_I$,

$$p(r,z,\phi) = \frac{i}{4}\sum_{m=0}^{\infty}\sum_{n=1}^{\infty} H_m^{(1)}(k_{rn}r_>)\left[H_m^{(2)}(k_{rn}r_<) - \frac{\Phi_m^{(2)}(k_{rn}r_I)}{\Phi_m^{(1)}(k_{rn}r_I)}H_m^{(1)}(k_{rn}r_<)\right] \times g_n(z_s)g_n(z)\Phi_m(\phi), \tag{3.18}$$

where $r_< = \min(r, r_s)$ and $r_> = \max(r, r_s)$.

2) **a soft cylinder**

(a) for $r_s > r \geq r_I$

$$p(r,z,\phi) = \frac{i}{4}\sum_{m=0}^{\infty}\sum_{n=1}^{\infty} H_m^{(1)}(k_{rn}r_s)\left[H_m^{(2)}(k_{rn}r) - \frac{H_m^{(2)}(k_{rn}r_I)}{H_m^{(1)}(k_{rn}r_I)}H_m^{(1)}(k_{rn}r)\right] \times g_n(z_s)g_n(z)\Phi_m(\phi), \tag{3.19}$$

(b) for $r \geq r_s$

$$p(r,z,\phi) = \frac{i}{4}\sum_{m=0}^{\infty}\sum_{n=1}^{\infty} H_m^{(1)}(k_{rn}r)\left[H_m^{(2)}(k_{rn}r_s) - \frac{H_m^{(2)}(k_{rn}r_I)}{H_m^{(1)}(k_{rn}r_I)}H_m^{(1)}(k_{rn}r_s)\right] \times g_n(z_s)g_n(z)\Phi_m(\phi). \tag{3.20}$$

We may also rewrite the solutions in Eqs. (3.19) and (3.20) uniformly. For a soft cylinder, in the region $r \geq r_I$,

$$\begin{aligned} p(r,z,\phi) =& \frac{i}{4}\sum_{m=0}^{\infty}\sum_{n=1}^{\infty} H_m^{(1)}(k_{rn}r_>)\left[H_m^{(2)}(k_{rn}r_<) - \frac{H_m^{(2)}(k_{rn}r_I)}{H_m^{(1)}(k_{rn}r_I)}H_m^{(1)}(k_{rn}r_<)\right] \\ & \times g_n(z_s)g_n(z)\Phi_m(\phi), \end{aligned} \tag{3.21}$$

where $r_< = \min(r, r_s)$ and $r_> = \max(r, r_s)$.

3.1.1 Convergence Analysis

In the soft cylinder case, for example, rewrite the solutions as below:

1) **for $\boldsymbol{r_s > r \geq r_I}$**

Rewrite Eq. (3.19) as

$$\begin{aligned} p(r,z,\phi) =& \frac{i}{4}\sum_{m=0}^{\infty}\sum_{n=1}^{\infty} H_m^{(1)}(k_{rn}r_s)H_m^{(1)}(k_{rn}r)\left[\frac{H_m^{(2)}(k_{rn}r)}{H_m^{(1)}(k_{rn}r)} - \frac{H_m^{(2)}(k_{rn}r_I)}{H_m^{(1)}(k_{rn}r_I)}\right] \\ & \times g_n(z_s)g_n(z)\Phi_m(\phi). \end{aligned} \tag{3.22}$$

Since for $m \gg |x|$, we have

$$\begin{aligned} \frac{H_m^{(2)}(x)}{H_m^{(1)}(x)} &= \frac{J_m(x) + iY_m(x)}{J_m(x) - iY_m(x)} \\ &\sim \frac{iY_m(x)}{-iY_m(x)} \\ &= -1, \end{aligned} \tag{3.23}$$

thus for $m \gg |k_{rn}r|$ ($m \gg |k_{rn}r_I|$ is also satisfied because $r \geq r_I$) we have

$$\frac{H_m^{(2)}(k_{rn}r)}{H_m^{(1)}(k_{rn}r)} - \frac{H_m^{(2)}(k_{rn}r_I)}{H_m^{(1)}(k_{rn}r_I)} \to (-1) - (-1) = 0, \tag{3.24}$$

from which we know that in the region $r_s > r \geq r_I$, $p(r,z,\phi)$ in Eq. (3.22) converges as $m \gg |k_{rn}r|$.

2) **for $r \geq r_s$**

Rewrite Eq. (3.20) as

$$\begin{aligned} p(r,z,\phi) =& \frac{i}{4}\sum_{m=0}^{\infty}\sum_{n=1}^{\infty} H_m^{(1)}(k_{rn}r)H_m^{(1)}(k_{rn}r_s)\left[\frac{H_m^{(2)}(k_{rn}r_s)}{H_m^{(1)}(k_{rn}r_s)} - \frac{H_m^{(2)}(k_{rn}r_I)}{H_m^{(1)}(k_{rn}r_I)}\right] \\ & \times g_n(z_s)g_n(z)\Phi_m(\phi). \end{aligned} \tag{3.25}$$

From Eq. (3.25) we know that for $m \gg |k_{rn}r_s|$ ($m \gg |k_{rn}r_I|$ is also satisfied), we have

$$\frac{H_m^{(2)}(k_{rn}r_s)}{H_m^{(1)}(k_{rn}r_s)} - \frac{H_m^{(2)}(k_{rn}r_I)}{H_m^{(1)}(k_{rn}r_I)} \rightarrow (-1) - (-1) = 0, \tag{3.26}$$

thus we know that in the region $r \geq r_s$, $p(r,z,\phi)$ in Eq. (3.25) converges as $m \gg |k_{rn}r_s|$.

From the above, we can draw our conclusion: To obtain convergent results at range r in the region $r_s > r \geq r_I$, the number of azimuthal modes should be at least $[kr]$, where k is the wavenumber in water and $[x]$ rounds x to the nearest integer towards infinity; to obtain convergent results at range r in the region $r \geq r_s$, the number of azimuthal modes should be at least $[kr_s]$. Or:

To obtain convergent results for both $r < r_s$ and $r \geq r_s$, we need at least $[kr_s]$ azimuthal modes .

The problem of slow convergence rates of the azimuthal series arises when the source is very far from the cylinder ($kr_s \rightarrow \infty$). Moreover, it is difficult to compute high-order Hankel functions numerically. So we should seek modifications to eliminate such disadvantages.

3.2 A New Approach with the Superposition Method as well as Normalized Bessel and Hankel Functions

Instead of B_{mn}, A_{mn} and C_{mn} as illustrated in Fig. 3-1, we denote the coefficients by b_{mn}, a_{mn} and c_{mn} in our work. First, we represent the field as:

1) for $r_s > r \geq r_I$,

$$p(r, z, \phi) = \sum_{m=0}^{\infty} \sum_{n=1}^{\infty} \left[b_{mn} \hat{J}_{mn}(r) + a_{mn} \hat{H}1_{mn}(r) \right] \Psi_n(z) \Phi_m(\phi), \tag{3.27}$$

where $\hat{J}_{mn}(r)$ and $\hat{H}1_{mn}(r)$ are normalized Bessel and Hankel functions,

$$\hat{J}_{mn}(r) = J_m(k_{rn} r) H_m^{(1)}(k_{rn} r_s), \tag{3.28}$$

$$\hat{H}1_{mn}(r) = \frac{H_m^{(1)}(k_{rn} r)}{H_m^{(1)}(k_{rn} r_I)}; \tag{3.29}$$

and

2) for $r \geq r_s$,

$$p(r, z, \phi) = \sum_{m=0}^{\infty} \sum_{n=1}^{\infty} c_{mn} \hat{H}1_{mn}(r) \Psi_n(z) \Phi_m(\phi), \tag{3.30}$$

where

$$\hat{H}1_{mn}(r) = \frac{H_m^{(1)}(k_{rn} r)}{H_m^{(1)}(k_{rn} r_s)}. \tag{3.31}$$

From Section 2.2.3 we know the coefficients c_{mn} can be expressed in a_{mn} and b_{mn} as

$$\begin{aligned} c_{mn} &= b_{mn} \hat{J}_{mn}(r_s) + a_{mn} \hat{H}1_{mn}(r_s) \\ &= b_{mn} J_m(k_{rn} r_s) H_m^{(1)}(k_{rn} r_s) + a_{mn} \frac{H_m^{(1)}(k_{rn} r_s)}{H_m^{(1)}(k_{rn} r_I)}. \end{aligned} \tag{3.32}$$

By substituting Eq. (3.31) and Eq. (3.32) into Eq. (3.30), we obtain

$$\begin{aligned}
&p(r,z,\phi)\\
=&\sum_{m=0}^{\infty}\sum_{n=1}^{\infty}\left[b_{mn}J_m(k_{rn}r_s)H_m^{(1)}(k_{rn}r_s)+a_{mn}\frac{H_m^{(1)}(k_{rn}r_s)}{H_m^{(1)}(k_{rn}r_I)}\right]\frac{H_m^{(1)}(k_{rn}r)}{H_m^{(1)}(k_{rn}r_s)}\Psi_n(z)\Phi_m(\phi)\\
=&\sum_{m=0}^{\infty}\sum_{n=1}^{\infty}\left[b_{mn}J_m(k_{rn}r_s)H_m^{(1)}(k_{rn}r)+a_{mn}\frac{H_m^{(1)}(k_{rn}r)}{H_m^{(1)}(k_{rn}r_I)}\right]\Psi_n(z)\Phi_m(\phi). \qquad (3.33)
\end{aligned}$$

Eq. (3.27) and Eq. (3.33) may be uniformly represented as the following. For $r \geq r_I$,

$$p(r,z,\phi)=\sum_{m=0}^{\infty}\sum_{n=1}^{\infty}\left[b_{mn}J_m(k_{rn}r_<)H_m^{(1)}(k_{rn}r_>)+a_{mn}\frac{H_m^{(1)}(k_{rn}r)}{H_m^{(1)}(k_{rn}r_I)}\right]\Psi_n(z)\Phi_m(\phi), \qquad (3.34)$$

where $r_< = \min(r, r_s)$ and $r_> = \max(r, r_s)$.

Note that in the above equations, $\Psi_n(z)$ are depth-dependent eigenfunctions satisfying the orthonormal relation (with a rigid bottom)

$$\int_0^h \frac{1}{\rho(z)}\Psi_n(z)\Psi_\nu(z)\mathrm{d}z = \delta_{n\nu},\ n,\nu = 1,2,\ldots, \qquad (3.35)$$

and $\Phi_m(\phi)$ are azimuthal eigenfunctions satisfying the orthonormal relation

$$\int_{-\pi}^{\pi} \Phi_m(\phi)\Phi_\mu(\phi)\mathrm{d}\phi = \delta_{m\mu},\ m,\mu = 0,1,2,\ldots, \qquad (3.36)$$

and from Section 2.2.2 we know the orthonormal relation in Eq. (3.36) corresponds to the following azimuthal eigenfunctions,

$$\Phi_m(\phi) = e_m \cos m(\phi - \phi_s),\ m = 0,1,2,\ldots, \qquad (3.37)$$

where

$$e_m = \begin{cases} \frac{1}{\sqrt{2\pi}}, & m = 0; \\ \frac{1}{\sqrt{\pi}}, & m \neq 0. \end{cases} \qquad (3.38)$$

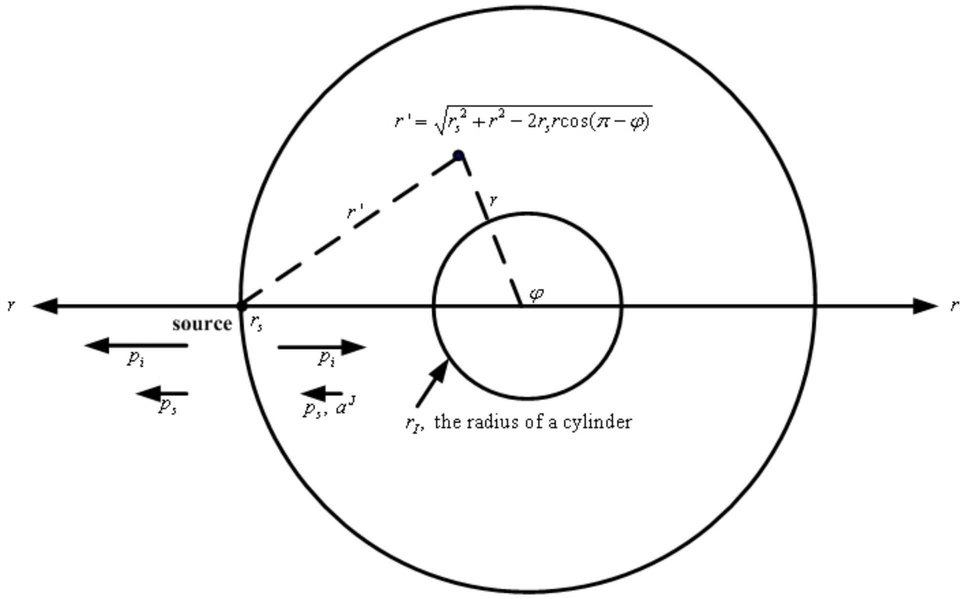

Figure 3-2: The superposition method.

With the equivalence of the spectral normal mode solution and the normal mode solution as demonstrated in Section 2.2.4, we know that in Eq. (3.34), the spectral normal mode expression involving coefficients b_{mn} may be replaced by the normal mode expression, i.e., the spectral normal mode expression

$$\sum_{m=0}^{\infty}\sum_{n=1}^{\infty} b_{mn} J_m(k_{rn} r_<) H_m^{(1)}(k_{rn} r_>) \Psi_n(z) \Phi_m(\phi)$$

may be replaced by the normal mode solution

$$p_i(r', z) = \frac{i}{4}\frac{1}{\rho(z_s)} \sum_{n=1}^{\infty} \Psi_n(z_s)\Psi_n(z) H_0^{(1)}(k_{rn} r').$$

Thus we may represent the field by a uniform expression for both $r_s > r \geq r_I$ and $r \geq r_s$,

$$p(r, z, \phi) = p_i(r', z) + \sum_{m=0}^{\infty}\sum_{n=1}^{\infty} a_{mn} \hat{H}1_{mn}(r) \Psi_n(z) \Phi_m(\phi), \tag{3.39}$$

where r' is the range of a field point (r, z, ϕ) with respect to the source (refer to Fig. 3-2) and $p_i(r', z)$ is the normal mode solution. r' and $p_i(r', z)$ are expressed as below:

$$r'(r,\phi) = \sqrt{r^2 + r_s^2 - 2rr_s\cos(\phi - \phi_s)}, \tag{3.40}$$

$$p_i(r', z) = \frac{i}{4}\frac{1}{\rho(z_s)}\sum_{n=1}^{\infty}\Psi_n(z_s)\Psi_n(z)H_0^{(1)}(k_{rn}r'). \tag{3.41}$$

$\hat{H}1_{mn}(r)$ in Eq. (3.39) is the Hankel function normalized at r_I:

$$\hat{H}1_{mn}(r) = \frac{H_m^{(1)}(k_{rn}r)}{H_m^{(1)}(k_{rn}r_I)}. \tag{3.42}$$

Note that in Eq. (3.40), if $\phi_s = \pi$, as illustrated in Fig. 3-2, then we have

$$r'(r,\phi) = \sqrt{r^2 + r_s^2 - 2rr_s\cos(\pi - \phi)}; \tag{3.43}$$

while if $\phi_s = 0$, as illustrated in Fig. 3-1, then we have

$$r'(r,\phi) = \sqrt{r^2 + r_s^2 - 2rr_s\cos\phi}. \tag{3.44}$$

3.2.1 To Obtain a_{mn} with Boundary Conditions

Represent the field in the region $r_s > r \geq r_I$ as

$$\begin{aligned} p(r,z,\phi) =& \sum_{m=0}^{\infty}\sum_{n=1}^{\infty}\left[b_{mn}\hat{J}_{mn}(r) + a_{mn}\hat{H}1_{mn}(r)\right]\Psi_n(z)\Phi_m(\phi) \\ =& \sum_{m=0}^{\infty}\sum_{n=1}^{\infty}\left[b_{mn}J_m(k_{rn}r)H_m^{(1)}(k_{rn}r_s) + a_{mn}\frac{H_m^{(1)}(k_{rn}r)}{H_m^{(1)}(k_{rn}r_I)}\right]\Psi_n(z)\Phi_m(\phi). \end{aligned} \tag{3.45}$$

From Section 2.2.3, the coefficients b_{mn} are obtained from source conditions and they are the same for both hard and soft cylinders,

$$b_{mn} = \frac{i}{2}\pi\frac{\Psi_n(z_s)}{\rho(z_s)}\Phi_m(\phi_s). \tag{3.46}$$

However, the coefficients a_{mn} are obtained from the boundary conditions at the boundary of a cylinder, therefore they are different for hard and soft cylinders.

1) **a hard cylinder**

For a hard cylinder, the boundary condition at $r = r_I$ is

$$\left.\frac{\partial p}{\partial r}\right|_{r=r_I} = 0, \tag{3.47}$$

i.e., the normal velocity at the boundary of a hard cylinder is zero. By substituting Eq. (3.45) into Eq. (3.47), we obtain

$$\sum_{m=0}^{\infty}\sum_{n=1}^{\infty}\left[b_{mn}\frac{\mathrm{d}J_m}{\mathrm{d}r}(k_{rn}r_I)\,H_m^{(1)}(k_{rn}r_s) + a_{mn}\frac{\frac{\mathrm{d}H_m^{(1)}}{\mathrm{d}r}(k_{rn}r_I)}{H_m^{(1)}(k_{rn}r_I)}\right]\Psi_n(z)\Phi_m(\phi) = 0, \tag{3.48}$$

which leads to

$$b_{mn}\frac{\mathrm{d}J_m}{\mathrm{d}r}(k_{rn}r_I)H_m^{(1)}(k_{rn}r_s) + a_{mn}\frac{\frac{\mathrm{d}H_m^{(1)}}{\mathrm{d}r}(k_{rn}r_I)}{H_m^{(1)}(k_{rn}r_I)} = 0, \tag{3.49}$$

or,

$$a_{mn} = -\frac{H_m^{(1)}(k_{rn}r_I)}{\frac{\mathrm{d}H_m^{(1)}}{\mathrm{d}r}(k_{rn}r_I)}\frac{\mathrm{d}J_m}{\mathrm{d}r}(k_{rn}r_I)H_m^{(1)}(k_{rn}r_s)b_{mn}. \tag{3.50}$$

By substituting Eq. (3.46) into Eq. (3.50), we obtain

$$a_{mn} = -\frac{i}{2}\pi\left[\frac{\mathrm{d}J_m}{\mathrm{d}r}(k_{rn}r_I)H_m^{(1)}(k_{rn}r_s)\right]\left[\frac{H_m^{(1)}(k_{rn}r_I)}{\frac{\mathrm{d}H_m^{(1)}}{\mathrm{d}r}(k_{rn}r_I)}\right]\frac{\Psi_n(z_s)}{\rho(z_s)}\Phi_m(\phi_s). \tag{3.51}$$

2) **a soft cylinder**

For a soft cylinder, the boundary condition at $r = r_I$ is

$$p|_{r=r_I} = 0, \tag{3.52}$$

i.e., the pressure at the boundary of a soft cylinder is zero. By substituting

Eq. (3.45) into Eq. (3.52), we obtain

$$b_{mn} J_m(k_{rn} r_I) H_m^{(1)}(k_{rn} r_s) + a_{mn} \frac{H_m^{(1)}(k_{rn} r_I)}{H_m^{(1)}(k_{rn} r_I)} = 0, \tag{3.53}$$

so,

$$a_{mn} = -b_{mn} J_m(k_{rn} r_I) H_m^{(1)}(k_{rn} r_s). \tag{3.54}$$

By substituting Eq. (3.46) into Eq. (3.54), we obtain

$$a_{mn} = -\frac{i}{2}\pi J_m(k_{rn} r_I) H_m^{(1)}(k_{rn} r_s) \frac{\Psi_n(z_s)}{\rho(z_s)} \Phi_m(\phi_s). \tag{3.55}$$

3.2.2 Convergence Analysis

The solution for $r \geq r_I$ is expressed uniformly in Eq. (3.39), in which

$$\hat{H}1_{mn}(r) = \frac{H_m^{(1)}(k_{rn} r)}{H_m^{(1)}(k_{rn} r_I)}, \tag{3.56}$$

we have:

1) if both $m \gg |k_{rn} r_I|$ and $m \gg |k_{rn} r|$ are satisfied, then we have

$$\hat{H}1_{mn}(r) = \frac{H_m^{(1)}(k_{rn} r)}{H_m^{(1)}(k_{rn} r_I)} \sim \frac{Y_m(k_{rn} r)}{Y_m(k_{rn} r_I)} \sim \left(\frac{r_I}{r}\right)^m \to 0; \text{ and} \tag{3.57}$$

2) if only $m \gg |k_{rn} r_I|$ is satisfied, then we have

$$\hat{H}1_{mn}(r) = \frac{H_m^{(1)}(k_{rn} r)}{H_m^{(1)}(k_{rn} r_I)} \sim \frac{H_m^{(1)}(k_{rn} r)}{iY_m(k_{rn} r_I)} \to \frac{\text{finite value}}{-i\infty} \to 0. \tag{3.58}$$

From Eqs. (3.57) and (3.58) we see that to obtain convergent results at $r \geq r_I$, we should choose the number of azimuthal modes at least $[kr_I]$, where k is the wavenumber in water and $[x]$ rounds x to the nearest integer towards infinity.

3.2.3 The Advantage of the Superposition Method

From the convergence analysis of Athanassoulis and Propathopoulos's approach in Section 3.1.1, we know that with that approach, to obtain convergent results for both $r < r_s$ and $r \geq r_s$, the number of azimuthal modes must be at least $[kr_s]$. For example, with $c = 1500$ m/s, $f = 60$ Hz and r_s=1000 m, at least 252 azimuthal modes are needed to obtain convergent results for both $r < r_s$ and $r \geq r_s$.

While for our approach with the superposition method, from the convergence analysis in Section 3.2.2, to obtain convergent results for both $r < r_s$ and $r \geq r_s$, i.e. $r \geq r_I$, the number of azimuthal modes leading to convergence is at least $[kr_I]$, which is independent of the range of the source. For the same example as the above, with r_I=200 m, at least 51 azimuthal modes are needed to obtain convergent results for both $r < r_s$ and $r \geq r_s$. Thus we see that our approach with the superposition method is much more efficient than Athanassoulis and Propathopoulos's approach.

3.2.4 Asymptotic Forms of Normalized Bessel and Hankel Functions

Overflow and underflow problems arise as calculating $H_m^{(1)}(x)$ and $J_m(x)$ for fixed x as $m \to \infty$, and underflow problems arise as calculating $H_m^{(1)}(x)$ for large arguments with large positive imaginary parts. However, the product of $J_m(x)$ and $H_m^{(1)}(x_n)$ and the ratio of $H_m^{(1)}(x)$ and $H_m^{(1)}(x_n)$ may be finite values in these cases. Thus, instead of evaluating $J_m(x)$ and $H_m^{(1)}(x)$ separately, we may evaluate the product $J_m(x)H_m^{(1)}(x_n)$ or the ratio $H_m^{(1)}(x)/H_m^{(1)}(x_n)$, i.e., evaluate the normalized Bessel and Hankel functions, to avoid the overflow or underflow problems.

We have the following asymptotic forms of Bessel and Hankel functions:

1) for $m \gg |x|$

$$H_m^{(1)}(x) \sim -\frac{i(m-1)!}{\pi}\left(\frac{2}{x}\right)^m, \tag{3.59}$$

$$J_m(x) \sim \frac{1}{m!}\left(\frac{x}{2}\right)^m; \text{ and} \tag{3.60}$$

2) for $m \ll |x|$

$$H_m^{(1)}(x) \sim \sqrt{\frac{2}{\pi x}} e^{i\left(x-\frac{m}{2}\pi-\frac{\pi}{4}\right)}, \tag{3.61}$$

$$J_m(x) \sim \sqrt{\frac{2}{\pi x}} \cos\left(x-\frac{m}{2}\pi-\frac{\pi}{4}\right). \tag{3.62}$$

From the above asymptotic forms of Bessel and Hankel functions, we may obtain the asymptotic forms of normalized Bessel and Hankel functions as below:

1) $\boldsymbol{m \gg |X|}$, $\boldsymbol{|X| \geq |x|}$

With Eqs. (3.59) and (3.60), we obtain

$$\frac{H_m^{(1)}(X)}{H_m^{(1)}(x)} \sim \left(\frac{x}{X}\right)^m, \tag{3.63}$$

$$\frac{H_m^{(1)\prime}(X)}{H_m^{(1)}(x)} \sim -mX^{-m-1}x^m = -m\left(\frac{x}{X}\right)^m \frac{1}{X}, \tag{3.64}$$

$$J_m(x)H_m^{(1)}(X) \sim -\frac{i}{m\pi}\left(\frac{x}{X}\right)^m, \tag{3.65}$$

$$J_m{}'(x)H_m^{(1)}(X) \sim -\frac{i}{m\pi}mx^{m-1}X^{-m} = -\frac{i}{\pi}\left(\frac{x}{X}\right)^m \frac{1}{x} = -\frac{i}{\pi}\left(\frac{x}{X}\right)^{m-1}\frac{1}{X}. \tag{3.66}$$

Note: Eq. (3.64) is obtained by $\frac{\mathrm{d}}{\mathrm{d}X}$Eq. (3.63), and Eq. (3.66) is obtained by $\frac{\mathrm{d}}{\mathrm{d}x}$Eq. (3.65).

For high orders, we may use the asymptotic forms listed above, or we may also use the Debye asymptotic expansions to obtain the asymptotic forms of the normalized Bessel and Hankel functions, as stated in Appendix F.

2) $\boldsymbol{m \ll |x|}$, $\boldsymbol{|X| \geq |x|}$

With Eqs. (3.61) and (3.62), we obtain

$$\frac{H_m^{(1)}(X)}{H_m^{(1)}(x)} \sim \sqrt{\frac{x}{X}} e^{i(X-x)}, \tag{3.67}$$

$$\frac{H_m^{(1)\prime}(X)}{H_m^{(1)}(x)} \sim i\sqrt{\frac{x}{X}} e^{i(X-x)}, \tag{3.68}$$

and

$$\begin{aligned} J_m(x)H_m^{(1)}(X) &\sim \frac{2}{\pi\sqrt{xX}}\cos\left(x-\frac{m}{2}\pi-\frac{\pi}{4}\right)e^{i\left(X-\frac{m}{2}\pi-\frac{\pi}{4}\right)} \\ &= \frac{2}{\pi\sqrt{xX}}\frac{1}{2}\left[e^{i\left(x-\frac{m}{2}\pi-\frac{\pi}{4}\right)}+e^{-i\left(x-\frac{m}{2}\pi-\frac{\pi}{4}\right)}\right]e^{i\left(X-\frac{m}{2}\pi-\frac{\pi}{4}\right)} \\ &= \frac{1}{\pi\sqrt{xX}}\left[e^{i\left(x+X-m\pi-\frac{\pi}{2}\right)}+e^{-i(x-X)}\right], \qquad (3.69) \\ J_m'(x)H_m^{(1)}(X) &\sim \frac{i}{\pi\sqrt{xX}}\left[e^{i\left(x+X-m\pi-\frac{\pi}{2}\right)}-e^{-i(x-X)}\right]. \qquad (3.70) \end{aligned}$$

Note: Eq. (3.68) is obtained by $\frac{\mathrm{d}}{\mathrm{d}X}$Eq. (3.67), and Eq. (3.70) is obtained by $\frac{\mathrm{d}}{\mathrm{d}x}$Eq. (3.69).

3.3 A Numerical Example: Application to a Soft or a Hard Cylindrical Island

As an example, the parameters in Fig. 3-1 are set as following: water depth $h = 250$ m, the radius of the cylindrical island $r_I = 200$ m, source depth and receiver depth $z_s = z_r = h/3$, the range of the point source with respect to the axle of the cylindrical island $r_s = 1000$ m, the azimuthal angle of the source $\phi_s = 0$, and the frequency of the source $f = 60$ Hz. Isovelocity case is considered in this example, and the sound speed in water is $c = 1500$ m/s, the density of the water is 1000 kg/m^3. The bottom is rigid. The cylindrical island is either hard or soft.

3.3.1 Numerical Convergence of Athanassoulis and Propathopoulos's Approach and of Our Approach with the Superposition Method

From Section 3.1.1 we know that for Athanassoulis and Propathopoulos's approach, to obtain convergent results for both $r_s > r \geq r_I$ and $r \geq r_s$, the number of azimuthal modes must be at least $[kr_s]$. In this example, $[kr_s] = \left[\frac{2\pi\times 60}{1500}\times 1000\right] = 252$, so at least 252 azimuthal modes are needed to reach convergence by using Athanassoulis and Propathopoulos's approach.

While for our approach with the superposition method, to obtain convergent results for $r \geq r_I$, the number of azimuthal modes must be at least $[kr_I]$. In this example, $[kr_I] = \left[\frac{2\pi\times 60}{1500} \times 200\right] = 51$, so at least 51 azimuthal modes are needed to reach convergence by using our approach.

Fig. 3-3 shows TL vs. range along azimuthal angle $\phi = \pi$, for a hard cylindrical island. From this figure we can see that the solution by our approach reaches convergence with $M = 61$, while Athanassoulis and Propathopoulos's approach gives almost convergent result with $M = 200$. Due to numerical problems calculating Hankel functions of high orders, Athanassoulis and Propathopoulos's method fails as $M > 200$, so we can not obtain convergent result up to range 1000 m with that method. From Fig. 3-3 we also notice that with $M = 200$, the result of Athanassoulis and Propathopoulos's method is convergent from r_I to 800 m approximately. According to our convergence analysis for Athanassoulis and Propathopoulos's method, to reach convergence at $r = 800$ m, the number of azimuthal modes must be at least $[kr] = \left[\frac{2\pi\times 60}{1500} \times 800\right] = 202$, which explains why the result of Athanassoulis and Propathopoulos's method is only convergent from r_I to 800 m approximately.

3.3.2 Results of the Hard Cylindrical Island Case

Fig. 3-4 shows TL in the horizontal plane at depth $z_r = h/3$. From Section 3.3.1, we know that the solution by our approach with the superposition method is convergent with $M = 61$, and our solution is shown in Fig. 3-4(a). From Figs. 3-4(b), 3-4(c) and 3-4(d), by comparing with Fig. 3-4(a), we see that Athanassoulis and Propathopoulos's approach gives almost convergent solutions as we raise the number of azimuthal modes up to 200.

Fig. 3-5 shows the azimuthal dependence of the pressure modulus around a hard cylinder, at depth $z_r = h/3$, from which we can see that when both our approach and Athanassoulis and Propathopoulos's approach reach convergence, they give results of the same level of accuracy.

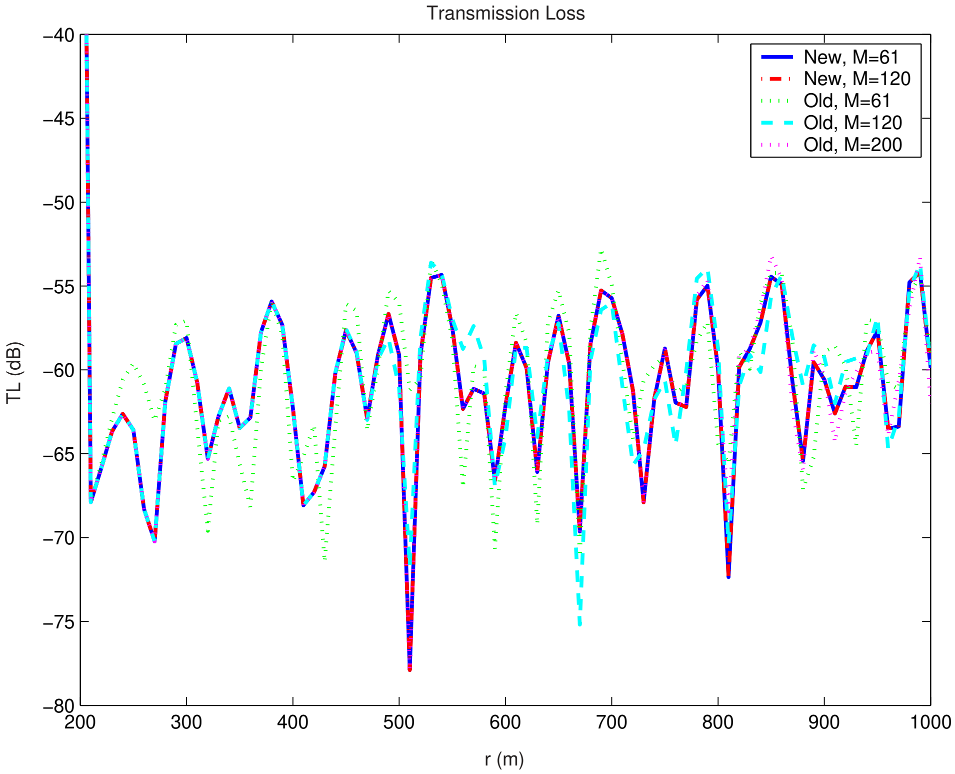

Figure 3-3: TL vs. range at $\theta = \pi$ (range is from the axle of the cylindrical island). Our approach gives convergent result from r_I (200 m) to 1000 m with 61 azimuthal modes, while Athanassoulis and Propathopoulos's approach gives an almost convergent result from r_I to 800 m with 200 azimuthal modes.

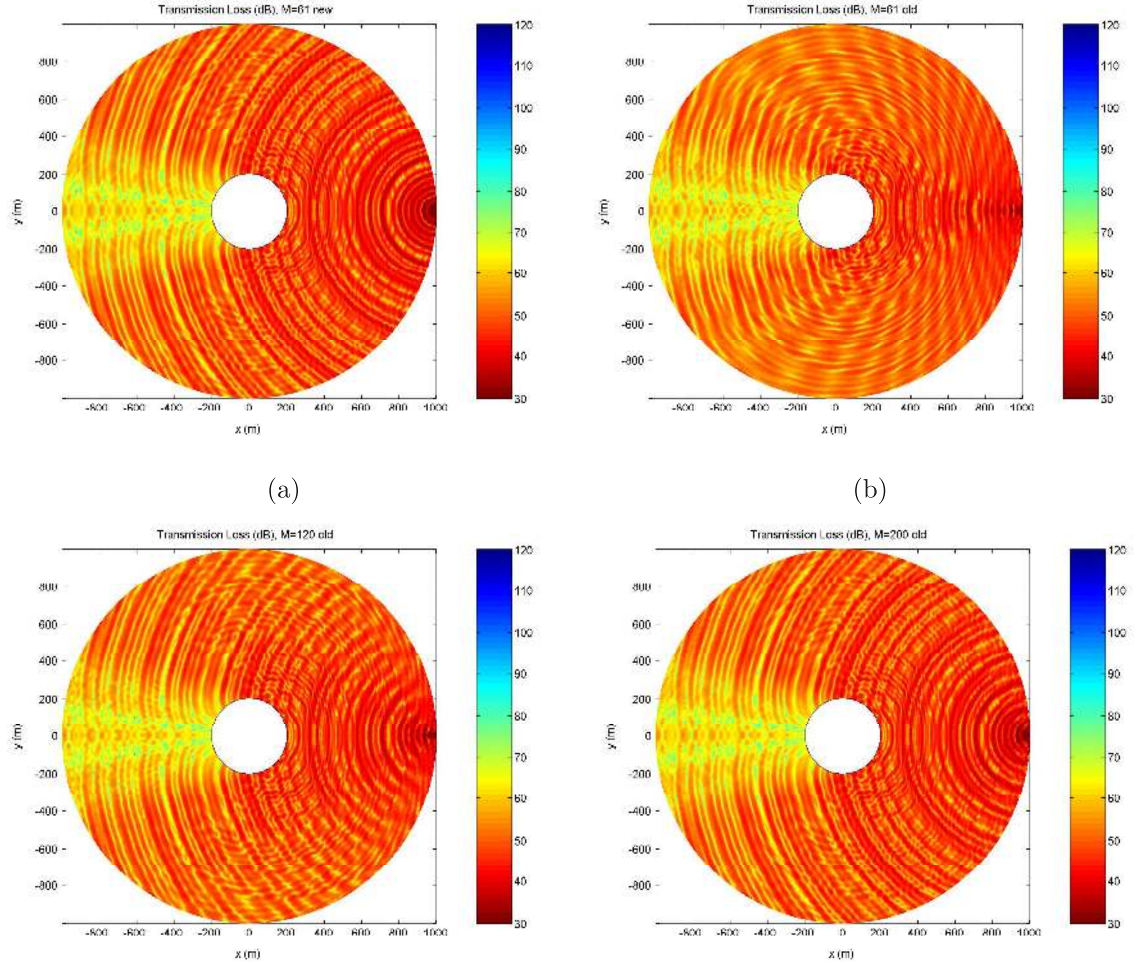

Transmission Loss (dB), M=61 new

Transmission Loss (dB), M=61 old

Transmission Loss (dB), M=120 old

Transmission Loss (dB), M=200 old

(a) (b)

(c) (d)

Figure 3-4: TL at $z_r = z_s = h/3$ in the hard cylinder case, (a) by our approach with the superposition method, M=61; (b) by Athanassoulis and Propathopoulos's approach, M=61; (c) by Athanassoulis and Propathopoulos's approach, M=120; (d) by Athanassoulis and Propathopoulos's approach, M=200. The result of our approach is convergent with 61 azimuthal modes, while the result of Athanassoulis and Propathopoulos's approach reaches convergence with more than 200 azimuthal modes.

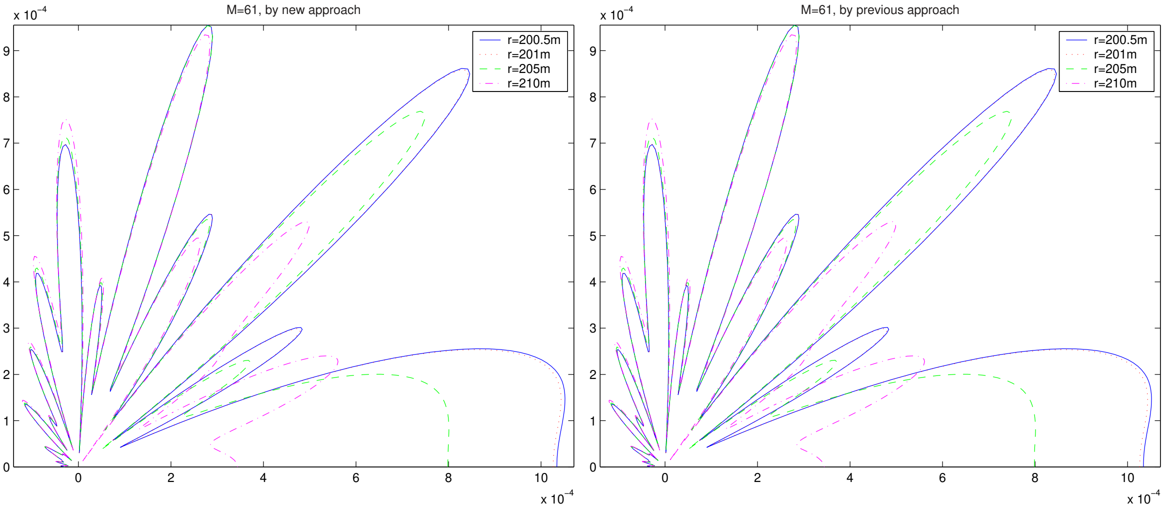

(a) (b)

Figure 3-5: Azimuthal dependence around a hard cylinder, (a) by our approach with the superposition method, M=61; (b) by Athanassoulis and Propathopoulos's approach, M=61. Our approach and Athanassoulis and Propathopoulos's approach converge to the same level of accuracy.

3.3.3 Results of the Soft Cylindrical Island Case

Fig. 3-6 shows TL in the horizontal plane at depth $z_r = h/3$. Similar to Fig. 3-4, Fig. 3-6 clearly shows that Athanassoulis and Propathopoulos's approach gives an almost convergent result up to range 1000 m with $M = 200$, while our approach with the superposition method gives convergent result with $M = 61$.

Fig. 3-7 shows the azimuthal dependence of the pressure modulus around a soft cylinder, at depth $z_r = h/3$, from which we can see that the results of our approach and of Athanassoulis and Propathopoulos's approach are of the same level of accuracy when both of them are convergent.

3.4 Conclusions

From the convergence analyses in Section 3.1 and Section 3.2, which are verified by a numerical example in Section 3.3, we can see clearly the advantages of our approach over Athanassoulis and Propathopoulos's approach, which are summarized as below:

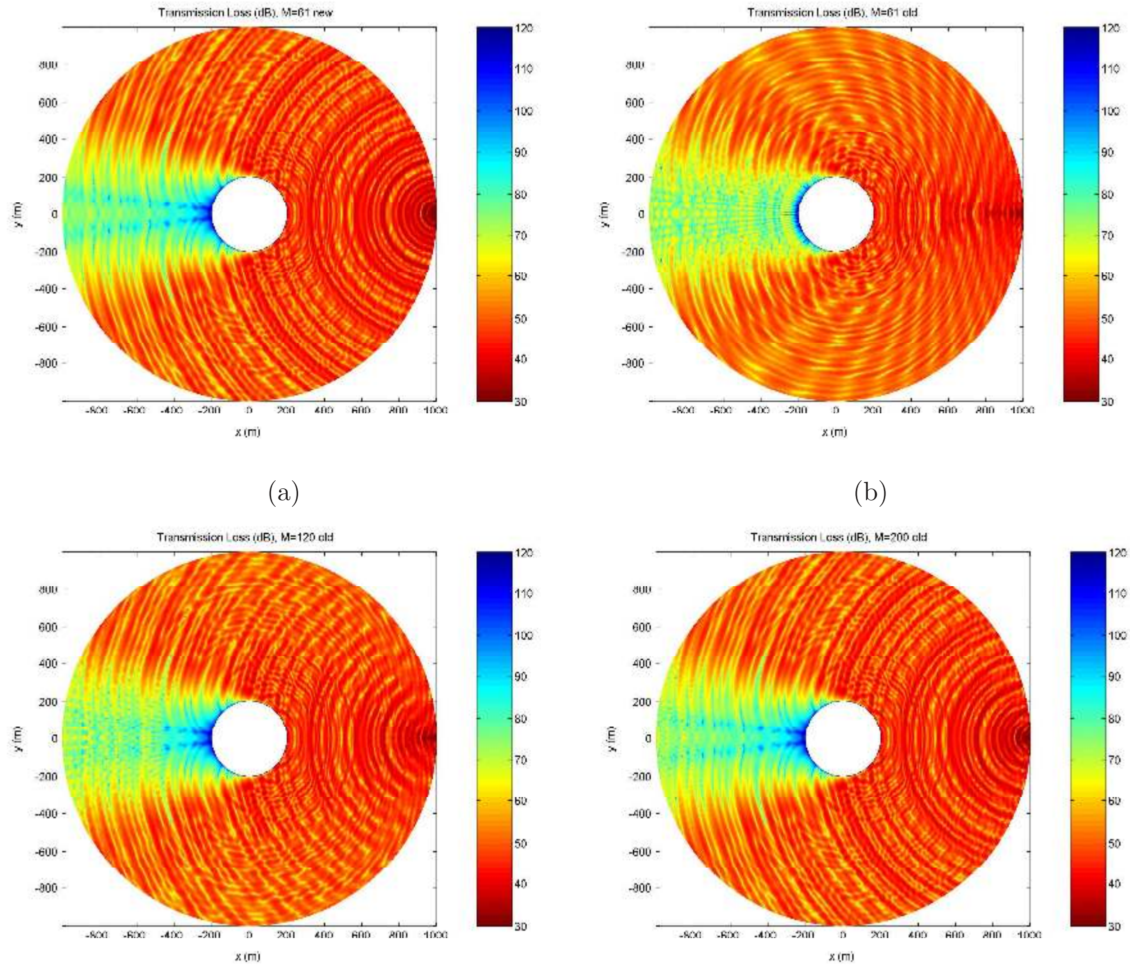

(a) (b)

(c) (d)

Figure 3-6: TL at $z_r = z_s = h/3$ of the soft cylinder case, (a) by our approach with the superposition method, M=61; (b) by Athanassoulis and Propathopoulos's approach, M=61; (c) by Athanassoulis and Propathopoulos's approach, M=120; (d) by Athanassoulis and Propathopoulos's approach, M=200. The result of our approach is convergent with 61 azimuthal modes, while the result of Athanassoulis and Propathopoulos's approach reaches convergence with more than 200 azimuthal modes.

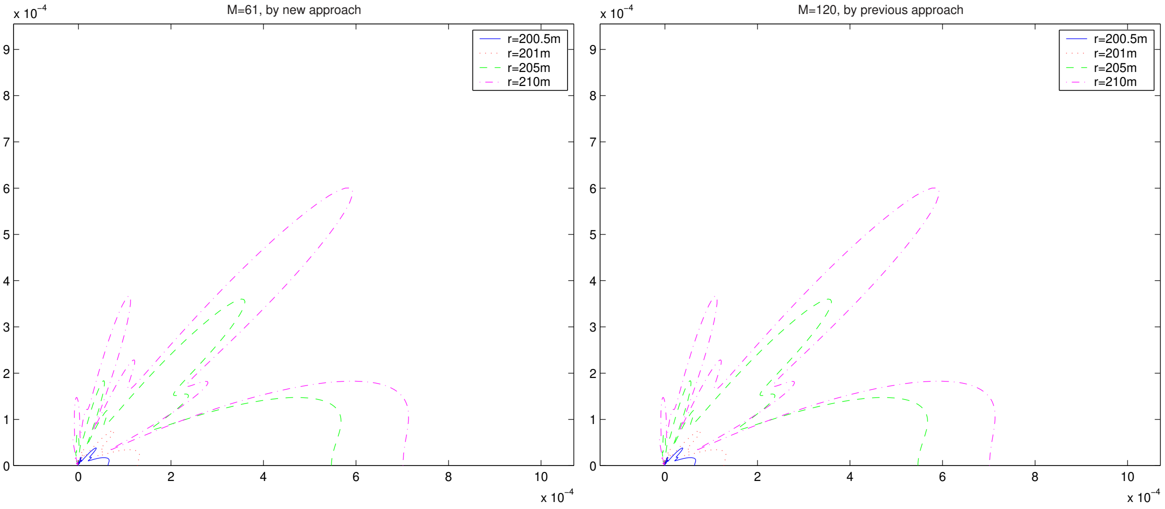

(a)

(b)

Figure 3-7: Azimuthal dependence around a soft cylinder, (a) by our approach with the superposition method, M=61; (b) by Athanassoulis and Propathopoulos's approach, M=120. Our approach and Athanassoulis and Propathopoulos's approach converge to the same level of accuracy.

1) By using the superposition method, our approach reduces the number of azimuthal modes from $[kr_s]$ to $[kr_I]$, so our approach is more efficient than Athanassoulis and Propathopoulos's approach. In addition, from the comparison between the numerical results of our approach and of Athanassoulis and Propathopoulos's approach, the high efficiency of our approach is obtained without sacrificing accuracy.

2) By using normalized Bessel and Hankel functions, our approach eliminates the overflow and underflow problems which exist in Athanassoulis and Propathopoulos's approach. So our approach is more stable than Athanassoulis and Propathopoulos's approach and is therefore applicable to high-frequency and large-scale problems.

Chapter 4

The Spectral Coupled Mode Approach to Three-Dimensional Propagation around a Conical Seamount

In the previous chapter, we apply the spectral normal mode approach to three-dimensional propagation around a cylindrical island, where no mode coupling happens. In this chapter, we will illustrate how to apply the spectral coupled mode approach to solve three-dimensional propagation problems involving a conical seamount, where mode coupling happens at each interface between neighboring rings.

In addition, as illustrated in the previous chapter, by applying the superposition method as well as normalized Bessel and Hankel functions, our approach is more efficient and stable than Athanassoulis and Propathopoulos's approach. These techniques work not only for cylindrical island problems, but also for conical seamount problems.

4.1 The Environment Model

Fig. 4-1 shows a conical seamount in a waveguide, together with a point source located in the water column. In the coupled mode approach, a number of range-independent rings are used to approximate a real conical seamount, as shown in Fig. 4-2 and Fig. 4-3. We label the rings from the inside to the outside, and denote

- r^j as the range of the interface of ring j and ring $j+1$;
- r_I as the radius of the base of the seamount;
- r_s as the range of the source;
- J as the total number of rings;
- M as the number of azimuthal modes;
- N as the number of normal modes;

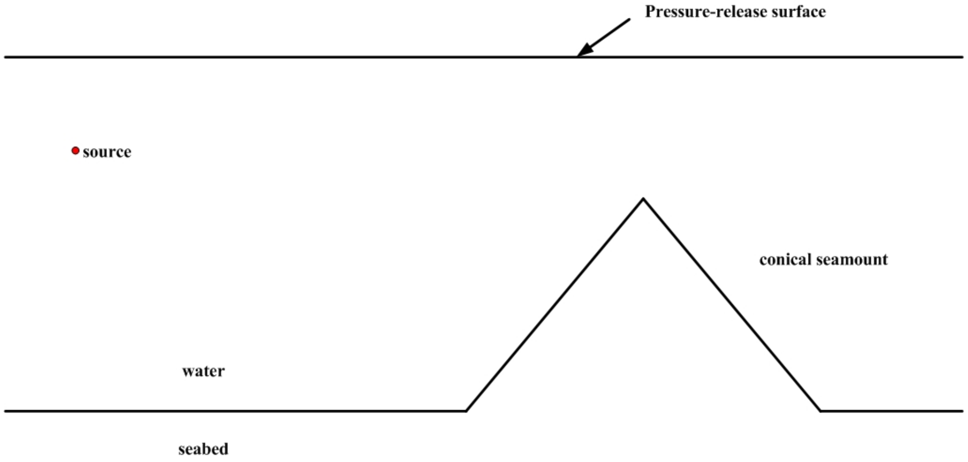

Figure 4-1: The schematic of a conical seamount problem (side view).

4.2 Representation of the Field

In our three-dimensional conical seamount model, we use a different representation of the field from what is used in Taroudakis's work [20] or in Eskenazi's work [6]. In

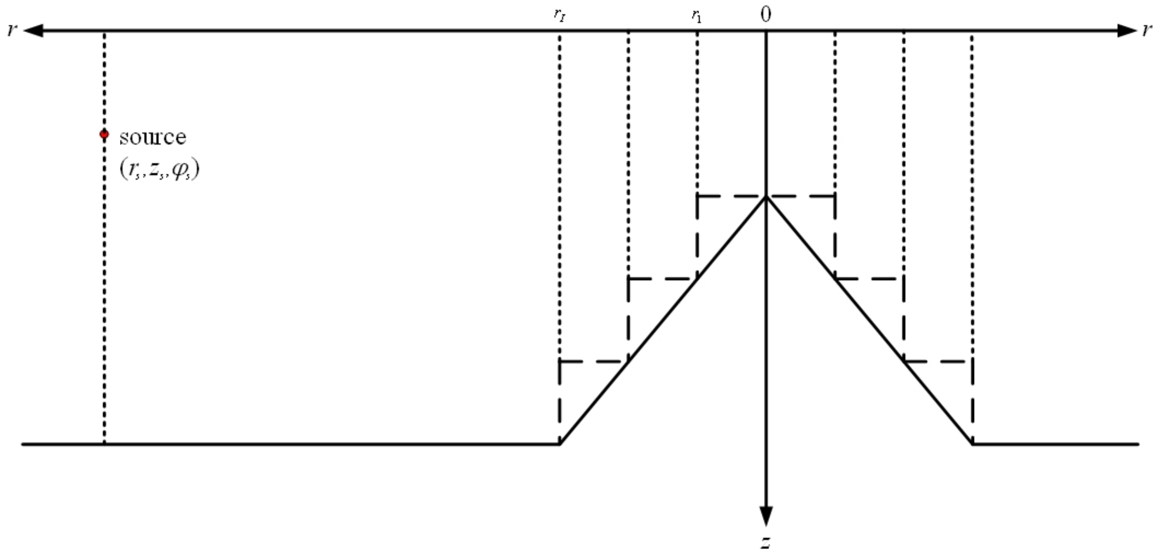

Figure 4-2: A conical seamount approximated by a number of rings (side view).

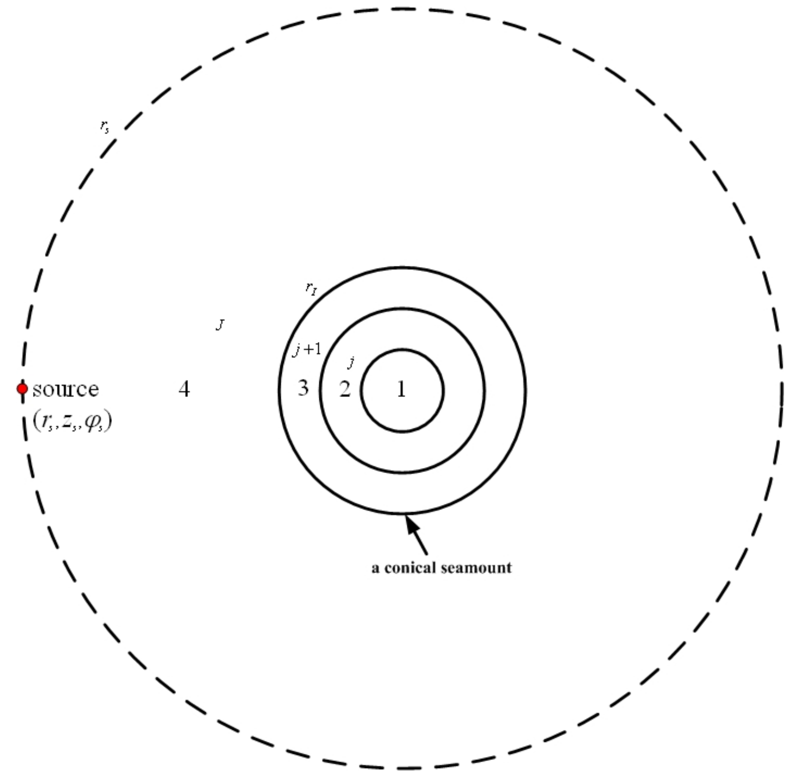

Figure 4-3: A conical seamount approximated by a number of rings (top view).

this section, first we provide the representation used in previous work ([20], [6]), then we show the representation of the field in our model.

4.2.1 Representation of the Field in Previous Work

The representation of the field used in Eskenazi's work [6] is similar to that used in Taroudakis's work [20]. Both of these two kinds of representations are divided into three regions as illustrated in Fig. 4-4. The difference of them is that in Taroudakis's work [20], unnormalized Hankel functions of the first kind and the second kind are used, while in Eskenazi's work [6], normalized Bessel functions of the first kind and normalized Hankel functions of the first kind are used instead.

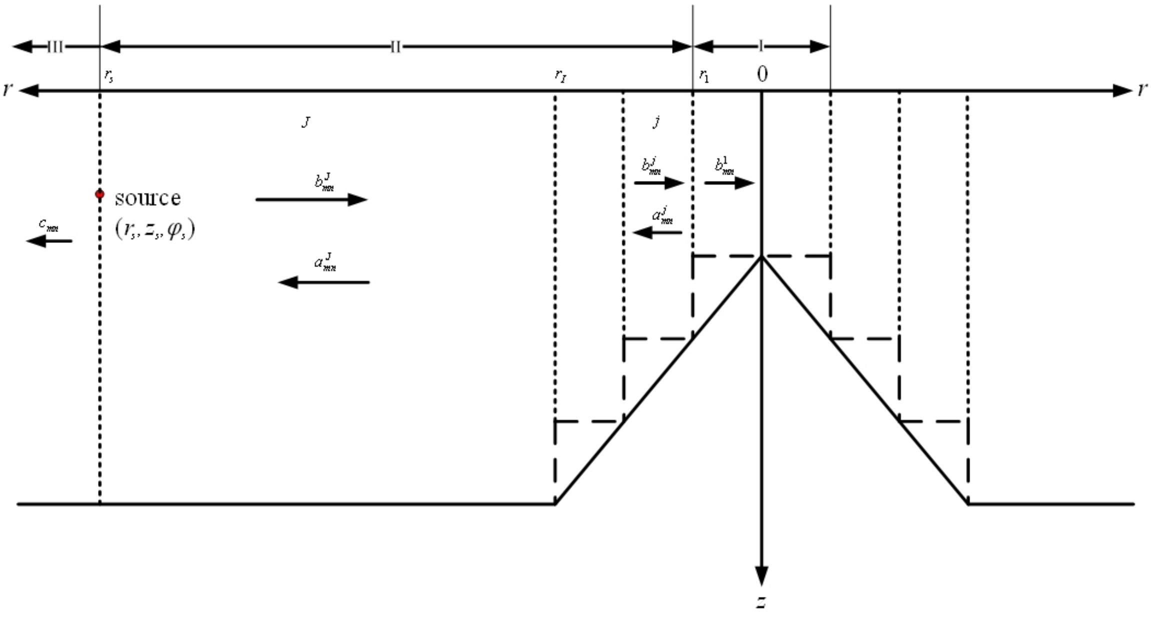

Figure 4-4: Representation of the field in previous work.

Representation of the Field in Taroudakis's Work [20]

As illustrated in Fig. 4-4, in Taroudakis's work [20], the field in ring j is represented as

$$p^j(r, z, \phi) = \sum_{m=0}^{\infty} \sum_{n=1}^{\infty} R_{mn}(r) \Psi_n^j(z) \Phi_m(\phi), \tag{4.1}$$

where $\Psi_n^j(z)$ are depth-dependent eigenfunctions satisfying the orthonormal relation

$$\int_0^\infty \frac{1}{\rho(z)} \Psi_n(z)\Psi_\nu(z)\mathrm{d}z = \delta_{n\nu},\ n, \nu = 1, 2, \ldots, \tag{4.2}$$

and $\Phi_m(\phi)$ are azimuthal eigenfunctions in the form

$$\Phi_m(\phi) = e_m \cos m\phi,\ m = 0, 1, \ldots. \tag{4.3}$$

$\Phi_m(\phi)$ satisfy the orthonormal relation

$$\int_{-\pi}^{\pi} \Phi_m(\phi)\Phi_\mu(\phi) = \delta_{m\mu},\ m, \mu = 0, 1, \ldots, \tag{4.4}$$

therefore the coefficients e_m are

$$e_m = \begin{cases} \frac{1}{\sqrt{2\pi}}, & m = 0; \\ \frac{1}{\sqrt{\pi}}, & m \neq 0. \end{cases} \tag{4.5}$$

$R_{mn}(r)$ takes different forms in the three regions, I, II, and III, as illustrated in Fig. 4-4, as:

1) I: $r \leq r^1$ (in the innermost ring)

$$R_{mn}(r) = A_{mn} J_m(k_{rn}^1 r);\ \text{and} \tag{4.6}$$

2) II: $r^1 < r \leq r_s$. In ring j,

$$R_{mn}(r) = B_{mn}^j H_m^{(1)}(k_{rn}^j r) + C_{mn}^j H_m^{(2)}(k_{rn}^j r);\ \text{and} \tag{4.7}$$

3) III: $r > r_s$ (outside the source range)

$$R_{mn}(r) = D_{mn} H_m^{(1)}(k_{rn}^J r). \tag{4.8}$$

In the above equations, A_{mn}, B_{mn}^j, C_{mn}^j and D_{mn} are called coupling coefficients in this thesis.

The above representation of the field has the following disadvantages:

1) Since $H_m^{(1)}(x)$ and $H_m^{(2)}(x)$ are not linearly independent for $m \gg |x|$ numerically, it is instable to solve the linear systems to obtain the coupling coefficients.

2) Computational problems become very serious in cases where the order of Hankel functions is much greater than the argument, since in this case the Neumann functions $Y_m(x)$ tend to $-\infty$ very quickly.

3) The number of azimuthal modes leading to convergence depends on the range of the source, i.e., M must be at least $[kr_s]$. If the source is very far from the seamount, the slow convergence rate of the azimuthal series will make this approach inapplicable.

Due to the above disadvantages, Taroudakis's approach is only applicable at very low frequencies and shallow water regions; in addition, the source should not be put too far from the seamount.

Representation of the Field in Eskenazi's Work [6]

As illustrated in Fig. 4-4, in Eskenazi's work [6], the field in ring j is represented as

$$p^j(r, z, \phi) = \sum_{m=0}^{\infty} \sum_{n=1}^{\infty} R_{mn}(r) \Psi_n^j(z) \Phi_m(\phi), \tag{4.9}$$

where $\Psi_n^j(z)$ and $\Phi_m(\phi)$ are the same as those defined in Taroudakis's work, and $R_{mn}(r)$ takes different forms in the three regions as:

1) I: $r \leq r^1$ (in the innermost ring)

$$R_{mn}(r) = b_{mn}^1 \hat{J}_{mn}^1(r); \text{ and} \tag{4.10}$$

2) II: $r^1 < r \leq r_s$. In ring j,

$$R_{mn}(r) = a_{mn}^j \hat{H}1_{mn}^j(r) + b_{mn}^j \hat{J}_{mn}^j(r); \text{ and} \tag{4.11}$$

3) III: $r > r_s$ (outside the source range)

$$R_{mn}(r) = c_{mn} \frac{H_m^{(1)}(k_{rn}^J r)}{H_m^{(1)}(k_{rn}^J r_s)}. \tag{4.12}$$

From Section 2.2.3, we have

$$\begin{aligned} b_{mn}^J &= \frac{i}{2}\pi \frac{\Psi_n^J(z_s)}{\rho(z_s)} \Phi_m(\phi_s), \text{ and} && (4.13) \\ c_{mn} &= \frac{i}{2}\pi \frac{\Psi_n^J(z_s)}{\rho(z_s)} \Phi_m(\phi_s) J_m(k_{rn}^J r_s) H_m^{(1)}(k_{rn}^J r_s) + a_{mn}^J \frac{H_m^{(1)}(k_{rn}^J r_s)}{H_m^{(1)}(k_{rn}^J r^{J-1})}, && (4.14) \end{aligned}$$

thus for $r > r_s$, by substituting Eq. (4.14) into Eq. (4.12), we obtain

$$\begin{aligned} R_{mn}(r) =& c_{mn} \frac{H_m^{(1)}(k_{rn}^J r)}{H_m^{(1)}(k_{rn}^J r_s)} \\ =& \frac{i}{2}\pi \frac{\Psi_n^J(z_s)}{\rho(z_s)} \Phi_m(\phi_s) J_m(k_{rn}^J r_s) H_m^{(1)}(k_{rn}^J r) + a_{mn}^J \frac{H_m^{(1)}(k_{rn}^J r)}{H_m^{(1)}(k_{rn}^J r^{J-1})}. \end{aligned} \tag{4.15}$$

In the above representation of the field, normalized Bessel and Hankel functions are used to obtain stable results, and they are defined as below,

$$\begin{aligned} \hat{H}1_{mn}^j(r) &\triangleq \frac{H_m^{(1)}(k_{rn}^j r)}{H_m^{(1)}(k_{rn}^j r^{j-1})}, && (4.16) \\ \hat{J}_{mn}^j(r) &\triangleq J_m(k_{rn}^j r) H_m^{(1)}(k_{rn}^j r^j). && (4.17) \end{aligned}$$

Eskenazi's approach successfully eliminates the first two disadvantages in Taroudakis's approach:

1) In Eskenazi's approach, $\hat{J}_{mn}(r)$ and $\hat{H}1_{mn}(r)$ are linearly independent for both high and low orders, so it is stable to solve the linear systems to obtain the coupling coefficients.

2) There is no overflow or underflow problems by using normalized Bessel and Hankel functions.

However, the third problem in Taroudakis's approach still exists in Eskenazi's approach, i.e., now the number of azimuthal modes required for convergence still depends on the range of the source.

4.2.2 New Representation of the Field

The representation of the field used in our model differs from what is used in Taroudakis's work [20] and in Eskenazi's work [6] in that in our model, region II extends from r_1 to the range of the base of the seamount, r_I, which is also the beginning of region III. Fig. 4-5 shows the new representation of the field in our model.

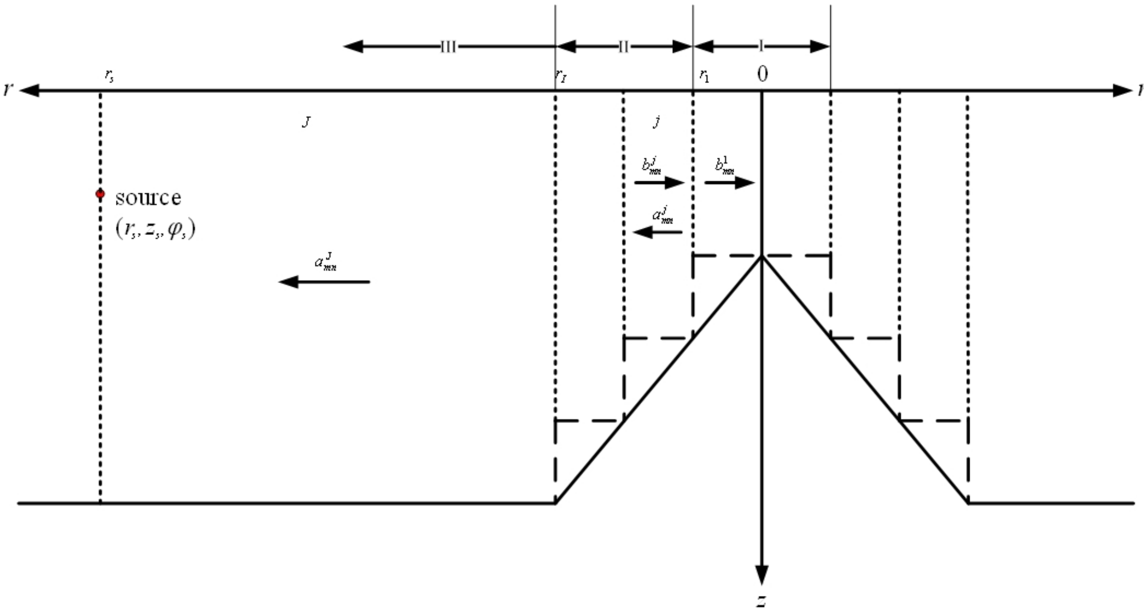

Figure 4-5: New representation of the field.

In our approach, as illustrated in Fig. 4-5, the field in different regions is represented as:

1) I: $r \le r_1$ (in the innermost ring)

$$p^1(r,z,\phi) = \sum_{m=0}^{\infty}\sum_{n=1}^{\infty} b^1_{mn}\hat{J}^1_{mn}(r)\Psi^1_n(z)\Phi_m(\phi);\ \text{and} \tag{4.18}$$

2) II: $r_1 < r \le r_I$, where r_I is the radius of the base of the seamount. In ring j, i.e.

$r^{j-1} < r \leq r^j$,

$$p^j(r,z,\phi) = \sum_{m=0}^{\infty}\sum_{n=1}^{\infty}\left[a^j_{mn}\hat{H}1^j_{mn}(r) + b^j_{mn}\hat{J}^j_{mn}(r)\right]\Psi^j_n(z)\Phi_m(\phi); \text{ and} \tag{4.19}$$

3) III: $r > r_I$ (outside the base of the seamount)

$$p(r,z,\phi) = p_i(r',z) + \sum_{m=0}^{\infty}\sum_{n=1}^{\infty} a^J_{mn}\hat{H}1^J_{mn}(r)\Psi^J_n(z)\Phi_m(\phi), \tag{4.20}$$

where r' is the range of a field point with respect to the source (refer to Fig. 4-6) and $p_i(r',z)$ is the normal mode solution, which are expressed as below,

$$r'(r,\phi) = \sqrt{r^2 + r_s^2 - 2rr_s\cos(\phi_s - \phi)}, \tag{4.21}$$

$$p_i(r',z) = \frac{i}{4}\frac{1}{\rho(z_s)}\sum_{n=1}^{\infty}\Psi^J_n(z_s)\Psi^J_n(z)H^{(1)}_0(k^J_{rn}r'). \tag{4.22}$$

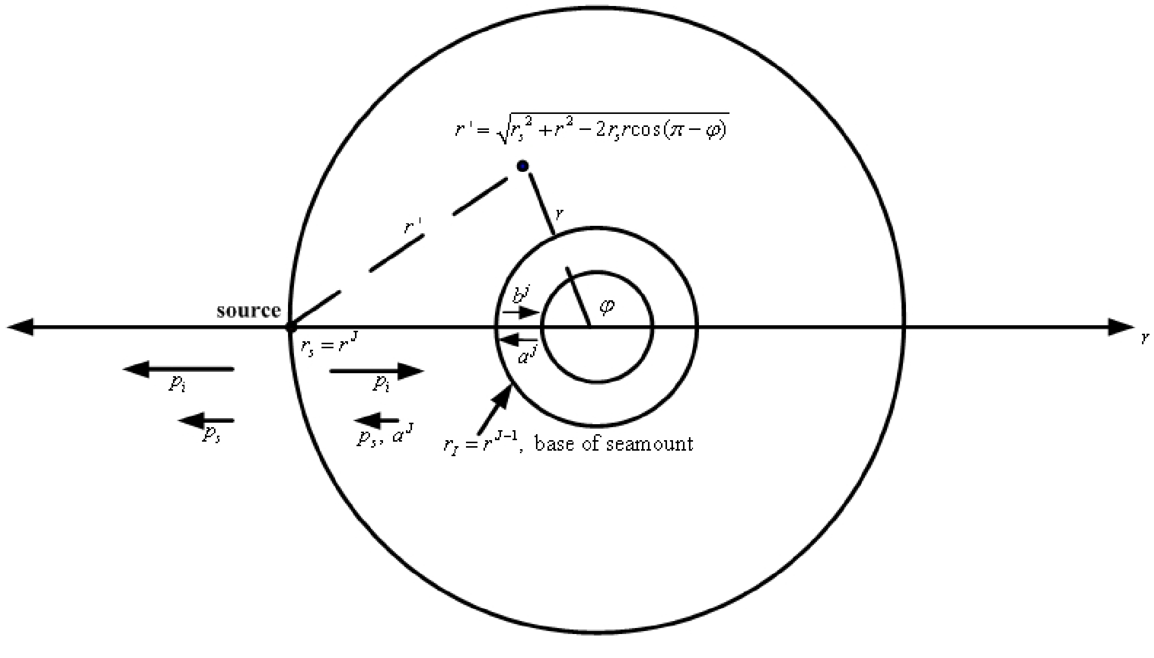

Figure 4-6: Use of the superposition method to obtain the field outside the seamount region.

In the above representation, the superposition method is applied for the region outside the seamount (refer to Section 2.2.4).

In the above representation of the field, $\Psi_n^j(z)$ and $\Phi_m(\phi)$ are the same as those defined in Taroudakis's approach and Eskenazi's approach. In addition, normalized Bessel and Hankel functions are used to obtain stable results, and they are defined as below (the same as those defined in Eskenazi's approach):

$$\hat{H}1_{mn}^j(r) \triangleq \frac{H_m^{(1)}(k_{rn}^j r)}{H_m^{(1)}(k_{rn}^j r^{j-1})}, \tag{4.23}$$

$$\hat{J}_{mn}^j(r) \triangleq J_m(k_{rn}^j r) H_m^{(1)}(k_{rn}^j r^j). \tag{4.24}$$

4.2.3 Convergence Analysis

We analyze the field in ring j, for example. From Eq. (4.19), for $r^{j-1} < r < r^j$, the field is

$$p^j(r, z, \phi) = \sum_{m=0}^{\infty} \sum_{n=1}^{\infty} \left[a_{mn}^j \hat{H}1_{mn}^j(r) + b_{mn}^j \hat{J}_{mn}^j(r) \right] \Psi_n^j(z) \Phi_m(\phi). \tag{4.25}$$

We know the summation of normal modes converges because the high-order modes, which are evanescent modes, leak energy into the bottom, thus for long-range propagation problems, we may only take into account the propagating modes. Below we will analyze what makes the summation of the azimuthal modes converge.

For $\mu \gg |x|$, we have the following asymptotic forms of Bessel and Hankel functions (refer to Appendix D):

1) **Bessel functions of the first kind**

$$J_\mu(x) \to \begin{cases} 1, & \text{if } \mu = 0; \\ 0, & \text{if } \mu \neq 0. \end{cases} \tag{4.26}$$

If μ is integer, then

$$J_\mu(x) \sim \frac{1}{\mu!} \left(\frac{x}{2} \right)^\mu. \tag{4.27}$$

2) **Bessel functions of the second kind (Neumann functions)**

$$Y_\mu(x) \to -\infty. \tag{4.28}$$

If μ is integer (nonzero), then

$$Y_\mu(x) \sim -\frac{1}{\pi}(\mu-1)!\left(\frac{2}{x}\right)^{\mu}. \tag{4.29}$$

3) **Hankel functions of the first kind**

$$H_\mu^{(1)}(x) = J_\mu(x) + iY_\mu(x) \sim iY_\mu(x). \tag{4.30}$$

With Eqs. (4.27), (4.29) and (4.30), we may obtain the asymptotic forms of normalized Hankel and Bessel functions for high-order azimuthal modes. For $m \gg |k_{rn}^j r|$, in the region $r^{j-1} < r < r^j$,

$$\begin{aligned} \hat{H}1_{mn}^j(r) &= \frac{H_m^{(1)}(k_{rn}^j r)}{H_m^{(1)}(k_{rn}^j r^{j-1})} \\ &\sim \frac{Y_m(k_{rn}^j r)}{Y_m(k_{rn}^j r^{j-1})} \\ &\sim \left(\frac{r^{j-1}}{r}\right)^m \\ &\to 0, \end{aligned} \tag{4.31}$$

and

$$\begin{aligned} \hat{J}_{mn}^j(r) &= J_m(k_{rn}^j r) H_m^{(1)}(k_{rn}^j r^j) \\ &\sim J_m(k_{rn}^j r) iY_m(k_{rn}^j r^j) \\ &\sim \frac{1}{m!}\left(\frac{\cancel{k_{rn}^j} r}{\cancel{2}}\right)^m i\left[-\frac{1}{\pi}(m-1)!\left(\frac{\cancel{2}}{\cancel{k_{rn}^j} r^j}\right)^m\right] \\ &\sim -\frac{i}{m\pi}\left(\frac{r}{r^j}\right)^m \\ &\to 0. \end{aligned} \tag{4.32}$$

From the above, we can see that as the order of azimuthal modes goes to a large number with respect to the argument $k_{rn}^{j} r$, the normalized Hankel and Bessel functions, $\hat{H}1_{mn}^{j}(r)$ and $\hat{J}_{mn}^{j}(r)$, approach zero, which makes the double summation in Eq. (4.25) approach zero. Thus we may use a finite number of azimuthal modes to obtain convergent results. In our three-dimensional spectral coupled mode model, the number of azimuthal modes is set to be $M = [kr_I]$ where k is the wavenumber in water, r_I is the radius of the base of the seamount, and $[x]$ rounds x to the nearest integer towards infinity.

4.2.4 Advantages of the New Representation of the Field

From Eqs. (4.11) and (4.12), we see that in Eskenazi's representation of the field, to compute the field outside the seamount region, i.e., $r > r_I$, both $\hat{H}1_{mn}^{J}(r)$ and $\hat{J}_{mn}^{J}(r)$ are needed to be evaluated. To make $\hat{H}1_{mn}^{J}(r) = \frac{H_m^{(1)}(k_{rn}^{J} r)}{H_m^{(1)}(k_{rn}^{J} r_I)}$ converge, the number of azimuthal modes must be at least $[k_{rn}^{J} r_I]$; however, to make $\hat{J}_{mn}^{J}(r) = J_m(k_{rn}^{J} r) H_m^{(1)}(k_{rn}^{J} r_s)$ converge, the number of azimuthal modes must be at least $M = \left[k_{rn}^{J} r_s\right]$. So, in Eskenazi's approach, the number of azimuthal modes depends on the range of the source, r_s. Similarly, in Taroudakis's approach, the number of azimuthal modes also depends on r_s.

While in the new approach, by using the superposition method, for $r > r_I$, from Eq. (4.20) we see that only $\hat{H}1_{mn}^{J}(r) = \frac{H_m^{(1)}(k_{rn}^{J} r)}{H_m^{(1)}(k_{rn}^{J} r_I)}$ is needed to be evaluated, and to make it converge, the number of azimuthal modes must be at least $M = \left[k_{rn}^{J} r_I\right]$. So, in the new approach, the number of azimuthal modes depends on the radius of the base of a seamount, r_I.

For example, if $f = 75$ Hz, $k = 2\pi f/1500$, $r_I = 26$ km, $r_s = 513.054$ km, then $[kr_s] = 161181$, while $[kr_I] = 8169$. So, in Eskenazi's approach or Taroudakis's approach, at least 161181 azimuthal modes are needed to reach convergence; while in our approach, at least 8169 azimuthal modes are needed to reach convergence. Thus we can see a great deal of computational effort is saved by using our approach.

From the above, we can see that our approach is more stable and more efficient than Taroudakis's approach and Eskenazi's approach.

4.3 Two-Way Coupling

We divide the whole coupling into two steps, as illustrated in Fig. 4-7. The first step addresses the inward marching coupling, where the single-scatter approximation is used, and the second step addresses the outward marching coupling, where the one-way approximation is used. These two steps lead to approximate two-way coupling.

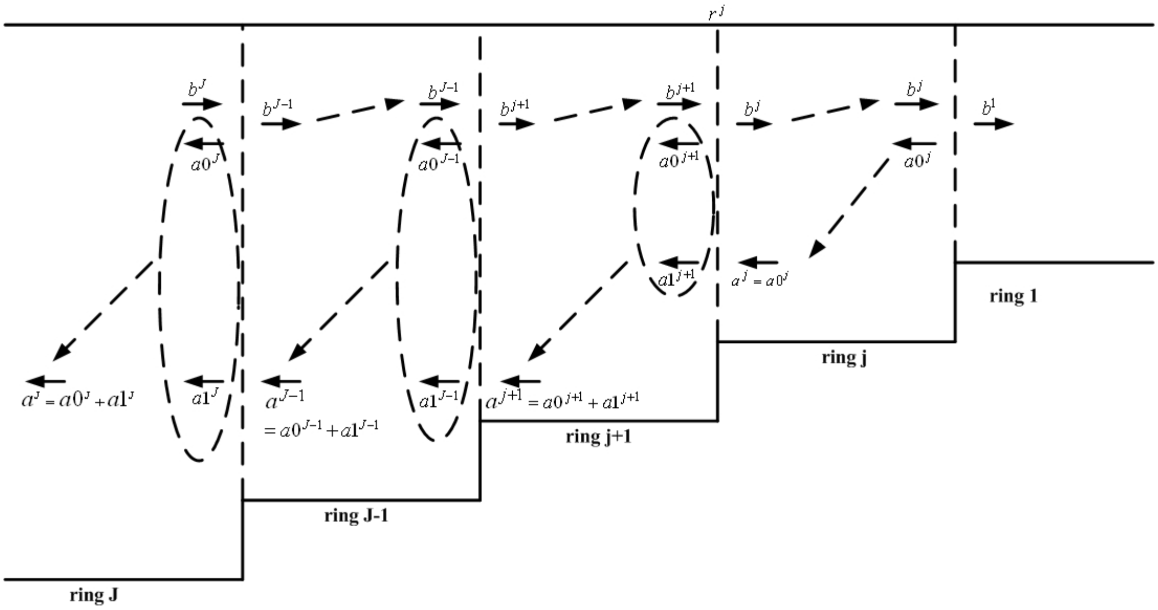

Figure 4-7: A two-way coupled mode model.

The advantage of this two-way coupling is that instead of solving a single large linear system (refer to the direct global matrix approach [12] and Eskenazi's work [6]), we divide it into multiple small linear systems. Since solving each of these small linear systems lowers the requirement for the memory of computers, this approach is applicable on personal computers.

4.3.1 Inward Marching

As shown in Fig. 4-8, the single-scatter approximation is applied in the inward marching. For the two neighboring rings, i.e. ring $j+1$ and ring j, with $\boldsymbol{b}_m^{j+1}$ known, we apply the boundary conditions at the interface $r = r^j$ to derive $\boldsymbol{a}_m^{j+1}$ and $\boldsymbol{b}_m^j$.

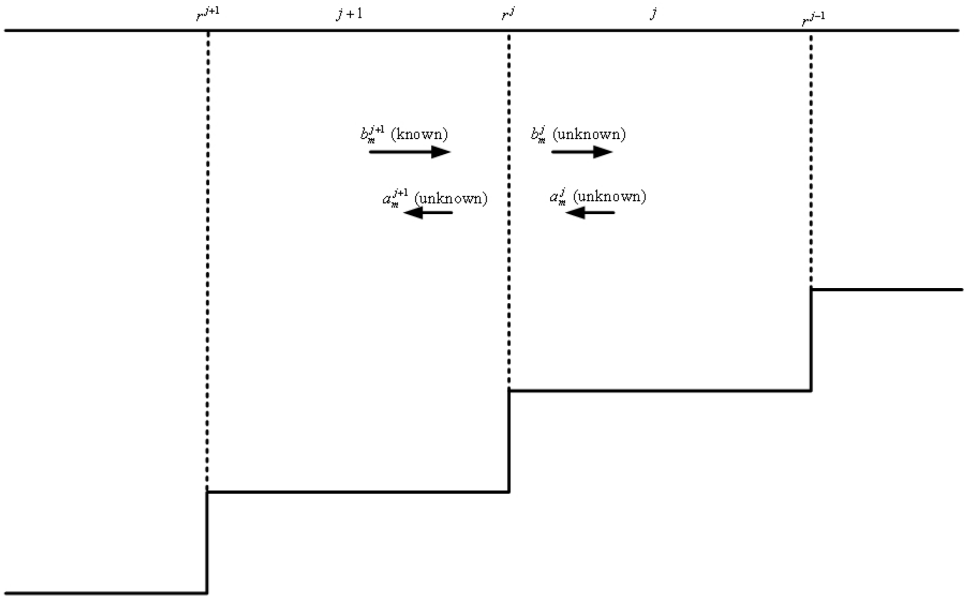

Figure 4-8: Coupling between two neighboring rings in inward marching, where the single-scatter approximation, $\boldsymbol{a}_m^j = \mathbf{0}$, is applied.

1) Continuity of pressure at $\boldsymbol{r = r^j}$

This boundary condition gives us

$$p^j(r^j, z, \phi) = p^{j+1}(r^j, z, \phi). \tag{4.33}$$

Substitute Eq. (4.19) into Eq. (4.33), and we obtain

$$\begin{aligned}&\sum_{m=0}^{\infty}\sum_{n=1}^{\infty}\left[a_{mn}^j \hat{H}1_{mn}^j(r^j) + b_{mn}^j \hat{J}_{mn}^j(r^j)\right]\Psi_n^j(z)\Phi_m(\phi)\\ =&\sum_{m=0}^{\infty}\sum_{n=1}^{\infty}\left[a_{mn}^{j+1} \hat{H}1_{mn}^{j+1}(r^j) + b_{mn}^{j+1} \hat{J}_{mn}^{j+1}(r^j)\right]\Psi_n^{j+1}(z)\Phi_m(\phi),\end{aligned} \tag{4.34}$$

for the m-th azimuthal mode, we have

$$\begin{aligned}&\sum_{n=1}^{\infty}\left[a_{mn}^j \hat{H}1_{mn}^j(r^j) + b_{mn}^j \hat{J}_{mn}^j(r^j)\right]\Psi_n^j(z)\\ =&\sum_{n=1}^{\infty}\left[a_{mn}^{j+1} \hat{H}1_{mn}^{j+1}(r^j) + b_{mn}^{j+1} \hat{J}_{mn}^{j+1}(r^j)\right]\Psi_n^{j+1}(z).\end{aligned} \tag{4.35}$$

By applying the operator $\int_0^\infty \frac{1}{\rho^j(z)} \Psi_\nu^j(z)\,(\cdot)\,\mathrm{d}z$ to Eq. (4.35), we obtain

$$\begin{aligned}&\left[a_{m\nu}^j \hat{H}1_{m\nu}^j(r^j) + b_{m\nu}^j \hat{J}_{m\nu}^j(r^j)\right]\\ &= \sum_{n=1}^{\infty} \left[a_{mn}^{j+1} \hat{H}1_{mn}^{j+1}(r^j) + b_{mn}^{j+1} \hat{J}_{mn}^{j+1}(r^j)\right] \int_0^\infty \frac{1}{\rho^j(z)} \Psi_\nu^j(z) \Psi_n^{j+1}(z) \mathrm{d}z. \end{aligned} \tag{4.36}$$

With notation

$$C_{a\nu n}^{\;j+1} \triangleq \int_0^\infty \frac{1}{\rho^j(z)} \Psi_\nu^j(z) \Psi_n^{j+1}(z) \mathrm{d}z, \tag{4.37}$$

Eq. (4.36) may be rewritten in the matrix form,

$$\hat{\boldsymbol{H}}\mathbf{1}_m^j \boldsymbol{a}_m^j + \hat{\boldsymbol{J}}_m^j \boldsymbol{b}_m^j = \boldsymbol{C}_{\boldsymbol{a}}^{j+1} \left(\hat{\boldsymbol{H}}\mathbf{1}_m^{j+1} \boldsymbol{a}_m^{j+1} + \hat{\boldsymbol{J}}_m^{j+1} \boldsymbol{b}_m^{j+1}\right), \tag{4.38}$$

where $\hat{\boldsymbol{H}}\mathbf{1}_m^j$, $\hat{\boldsymbol{J}}_m^j$, $\hat{\boldsymbol{H}}\mathbf{1}_m^{j+1}$ and $\hat{\boldsymbol{J}}_m^{j+1}$ are diagonal matrixes like

$$\hat{\boldsymbol{H}}\mathbf{1}_m^j = \mathrm{diag}\left(\hat{H}1_{mn}^j(r^j)\right)_{n=1,2,\ldots,N} = \mathrm{diag}\left(\frac{H_m^{(1)}(k_{rn}^j r^j)}{H_m^{(1)}(k_{rn}^j r^{j-1})}\right)_{n=1,2,\ldots,N},$$

etc, and $\boldsymbol{a}_m^j$, $\boldsymbol{b}_m^j$, $\boldsymbol{a}_m^{j+1}$ and $\boldsymbol{b}_m^{j+1}$ are column vectors like

$$\boldsymbol{a}_m^j = \begin{bmatrix} a_{m1}^j \\ a_{m2}^j \\ \vdots \\ a_{mN}^j \end{bmatrix},$$

where N is the number of normal modes, and $\boldsymbol{C}_{\boldsymbol{a}}^{j+1} = \left[C_{a\nu n}^{\;j+1}\right]$, $\nu = 1, \ldots, N$, $n = 1, \ldots, N$.

2) Continuity of normal particle velocity at $r = r^j$

This boundary condition gives us

$$\frac{1}{\rho^j} \frac{\partial p^j}{\partial r}\bigg|_{r^j} = \frac{1}{\rho^{j+1}} \frac{\partial p^{j+1}}{\partial r}\bigg|_{r^j}. \tag{4.39}$$

With notations

$$D\hat{H}1^j_{mn}(r) \triangleq \frac{\frac{\mathrm{d}H^{(1)}_m(k^j_{rn}r)}{\mathrm{d}(k^j_{rn}r)}}{H^{(1)}_m(k^j_{rn}r^{j-1})}, \tag{4.40}$$

$$D\hat{J}^j_{mn}(r) \triangleq \frac{\mathrm{d}J_m(k^j_{rn}r)}{\mathrm{d}(k^j_{rn}r)} H^{(1)}_m(k^j_{rn}r^j), \tag{4.41}$$

we have

$$\frac{\mathrm{d}\hat{H}1^j_{mn}(r)}{\mathrm{d}r} = \frac{\frac{\mathrm{d}H^{(1)}_m(k^j_{rn}r)}{\mathrm{d}r}}{H^{(1)}_m(k^j_{rn}r^{j-1})} = \frac{k^j_{rn}\frac{\mathrm{d}H^{(1)}_m(k^j_{rn}r)}{\mathrm{d}(k^j_{rn}r)}}{H^{(1)}_m(k^j_{rn}r^{j-1})} = k^j_{rn}D\hat{H}1^j_{mn}(r), \tag{4.42}$$

$$\frac{\mathrm{d}\hat{J}^j_{mn}(r)}{\mathrm{d}r} = \frac{\mathrm{d}J_m(k^j_{rn}r)}{\mathrm{d}r} H^{(1)}_m(k^j_{rn}r^j) = k^j_{rn}\frac{\mathrm{d}J_m(k^j_{rn}r)}{\mathrm{d}(k^j_{rn}r)} H^{(1)}_m(k^j_{rn}r^j) = k^j_{rn}D\hat{J}^j_{mn}(r). \tag{4.43}$$

Substitute Eq. (4.19) into Eq. (4.39), together with Eqs. (4.42) and (4.43), then for the m-th azimuthal mode, we have

$$\begin{aligned}&\frac{1}{\rho^j}\sum_{n=1}^{\infty}\left[a^j_{mn}k^j_{rn}D\hat{H}1^j_{mn}(r^j) + b^j_{mn}k^j_{rn}D\hat{J}^j_{mn}(r^j)\right]\Psi^j_n(z)\\ =&\frac{1}{\rho^{j+1}}\sum_{n=1}^{\infty}\left[a^{j+1}_{mn}k^{j+1}_{rn}D\hat{H}1^{j+1}_{mn}(r^j) + b^{j+1}_{mn}k^{j+1}_{rn}D\hat{J}^{j+1}_{mn}(r^j)\right]\Psi^{j+1}_n(z),\end{aligned} \tag{4.44}$$

by applying the operator $\int_0^\infty \Psi^j_\nu(z)\,(\cdot)\,\mathrm{d}z$ to Eq. (4.44), we obtain

$$\begin{aligned}&k^j_{r\nu}\left[a^j_{m\nu}D\hat{H}1^j_{m\nu}(r^j) + b^j_{m\nu}D\hat{J}^j_{m\nu}(r^j)\right]\\ =&\sum_{n=1}^{\infty}k^{j+1}_{rn}\left[a^{j+1}_{mn}D\hat{H}1^{j+1}_{mn}(r^j) + b^{j+1}_{mn}D\hat{J}^{j+1}_{mn}(r^j)\right]\int_0^\infty\frac{1}{\rho^{j+1}(z)}\Psi^j_\nu(z)\Psi^{j+1}_n(z)\mathrm{d}z,\end{aligned}$$

or,

$$\begin{aligned}&a^j_{m\nu}D\hat{H}1^j_{m\nu}(r^j) + b^j_{m\nu}D\hat{J}^j_{m\nu}(r^j)\\ =&\sum_{n=1}^{\infty}\left[a^{j+1}_{mn}D\hat{H}1^{j+1}_{mn}(r^j) + b^{j+1}_{mn}D\hat{J}^{j+1}_{mn}(r^j)\right]\frac{k^{j+1}_{rn}}{k^j_{r\nu}}\int_0^\infty\frac{1}{\rho^{j+1}(z)}\Psi^j_\nu(z)\Psi^{j+1}_n(z)\mathrm{d}z.\end{aligned} \tag{4.45}$$

With notation

$$C_{b\nu n}^{j+1} \triangleq \frac{k_{rn}^{j+1}}{k_{r\nu}^{j}} \int_0^\infty \frac{1}{\rho^{j+1}(z)} \Psi_\nu^j(z) \Psi_n^{j+1}(z) \mathrm{d}z, \tag{4.46}$$

Eq. (4.45) may be rewritten in the matrix form,

$$\boldsymbol{D\hat{H}1}_m^j \boldsymbol{a}_m^j + \boldsymbol{D\hat{J}}_m^j \boldsymbol{b}_m^j = \boldsymbol{C}_{\boldsymbol{b}}^{j+1} \left(\boldsymbol{D\hat{H}1}_m^{j+1} \boldsymbol{a}_m^{j+1} + \boldsymbol{D\hat{J}}_m^{j+1} \boldsymbol{b}_m^{j+1} \right), \tag{4.47}$$

where $\boldsymbol{D\hat{H}1}_m^j$, $\boldsymbol{D\hat{J}}_m^j$, $\boldsymbol{D\hat{H}1}_m^{j+1}$ and $\boldsymbol{D\hat{J}}_m^{j+1}$ are diagonal matrixes, and $\boldsymbol{a}_m^j$, $\boldsymbol{b}_m^j$, $\boldsymbol{a}_m^{j+1}$ and $\boldsymbol{b}_m^{j+1}$ are column vectors.

From the above, we have two equations for $\boldsymbol{a}_m^j$ and $\boldsymbol{b}_m^j$:

$$\boldsymbol{\hat{H}1}_m^j \boldsymbol{a}_m^j + \boldsymbol{\hat{J}}_m^j \boldsymbol{b}_m^j = \boldsymbol{C}_{\boldsymbol{a}}^{j+1} \left(\boldsymbol{\hat{H}1}_m^{j+1} \boldsymbol{a}_m^{j+1} + \boldsymbol{\hat{J}}_m^{j+1} \boldsymbol{b}_m^{j+1} \right), \tag{4.48}$$

$$\boldsymbol{D\hat{H}1}_m^j \boldsymbol{a}_m^j + \boldsymbol{D\hat{J}}_m^j \boldsymbol{b}_m^j = \boldsymbol{C}_{\boldsymbol{b}}^{j+1} \left(\boldsymbol{D\hat{H}1}_m^{j+1} \boldsymbol{a}_m^{j+1} + \boldsymbol{D\hat{J}}_m^{j+1} \boldsymbol{b}_m^{j+1} \right). \tag{4.49}$$

Next we will solve $\boldsymbol{a}_m^j$ and $\boldsymbol{b}_m^j$ in terms of $\boldsymbol{a}_m^{j+1}$ and $\boldsymbol{b}_m^{j+1}$ from Eqs. (4.48) and (4.49).

1) **To solve $\boldsymbol{b}_m^j$**

By applying $\boldsymbol{D\hat{H}1}_m^j \times$ Eq. (4.48) $-$ $\boldsymbol{\hat{H}1}_m^j \times$ Eq. (4.49), we obtain

$$\begin{aligned} &\left(\boldsymbol{D\hat{H}1}_m^j \boldsymbol{\hat{J}}_m^j - \boldsymbol{\hat{H}1}_m^j \boldsymbol{D\hat{J}}_m^j \right) \boldsymbol{b}_m^j \\ =& \left(\boldsymbol{D\hat{H}1}_m^j \boldsymbol{C}_{\boldsymbol{a}}^{j+1} \boldsymbol{\hat{H}1}_m^{j+1} - \boldsymbol{\hat{H}1}_m^j \boldsymbol{C}_{\boldsymbol{b}}^{j+1} \boldsymbol{D\hat{H}1}_m^{j+1} \right) \boldsymbol{a}_m^{j+1} \\ &+ \left(\boldsymbol{D\hat{H}1}_m^j \boldsymbol{C}_{\boldsymbol{a}}^{j+1} \boldsymbol{\hat{J}}_m^{j+1} - \boldsymbol{\hat{H}1}_m^j \boldsymbol{C}_{\boldsymbol{b}}^{j+1} \boldsymbol{D\hat{J}}_m^{j+1} \right) \boldsymbol{b}_m^{j+1}. \end{aligned} \tag{4.50}$$

Denote

$$\boldsymbol{F}_b^j \triangleq \boldsymbol{D\hat{H}}1_m^j \boldsymbol{\hat{J}}_m^j - \boldsymbol{\hat{H}1}_m^j \boldsymbol{D\hat{J}}_m^j, \tag{4.51}$$

since

$$
\begin{aligned}
&\left(\boldsymbol{D}\hat{\boldsymbol{H}}\boldsymbol{1}_m^j\right)_{\nu\nu}\left(\hat{\boldsymbol{J}}_m^j\right)_{\nu\nu}-\left(\hat{\boldsymbol{H}}\boldsymbol{1}_m^j\right)_{\nu\nu}\left(\boldsymbol{D}\hat{\boldsymbol{J}}_m^j\right)_{\nu\nu}\\
=&\frac{\frac{\mathrm{d}H_m^{(1)}}{\mathrm{d}(k_{r\nu}^j r)}(k_{r\nu}^j r^j)}{H_m^{(1)}(k_{r\nu}^j r^{j-1})}J_m(k_{r\nu}^j r^j)H_m^{(1)}(k_{r\nu}^j r^j)-\frac{H_m^{(1)}(k_{r\nu}^j r^j)}{H_m^{(1)}(k_{r\nu}^j r^{j-1})}\frac{\mathrm{d}J_m}{\mathrm{d}(k_{r\nu}^j r)}(k_{r\nu}^j r^j)H_m^{(1)}(k_{r\nu}^j r^j)\\
=&\frac{H_m^{(1)}(k_{r\nu}^j r^j)}{H_m^{(1)}(k_{r\nu}^j r^{j-1})}\left[J_m(k_{r\nu}^j r^j)\frac{\mathrm{d}H_m^{(1)}}{\mathrm{d}(k_{r\nu}^j r)}(k_{r\nu}^j r^j)-\frac{\mathrm{d}J_m}{\mathrm{d}(k_{r\nu}^j r)}(k_{r\nu}^j r^j)H_m^{(1)}(k_{r\nu}^j r^j)\right]\\
=&\frac{H_m^{(1)}(k_{r\nu}^j r^j)}{H_m^{(1)}(k_{r\nu}^j r^{j-1})}W\left[J_m(k_{r\nu}^j r^j),H_m^{(1)}(k_{r\nu}^j r^j)\right]\\
&W\left[J_m(x),H_m^{(1)}(x)\right]=\frac{2i}{\pi x}\\
=&\frac{2i}{\pi r^j}\left(\frac{1}{k_{r\nu}^j}\frac{H_m^{(1)}(k_{r\nu}^j r^j)}{H_m^{(1)}(k_{r\nu}^j r^{j-1})}\right),
\end{aligned}
\tag{4.52}
$$

thus Eq. (4.51) becomes

$$
\begin{aligned}
\boldsymbol{F}_{\boldsymbol{b}}^j &= \boldsymbol{D}\hat{\boldsymbol{H}}\boldsymbol{1}_m^j\hat{\boldsymbol{J}}_m^j-\hat{\boldsymbol{H}}\boldsymbol{1}_m^j\boldsymbol{D}\hat{\boldsymbol{J}}_m^j\\
&= \frac{2i}{\pi r^j}\mathrm{diag}\left(\frac{1}{k_{r\nu}^j}\frac{H_m^{(1)}(k_{r\nu}^j r^j)}{H_m^{(1)}(k_{r\nu}^j r^{j-1})}\right),\ \nu=1,2,\ldots,N,
\end{aligned}
\tag{4.53}
$$

and its inverse matrix is

$$
\left(\boldsymbol{F}_{\boldsymbol{b}}^{\boldsymbol{j}}\right)^{-1}=\frac{\pi r^j}{2i}\mathrm{diag}\left(k_{r\nu}^j\frac{H_m^{(1)}(k_{r\nu}^j r^{j-1})}{H_m^{(1)}(k_{r\nu}^j r^j)}\right),\ \nu=1,2,\ldots,N.
\tag{4.54}
$$

Substitute Eq. (4.54) into Eq. (4.50) and we obtain

$$
\begin{aligned}
\boldsymbol{b}_m^j &= \left(\boldsymbol{F}_b^j\right)^{-1}\left(\boldsymbol{D}\hat{\boldsymbol{H}}\boldsymbol{1}_m^j\boldsymbol{C}_{\boldsymbol{a}}^{j+1}\hat{\boldsymbol{H}}\boldsymbol{1}_m^{j+1}-\hat{\boldsymbol{H}}\boldsymbol{1}_m^j\boldsymbol{C}_{\boldsymbol{b}}^{j+1}\boldsymbol{D}\hat{\boldsymbol{H}}\boldsymbol{1}_m^{j+1}\right)\boldsymbol{a}_m^{j+1}\\
&\quad+\left(\boldsymbol{F}_b^j\right)^{-1}\left(\boldsymbol{D}\hat{\boldsymbol{H}}\boldsymbol{1}_m^j\boldsymbol{C}_{\boldsymbol{a}}^{j+1}\hat{\boldsymbol{J}}_m^{j+1}-\hat{\boldsymbol{H}}\boldsymbol{1}_m^j\boldsymbol{C}_{\boldsymbol{b}}^{j+1}\boldsymbol{D}\hat{\boldsymbol{J}}_m^{j+1}\right)\boldsymbol{b}_m^{j+1}\\
&\triangleq \boldsymbol{R}_{m3}^{j+1}\boldsymbol{a}_m^{j+1}+\boldsymbol{R}_{m4}^{j+1}\boldsymbol{b}_m^{j+1},
\end{aligned}
\tag{4.55}
$$

and we notice that in Eq. (4.55) we have $\hat{\boldsymbol{H}}\boldsymbol{1}_m^{j+1}=\boldsymbol{I}$.

2) **To solve $\boldsymbol{a}_m^j$**

By applying $\boldsymbol{D}\hat{\boldsymbol{J}}_m^j \times$ Eq. (4.48) $-$ $\hat{\boldsymbol{J}}_m^j \times$ Eq. (4.49), we obtain

$$\begin{aligned}
&\left(\boldsymbol{D}\hat{\boldsymbol{J}}_m^j \hat{\boldsymbol{H}}\boldsymbol{1}_m^j - \hat{\boldsymbol{J}}_m^j \boldsymbol{D}\hat{\boldsymbol{H}}\boldsymbol{1}_m^j\right) \boldsymbol{a}_m^j \\
=&\left(\boldsymbol{D}\hat{\boldsymbol{J}}_m^j \boldsymbol{C}_{\boldsymbol{a}}^{j+1} \hat{\boldsymbol{H}}\boldsymbol{1}_m^{j+1} - \hat{\boldsymbol{J}}_m^j \boldsymbol{C}_{\boldsymbol{b}}^{j+1} \boldsymbol{D}\hat{\boldsymbol{H}}\boldsymbol{1}_m^{j+1}\right) \boldsymbol{a}_m^{j+1} \\
&+\left(\boldsymbol{D}\hat{\boldsymbol{J}}_m^j \boldsymbol{C}_{\boldsymbol{a}}^{j+1} \hat{\boldsymbol{J}}_m^{j+1} - \hat{\boldsymbol{J}}_m^j \boldsymbol{C}_{\boldsymbol{b}}^{j+1} \boldsymbol{D}\hat{\boldsymbol{J}}_m^{j+1}\right) \boldsymbol{b}_m^{j+1}.
\end{aligned} \tag{4.56}$$

Denote

$$\boldsymbol{F}_{\boldsymbol{a}}^j \triangleq \boldsymbol{D}\hat{\boldsymbol{J}}_m^j \hat{\boldsymbol{H}}\boldsymbol{1}_m^j - \hat{\boldsymbol{J}}_m^j \boldsymbol{D}\hat{\boldsymbol{H}}\boldsymbol{1}_m^j. \tag{4.57}$$

By comparing Eq. (4.57) with Eq. (4.51), since $\boldsymbol{D}\hat{\boldsymbol{J}}_m^j$, $\hat{\boldsymbol{H}}\boldsymbol{1}_m^j$, $\hat{\boldsymbol{J}}_m^j$ and $\boldsymbol{D}\hat{\boldsymbol{H}}\boldsymbol{1}_m^j$ are diagonal matrixes, we have

$$\boldsymbol{F}_{\boldsymbol{a}}^j = -\boldsymbol{F}_{\boldsymbol{b}}^j, \tag{4.58}$$

and thus Eq. (4.56) leads to

$$\begin{aligned}
\boldsymbol{a}_m^j &= \left(\boldsymbol{F}_{\boldsymbol{a}}^j\right)^{-1} \left(\boldsymbol{D}\hat{\boldsymbol{J}}_m^j \boldsymbol{C}_{\boldsymbol{a}}^{j+1} \hat{\boldsymbol{H}}\boldsymbol{1}_m^{j+1} - \hat{\boldsymbol{J}}_m^j \boldsymbol{C}_{\boldsymbol{b}}^{j+1} \boldsymbol{D}\hat{\boldsymbol{H}}\boldsymbol{1}_m^{j+1}\right) \boldsymbol{a}_m^{j+1} \\
&\quad + \left(\boldsymbol{F}_{\boldsymbol{a}}^j\right)^{-1} \left(\boldsymbol{D}\hat{\boldsymbol{J}}_m^j \boldsymbol{C}_{\boldsymbol{a}}^{j+1} \hat{\boldsymbol{J}}_m^{j+1} - \hat{\boldsymbol{J}}_m^j \boldsymbol{C}_{\boldsymbol{b}}^{j+1} \boldsymbol{D}\hat{\boldsymbol{J}}_m^{j+1}\right) \boldsymbol{b}_m^{j+1} \\
&= -\left(\boldsymbol{F}_{\boldsymbol{b}}^j\right)^{-1} \left(\boldsymbol{D}\hat{\boldsymbol{J}}_m^j \boldsymbol{C}_{\boldsymbol{a}}^{j+1} \hat{\boldsymbol{H}}\boldsymbol{1}_m^{j+1} - \hat{\boldsymbol{J}}_m^j \boldsymbol{C}_{\boldsymbol{b}}^{j+1} \boldsymbol{D}\hat{\boldsymbol{H}}\boldsymbol{1}_m^{j+1}\right) \boldsymbol{a}_m^{j+1} \\
&\quad - \left(\boldsymbol{F}_{\boldsymbol{b}}^j\right)^{-1} \left(\boldsymbol{D}\hat{\boldsymbol{J}}_m^j \boldsymbol{C}_{\boldsymbol{a}}^{j+1} \hat{\boldsymbol{J}}_m^{j+1} - \hat{\boldsymbol{J}}_m^j \boldsymbol{C}_{\boldsymbol{b}}^{j+1} \boldsymbol{D}\hat{\boldsymbol{J}}_m^{j+1}\right) \boldsymbol{b}_m^{j+1} \\
&\triangleq \boldsymbol{R}_{m1}^{j+1} \boldsymbol{a}_m^{j+1} + \boldsymbol{R}_{m2}^{j+1} \boldsymbol{b}_m^{j+1}.
\end{aligned} \tag{4.59}$$

Combine Eqs. (4.55) and (4.59) together, then we obtain

$$\begin{bmatrix} \boldsymbol{b}_m^j \\ \boldsymbol{a}_m^j \end{bmatrix} = \begin{bmatrix} \boldsymbol{R}_{m4}^{j+1} & \boldsymbol{R}_{m3}^{j+1} \\ \boldsymbol{R}_{m2}^{j+1} & \boldsymbol{R}_{m1}^{j+1} \end{bmatrix} \begin{bmatrix} \boldsymbol{b}_m^{j+1} \\ \boldsymbol{a}_m^{j+1} \end{bmatrix}, \tag{4.60}$$

where

$$\boldsymbol{R}_{m1}^{j+1} = -\left(\boldsymbol{F}_{\boldsymbol{b}}^{j}\right)^{-1}\left(\boldsymbol{D}\hat{\boldsymbol{J}}_{m}^{j}\boldsymbol{C}_{\boldsymbol{a}}^{j+1}\hat{\boldsymbol{H}}\mathbf{1}_{m}^{j+1} - \hat{\boldsymbol{J}}_{m}^{j}\boldsymbol{C}_{\boldsymbol{b}}^{j+1}\boldsymbol{D}\hat{\boldsymbol{H}}\mathbf{1}_{m}^{j+1}\right), \tag{4.61}$$

$$\boldsymbol{R}_{m2}^{j+1} = -\left(\boldsymbol{F}_{\boldsymbol{b}}^{j}\right)^{-1}\left(\boldsymbol{D}\hat{\boldsymbol{J}}_{m}^{j}\boldsymbol{C}_{\boldsymbol{a}}^{j+1}\hat{\boldsymbol{J}}_{m}^{j+1} - \hat{\boldsymbol{J}}_{m}^{j}\boldsymbol{C}_{\boldsymbol{b}}^{j+1}\boldsymbol{D}\hat{\boldsymbol{J}}_{m}^{j+1}\right), \tag{4.62}$$

$$\boldsymbol{R}_{m3}^{j+1} = \left(\boldsymbol{F}_{b}^{j}\right)^{-1}\left(\boldsymbol{D}\hat{\boldsymbol{H}}\mathbf{1}_{m}^{j}\boldsymbol{C}_{\boldsymbol{a}}^{j+1}\hat{\boldsymbol{H}}\mathbf{1}_{m}^{j+1} - \hat{\boldsymbol{H}}\mathbf{1}_{m}^{j}\boldsymbol{C}_{\boldsymbol{b}}^{j+1}\boldsymbol{D}\hat{\boldsymbol{H}}\mathbf{1}_{m}^{j+1}\right), \tag{4.63}$$

$$\boldsymbol{R}_{m4}^{j+1} = \left(\boldsymbol{F}_{b}^{j}\right)^{-1}\left(\boldsymbol{D}\hat{\boldsymbol{H}}\mathbf{1}_{m}^{j}\boldsymbol{C}_{\boldsymbol{a}}^{j+1}\hat{\boldsymbol{J}}_{m}^{j+1} - \hat{\boldsymbol{H}}\mathbf{1}_{m}^{j}\boldsymbol{C}_{\boldsymbol{b}}^{j+1}\boldsymbol{D}\hat{\boldsymbol{J}}_{m}^{j+1}\right), \tag{4.64}$$

$$\left(\boldsymbol{F}_{\boldsymbol{b}}^{\boldsymbol{j}}\right)^{-1} = \frac{\pi r^{j}}{2i}\operatorname{diag}\left(k_{r\nu}^{j}\frac{H_{m}^{(1)}(k_{r\nu}^{j}r^{j-1})}{H_{m}^{(1)}(k_{r\nu}^{j}r^{j})}\right),\ \nu = 1, 2, \ldots, N. \tag{4.65}$$

To apply the single-scatter approximation, let $\boldsymbol{a}_{m}^{j} = \mathbf{0}$, then from Eq. (4.60) we have

$$\boldsymbol{R}_{m2}^{j+1}\boldsymbol{b}_{m}^{j+1} + \boldsymbol{R}_{m1}^{j+1}\boldsymbol{a}_{m}^{j+1} = 0, \tag{4.66}$$

which leads to

$$\boldsymbol{a}_{m}^{j+1} = -\left(\boldsymbol{R}_{m1}^{j+1}\right)^{-1}\boldsymbol{R}_{m2}^{j+1}\boldsymbol{b}_{m}^{j+1}. \tag{4.67}$$

With $\boldsymbol{a}_{m}^{j+1}$ computed by Eq. (4.67), we may obtain $\boldsymbol{b}_{m}^{j}$ from Eq. (4.60),

$$\boldsymbol{b}_{m}^{j} = \boldsymbol{R}_{m4}^{j+1}\boldsymbol{b}_{m}^{j+1} + \boldsymbol{R}_{m3}^{j+1}\boldsymbol{a}_{m}^{j+1}. \tag{4.68}$$

4.3.2 Outward Marching

As illustrated in Fig. 4-9, in outward marching, we need to obtain $\boldsymbol{a}_{m}^{j+1}$, with $\boldsymbol{a}_{m}^{j}$ known, by means of the one-way approximation.

Similar to the derivation in the inward marching, we reach the equation as below (refer to Appendix H),

$$\begin{bmatrix} \boldsymbol{b}_{m}^{j+1} \\ \boldsymbol{a}_{m}^{j+1} \end{bmatrix} = \begin{bmatrix} \boldsymbol{S}_{m4}^{j} & \boldsymbol{S}_{m3}^{j} \\ \boldsymbol{S}_{m2}^{j} & \boldsymbol{S}_{m1}^{j} \end{bmatrix} \begin{bmatrix} \boldsymbol{b}_{m}^{j} \\ \boldsymbol{a}_{m}^{j} \end{bmatrix}, \tag{4.69}$$

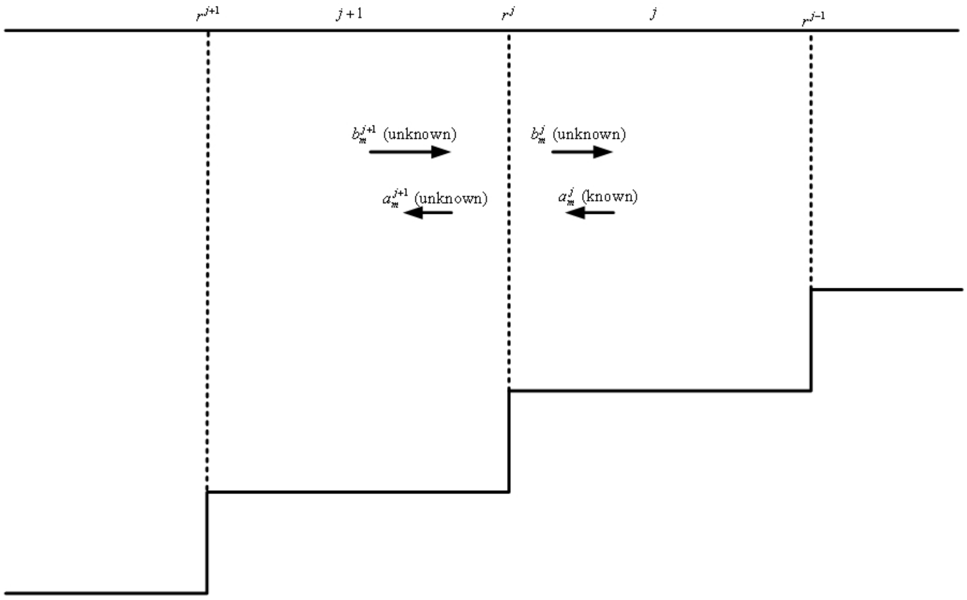

Figure 4-9: Coupling between two neighboring rings in outward marching, where the one-way approximation, $\boldsymbol{b}_m^{j+1} = \mathbf{0}$ and $\boldsymbol{b}_m^j = \mathbf{0}$, is applied.

with the one-way approximation, let $\boldsymbol{b}_m^{j+1} = \mathbf{0}$ and $\boldsymbol{b}_m^j = \mathbf{0}$, then we obtain

$$\boldsymbol{a}_m^{j+1} = \boldsymbol{S}_{m1}^j \boldsymbol{a}_m^j, \tag{4.70}$$

where

$$\boldsymbol{S}_{m1}^j = \left(\boldsymbol{G}_{\boldsymbol{a}}^{j+1}\right)^{-1} \left[\boldsymbol{D}\hat{\boldsymbol{J}}_m^{j+1}\boldsymbol{C}_{\boldsymbol{c}}^j\hat{\boldsymbol{H}}\mathbf{1}_m^j - \hat{\boldsymbol{J}}_m^{j+1}\boldsymbol{C}_{\boldsymbol{d}}^j\boldsymbol{D}\hat{\boldsymbol{H}}\mathbf{1}_m^j\right], \tag{4.71}$$

$$\boldsymbol{C}_{\boldsymbol{c}\nu n}^j = \int_0^\infty \frac{1}{\rho^{j+1}(z)} \Psi_\nu^{j+1}(z)\Psi_n^j(z)\mathrm{d}z, \tag{4.72}$$

$$\boldsymbol{C}_{\boldsymbol{d}\nu n}^j = \frac{k_{rn}^j}{k_{r\nu}^{j+1}} \int_0^\infty \frac{1}{\rho^j(z)} \Psi_\nu^{j+1}(z)\Psi_n^j(z)\mathrm{d}z, \tag{4.73}$$

$$\left(\boldsymbol{G}_{\boldsymbol{a}}^{j+1}\right)^{-1} = i\frac{\pi r^j}{2}\mathrm{diag}\left(k_{r\nu}^{j+1}\frac{H_m^{(1)}(k_{r\nu}^{j+1}r^j)}{H_m^{(1)}(k_{r\nu}^{j+1}r^{j+1})}\right). \tag{4.74}$$

4.3.3 Numerical Stability

In Section 4.3.1 and Section 4.3.2, we give the formulas for inward marching coupling and outward marching coupling, which, by combining together in the way as illustrated in Fig. 4-7, lead to two-way coupling. However, we should take some special treatments to achieve stable solutions.

Stable Inward Marching Formulas

1) **To obtain stable $\boldsymbol{R}_{m3}^{j+1}$ and $\boldsymbol{R}_{m4}^{j+1}$**

$\left(\boldsymbol{F}_{\boldsymbol{b}}^{j}\right)^{-1}$ is not stable for $m \gg |k_{r\nu}^{j} r^{j}|$ and $m \ll |k_{r\nu}^{j} r^{j}|$, because from Eq. (4.65) we see that $\left(\boldsymbol{F}_{\boldsymbol{b}}^{j}\right)_{\nu\nu}^{-1}$ depends on $\frac{H_m^{(1)}(k_{r\nu}^{j} r^{j-1})}{H_m^{(1)}(k_{r\nu}^{j} r^{j})}$, which is not properly normalized, thus it will blow up when $m \gg |k_{r\nu}^{j} r^{j}|$ and $m \ll |k_{r\nu}^{j} r^{j}|$. (We know that $\frac{H_m^{(1)}(k_{r\nu}^{j} r^{j})}{H_m^{(1)}(k_{r\nu}^{j} r^{j-1})}$ is properly normalized and thus stable.)

However, we may compute the products $\left(\boldsymbol{F}_{\boldsymbol{b}}^{j}\right)^{-1} \boldsymbol{D}\hat{\boldsymbol{H}}\mathbf{1}_{m}^{j}$ and $\left(\boldsymbol{F}_{\boldsymbol{b}}^{j}\right)^{-1} \hat{\boldsymbol{H}}\mathbf{1}_{m}^{j}$ in Eqs. (4.63) and (4.64) to avoid evaluating $\left(\boldsymbol{F}_{\boldsymbol{b}}^{j}\right)^{-1}$, and in this way we will obtain stable results of $\boldsymbol{R}_{m3}^{j+1}$ and $\boldsymbol{R}_{m4}^{j+1}$. We have

$$\left(\boldsymbol{F}_{\boldsymbol{b}}^{j}\right)_{\nu\nu}^{-1} = \frac{\pi r^{j}}{2i} k_{r\nu}^{j} \frac{H_m^{(1)}(k_{r\nu}^{j} r^{j-1})}{H_m^{(1)}(k_{r\nu}^{j} r^{j})}, \tag{4.75}$$

$$\left(\hat{\boldsymbol{H}}\mathbf{1}_{m}^{j}\right)_{\nu\nu} = \frac{H_m^{(1)}(k_{r\nu}^{j} r^{j})}{H_m^{(1)}(k_{r\nu}^{j} r^{j-1})}, \tag{4.76}$$

$$\left(\boldsymbol{D}\hat{\boldsymbol{H}}\mathbf{1}_{m}^{j}\right)_{\nu\nu} = \frac{\frac{\mathrm{d}H_m^{(1)}}{\mathrm{d}(k_{r\nu}^{j} r)}(k_{r\nu}^{j} r^{j})}{H_m^{(1)}(k_{r\nu}^{j} r^{j-1})}, \tag{4.77}$$

so,

$$\left(\boldsymbol{F}_{\boldsymbol{b}}^{j}\right)_{\nu\nu}^{-1} \left(\hat{\boldsymbol{H}}\mathbf{1}_{m}^{j}\right)_{\nu\nu} = \frac{\pi r^{j}}{2i} k_{r\nu}^{j}, \tag{4.78}$$

$$\left(\boldsymbol{F}_{\boldsymbol{b}}^{j}\right)_{\nu\nu}^{-1} \left(\boldsymbol{D}\hat{\boldsymbol{H}}\mathbf{1}_{m}^{j}\right)_{\nu\nu} = \frac{\pi r^{j}}{2i} k_{r\nu}^{j} \frac{\frac{\mathrm{d}H_m^{(1)}}{\mathrm{d}(k_{r\nu}^{j} r)}(k_{r\nu}^{j} r^{j})}{H_m^{(1)}(k_{r\nu}^{j} r^{j})}, \tag{4.79}$$

or,

$$\left(\boldsymbol{F}_{\boldsymbol{b}}^{j}\right)^{-1} \hat{\boldsymbol{H}}\mathbf{1}_{m}^{j} = \frac{\pi r^{j}}{2i} \mathrm{diag}\left(k_{r\nu}^{j}\right), \ \nu = 1, 2, \ldots, N, \tag{4.80}$$

$$\left(\boldsymbol{F}_{\boldsymbol{b}}^{j}\right)^{-1} \boldsymbol{D}\hat{\boldsymbol{H}}\mathbf{1}_{m}^{j} = \frac{\pi r^{j}}{2i} \mathrm{diag}\left(k_{r\nu}^{j} \frac{\frac{\mathrm{d}H_m^{(1)}}{\mathrm{d}(k_{r\nu}^{j} r)}(k_{r\nu}^{j} r^{j})}{H_m^{(1)}(k_{r\nu}^{j} r^{j})} \right), \ \nu = 1, 2, \ldots, N. \tag{4.81}$$

$\left(\boldsymbol{F}_{\boldsymbol{b}}^{j}\right)^{-1}\hat{\boldsymbol{H}}\mathbf{1}_{m}^{j}$ and $\left(\boldsymbol{F}_{\boldsymbol{b}}^{j}\right)^{-1}\boldsymbol{D}\hat{\boldsymbol{H}}\mathbf{1}_{m}^{j}$ in Eqs. (4.80) and (4.81) are stable, thus by substituting Eqs. (4.80) and (4.81) back into Eqs. (4.63) and (4.64), we will obtain stable $\boldsymbol{R}_{m3}^{j+1}$ and $\boldsymbol{R}_{m4}^{j+1}$.

2) **To obtain stable $\left(\boldsymbol{R}_{m1}^{j+1}\right)^{-1}\boldsymbol{R}_{m2}^{j+1}$**

As stated above, $\left(\boldsymbol{F}_{\boldsymbol{b}}^{j}\right)^{-1}$ is instable. However, from Eq. (4.67), we may compute the product $\left(\boldsymbol{R}_{m1}^{j+1}\right)^{-1}\boldsymbol{R}_{m2}^{j+1}$ to avoid evaluating $\left(\boldsymbol{F}_{\boldsymbol{b}}^{j}\right)^{-1}$ in obtaining $\boldsymbol{a}_{m}^{j+1}$. From Eqs. (4.61) and (4.62), we have

$$\begin{aligned}
&\left(\boldsymbol{R}_{m1}^{j+1}\right)^{-1}\boldsymbol{R}_{m2}^{j+1}\\
&=\left(\boldsymbol{D}\hat{\boldsymbol{J}}_{m}^{j}\boldsymbol{C}_{\boldsymbol{a}}^{j+1}\hat{\boldsymbol{H}}\mathbf{1}_{m}^{j+1}-\hat{\boldsymbol{J}}_{m}^{j}\boldsymbol{C}_{\boldsymbol{b}}^{j+1}\boldsymbol{D}\hat{\boldsymbol{H}}\mathbf{1}_{m}^{j+1}\right)^{-1}\boldsymbol{F}_{\boldsymbol{b}}^{j}\left(\boldsymbol{F}_{\boldsymbol{b}}^{j}\right)^{-1}\left(\boldsymbol{D}\hat{\boldsymbol{J}}_{m}^{j}\boldsymbol{C}_{\boldsymbol{a}}^{j+1}\hat{\boldsymbol{J}}_{m}^{j+1}-\hat{\boldsymbol{J}}_{m}^{j}\boldsymbol{C}_{\boldsymbol{b}}^{j+1}\boldsymbol{D}\hat{\boldsymbol{J}}_{m}^{j+1}\right)\\
&=\left(\boldsymbol{D}\hat{\boldsymbol{J}}_{m}^{j}\boldsymbol{C}_{\boldsymbol{a}}^{j+1}\hat{\boldsymbol{H}}\mathbf{1}_{m}^{j+1}-\hat{\boldsymbol{J}}_{m}^{j}\boldsymbol{C}_{\boldsymbol{b}}^{j+1}\boldsymbol{D}\hat{\boldsymbol{H}}\mathbf{1}_{m}^{j+1}\right)^{-1}\left(\boldsymbol{D}\hat{\boldsymbol{J}}_{m}^{j}\boldsymbol{C}_{\boldsymbol{a}}^{j+1}\hat{\boldsymbol{J}}_{m}^{j+1}-\hat{\boldsymbol{J}}_{m}^{j}\boldsymbol{C}_{\boldsymbol{b}}^{j+1}\boldsymbol{D}\hat{\boldsymbol{J}}_{m}^{j+1}\right).
\end{aligned} \tag{4.82}$$

$\left(\boldsymbol{R}_{m1}^{j+1}\right)^{-1}\boldsymbol{R}_{m2}^{j+1}$ evaluated by Eq. (4.82) is stable and so $\boldsymbol{a}_{m}^{j+1}$ computed by Eq. (4.67) is also stable.

Stable Outward Marching Formulas

$(\boldsymbol{G}_{\boldsymbol{a}}^{j+1})^{-1}$ in Eq. (4.74) is not stable, because $\frac{H_m^{(1)}(k_{r\nu}^{j+1}r^j)}{H_m^{(1)}(k_{r\nu}^{j+1}r^{j+1})}$ is not properly normalized, thus we should avoid computing it in obtaining $\boldsymbol{a}_{m}^{j+1}$ by Eqs. (4.70) and (4.71). Instead, we may compute the products $(\boldsymbol{G}_{\boldsymbol{a}}^{j+1})^{-1}\boldsymbol{D}\hat{\boldsymbol{J}}_{m}^{j+1}$ and $(\boldsymbol{G}_{\boldsymbol{a}}^{j+1})^{-1}\hat{\boldsymbol{J}}_{m}^{j+1}$.

Since

$$\begin{aligned}
\left(\boldsymbol{G}_{\boldsymbol{a}}^{j+1}\right)_{\nu\nu}^{-1}&=i\frac{\pi r^j}{2}k_{r\nu}^{j+1}\frac{H_m^{(1)}(k_{r\nu}^{j+1}r^j)}{H_m^{(1)}(k_{r\nu}^{j+1}r^{j+1})},\\
\left(\hat{\boldsymbol{J}}_{m}^{j+1}\right)_{\nu\nu}&=J_m(k_{r\nu}^{j+1}r^j)H_m^{(1)}(k_{r\nu}^{j+1}r^{j+1}),\\
\left(\boldsymbol{D}\hat{\boldsymbol{J}}_{m}^{j+1}\right)_{\nu\nu}&=\frac{\mathrm{d}J_m}{\mathrm{d}(k_{r\nu}^{j+1}r)}(k_{r\nu}^{j+1}r^j)H_m^{(1)}(k_{r\nu}^{j+1}r^{j+1}),
\end{aligned}$$

we have

$$\left(\boldsymbol{G}_{\boldsymbol{a}}^{j+1}\right)_{\nu\nu}^{-1}\left(\hat{\boldsymbol{J}}_m^{j+1}\right)_{\nu\nu} = i\frac{\pi r^j}{2}k_{r\nu}^{j+1}J_m(k_{r\nu}^{j+1}r^j)H_m^{(1)}(k_{r\nu}^{j+1}r^j), \tag{4.83}$$

$$\left(\boldsymbol{G}_{\boldsymbol{a}}^{j+1}\right)_{\nu\nu}^{-1}\left(\boldsymbol{D}\hat{\boldsymbol{J}}_m^{j+1}\right)_{\nu\nu} = i\frac{\pi r^j}{2}k_{r\nu}^{j+1}\frac{\mathrm{d}J_m}{\mathrm{d}(k_{r\nu}^{j+1}r)}(k_{r\nu}^{j+1}r^j)H_m^{(1)}(k_{r\nu}^{j+1}r^j). \tag{4.84}$$

We know that $J_m(k_{r\nu}^{j+1}r^j)H_m^{(1)}(k_{r\nu}^{j+1}r^j)$ and $\frac{\mathrm{d}J_m}{\mathrm{d}(k_{r\nu}^{j+1}r)}(k_{r\nu}^{j+1}r^j)H_m^{(1)}(k_{r\nu}^{j+1}r^j)$ are properly normalized and thus stable, so we should apply Eqs. (4.83) and (4.84) in computing $\boldsymbol{S}_{m1}^j$ by Eq. (4.71).

4.3.4 Analytical Forms of Coupling Matrixes for Ideal Waveguides

We apply the C-SNAP model to compute the eigenvalues, eigenfunctions, and coupling matrixes $\boldsymbol{C_a}$, $\boldsymbol{C_b}$, $\boldsymbol{C_c}$ and $\boldsymbol{C_d}$ for general waveguides, either with a nonpenetrable (rigid or soft) bottom or with a penetrable bottom. For ideal waveguide problems in which isovelocity in the water column is considered together with a rigid or a soft bottom, we have analytical forms of the eigenvalues, eigenvectors and therefore, the coupling matrixes. Below we give these analytical solutions to ideal waveguide problems with a rigid bottom.

Analytical Solutions for Eigenvalues and Eigenfunctions

In an ideal waveguide with water depth D, we have analytical solutions for eigenvalues and eigenfunctions (refer to Section 5.4 in [12]).

1) **Eigenfunctions**

The eigenfunctions take the form

$$\Psi_n(z) = \sqrt{\frac{2\rho}{D}}\sin(k_{zn}z),\ n = 1, 2, \ldots, \tag{4.85}$$

where ρ is the constant density in the water column, and k_{zn} is the z-component of the wavenumber of mode n in the water column.

2) **Eigenvalues**

The eigenvalues take the form

$$k_{zn} = \tfrac{\pi}{D}\left(n - \tfrac{1}{2}\right), \qquad n = 1, 2, \ldots, \tag{4.86}$$

$$k_{rn} = \sqrt{k^2 - k_{zn}^2}, \qquad n = 1, 2, \ldots, \tag{4.87}$$

where $k = \frac{\omega}{c}$ is the wavenumber in the water column.

3) **The number of propagating modes**

The number of propagating modes is determined by

$$N = \left[\frac{2D}{\lambda} + \frac{1}{2}\right], \tag{4.88}$$

where $[x]$ rounds x to the nearest integer towards minus infinity.

Analytical Forms of Coupling Matrixes

From Section 4.3.1 and Section 4.3.2, we have the following expressions for the coupling matrixes,

$$\begin{aligned}
{\boldsymbol{C}_{\boldsymbol{a}}^{j+1}}_{\nu n} &= \int_0^\infty \frac{1}{\rho^j(z)} \Psi_\nu^j(z) \Psi_n^{j+1}(z) \mathrm{d}z, && \text{(4.89a)}\\
{\boldsymbol{C}_{\boldsymbol{b}}^{j+1}}_{\nu n} &= \frac{k_{rn}^{j+1}}{k_{r\nu}^j} \int_0^\infty \frac{1}{\rho^{j+1}(z)} \Psi_\nu^j(z) \Psi_n^{j+1}(z) \mathrm{d}z, && \text{(4.89b)}\\
\boldsymbol{C}_{\boldsymbol{c}\nu n}^{j} &= \int_0^\infty \frac{1}{\rho^{j+1}(z)} \Psi_\nu^{j+1}(z) \Psi_n^{j}(z) \mathrm{d}z, && \text{(4.89c)}\\
\boldsymbol{C}_{\boldsymbol{d}\nu n}^{j} &= \frac{k_{rn}^{j}}{k_{r\nu}^{j+1}} \int_0^\infty \frac{1}{\rho^{j}(z)} \Psi_\nu^{j+1}(z) \Psi_n^{j}(z) \mathrm{d}z. && \text{(4.89d)}
\end{aligned}$$

By substituting the analytical expressions of eigenfunctions in Eq. (4.85) into Eq. (4.89), we may obtain the analytical forms of the coupling matrixes for ideal waveguides.

As illustrated in Fig. 4-10, we have $\min(D^j, D^{j+1}) = D^j \triangleq D$. Substitute

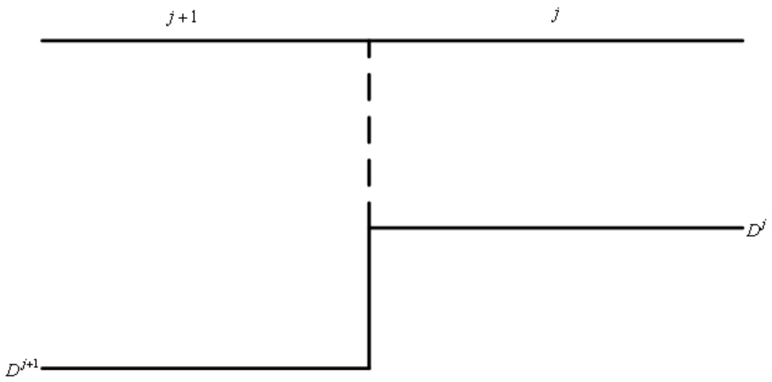

Figure 4-10: Two neighboring rings, ring j with water depth D^j, and ring $j+1$ with water depth D^{j+1}.

Eq. (4.85) into Eq. (4.89a) and we obtain

$$\begin{aligned}
\boldsymbol{C_a}{}^{j+1}_{\nu n} &= \int_0^\infty \frac{1}{\rho^j(z)} \Psi^j_\nu(z)\Psi^{j+1}_n(z)\mathrm{d}z \\
&= \int_0^D \frac{1}{\rho} \Psi^j_\nu(z)\Psi^{j+1}_n(z)\mathrm{d}z \\
&= \int_0^D \frac{1}{\rho}\sqrt{\frac{2\rho}{D^j}} \sin\left(k^j_{z\nu} z\right) \sqrt{\frac{2\rho}{D^{j+1}}} \sin\left(k^{j+1}_{zn} z\right) \mathrm{d}z \\
&= \frac{2}{\sqrt{D^j D^{j+1}}} \int_0^D \sin\left(k^j_{z\nu} z\right) \sin\left(k^{j+1}_{zn} z\right) \mathrm{d}z. \qquad (4.90)
\end{aligned}$$

Denote the integral in Eq. (4.90) by I, and we have

$$\begin{aligned}
I &= \int_0^D \sin\left(k^j_{z\nu} z\right) \sin\left(k^{j+1}_{zn} z\right) \mathrm{d}z \\
&= \int_0^D \frac{1}{2}\left[\cos\left(k^j_{z\nu} - k^{j+1}_{zn}\right) z - \cos\left(k^j_{z\nu} + k^{j+1}_{zn}\right) z\right] \mathrm{d}z \\
&= \frac{1}{2}\left[\frac{1}{k^j_{z\nu} - k^{j+1}_{zn}} \sin\left(k^j_{z\nu} - k^{j+1}_{zn}\right) D - \frac{1}{k^j_{z\nu} + k^{j+1}_{zn}} \sin\left(k^j_{z\nu} + k^{j+1}_{zn}\right) D\right], \qquad (4.91)
\end{aligned}$$

by substituting Eq. (4.91) into Eq. (4.90), we obtain

$$\begin{aligned}
\boldsymbol{C_a}{}^{j+1}_{\nu n} &= \frac{2}{\sqrt{D^j D^{j+1}}} I \\
&= \frac{1}{\sqrt{D^j D^{j+1}}}\left[\frac{1}{k^j_{z\nu} - k^{j+1}_{zn}} \sin\left(k^j_{z\nu} - k^{j+1}_{zn}\right) D - \frac{1}{k^j_{z\nu} + k^{j+1}_{zn}} \sin\left(k^j_{z\nu} + k^{j+1}_{zn}\right) D\right]. \qquad (4.92)
\end{aligned}$$

Similarly, we may obtain

$$\begin{aligned}
\boldsymbol{C}_{\boldsymbol{b}\nu n}^{\,j+1} &= \frac{k_{rn}^{j+1}}{k_{r\nu}^{j}} \int_{0}^{\infty} \frac{1}{\rho^{j+1}(z)} \Psi_{\nu}^{j}(z) \Psi_{n}^{j+1}(z) \mathrm{d}z \\
&= \frac{k_{rn}^{j+1}}{k_{r\nu}^{j}} \int_{0}^{D} \frac{1}{\rho} \Psi_{\nu}^{j}(z) \Psi_{n}^{j+1}(z) \mathrm{d}z \\
&= \frac{k_{rn}^{j+1}}{k_{r\nu}^{j}} \boldsymbol{C}_{\boldsymbol{a}\nu n}^{\,j+1}, \qquad (4.93)
\end{aligned}$$

$$\begin{aligned}
\boldsymbol{C}_{\boldsymbol{c}\nu n}^{\,j} &= \int_{0}^{\infty} \frac{1}{\rho^{j+1}(z)} \Psi_{\nu}^{j+1}(z) \Psi_{n}^{j}(z) \mathrm{d}z \\
&= \int_{0}^{D} \frac{1}{\rho} \Psi_{n}^{j}(z) \Psi_{\nu}^{j+1}(z) \mathrm{d}z \\
&= \boldsymbol{C}_{\boldsymbol{a}n\nu}^{\,j+1}, \qquad (4.94)
\end{aligned}$$

and

$$\begin{aligned}
\boldsymbol{C}_{\boldsymbol{d}\nu n}^{\,j} &= \frac{k_{rn}^{j}}{k_{r\nu}^{j+1}} \int_{0}^{\infty} \frac{1}{\rho^{j}(z)} \Psi_{\nu}^{j+1}(z) \Psi_{n}^{j}(z) \mathrm{d}z \\
&= \frac{k_{rn}^{j}}{k_{r\nu}^{j+1}} \int_{0}^{D} \frac{1}{\rho} \Psi_{n}^{j}(z) \Psi_{\nu}^{j+1}(z) \mathrm{d}z \\
&= \frac{k_{rn}^{j}}{k_{r\nu}^{j+1}} \boldsymbol{C}_{\boldsymbol{a}n\nu}^{\,j+1}. \qquad (4.95)
\end{aligned}$$

In the above we give the analytical forms of coupling matrixes, which we may apply to our three-dimensional propagation model involved with a rigid conical seamount and a rigid bottom. We may also check the accuracy of C-SNAP, which computes these coupling matrixes numerically, by comparing the coupling matrixes obtained by the above analytical forms and by C-SNAP.

4.4 The $N\times$2D Seamount Model

Perkins and Baer [16] introduced the $N\times$2D approach to solve N two-dimensional problems, one for each of N vertical planes passing through the point source, and combine the results to form an approximate 3D solution. In their work [16], parabolic-equation programs are applied to solve each two-dimensional problem.

C-SNAP is an efficient coupled-mode model that can solve two-dimensional range-dependent problems, either in cylindrical geometry with a point source, or in plane geometry with a line source. Below we will show how to apply this two-dimensional model, C-SNAP, to obtain an approximate three-dimensional solution to a conical seamount problem.

4.4.1 Bathymetry at Azimuthal Angle ϕ with respect to the Source

To apply the $N\times 2$D model, different bathymetry is used for each azimuthal angle ϕ with respect to the source. Below we show how to obtain the bathymetry at azimuthal angle ϕ with respect to the source.

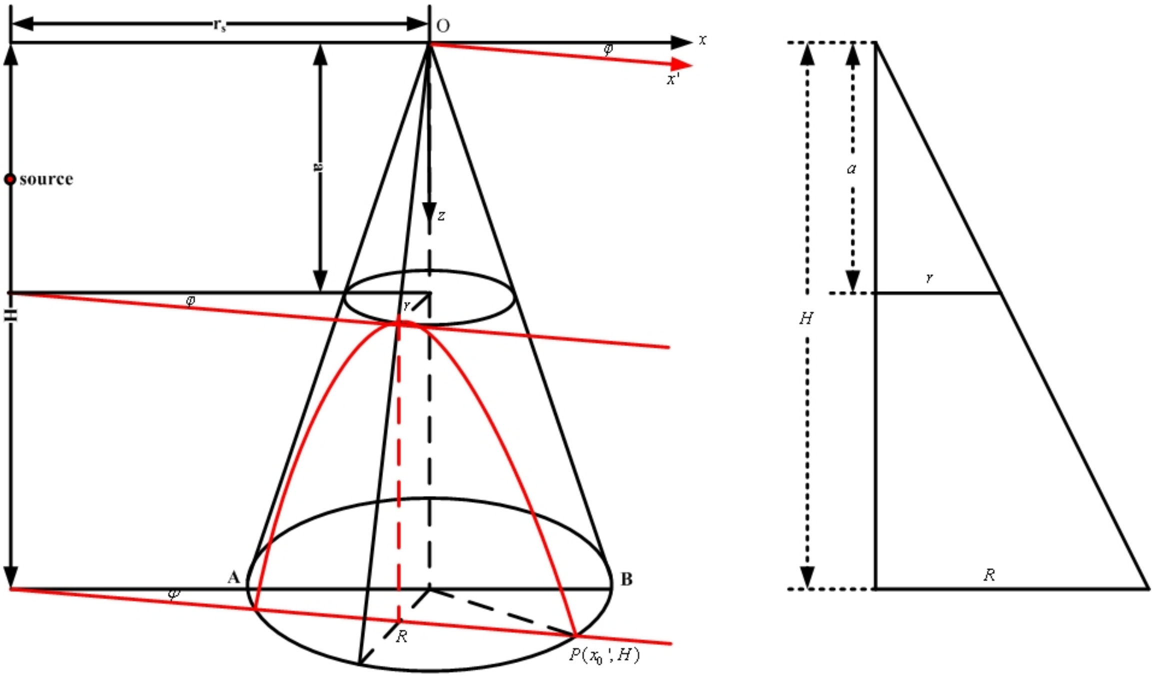

Figure 4-11: Hyperbola $\frac{z^2}{a^2} - \frac{x'^2}{b^2} = 1$.

As illustrated in Fig. 4-11 and Fig. 4-12, the bathymetry at azimuthal angle ϕ with respect to the source is determined as below:

1) at azimuthal angle $\phi = 0$, the shape of the seamount is the triangle OAB, as shown

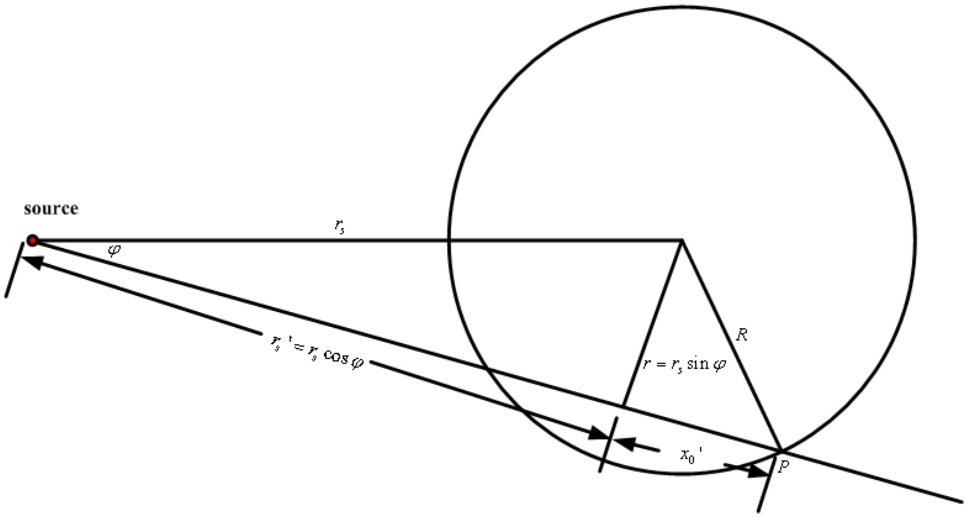

Figure 4-12: The base of a conical seamount.

in Fig. 4-13(a);

2) at azimuthal angle $\phi \geq \phi_c$, where ϕ_c is the tangent angle determined by

$$\phi_c = \arcsin\left(\frac{R}{r_s}\right), \tag{4.96}$$

the seamount is of height zero, i.e., now the waveguide is range-independent, as shown in Fig. 4-13(c);

3) at azimuthal angle $\phi_c > \phi > 0$, the shape of the seamount is a branch of hyperbolas, as shown in Fig. 4-13(b). The equation of the hyperbolas is

$$\frac{z^2}{a^2} - \frac{x'^2}{b^2} = 1, \tag{4.97}$$

where a is determined by (refer to Fig. 4-11)

$$\frac{a}{H} = \frac{r}{R},$$

which leads to

$$a = \frac{r}{R}H = \frac{r_s \sin\phi}{R}H. \tag{4.98}$$

To determine b, we substitute the coordinates of the point $P(x'_0, H)$ into Eq. (4.97),

$$\frac{H^2}{a^2} - \frac{x'^2_0}{b^2} = 1, \tag{4.99}$$

with $x'^2_0 = R^2 - r^2$ (refer to Fig. 4-12), then we can solve b from Eq. (4.99),

$$b^2 = \frac{x'^2_0}{\frac{H^2}{a^2} - 1} = \frac{R^2 - r^2}{\left(\frac{R}{r}\right)^2 - 1} = r^2,$$

i.e.,

$$b = r = r_s \sin\phi. \tag{4.100}$$

4.4.2 Comparison between the $N\times$2D Model and the Three-Dimensional Model

For the conical seamount problem, because the seamount is symmetric with respect to the plane $\phi = 0$, the field near the plane $\phi = 0$ computed by the $N\times$2D model is relatively better than the field computed in a plane ϕ with $\phi_c > \phi > 0$, where no such symmetry for the seamount exists. Since the scattering from the seamount is mainly restricted in the region $\phi < \phi_c$, in any plane ϕ with $\phi \geq \phi_c$, the result computed by the $N\times$2D model is a good approximation of that computed by the three-dimensional model[1].

Furthermore, in the $N\times$2D model, only in-plane scattering is involved; however, in our three-dimensional model, both in-plane and out-of-plane scattering are taken into account. So, when three-dimensional effects are insignificant, where out-of-plane scattering can be neglected, the $N\times$2D model is a good approximation of the three-dimensional model; when three-dimensional effects are significant, where out-of-plane scattering can not be neglected, the approximation of the $N\times$2D model to a true three-dimensional model is not accurate enough. The bottom type, the height of

---

[1] In this section, the azimuthal angle ϕ is with respect to the source.

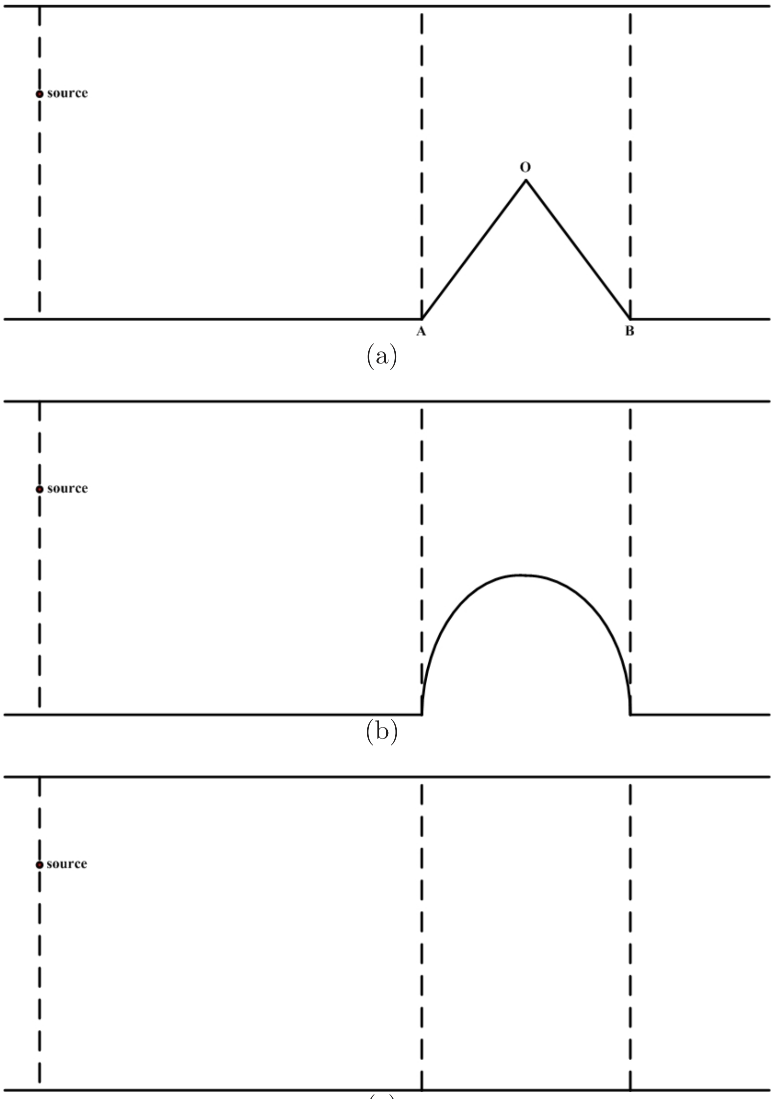

(a)

(b)

(c)

Figure 4-13: Bathymetry at azimuthal angle ϕ with respect to the source. (a) $\phi = 0$, a triangle; (b) $\phi_c > \phi > 0$, hyperbola shape; (c) $\phi \geq \phi_c$, a range-independent waveguide.

seamounts (or, the slope of seamounts), etc, contribute to the significance of three-dimensional effects.

Chapter 5

Physics of Three-Dimensional Seamount Scattering

Two approaches for three-dimensional propagation around a conical seamount were discussed in the previous chapter, i.e., the three-dimensional spectral coupled mode approach, which is a true three-dimensional model, and the $N\times 2$D approach, which gives an approximate three-dimensional solution. Since the $N\times 2$D method does not account for horizontal diffraction, in other words, it does not have the capability of computing the out-of-plane scattering, the $N\times 2$D method does not always give good approximate three-dimensional solutions. In this chapter we will discuss the factors contributing to the three-dimensional effects.

By using uniform stair-step discretization to represent a conical seamount, if the discretization is not fine enough, artificial backscattering beams will appear. We will give criteria to eliminate such artificial backscattering beams. In addition, we will demonstrate that by using random step sizes instead of a uniform step size, such artificial backscattering beams can be smeared out.

5.1 Schematics

Several numerical examples are used to investigate the physics of three-dimensional seamount scattering, which include: propagation in a range-independent waveguide (sanity check), shallow water propagation around a seamount in an ideal waveguide with a rigid bottom, shallow water propagation around a seamount in a waveguide with a penetrable bottom, and deep water propagation around a seamount.

5.1.1 Case 1: Propagation in Range-Independent Waveguide

In case 1, the range-independent waveguide consists of a 250 m water column bounded above by a pressure-release surface and below by a rigid bottom. The water column is isovelocity with $c_w = 1500$ m/s. A 40 Hz point source is located at 100 m depth below the surface. This case is used for the sanity check of our three-dimensional spectral coupled mode seamount model. The schematic is shown in Fig. 5-1.

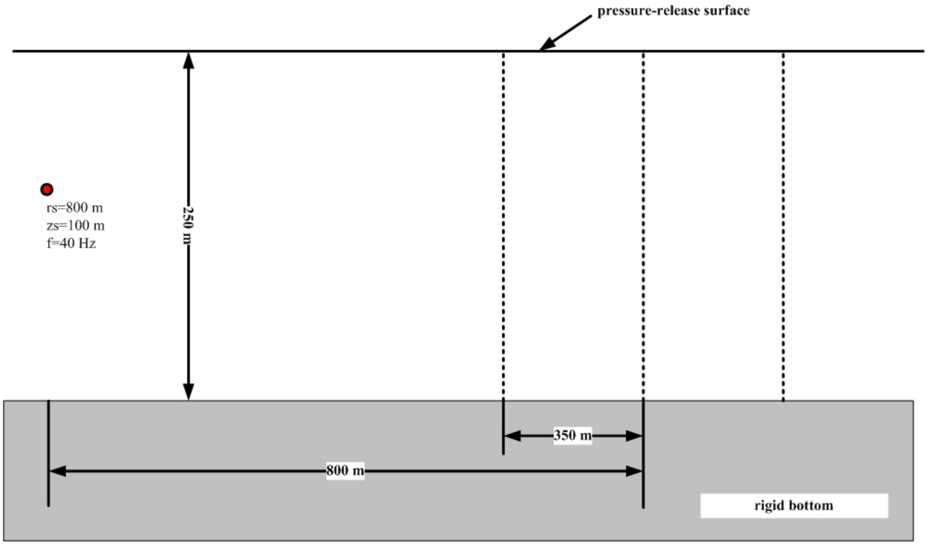

Figure 5-1: The schematic of a range-independent waveguide with a point source (case 1).

5.1.2 Case 2: Shallow Water Propagation around a Seamount

In case 2, the waveguide consists of a 250 m water column bounded above by a pressure-release surface and below by a bottom, either rigid or penetrable. The water column is isovelocity with $c_w = 1500$ m/s. The seamount is 100 m high, placed 800 m from the point source, with a radius of the base 350 m, and having the same acoustic properties as the bottom. We label the case with a rigid bottom as case 2a, and the case with a penetrable bottom as case 2b, in which the properties of the bottom are $c_B = 1800$ m/s, $\beta_B = 0.1$ dB/λ, and $\rho_B = 2.0$ g/cm^3. The schematic of case 2a is shown in Fig. 5-2 and the schematic of case 2b is shown in Fig. 5-3.

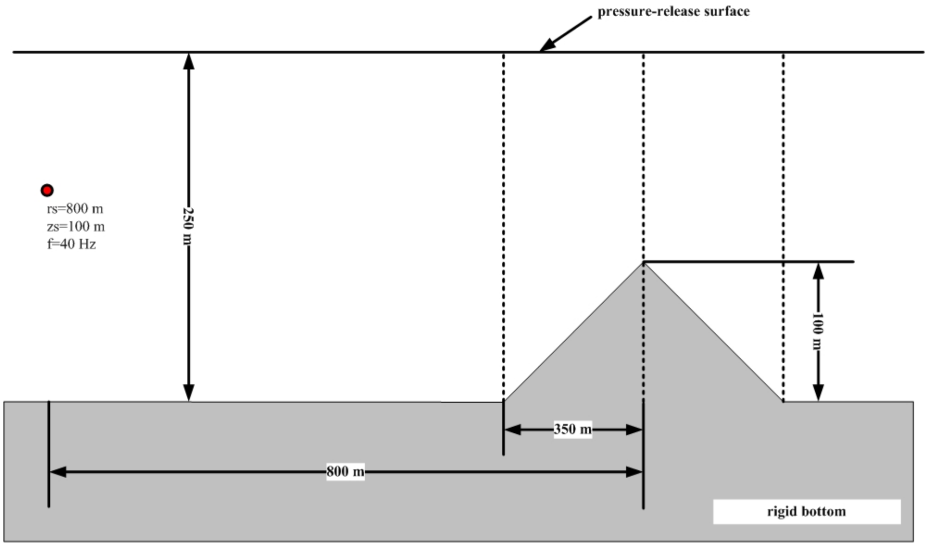

Figure 5-2: The schematic of a shallow water waveguide with a conical seamount and a rigid bottom (case 2a).

5.1.3 Case 3: Deep Water Propagation around a Seamount

In case 3, the waveguide consists of a inhomogeneous water column limited above by a pressure-release flat sea surface and below by a homogeneous fluid half space with a compressional speed of 2000 m/s, a density of 1 g/cm^3, and an attenuation of 0.1 dB/λ. The seamount is 100 km from the source, and has a height of 1000 m and a radius of the base of 20 km, as well as the same acoustic properties as the bottom. The source depth is 100 m. The schematic of this problem is shown in Fig. 5-4.

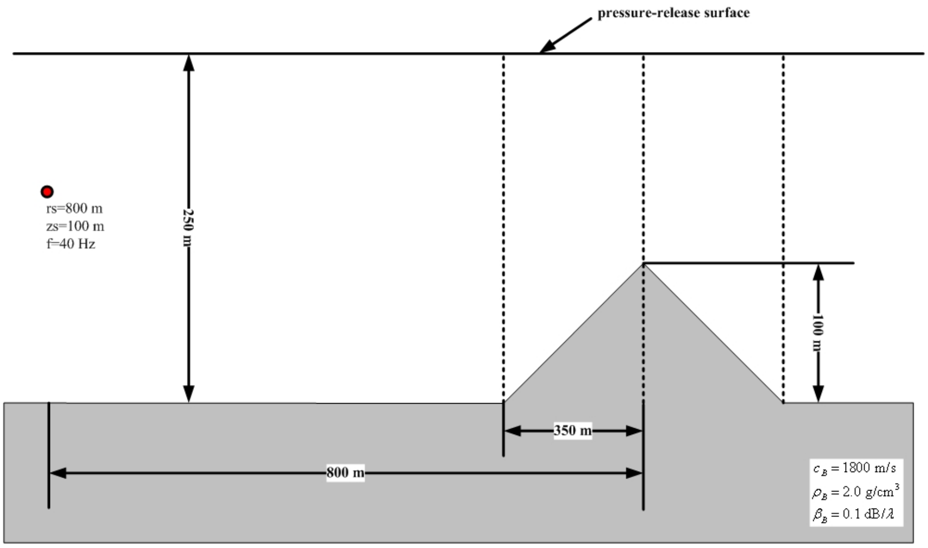

Figure 5-3: The schematic of a shallow water waveguide with a conical seamount and a penetrable bottom (case 2b).

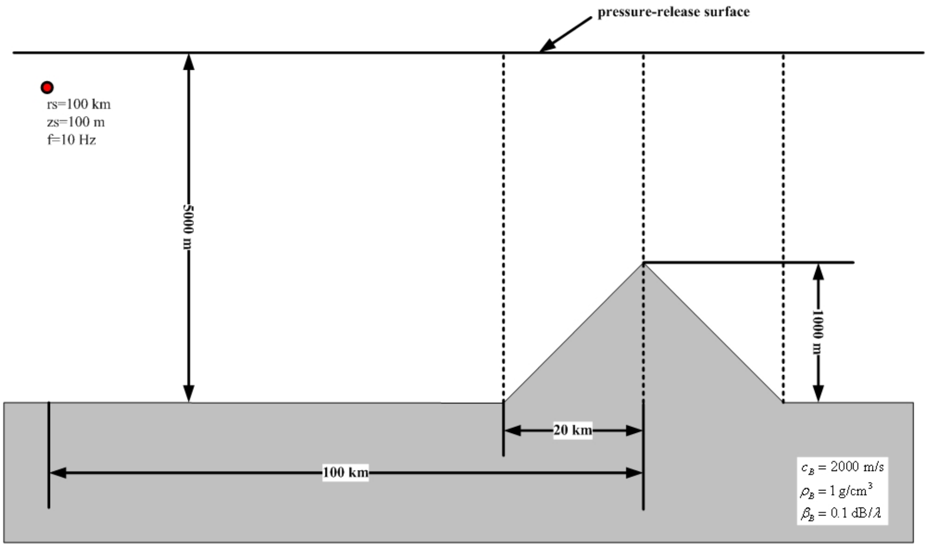

Figure 5-4: The schematic of a deep water waveguide with a conical seamount (case 3).

5.2 Sanity Check

For the range-independent problem in case 1, we know the field may be obtained by the two-dimensional, range-independent normal mode solution (Refer to B.2),

$$p(r,z) = \frac{i}{4\rho(z_s)} \sum_{n=1}^{\infty} \Psi_n(z_s)\Psi_n(z)H_0^{(1)}(k_{rn}r). \tag{5.1}$$

To apply our three-dimensional seamount model, we set a zero-height seamount 800 m from the point source, with a radius of the base 350 m, as illustrated in Fig. 5-1.

Fig. 5-5 shows transmission loss in the horizontal plane at depth 100 m, computed by the two-dimensional normal mode solution in Eq. (5.1), and by our three-dimensional seamount model.

Fig. 5-6 shows transmission loss in vertical planes passing through the point source, computed by the two-dimensional normal mode solution in Eq. (5.1), and by our three-dimensional seamount model. In this case, the field should be axis-symmetric around the point source, i.e. without azimuthal dependence.

From Figs. 5-5 and 5-6 we can see that for a range-independent (and azimuth-independent) problem, the three-dimensional seamount model gives the same results as those of the two-dimensional, range-independent solution. (A detailed discussion can be found in Appendix I.)

5.3 Numerical Issues

5.3.1 Accuracy of C-SNAP

For the ideal waveguide problem in case 2a, as shown in Fig. 5-2, we have analytical expressions for eigenvalues, eigenfunctions and coupling matrixes (refer to Section 4.3.4). We may compare the mode shapes and coupling matrixes computed by the analytical expressions with those computed by C-SNAP numerically and check the accuracy of C-SNAP.

Fig. 5-7 shows the mode shapes of the first three modes in the outmost ring, each

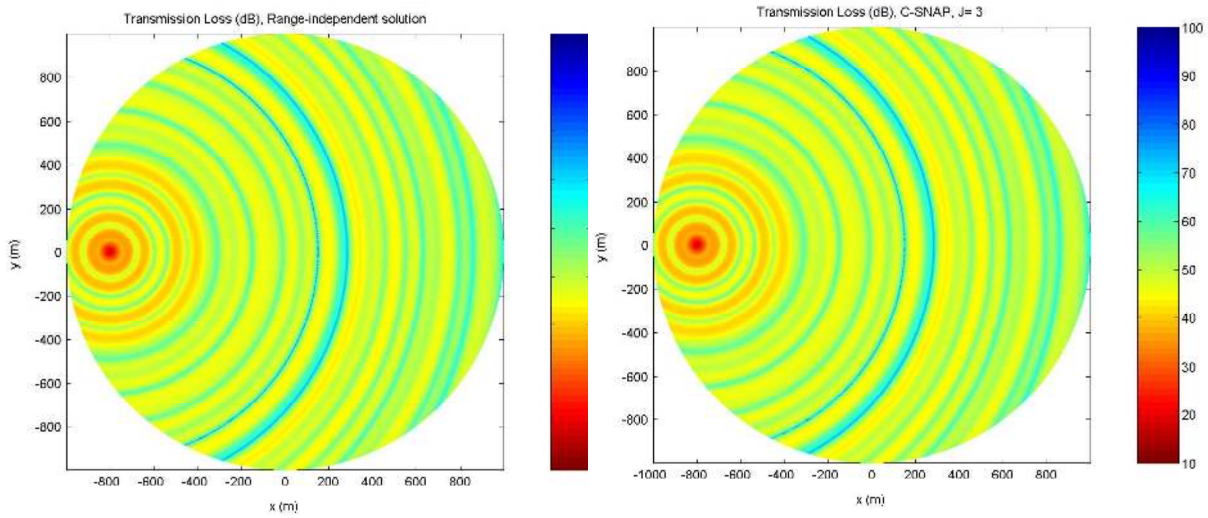

(a) (b)

Figure 5-5: Transmission loss in the horizontal plane at depth 100 m, (a) by using the two-dimensional, range-independent normal mode solution, (b) by the three-dimensional seamount model. For a range-independent problem, the result of our three-dimensional seamount model is the same as that of the two-dimensional normal mode solution.

computed by analytical expressions and by C-SNAP. Fig. 5-8 shows the coupling matrixes at the outmost interface computed by analytical expressions, and Fig. 5-9 shows the coupling matrixes at the outmost interface computed by C-SNAP. From Fig. 5-7, Fig. 5-8 and Fig. 5-9 we can see that C-SNAP computes the eigenfunctions and coupling matrixes accurately.

Fig. 5-10 shows transmission loss in the horizontal plane at depth 100 m, and transmission loss in the vertical plane at azimuthal angle $\phi = 0$ with respect to the source, computed by our three-dimensional seamount model with analytical eigenfunctions and coupling matrixes, and with their numerical solutions by C-SNAP. From Fig. 5-10 we see that the two sets of results show good agreement, which means C-SNAP is a very accurate model.

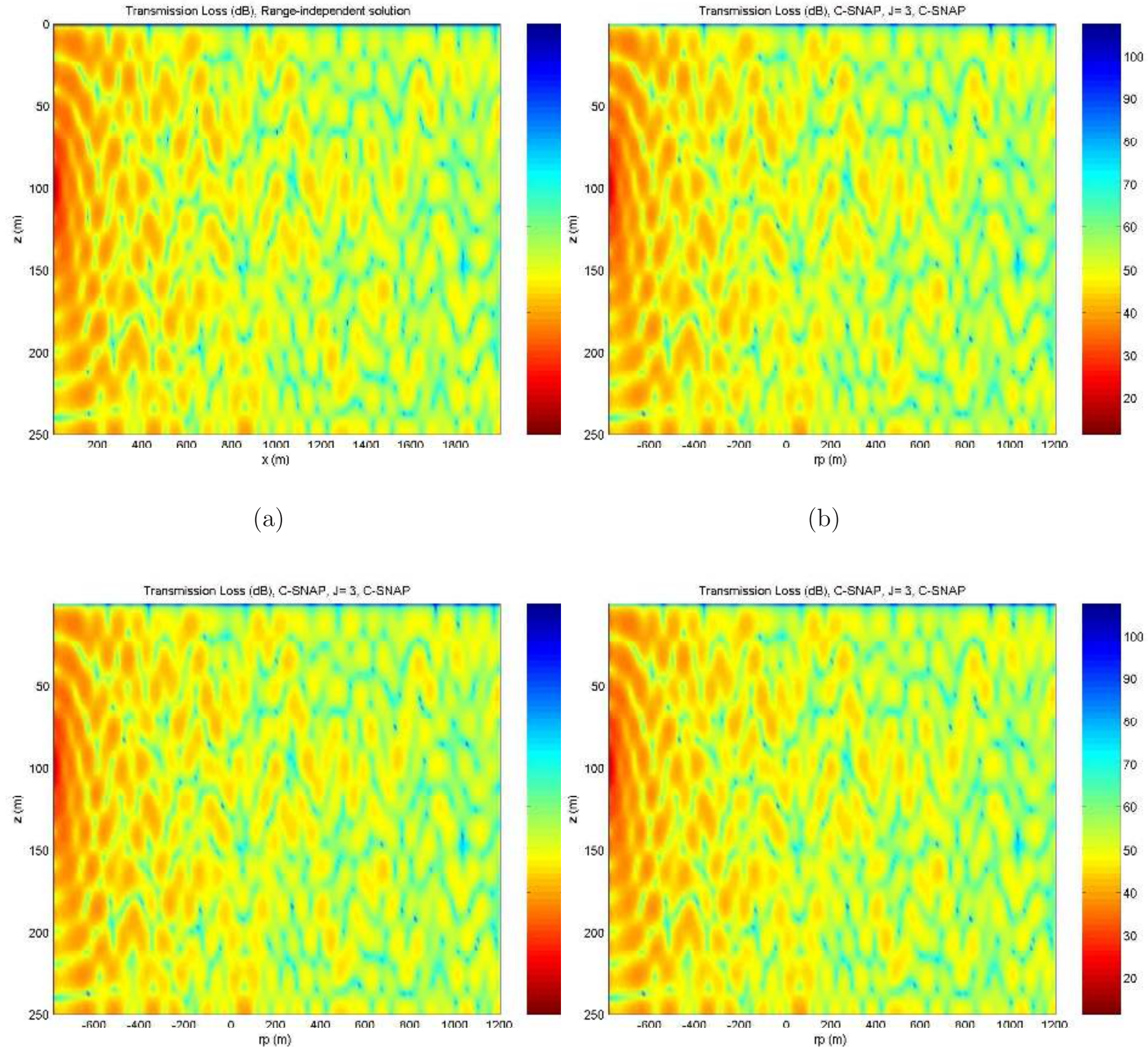

(a) (b)

(c) (d)

Figure 5-6: Transmission loss in vertical planes, (a) the two-dimensional, range-independent normal mode solution, (b) by the three-dimensional seamount model, azimuthal angle $\phi = 0$, (c) by the three-dimensional seamount model, azimuthal angle $\phi = \frac{\pi}{4}$, (d) by the three-dimensional seamount model, azimuthal angle $\phi = \frac{\pi}{2}$. (Azimuthal angle ϕ is with respect to the source.) For a range-independent problem, the result of our three-dimensional seamount model is the same as that of the two-dimensional normal mode solution.

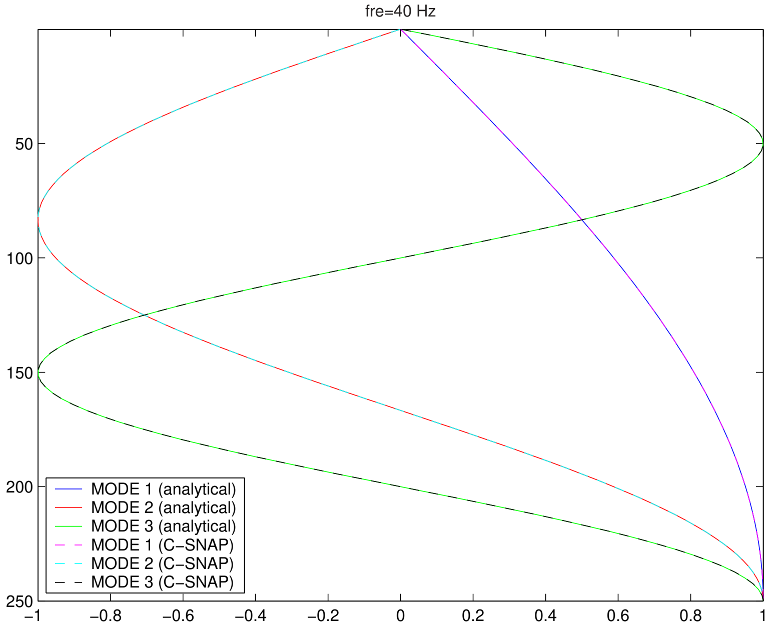

Figure 5-7: Case 2a, mode shapes in the outmost ring (ring J=65) computed by analytical expressions and by C-SNAP are the same, which means C-SNAP is accurate in computing the eigenfunctions.

5.3.2 The Number of Azimuthal Modes

From Section 4.2.3, we know that the number of azimuthal modes leading to convergence is $M = [kr_I]$, where r_I is the radius of the base of a seamount. In case 1, for example, the number of azimuthal modes leading to convergence is

$$M = [kr_I] = \left[\frac{2\pi \times 40}{1500} \times 350\right] = 59.$$

Fig. 5-11 shows transmission loss in the horizontal plane at depth 100 m with different numbers of azimuthal modes, from which we can see that $M = 59$ is enough to reach convergence.

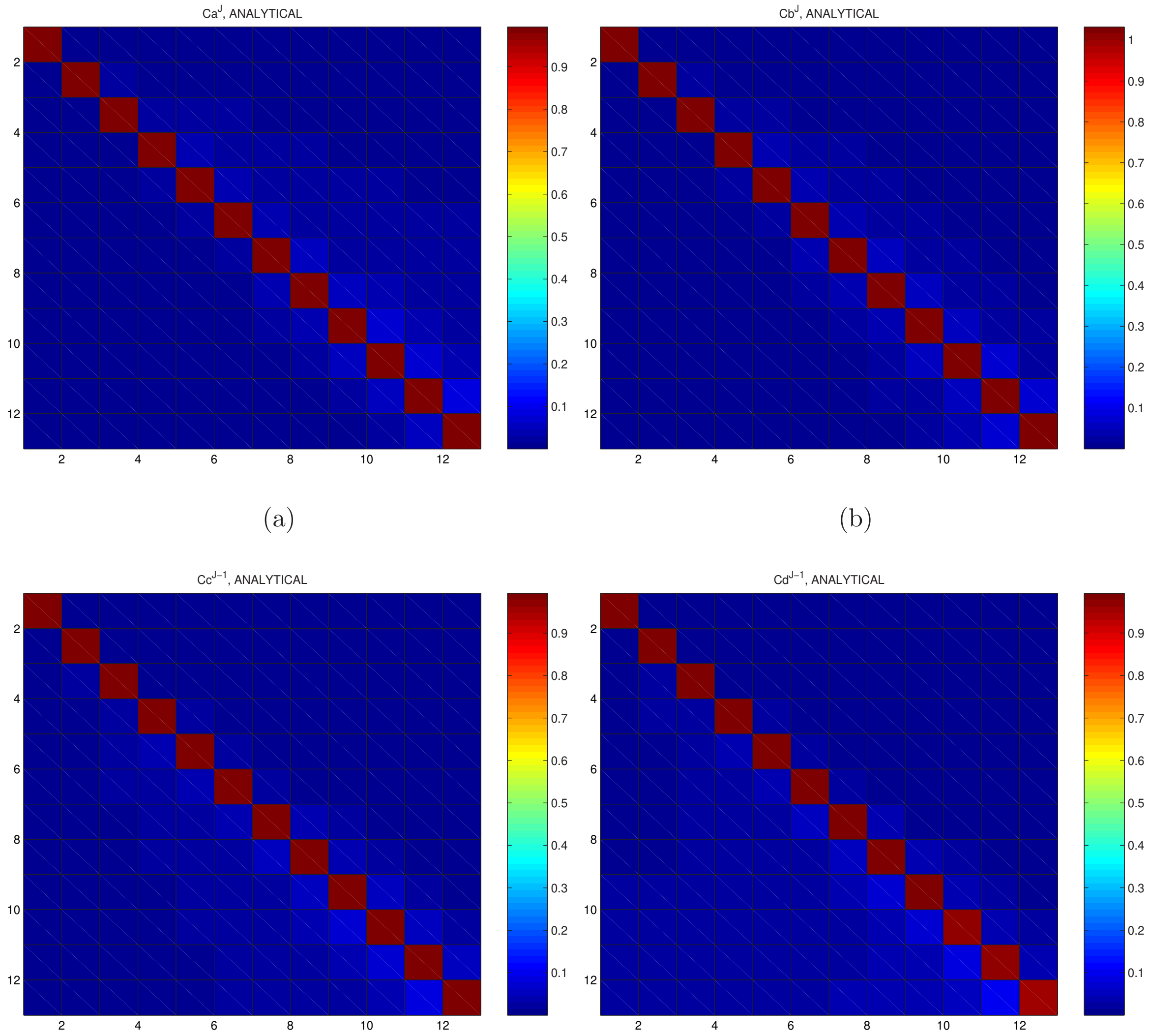

(a) (b)

(c) (d)

Figure 5-8: Case 2a, coupling matrixes at the outmost interface (J=65) computed by analytical expressions. (a) $\boldsymbol{C}_{\boldsymbol{a}}^{J}$, (b) $\boldsymbol{C}_{\boldsymbol{b}}^{J}$, (c) $\boldsymbol{C}_{\boldsymbol{c}}^{J-1}$, (d) $\boldsymbol{C}_{\boldsymbol{d}}^{J-1}$.

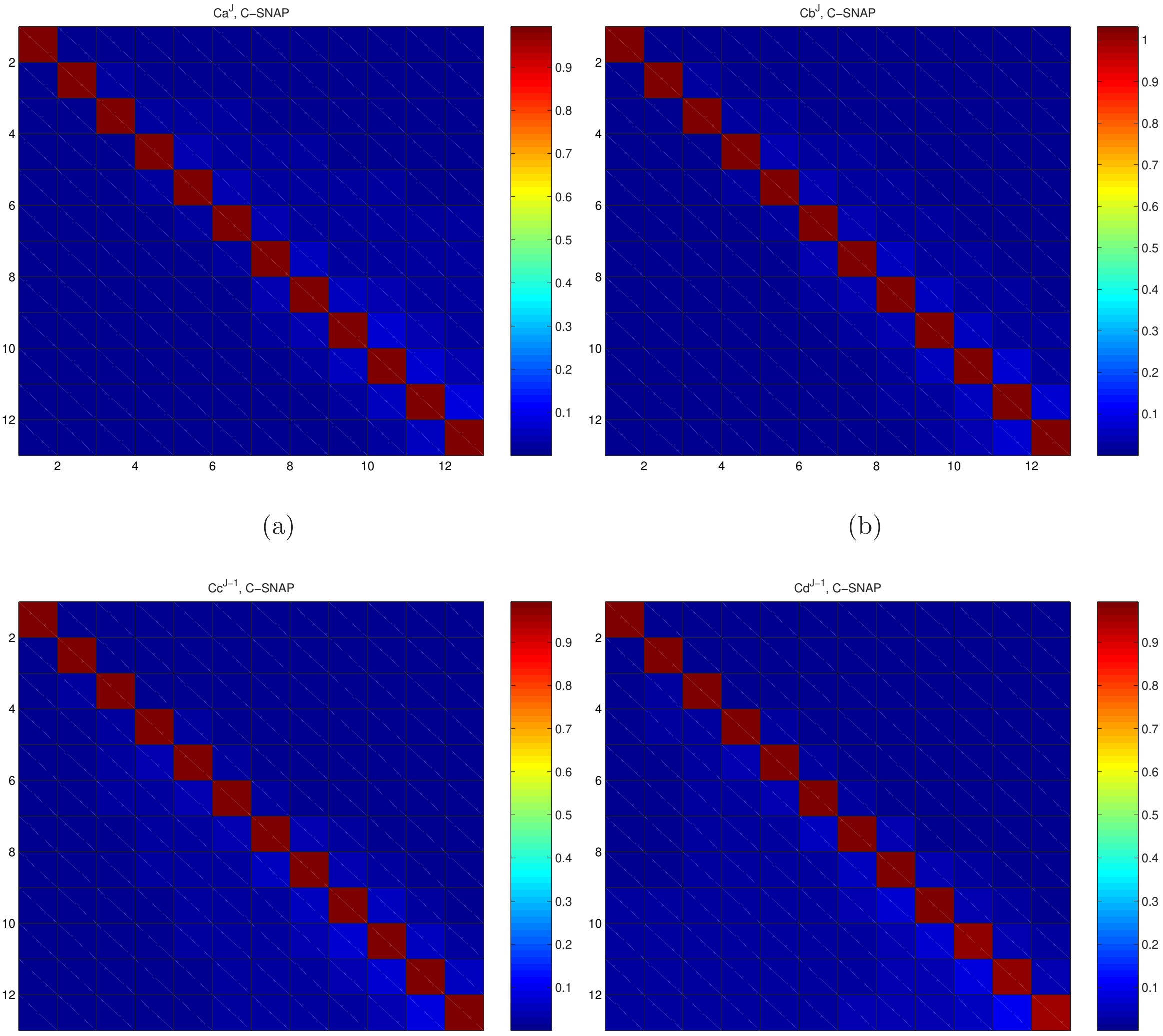

(a) (b) (c) (d)

Figure 5-9: Case 2a, coupling matrixes at the outmost interface (J=65) computed by C-SNAP. (a) $\boldsymbol{C_a^J}$, (b) $\boldsymbol{C_b^J}$, (c) $\boldsymbol{C_c^{J-1}}$, (d) $\boldsymbol{C_d^{J-1}}$.

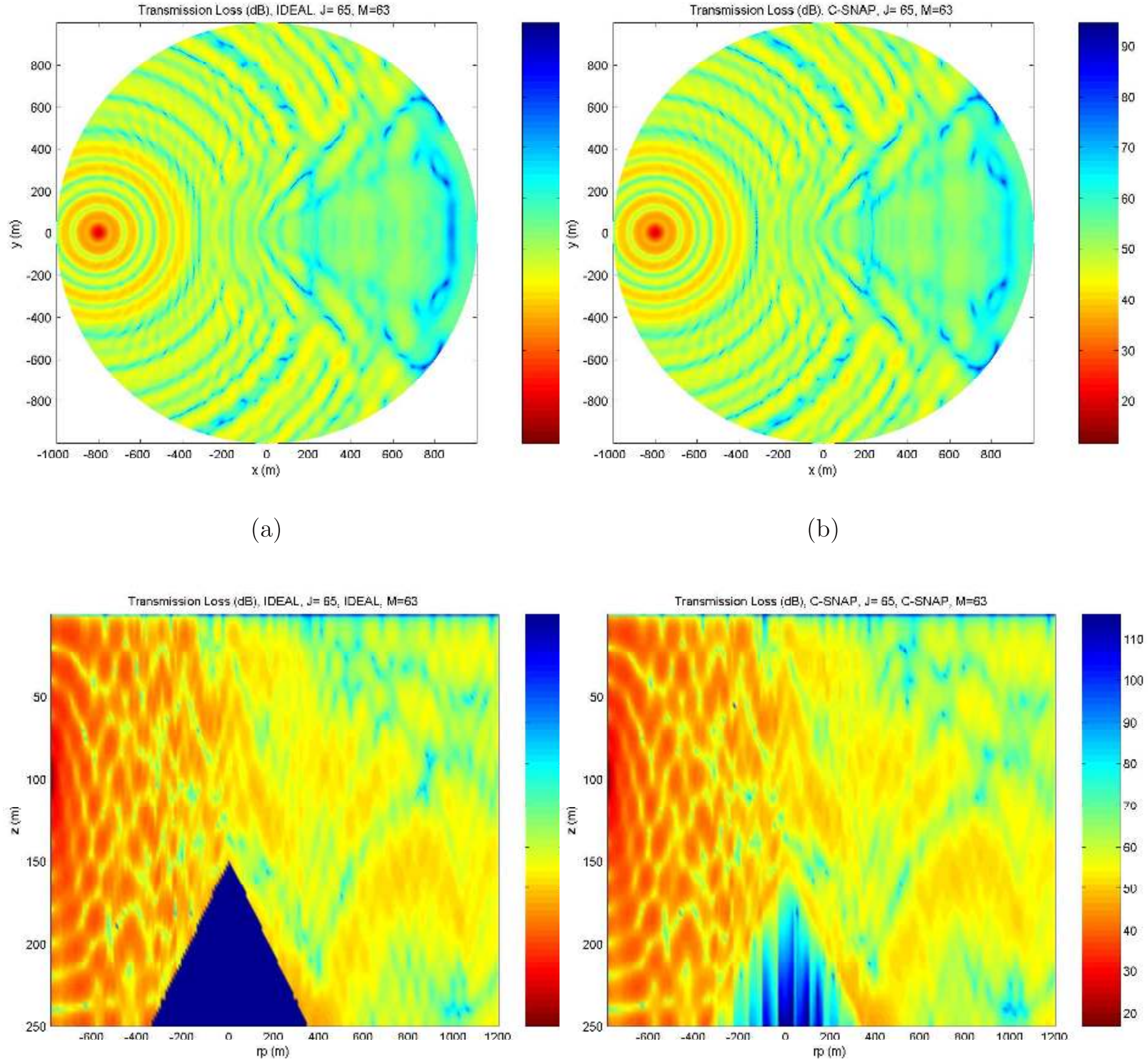

(a)

(b)

(c)

(d)

Figure 5-10: Case 2a results. (a) TL in the horizontal plane at depth 100 m, with analytical eigenfunctions and coupling matrixes, (b) TL in the horizontal plane at depth 100 m, with numerical solutions by C-SNAP; (c) TL in the vertical plane at azimuthal angle $\phi = 0$ (with respect to the source), with analytical eigenfunctions and coupling matrixes, (d) TL in the vertical plane at azimuthal angle $\phi = 0$ (with respect to the source), with numerical solutions by C-SNAP. Results computed by C-SNAP show good agreement with those by using analytical solutions for eigenfunctions and coupling matrixes.

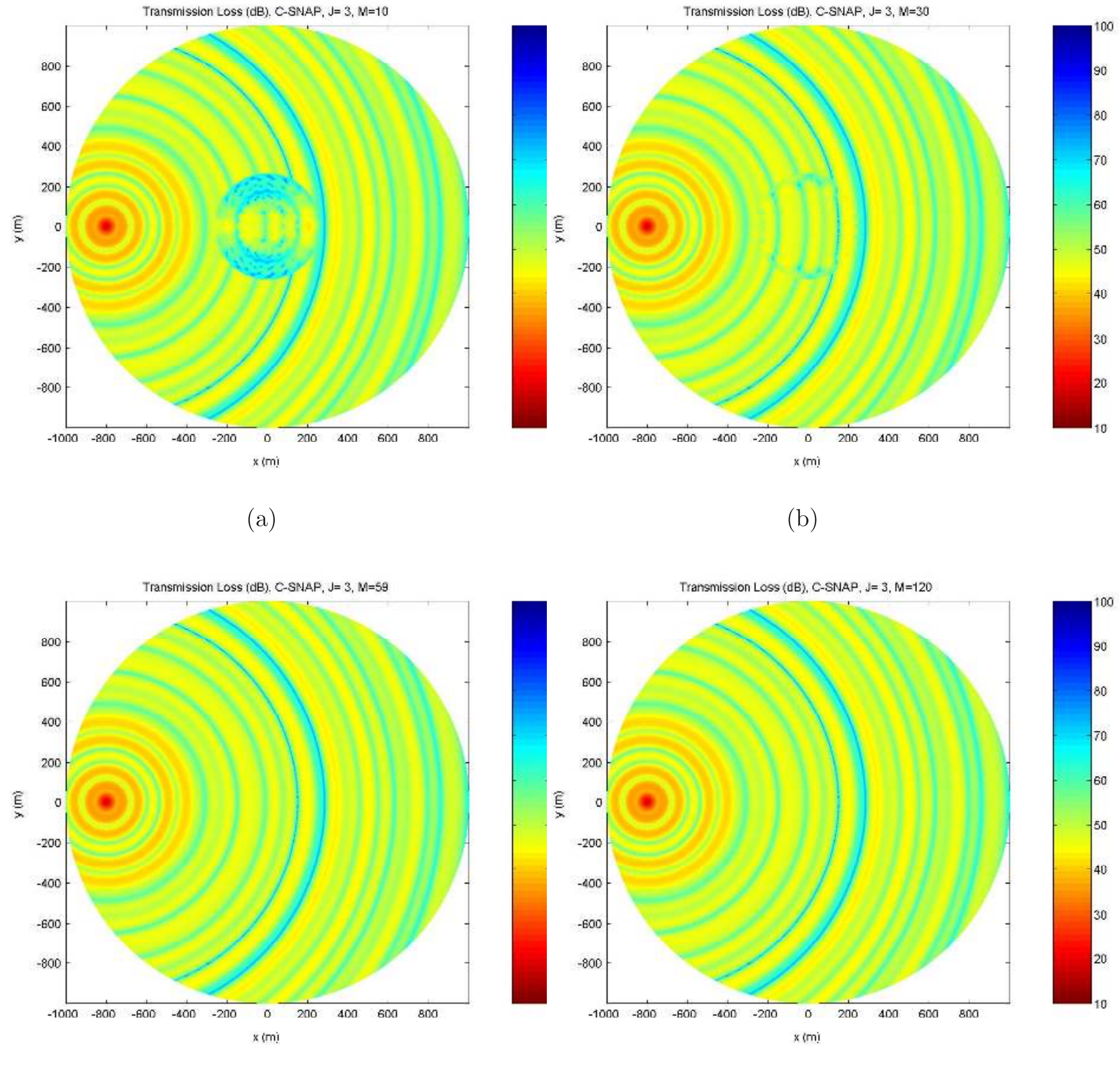

(a) (b)

(c) (d)

Figure 5-11: Case 1, convergence of azimuthal series. (a) M=10, not convergent, (b) M=30, not convergent, (c) M=59, convergent, (d) M=120, convergent. In this case, $[kr_I] = 59$, so using 59 azimuthal modes leads to convergence.

5.3.3 The Number of Rings

In the coupled mode approach, it is common to use small stair steps (or rings) to represent smoothly varying bathymetry. In this section we will discuss how many stair steps (or rings) are required to obtain a smooth-problem solution. In Jensen's paper [11], a criterion is presented which applies for backscattering and forward scattering in vertical planes. For seamount problems, we also need to consider backscattering and forward scattering in horizontal planes. This issue is important since the computational effort to compute a two-way solution increases dramatically with the number of stair steps (or rings) used to represent a smoothly varying bathymetry, for example, a conical seamount.

Stair-step Discretization Criteria for Accurate Backscattering and Forward Scattering

As shown in Fig. 5-12, with respect to the center of the conical seamount, the coefficients b^j, j=1, 2, …, J, correspond to the inward scattering, while the coefficients a^j, $j = 2, 3, \ldots, J$, correspond to the outward scattering.

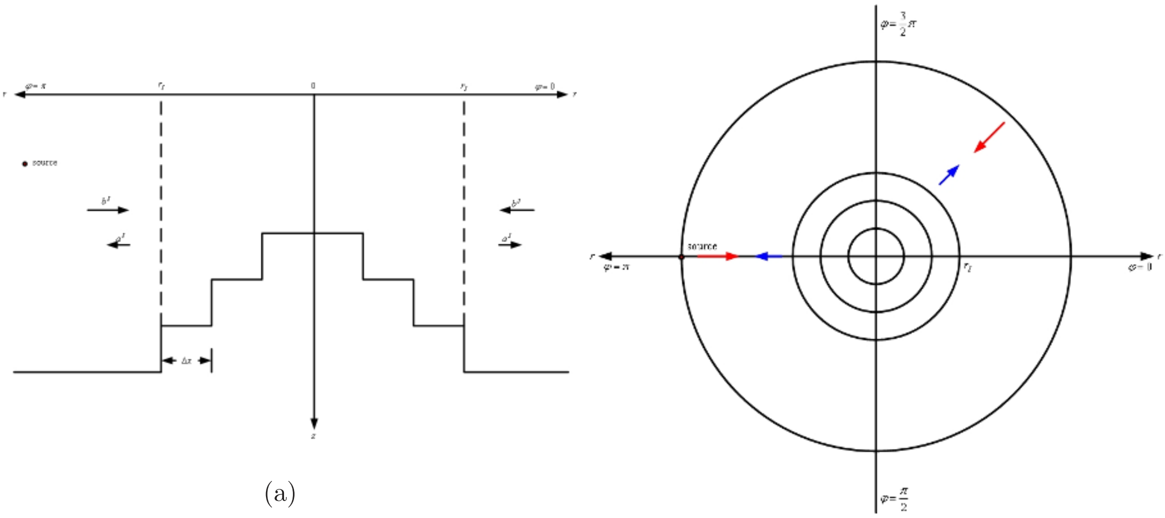

(a)

(b)

Figure 5-12: Inward scattering and outward scattering in the three-dimensional seamount model, (a) side view, (b) top view.

Paper [11] shows stair-step discretization criteria for accurately representing smoothly varying vertical bathymetry changes in numerical models. Below we give a brief review of the work in Paper [11].

1) **Backscattering**

A simple model of the scattering process can be established by assuming that each stair step acts as a point scatterer, and that the full stair case consequently acts as an array of point scatterers. The schematic is shown in Fig. 5-13.

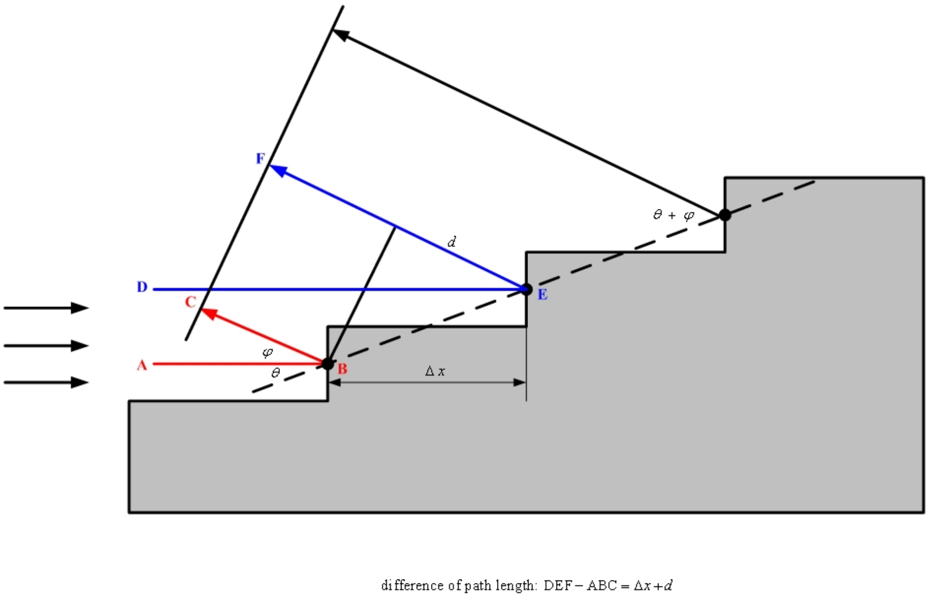

Figure 5-13: Geometry for coherent backscattering from individual stair steps.

As shown in Fig. 5-13, the difference of path lengths of paths ABC and DEF is

$$\begin{aligned} \text{path length difference} &= \Delta x + d \\ &= \Delta x + \frac{\Delta x}{\cos\theta}\cos(\theta + \phi), \end{aligned} \tag{5.2}$$

to have a coherent wavefront, it must be satisfied that

$$\Delta x + d = n\lambda, \;\; n = 0, 1, 2, \ldots, \tag{5.3}$$

or,

$$\Delta x + \frac{\Delta x}{\cos\theta}\cos(\theta+\phi) = n\lambda. \tag{5.4}$$

From Eq. (5.4) we obtain

$$\begin{aligned}\cos(\theta+\phi) &= (n\lambda - \Delta x)\frac{\cos\theta}{\Delta x} \\ &= \left(\frac{n\lambda}{\Delta x} - 1\right)\cos\theta. \end{aligned} \tag{5.5}$$

Only the fundamental lobe $n = 0$ is physically meaningful for a smooth bottom facet, which leads to the criterion for backscattering,

$$\left(\frac{\lambda}{\Delta x} - 1\right)\cos\theta > 1, \tag{5.6}$$

or,

$$\Delta x < \lambda\frac{\cos\theta}{\cos\theta + 1}. \tag{5.7}$$

For small slope angles, the criterion in Eq. (5.7) is equivalent to $\Delta x < \frac{\lambda}{2}$. In practice, a slightly stricter criterion, e.g. $\Delta x < \frac{\lambda}{4}$, should be satisfied. From Paper [11] we also know that we generally have high backscatter levels from $\Delta x > \frac{\lambda}{2}$ followed by a rapid transition to much lower levels for $\Delta x < \frac{\lambda}{4}$.

2) **Forward scattering**

As shown in Paper [11], when the backscatter is weak, the forward scatter problem can be accurately solved with an order-or-magnitude larger step sizes.

In seamount problems, we are more interested in the field outside the seamount region, i.e., $r > r_I$, thus theoretically the backscattering criterion $\Delta x < \frac{\lambda}{4}$ should be satisfied.

As an example, we compute the backscattered field in case 2b, with a different number of rings.

In case 2b, we have

$$\lambda = \frac{c}{f} = \frac{1500}{40} = 37.5 \text{ (m)},$$

and

- $n = 2$,

$$\Delta x = \frac{r_I}{2^n} = \frac{350}{4} = 87.5 \text{ (m)};$$

- $n = 3$,

$$\Delta x = \frac{r_I}{2^n} = \frac{350}{8} = 43.75 \text{ (m)} \sim \lambda;$$

- $n = 4$,

$$\Delta x = \frac{r_I}{2^n} = \frac{350}{16} = 21.85 \text{ (m)} \sim \frac{\lambda}{2};$$

- $n = 5$,

$$\Delta x = \frac{r_I}{2^n} = \frac{350}{32} = 10.94 \text{ (m)} \sim \frac{\lambda}{4};$$

- $n = 6$,

$$\Delta x = \frac{r_I}{2^n} = \frac{350}{64} = 5.47 \text{ (m)} \sim \frac{\lambda}{8}.$$

In C-SNAP, a parameter, denoted by n, is used to control the number of range subdivisions to be introduced in the interval from the starting of the current input profile until the end of the subsequent one. In our three-dimensional seamount model, the parameter n corresponds to the number of rings as $J = 2^n + 1$.

The results of the backscattered field with n = 2, 3, 4, 5 and 6 are shown in Fig. 5-16 and Fig. 5-17, from which we can see:

1) The backscattered field converges from $n = 5$, where the stair-step size is almost $\frac{\lambda}{4}$.

2) From $n = 4$ to $n = 5$, or, the stair-step size from $\frac{\lambda}{2}$ to $\frac{\lambda}{4}$ approximately, we find a rapid transition from high level to low level.

3) From Fig. 5-16 we find that the field between $\phi = \frac{3\pi}{2}$ to $\phi = \frac{\pi}{2}$ converges much faster than that in the other half plane, where ϕ is the azimuthal angle with respect to the axle of the seamount. The field from $\frac{\pi}{2}$ to $\frac{3}{2}\pi$ converges until $n = 5$; however, the field from $\frac{3}{2}\pi$ to $\frac{\pi}{2}$ converges from $n = 3$. Thus, if we are only interested in

the field from $\frac{3}{2}\pi$ to $\frac{\pi}{2}$, we may use fewer rings to obtain convergent results than what the criterion $\Delta x < \frac{\lambda}{4}$ requires.

The Azimuthal Feature of Backscattering and the Step Size

In three-dimensional conical seamount problems, there is an azimuthal feature which does not exist in two-dimensional range-dependent problems in which the field only depends on range and depth. As illustrated in Fig. 5-14, the length difference of paths ABC and ADE is

$$\begin{aligned} \text{path length difference} &= \Delta x + d \\ &= \Delta x + \Delta x \cos\phi', \end{aligned} \tag{5.8}$$

where $\phi = \pi - \phi'$, and Δx is the step size.

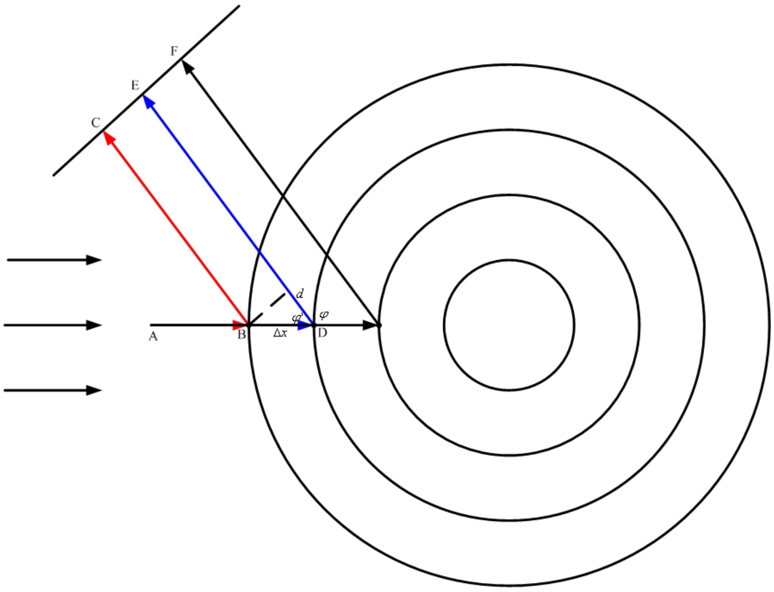

Figure 5-14: Geometry for coherent backscattering from individual rings in a horizontal plane.

To have a coherent wavefront for the backscatter at azimuthal angle ϕ, it must be satisfied that

$$\Delta x + d = k\lambda,\ \ k = 0, 1, 2, \ldots, \tag{5.9}$$

or,

$$\Delta x(1+\cos\phi_k') = k\lambda,\ \ k = 0, 1, 2, \ldots \tag{5.10}$$

From Eq. (5.10) we obtain

$$\cos\phi_k' = k\frac{\lambda}{\Delta x} - 1,\ \ k = 0, 1, 2, \ldots. \tag{5.11}$$

To have only the main lobe, it must be satisfied that

$$\frac{\lambda}{\Delta x} - 1 > 1, \tag{5.12}$$

or,

$$\Delta x < \frac{\lambda}{2}. \tag{5.13}$$

In practice, a more stricter criterion, e.g. $\Delta x < \frac{\lambda}{4}$, should be satisfied.

On the Use of Random Step Sizes to Approximate Bathymetry Changes

In Paper [11] and the above discussion, a uniform step size is used to obtain the criteria for backscatter and forward scatter. Theoretically, applying random step sizes can decrease the number of side lobes than that with a uniform step size.

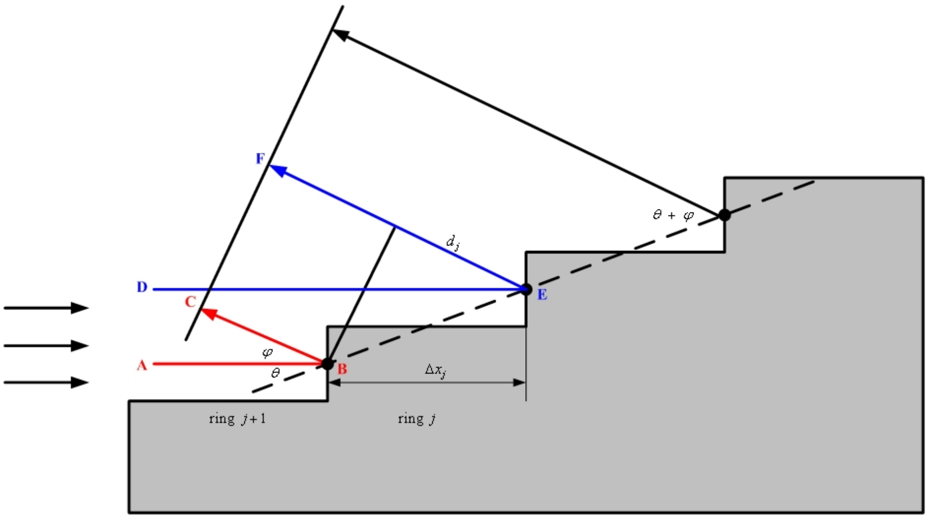

Figure 5-15: Geometry for coherent backscattering from individual stair steps with random step sizes.

As illustrated in Fig. 5-15, the stair step size of ring j is

$$\Delta x_j = (1+\alpha)\Delta x, \tag{5.14}$$

where α is a random number from -0.3 to 0.3, and Δx is the uniform step size. To have a coherent wavefront at angle ϕ for the backscatter from ring j and ring $j+1$, it must be satisfied that the difference of path length is an integer times wavelength, i.e.,

$$\Delta x_j + d_j = \Delta x_j + \frac{\Delta x_j}{\cos\theta}\cos(\theta+\phi) = \Delta x_j \left[1 + \frac{\cos(\theta+\phi)}{\cos\theta}\right] = n_j\lambda,\ j = 2, \ldots, J-1. \tag{5.15}$$

The condition in Eq. (5.15) is harder to satisfy for all the rings, than the condition in the uniform step size case, which is only one equation,

$$\Delta x + d = \Delta x \left[1 + \frac{\cos(\theta+\phi)}{\cos\theta}\right] = n\lambda, \tag{5.16}$$

thus using random step sizes leads to fewer side lobes than using a uniform step size. In addition, using random step sizes adds no additional computational effort.

The results of the backscattered field with random step sizes are shown in Fig. 5-18 and Fig. 5-19. By comparing with the results with a uniform step size shown in Fig. 5-16 and Fig. 5-17, we can see that the number of side lobes with random step sizes is less than that with a uniform step size.

The formulas for random step sizes can be found in Appendix K.

5.4 Three-Dimensional Effects vs. Two-Dimensional Effects

For a three-dimensional propagation problem, if the azimuthal variation is strong, we say three-dimensional effects are significant; if the azimuthal variation is weak, we say two-dimensional effects are significant. When three-dimensional effects are insignifi-

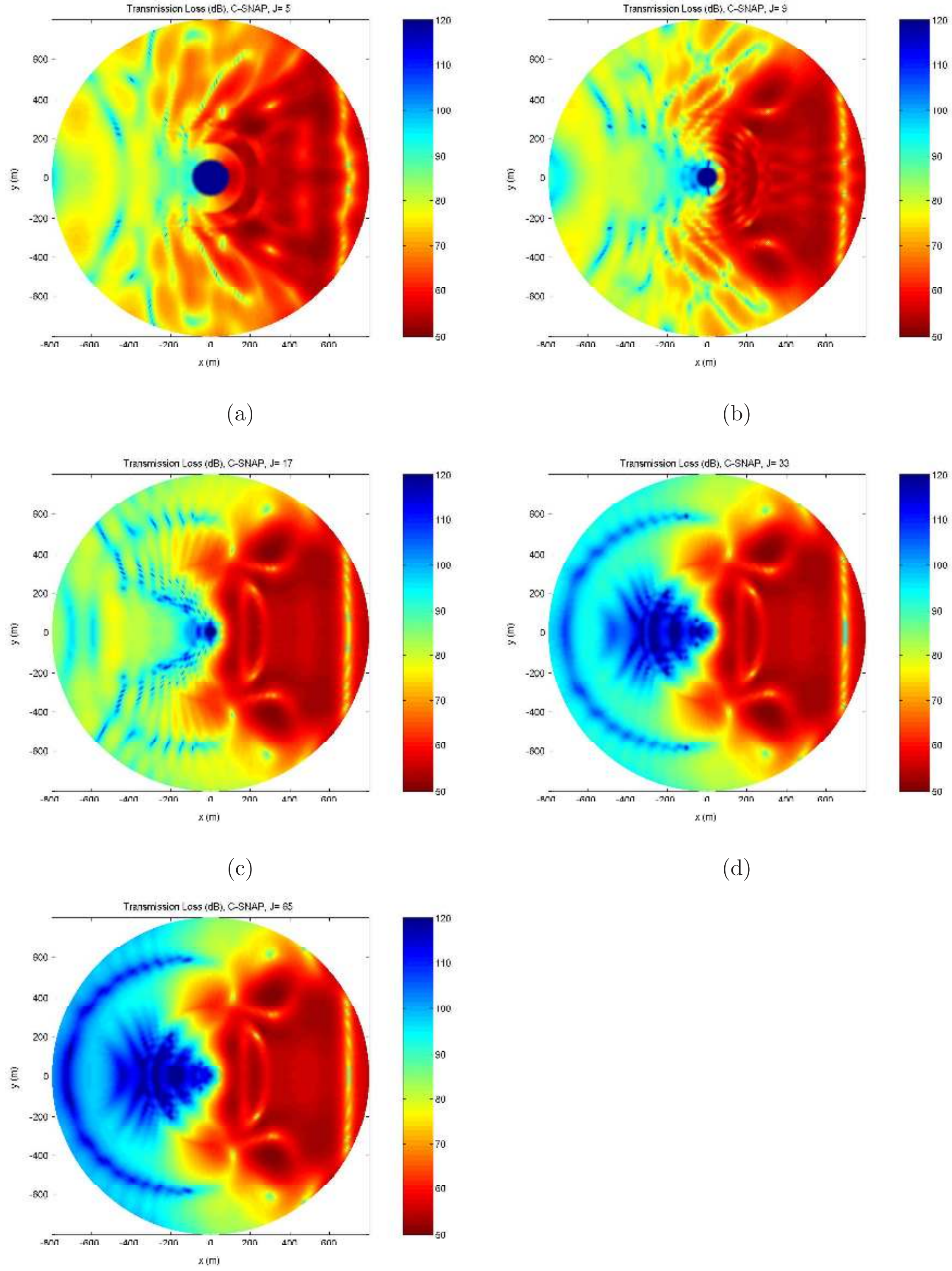

(a)

(b)

(c)

(d)

(e)

Figure 5-16: The scattered field in the horizontal plane at depth 100 m, with a uniform step size. (a) $n = 2$, (b) $n = 3$, (c) $n = 4$, (d) $n = 5$, (e) $n = 6$. The backscattered field converges from $n = 5$, i.e. 32 rings, where the step size is approximately $\lambda/4$.

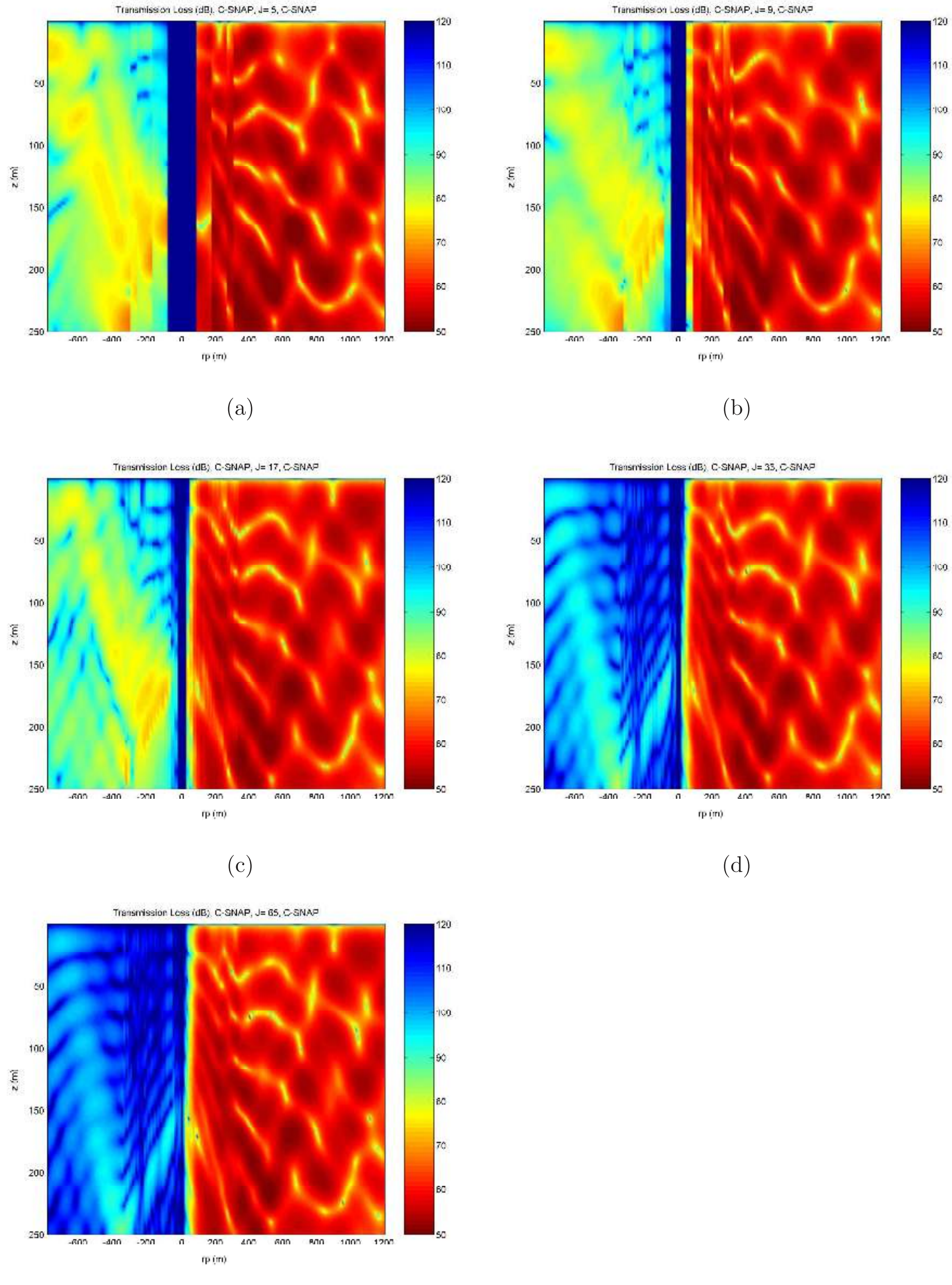

(a)

(b)

(c)

(d)

(e)

Figure 5-17: The scattered field in the vertical plane at azimuthal angle $\phi = 0$ (with respect to the source), with a uniform step size. (a) $n = 2$, (b) $n = 3$, (c) $n = 4$, (d) $n = 5$, (e) $n = 6$. The backscattered field converges from $n = 5$, i.e. 32 rings, where the step size is approximately $\lambda/4$.

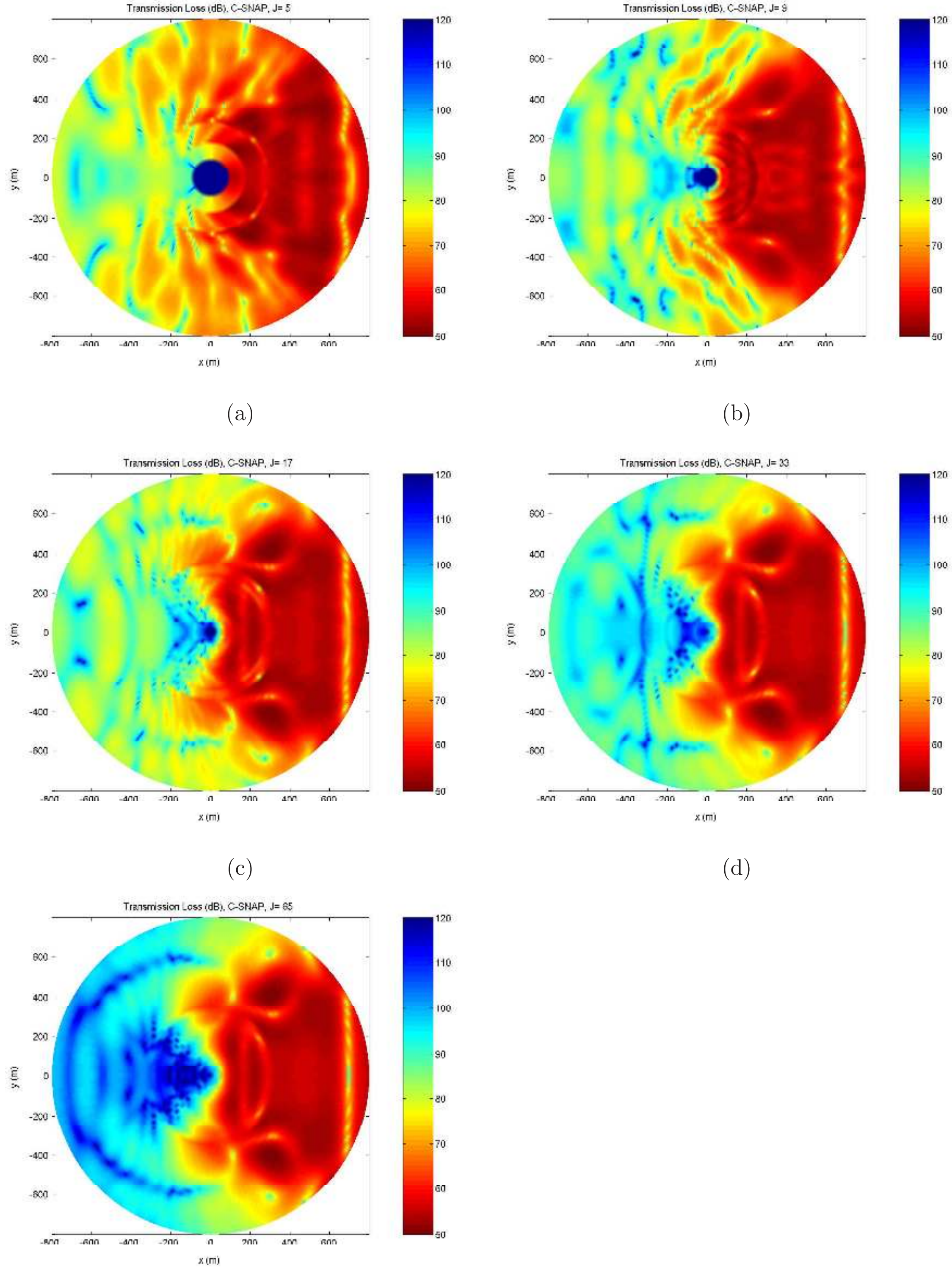

(a) (b)

(c) (d)

(e)

Figure 5-18: The scattered field in the horizontal plane at depth 100 m, with random stair-step sizes. (a) $n = 2$, (b) $n = 3$, (c) $n = 4$, (d) $n = 5$, (e) $n = 6$.

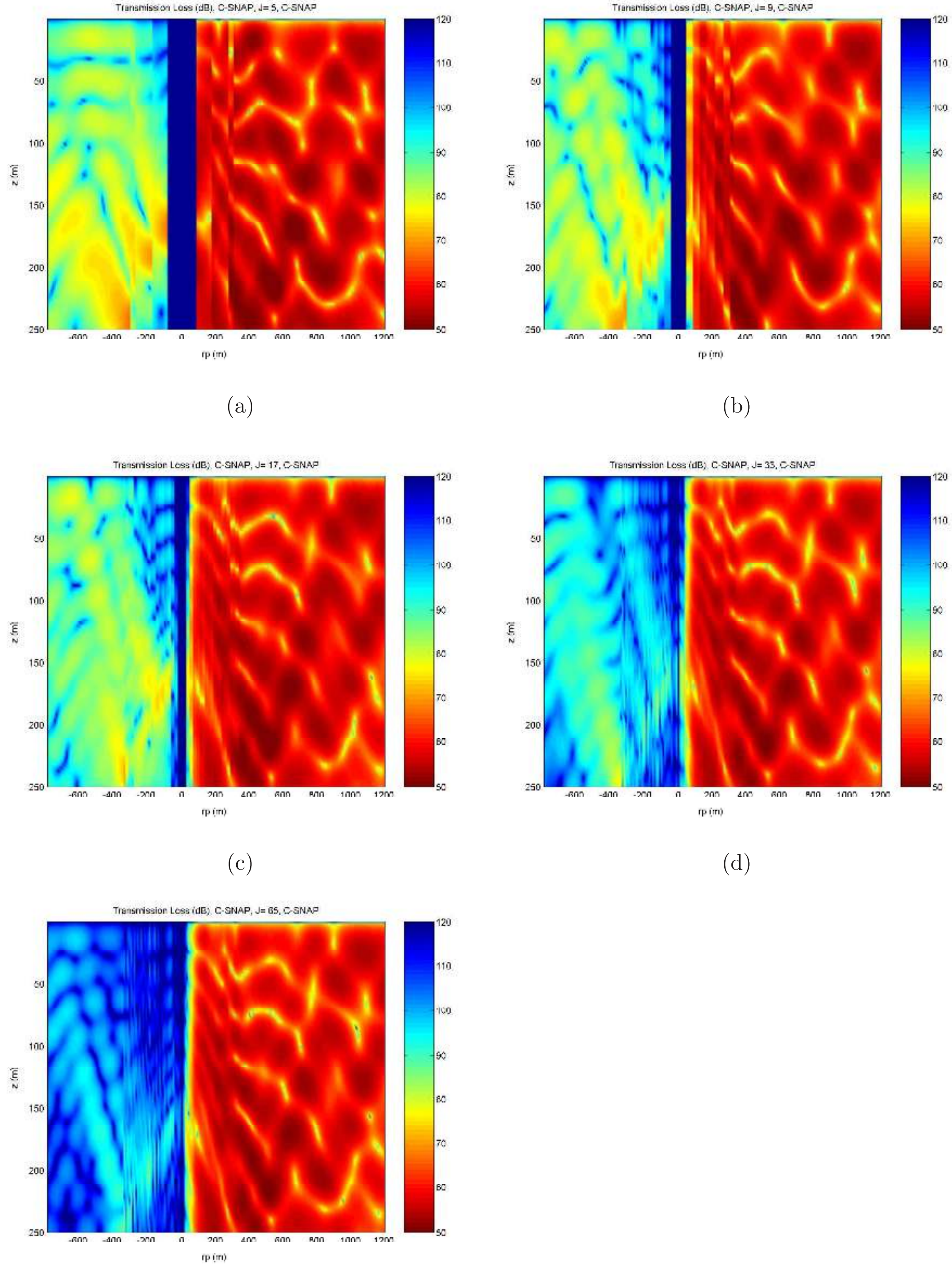

(a)

(b)

(c)

(d)

(e)

Figure 5-19: The scattered field in the vertical plane at azimuthal angle $\phi = 0$ (with respect to the source), with random stair-step sizes. (a) $n = 2$, (b) $n = 3$, (c) $n = 4$, (d) $n = 5$, (e) $n = 6$.

cant and two-dimensional effects dominate, the method discussed in Section 4.4, i.e., the $N\times 2$D approach, gives a good approximation of the three-dimensional solution. However, when three-dimensional effects become more significant, the approximation of the $N\times 2$D approach deteriorates.

Two of the factors that contribute to the significance of three-dimensional effects are the bottom type and the height of the seamount (or, the slope of the seamount). We will discuss these factors separately below.

5.4.1 Bottom Types

Two bottom types are considered, one is the rigid bottom, the other is the penetrable bottom. With all the other parameters remaining the same, the rigid bottom type leads to more significant three-dimensional effects than the penetrable bottom type. This can be seen clearly by comparing the fields in case 2a and in case 2b.

Bathymetry at Azimuthal Angle ϕ in Case 2a and Case 2b

To apply the $N\times 2$D approach, we need the bathymetry at azimuthal angle ϕ with respect to the source. From Section 4.4.1 we know that at $\phi = 0$, the shape of the seamount is a triangle; at $\phi \geq \phi_c = \arcsin(r_I/r_s)$, the shape of the seamount is flat, i.e., beyond the tangent angle $\phi_c = \arcsin(r_I/r_s)$, a range-independent problem is solved by the $N\times 2$D approach; at $\phi_c > \phi > 0$, the shape of the seamount is a branch of hyperbolas. In case 2a and case 2b, ϕ_c is

$$\phi_c = \arcsin(r_I/r_s) = \arcsin(350/800) \approx 0.453 \text{ (rad)} \approx 25.944 \text{ (deg)}. \tag{5.17}$$

Fig. 5-20 shows the bathymetry at azimuthal angle ϕ with respect to the source (range origin is set at the source) in case 2a and case 2b, and such bathymetries are used in the $N\times 2$D approach to give approximate three-dimensional results.

Comparison of 3D and $N\times 2$D Results for Case 2a

Case 2a is a shallow water problem with a rigid bottom, as shown in Fig. 5-2.

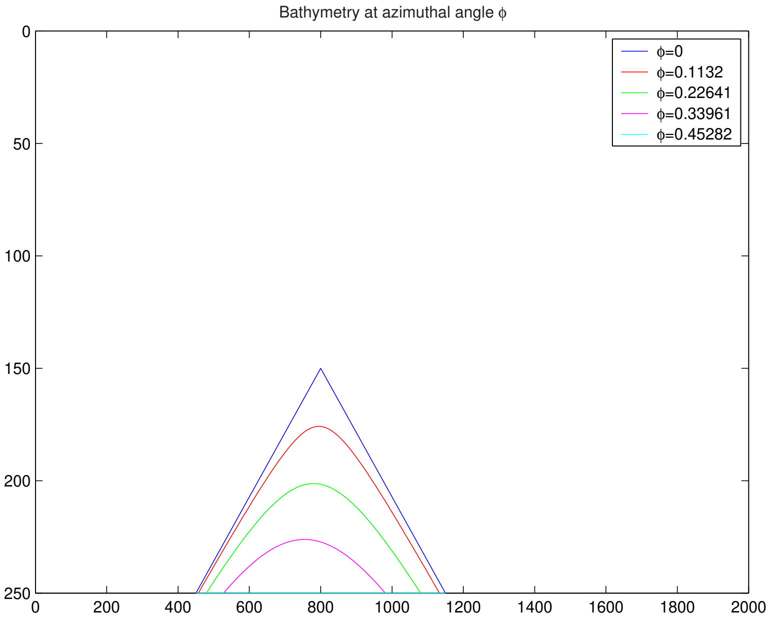

Figure 5-20: Bathymetry at azimuthal angle ϕ with respect to the source.

Fig. 5-21 through Fig. 5-25 show transmission loss vs. range at depth 100 m, azimuthal angle $\phi = 0$, $\frac{1}{4}\phi_c$, $\frac{2}{4}\phi_c$, $\frac{3}{4}\phi_c$ and ϕ_c, respectively, where the azimuthal angle ϕ is with respect to the source. From these figures we can see that at azimuthal angle $\phi = 0$ and $\phi \geq \phi_c$, the results of the $N\times$2D method are comparable to those of the three-dimensional seamount model; while for $\phi_c > \phi > 0$, the results of the $N\times$2D method are greatly different from those of the three-dimensional model.

Fig. 5-26 shows transmission loss in the horizontal plane at depth 100 m computed by the three-dimensional seamount model and by the $N\times$2D model.

Fig. 5-27 shows transmission loss in the vertical plane at azimuthal angle $\phi = 0$ with respect to the source, computed by the three-dimensional seamount model and by the $N\times$2D model.

From the above results we can see that in this case the three-dimensional effects are so significant that the $N\times$2D model is a poor approximation of the three-dimensional model.

Comparison of 3D and $N\times$2D Results for Case 2b

Case 2b is a shallow water problem with a penetrable bottom as shown in Fig. 5-3.

Fig. 5-28 through Fig. 5-32 show transmission loss vs. range at depth 100 m, azimuthal angle $\phi = 0$, $\frac{1}{4}\phi_c$, $\frac{2}{4}\phi_c$, $\frac{3}{4}\phi_c$, and ϕ_c, respectively, where the azimuthal angle ϕ is with respect to the source and $\phi_c \approx 25.944$ degrees.

Fig. 5-33 shows transmission loss in the horizontal plane at depth 100 m, computed by the three-dimensional seamount model and by the $N\times 2$D model.

Fig. 5-34 shows transmission loss in the vertical plane at azimuthal angle $\phi = 0$ with respect to the source, computed by the three-dimensional seamount model and by the $N\times 2$D model.

From the above results, especially the results shown in Fig. 5-28 to Fig. 5-32, we can see that the three-dimensional effects are weaker in this case than in case 2a; therefore, the $N\times 2$D method gives better approximations of the three-dimensional solutions than in case 2a.

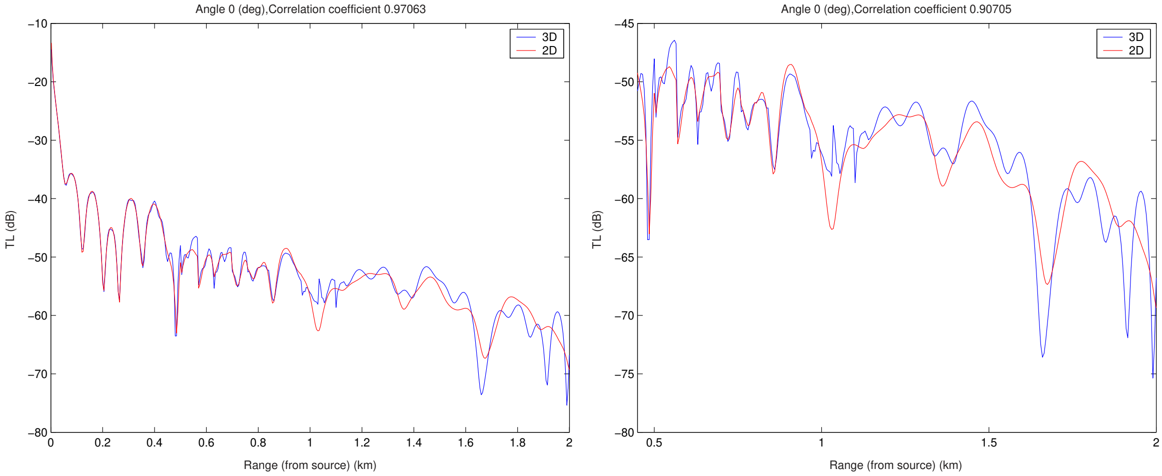

(a) (b)

Figure 5-21: Transmission loss vs. range at depth 100 m and azimuthal angle $\phi = 0$ (with respect to the source) in case 2a, (a) from the source, (b) from the beginning of the seamount. There is no visible difference between the 3D result and the $N\times 2$D result from the source to the beginning of the seamount. From the beginning of the seamount to 2 km, the correlation coefficient between the 3D result and the $N\times 2$D result is 0.91 approximately.

Conclusions

From the results of case 2a and case 2b, we can see that:

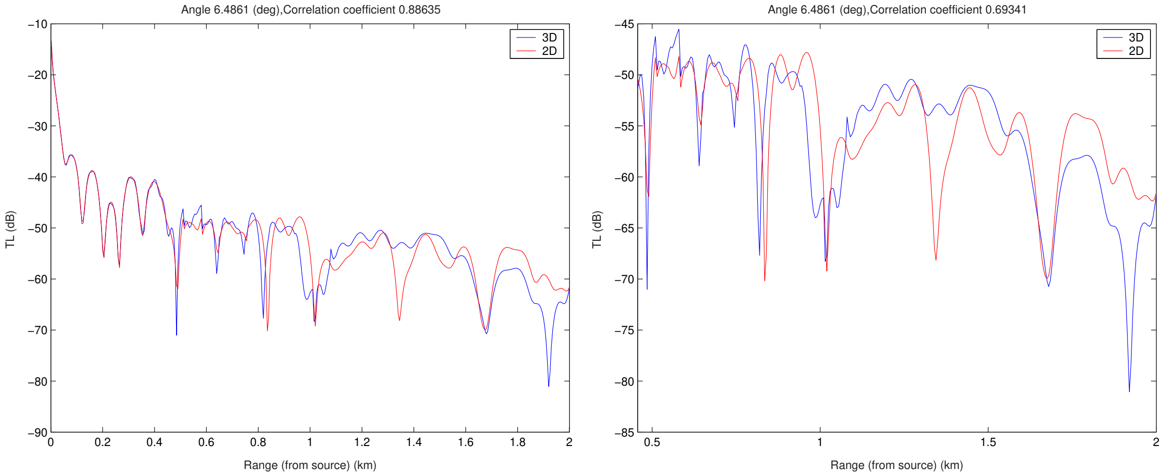

(a) (b)

Figure 5-22: Transmission loss vs. range at depth 100 m and azimuthal angle $\phi = \frac{1}{4}\phi_c$ (with respect to the source) in case 2a, (a) from the source, (b) from the beginning of the seamount. There is no visible difference between the 3D result and the $N\times$2D result from the source to the beginning of the seamount. From the beginning of the seamount to 2 km, the correlation coefficient between the 3D result and the $N\times$2D result is 0.69 approximately.

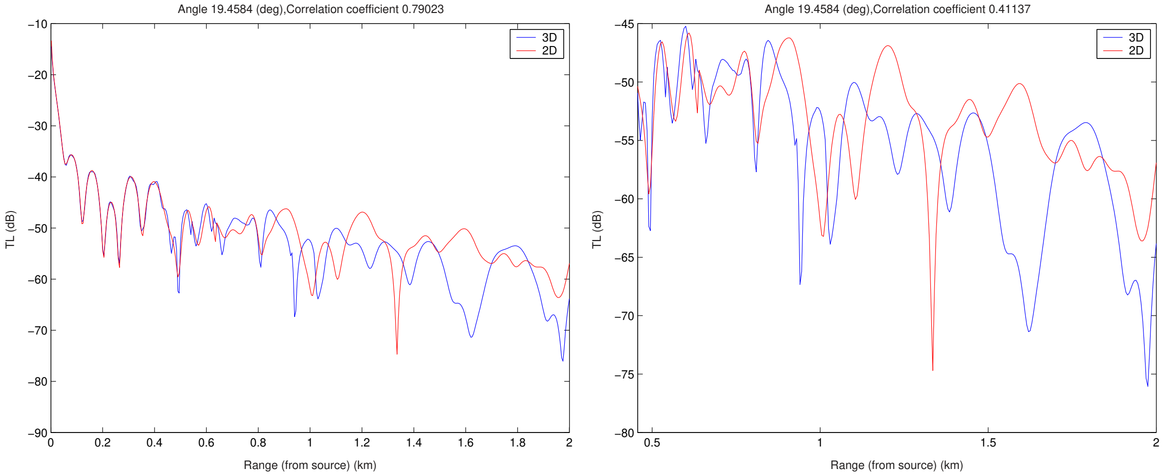

(a) (b)

Figure 5-23: Transmission loss vs. range at depth 100 m and azimuthal angle $\phi = \frac{2}{4}\phi_c$ (with respect to the source) in case 2a, (a) from the source, (b) from the beginning of the seamount. There is no visible difference between the 3D result and the $N\times$2D result from the source to the beginning of the seamount. From the beginning of the seamount to 2 km, the correlation coefficient between the 3D result and the $N\times$2D result is 0.41 approximately.

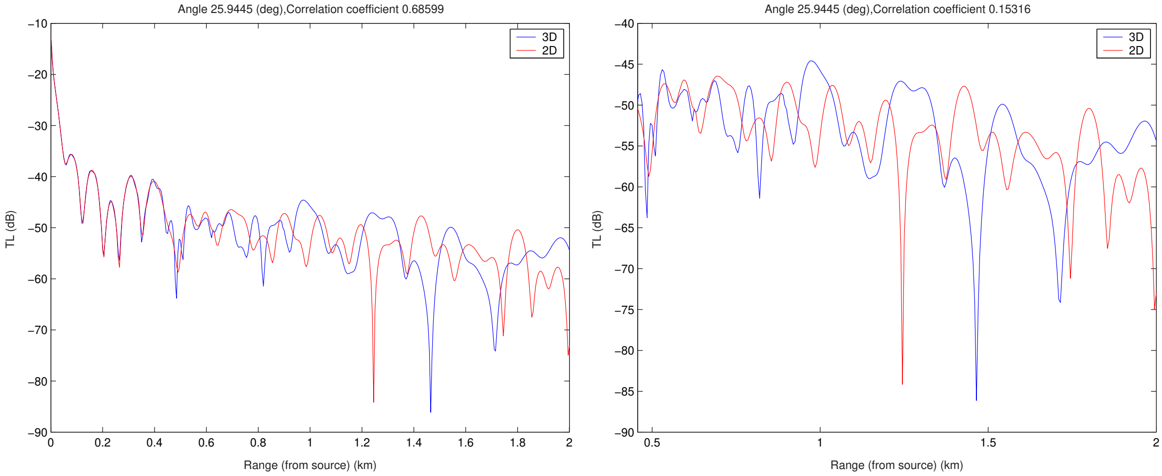

(a) (b)

Figure 5-24: Transmission loss vs. range at depth 100 m and azimuthal angle $\phi = \frac{3}{4}\phi_c$ (with respect to the source) in case 2a, (a) from the source, (b) from the beginning of the seamount. There is no visible difference between the 3D result and the $N\times2$D result from the source to the beginning of the seamount. From the beginning of the seamount to 2 km, the correlation coefficient between the 3D result and the $N\times2$D result is 0.15 approximately.

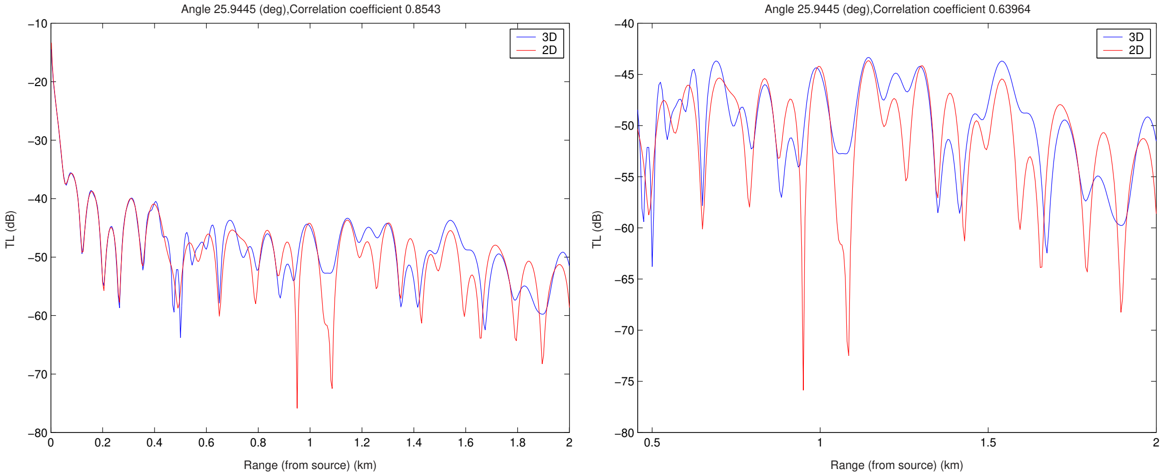

(a) (b)

Figure 5-25: Transmission loss vs. range at depth 100 m and azimuthal angle $\phi = \phi_c$ (with respect to the source) in case 2a, (a) from the source, (b) from the beginning of the seamount. There is no visible difference between the 3D result and the $N\times2$D result from the source to the beginning of the seamount. From the beginning of the seamount to 2 km, the correlation coefficient between the 3D result and the $N\times2$D result is 0.64 approximately.

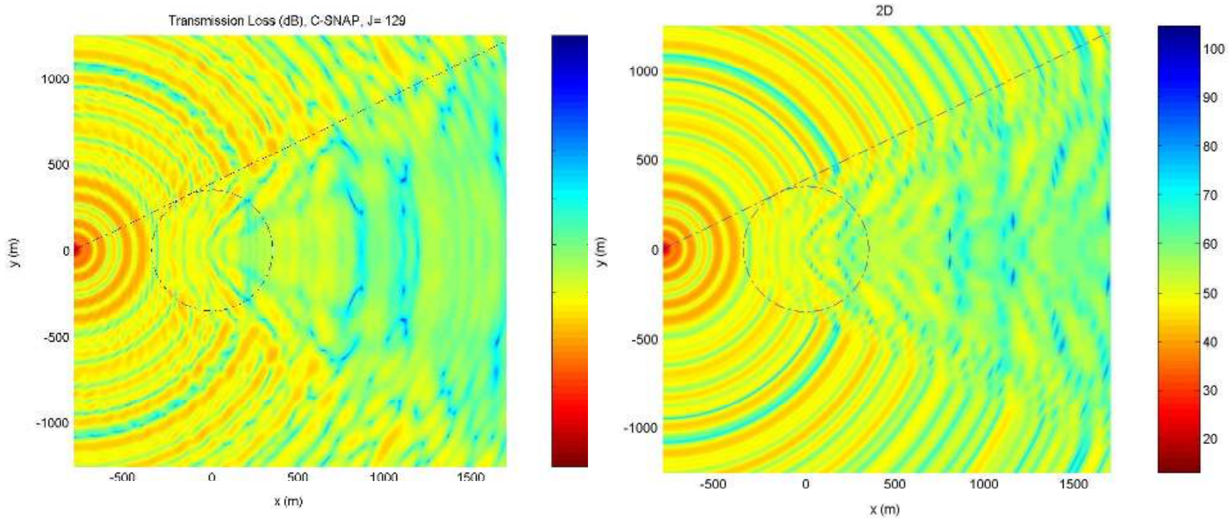

(a) (b)

Figure 5-26: Transmission loss in the horizontal plane at depth 100 m in case 2a, (a) by our 3D model, (b) by the $N \times 2$D model. There is great difference between the 3D result and the $N \times 2$D result in the perturbation zone.

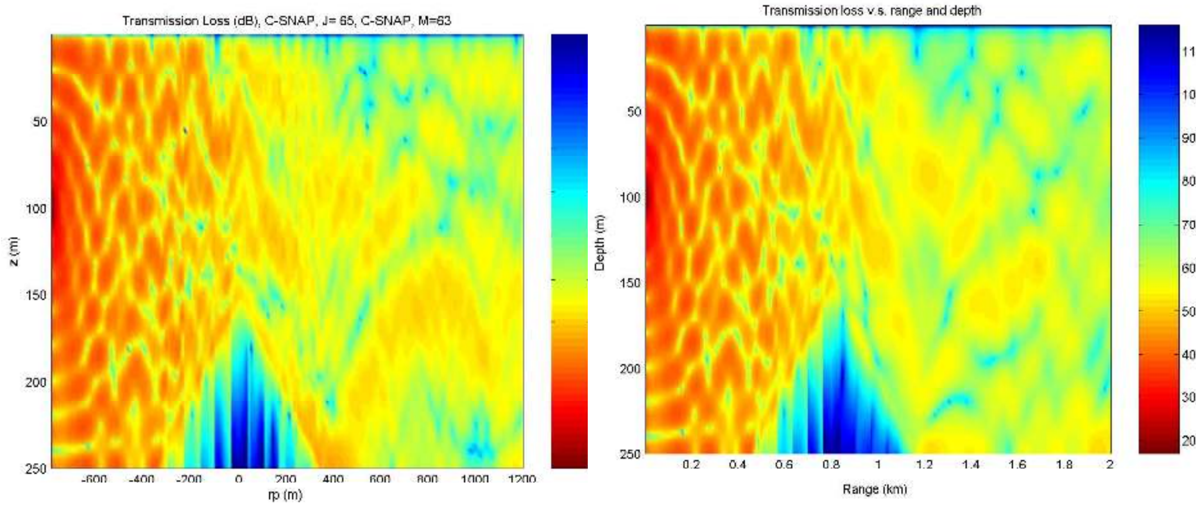

(a) (b)

Figure 5-27: Transmission loss in the vertical plane at azimuthal angle $\phi = 0$ (with respect to the source) in case 2a, (a) by our 3D model, (b) by the $N \times 2$D model. There is no visible difference between the 3D result and the $N \times 2$D result from the source to the beginning of the seamount; however, great difference appears from the beginning of the seamount.

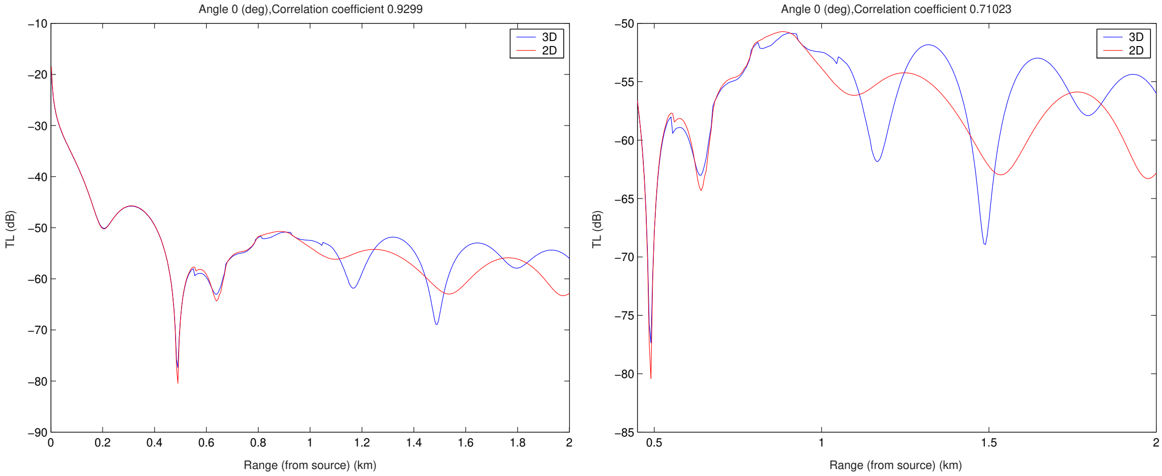

(a) (b)

Figure 5-28: Transmission loss vs. range at depth 100 m, azimuthal angle $\phi = 0$ (with respect to the source) in case 2b, (a) from the source, (b) from the beginning of the seamount. There is no visible difference between the 3D result and the $N\times$2D result from the source to the beginning of the seamount. From the beginning of the seamount to 2 km, the correlation coefficient between the 3D result and the $N\times$2D result is 0.71 approximately.

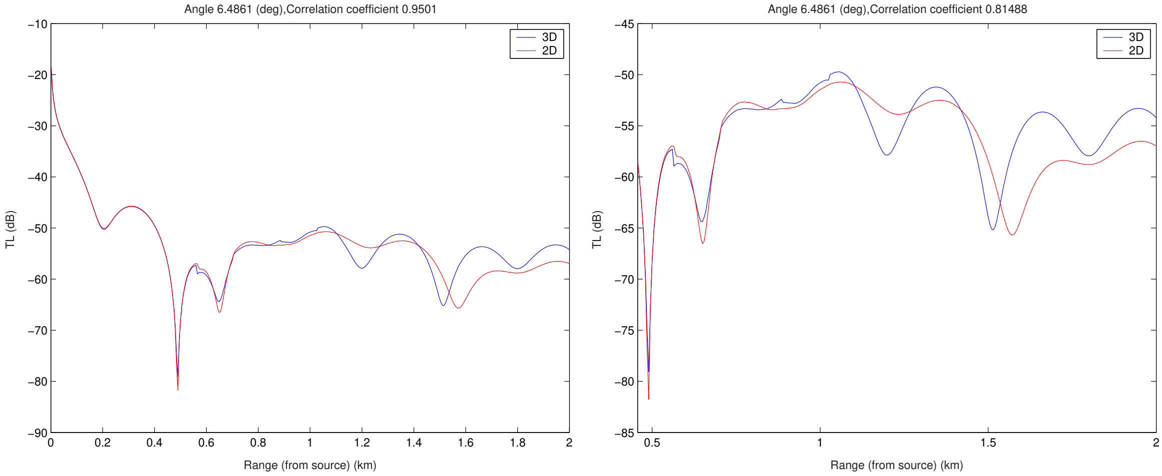

(a) (b)

Figure 5-29: Transmission loss vs. range at depth 100 m, azimuthal angle $\phi = \frac{1}{4}\phi_c$ (with respect to the source) in case 2b, (a) from the source, (b) from the beginning of the seamount. There is no visible difference between the 3D result and the $N\times$2D result from the source to the beginning of the seamount. From the beginning of the seamount to 2 km, the correlation coefficient between the 3D result and the $N\times$2D result is 0.81 approximately.

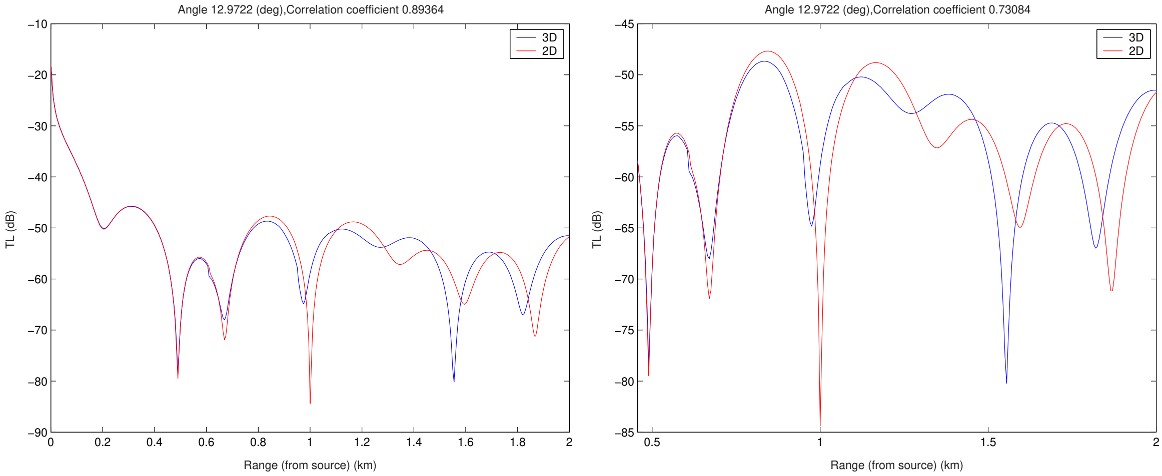

(a) (b)

Figure 5-30: Transmission loss vs. range at depth 100 m, azimuthal angle $\phi = \frac{2}{4}\phi_c$ (with respect to the source) in case 2b, (a) from the source, (b) from the beginning of the seamount. There is no visible difference between the 3D result and the $N\times$2D result from the source to the beginning of the seamount. From the beginning of the seamount to 2 km, the correlation coefficient between the 3D result and the $N\times$2D result is 0.73 approximately.

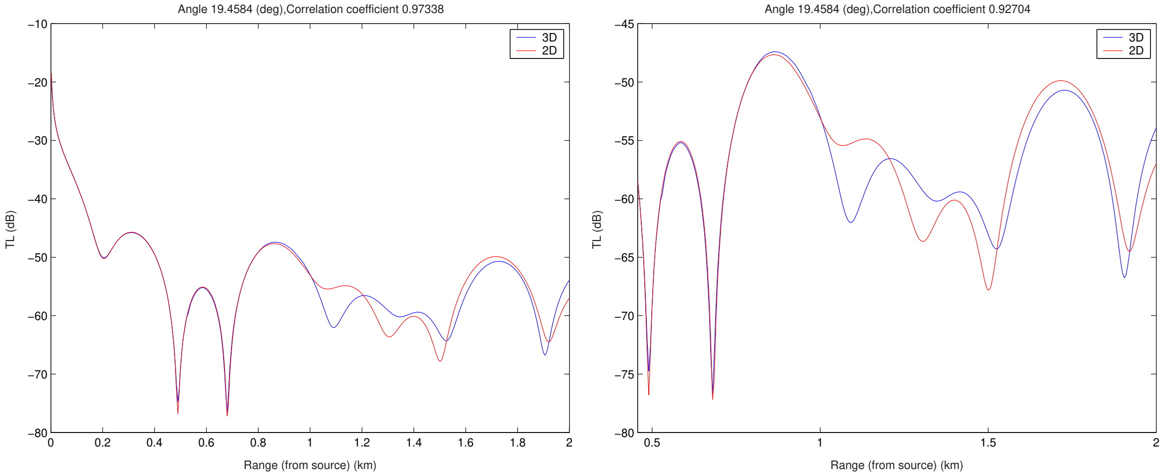

(a) (b)

Figure 5-31: Transmission loss vs. range at depth 100 m, azimuthal angle $\phi = \frac{3}{4}\phi_c$ (with respect to the source) in case 2b, (a) from the source, (b) from the beginning of the seamount. There is no visible difference between the 3D result and the $N\times$2D result from the source to the beginning of the seamount. From the beginning of the seamount to 2 km, the correlation coefficient between the 3D result and the $N\times$2D result is 0.93 approximately.

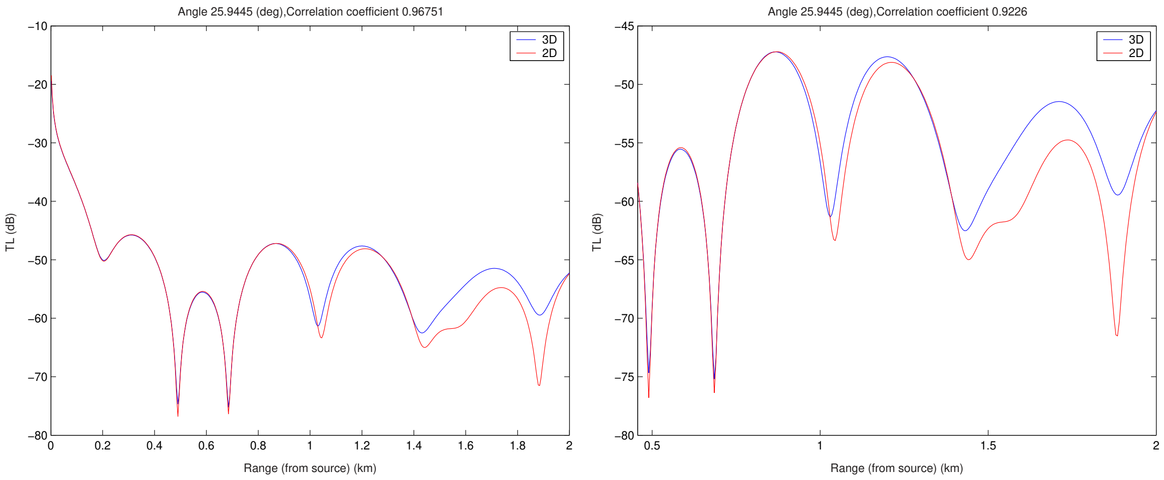

(a) (b)

Figure 5-32: Transmission loss vs. range at depth 100 m, azimuthal angle $\phi = \phi_c$ (with respect to the source) in case 2b, (a) from the source, (b) from the beginning of the seamount. There is no visible difference between the 3D result and the $N\times$2D result from the source to the beginning of the seamount. From the beginning of the seamount to 2 km, the correlation coefficient between the 3D result and the $N\times$2D result is 0.92 approximately.

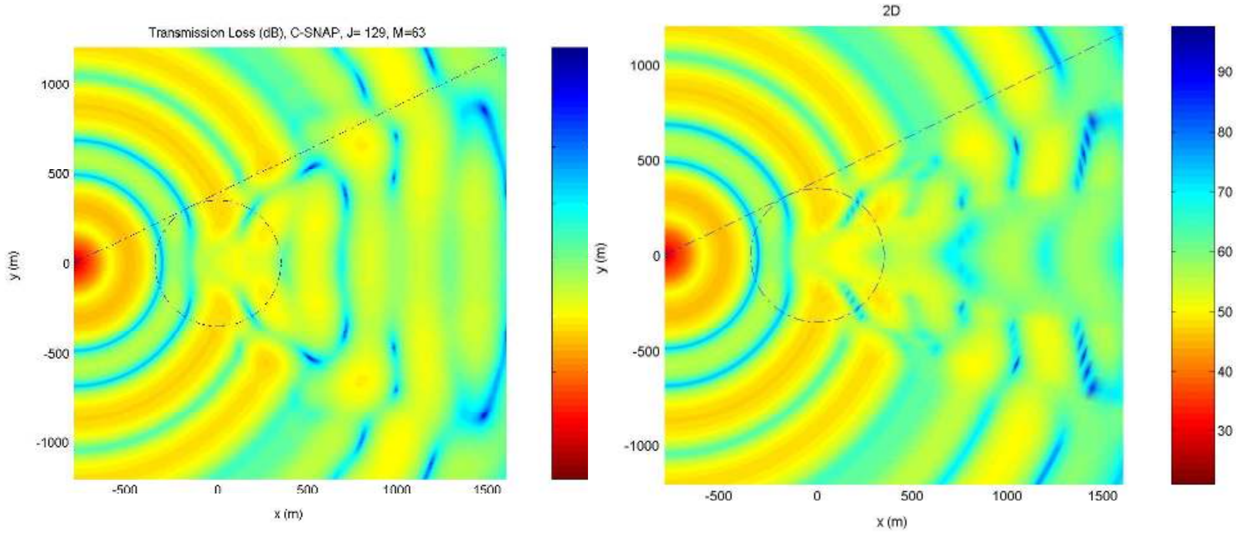

(a) (b)

Figure 5-33: Transmission loss in the horizontal plane at depth 100 m in case 2b, (a) by our 3D model, (b) by the $N\times$2D model. There is great difference between the 3D result and the $N\times$2D result in the perturbation zone.

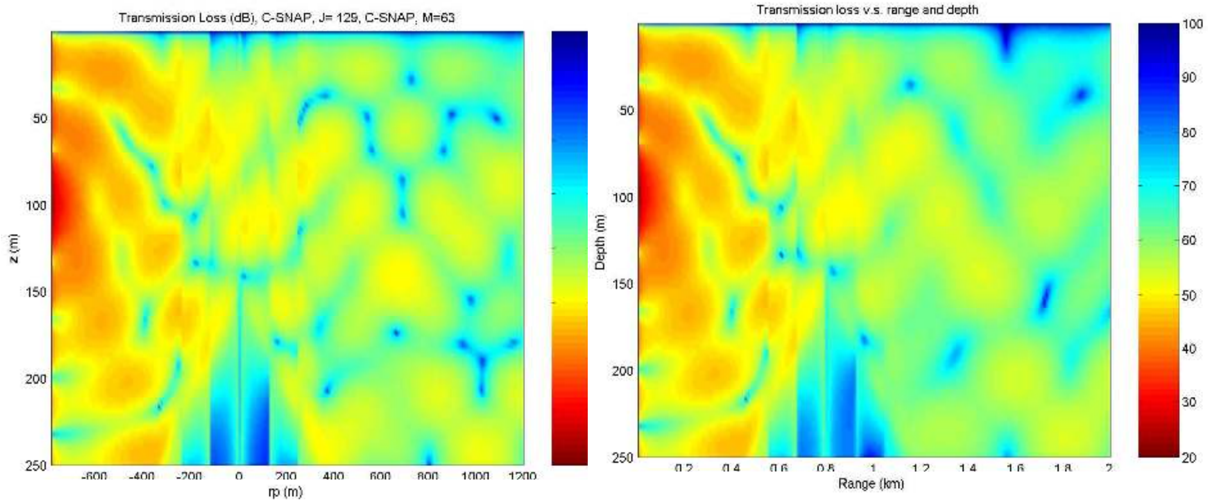

(a) (b)

Figure 5-34: Transmission loss in the vertical plane at azimuthal angle $\phi = 0$ (with respect to the source) in case 2b, (a) by our 3D model, (b) by the $N\times$2D model. There is no visible difference between the 3D result and the $N\times$2D result from the source to the beginning of the seamount; however, difference appears from the beginning of the seamount.

1) The three-dimensional effects in a waveguide with a rigid bottom are more significant than in a waveguide with a penetrable bottom.

2) As shown in Fig. 5-26, when three-dimensional effects are significant, the perturbation zone by the three-dimensional seamount model spans a larger azimuthal range than that by the $N\times$2D model. However, when three-dimensional effects are not significant, as shown in Fig. 5-33, the perturbation zone by the three-dimensional seamount model and that by the $N\times$2D model span almost the same range. The reason is as below:

   (a) When three-dimensional effects are not significant, in-plane scattering dominates and out-of-plane scattering is negligible; however, when three-dimensional effects are significant, out-of-plane scattering is not negligible.

   (b) In the $N\times$2D model, only in-plane scattering is involved; however, in the three-dimensional model, both in-plane and out-of-plane scattering are involved.

5.4.2 Height of Seamounts

The relation between the height of seamounts and the significance of the three-dimensional effects is illustrated by case 2b, i.e., shallow water propagation around a seamount, and case 3, i.e., deep water propagation around a seamount.

Case 2b

In case 2b, as shown in Fig. 5-3, we change the height of the seamount from 25 m to 50 m, then to 100 m, and compare the transmission loss in the horizontal plane at depth 100 m. The results are shown in Fig. 5-35, for the height of the seamount as 25 m, 50 m and 100 m.

From Figs. 5-35(a) and 5-35(b) we can see that when the height of the seamount is 25 m, which is relatively small, the three-dimensional effects are insignificant and the $N\times 2$D model is a good approximation of the three-dimensional seamount model. As the height of the seamount rises to 50 m, the 3D and $N\times 2$D results are shown in Figs. 5-35(c) and 5-35(d), from which we see that the three-dimensional effects become a little more significant and the approximation of the $N\times 2$D model deteriorates. As the height of the seamount rises to 100 m, the 3D and $N\times 2$D results are shown in Figs. 5-35(e) and 5-35(f), from which we see that the approximation of the $N\times 2$D model to the three-dimensional seamount model is even worse, and the span of the perturbation zone in the 3D result is larger than that in the $N\times 2$D result. This is because as the height of the seamount is 100 m, the three-dimensional effects are significant so that the out-of-plane scattering can not be neglected.

Case 3

As illustrated in Fig. 5-4, case 3 is a problem of deep water propagation around a conical seamount. To show the three-dimensional effects in this case, we first set the height of the seamount to 1000 m, and compare the results of the three-dimensional seamount model with those of the $N\times 2$D model; next, we set the height of the seamount to 3800 m, and do the comparison again. In both of these two sets, the

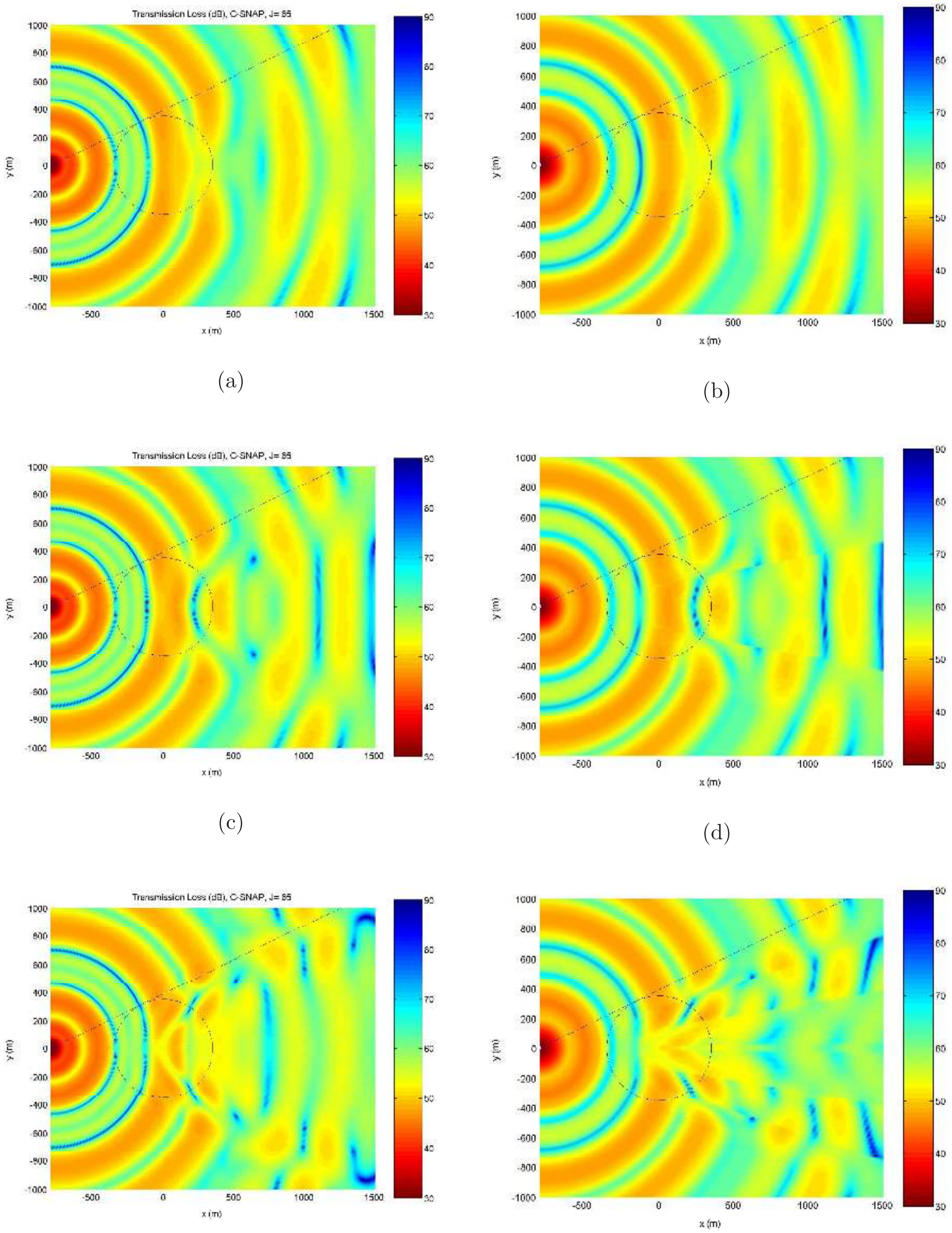

(a)

(b)

(c)

(d)

(e)

(f)

Figure 5-35: TL in the horizontal plane at depth 100 m. (a) H is 25 m, the 3D result, (b) H is 25 m, the $N\times$2D result; (c) H is 50 m, the 3D result, (d) H is 50 m, the $N\times$2D result; (e) H is 100 m, the 3D result, (f) H is 100 m, the $N\times$2D result. (H is the height of a seamount.)

radius of the seamount is set to be 20 km. Thus, the seamount of height 3800 m is steeper than the seamount of height 1000 m.

1) results of a seamount of height 1000 m

   Fig. 5-36 shows transmission loss in horizontal planes with a seamount of height 1000 m. From Fig. 5-36 we can see that for seamounts of small slope angles, the three-dimensional effects are insignificant and the $N\times 2$D model is a good approximation of the three-dimensional seamount model.

2) results of a seamount of height 3800 m

   Fig. 5-37 shows transmission loss in horizontal planes with a seamount of height 3800 m. From Fig. 5-37 we can see that for seamounts of large slope angles, the three-dimensional effects are significant, and the $N\times 2$D model is a poor approximation of the three-dimensional seamount model.

Conclusion

From the above discussion, we can see that as the height of seamounts becomes larger, or the slope angle of a seamount becomes larger, the three-dimensional effects become more significant, and as a result, the $N\times 2$D model becomes a poorer approximation of the three-dimensional model.

5.5 The Effect of the Shear Wave in Seamounts on Sound Propagation

In the numerical examples in previous sections in this chapter, we assume that the seamount is composed of fluid material, i.e. no shear wave is considered in the seamount. However, in reality, the seamount is composed of material erupted by means of volcano activity. Thus it is appropriate to include the shear wave in the seamount.

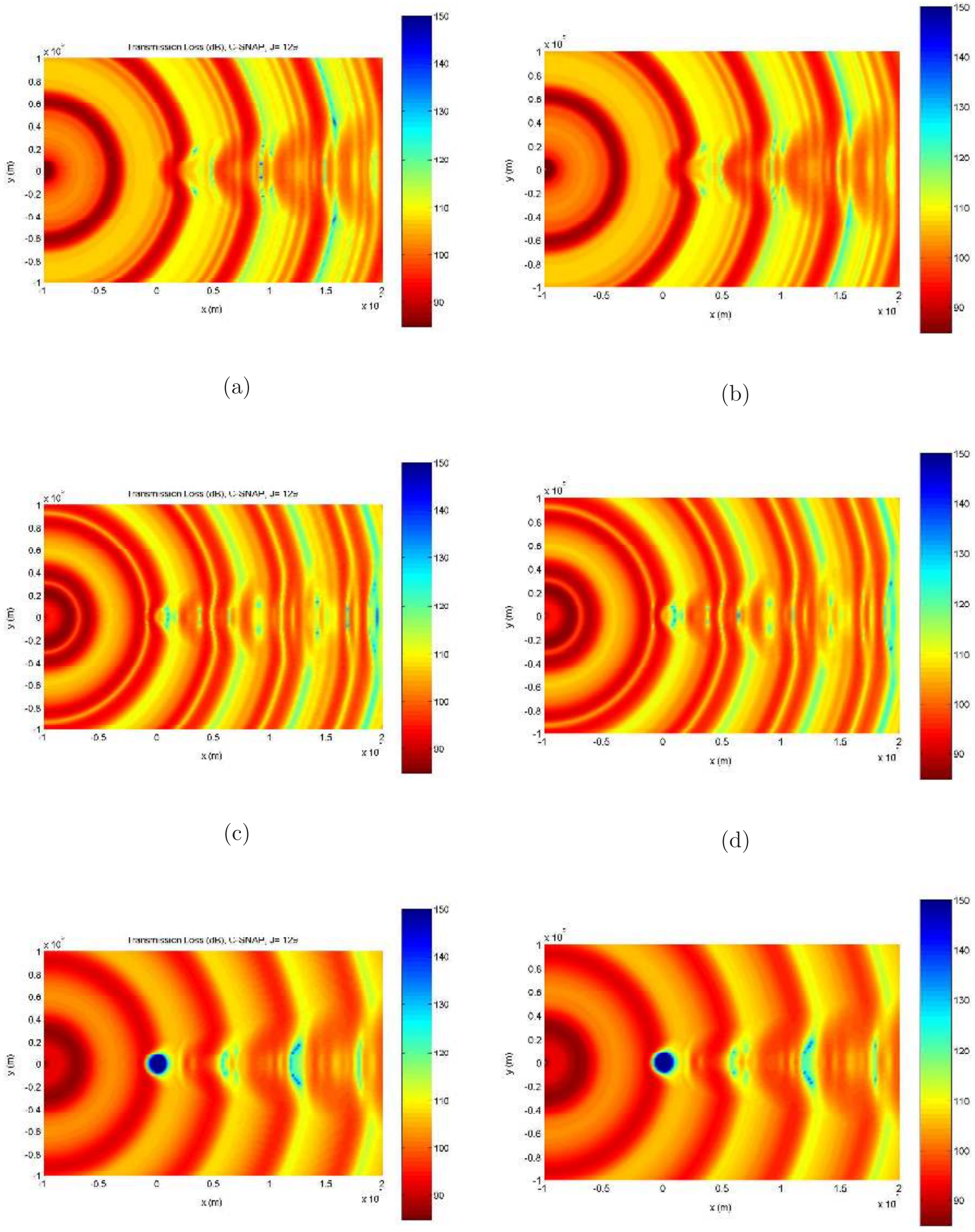

(a)

(b)

(c)

(d)

(e)

(f)

Figure 5-36: TL in horizontal planes with a seamount of height 1000 m, (a) at depth 300 m, the 3D result, (b) at depth 300 m, the $N\times2$D result; (c) at depth 3800 m, the 3D result, (d) at depth 3800 m, the $N\times2$D result; (e) at depth 4500 m, the 3D result, (f) at depth 4500 m, the $N\times2$D result. When the seamount is relatively low, the $N\times2$D model is a good approximation of the 3D model.

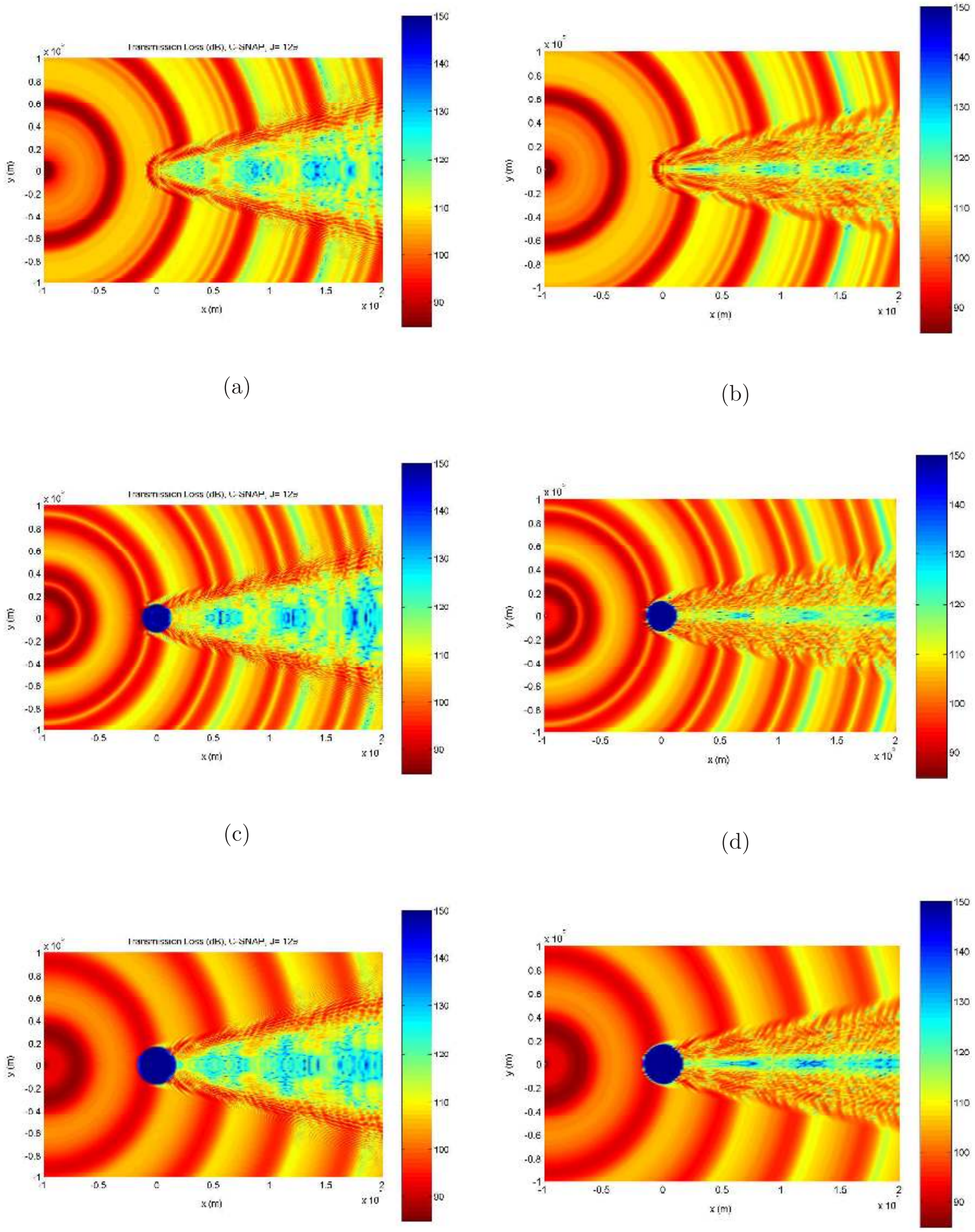

(a)

(b)

(c)

(d)

(e)

(f)

Figure 5-37: TL in horizontal planes with a seamount of height 3800 m, (a) at depth 300 m, the 3D result, (b) at depth 300 m, the $N\times 2$D result; (c) at depth 3800 m, the 3D result, (d) at depth 3800 m, the $N\times 2$D result; (e) at depth 4500 m, the 3D result, (f) at depth 4500 m, the $N\times 2$D result. When the seamount is relatively high, the $N\times 2$D model is not a good approximation of the 3D model.

To take into account the the shear wave in the seamount, we apply the schematic illustrated in Fig. 5-38, in which the seamount is composed of basalt with $c_p = 5250$ m/s, $c_s = 2500$ m/s, $\alpha_p = 0.1$ dB/λ_p, $\alpha_s = 0.2$ dB/λ_s, and $\rho = 2.7$ g/cm^3. (p stands for the compressional wave and s stands for the shear wave.) We use case 3, with the seamount of the properties as above, to demonstrate this issue.

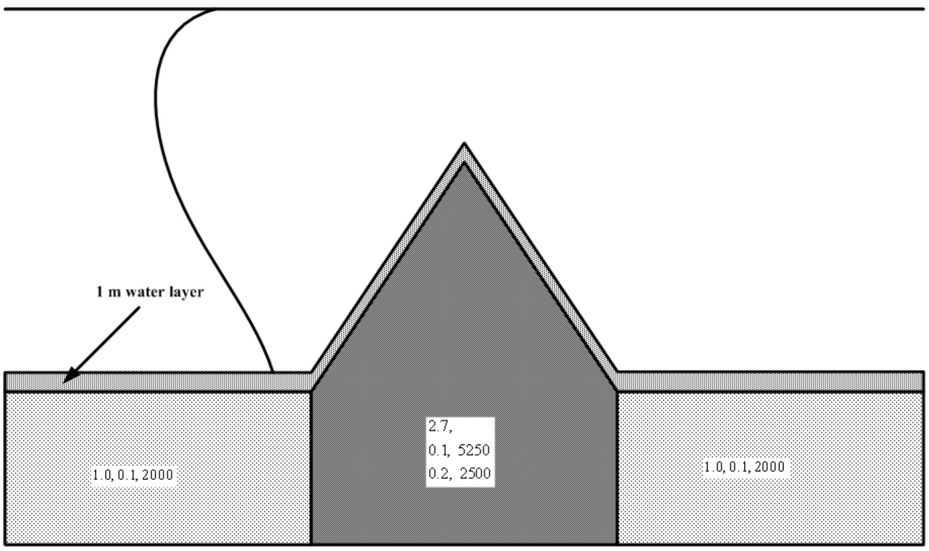

Figure 5-38: A conical seamount composed of basalt.

In modified case 3, with source depth 100 m, height of the seamount 1200 m, receiver depth 300 m, 3800 m and 4500 m, the results of transmission loss in horizontal planes are shown in Fig. 5-39. From these results we find that it makes little difference by introducing the shear wave in the seamount. The reason is that in long-range, deep water propagation problems, the field is not sensitive to the acoustic properties of the bottom.

We use a range-independent waveguide propagation problem (case 3 with the seamount removed) to illustrate that in deep water propagation problems, the acoustic field is not sensitive to the acoustics properties of the bottom. First, we compute the field with the shear wave in the bottom, with $c_p = 5250$ m/s, $c_s = 2500$ m/s, $\alpha_p = 0.1$ dB/λ_p, $\alpha_s = 0.2$ dB/λ_s, $\rho = 2.7$ g/cm^3. Next, we assume that there is no shear wave in the bottom, i.e. we use a fluid bottom with $c_p = 5250$ m/s, $\alpha_p = 0.1$ dB/λ_p, and $\rho = 2.7$ g/cm^3. In the last case, we compute the field with a fluid bottom whose

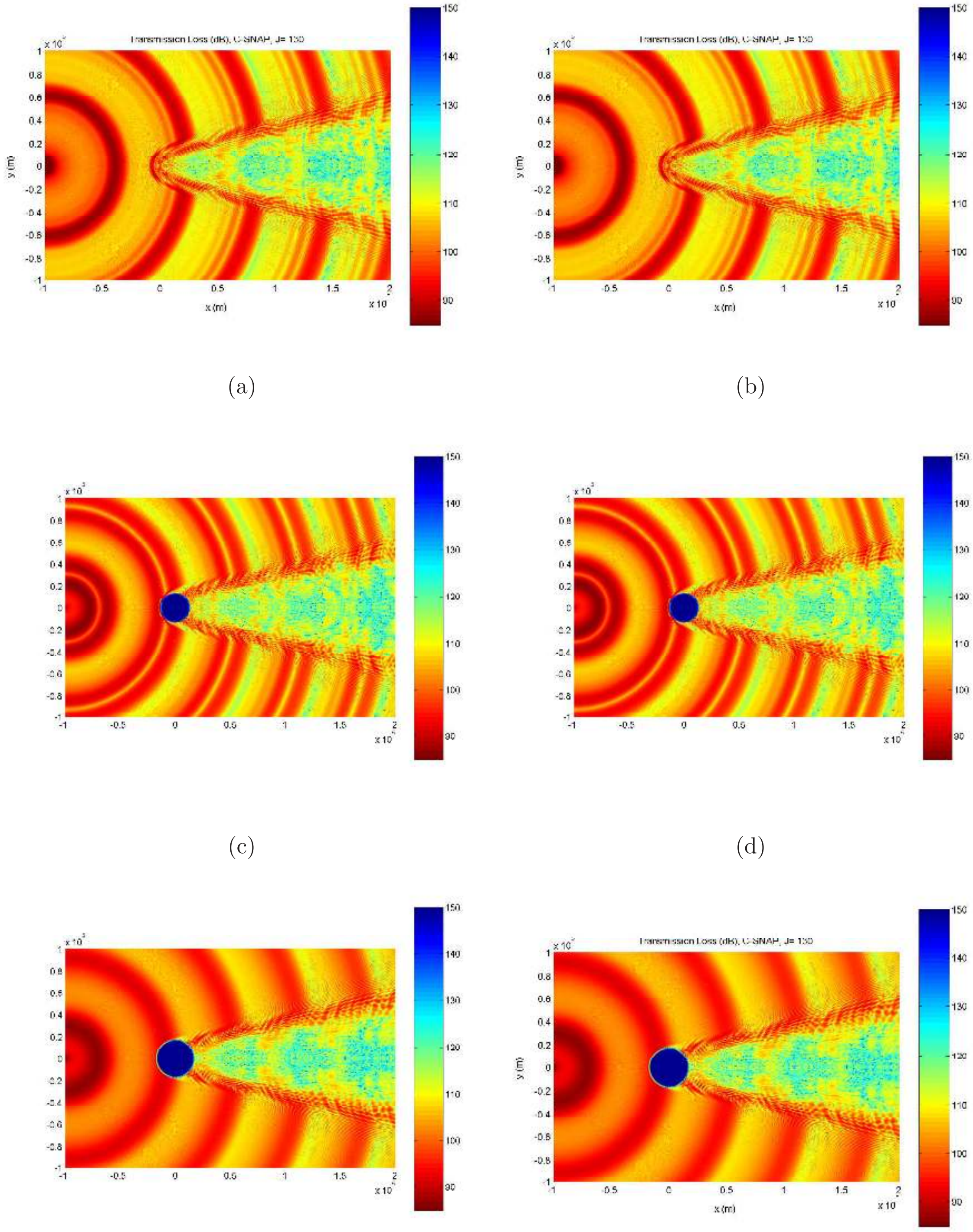

(a) (b)

(c) (d)

(e) (f)

Figure 5-39: TL in horizontal planes, (a) with the shear wave, at depth 300 m, (b) without the shear wave, at depth 300 m; (c) with the shear wave, at depth 3800 m, (d) without the shear wave, at depth 3800 m; (e) with the shear wave, at depth 4500 m, (f) without the shear wave, at depth 4500 m. No visible difference is introduced by including the shear wave in the seamount.

acoustic properties are $c_p = 2000$ m/s, $\alpha_p = 0.1$ dB/λ_p, and $\rho = 1.0$ g/cm^3. Fig. 5-40 shows the results with these three bottom settings, from which we can see that the field is insensitive to the acoustic properties of the bottom in deep water propagation problems.

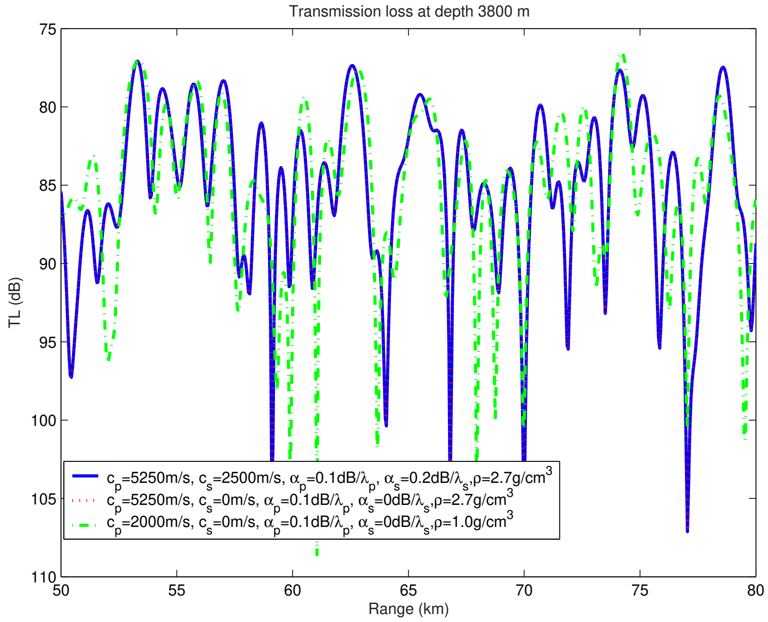

Figure 5-40: Long-range propagation in a deep water waveguide with different bottom properties. No visible difference is introduced by including the shear wave in the seamount.

Conclusion: In problems of long-range, deep water propagation around a seamount, we may ignore the effect of the shear wave in the seamount.

5.6 Mode Amplitude in the Scattered Field at Azimuthal Angle ϕ with a Single Incident Mode

As illustrated in Fig. 5-41, in this section we will investigate the scattered field excited by only one incident mode.

The incident field is represented as

$$p_{\text{inc}}(r, z, \phi) = \sum_{m=0}^{\infty} \sum_{n=1}^{\infty} b_{mn}^{J} \hat{J}_{mn}^{J}(r) \Psi_n^J(z) \Phi_m(\phi). \tag{5.18}$$

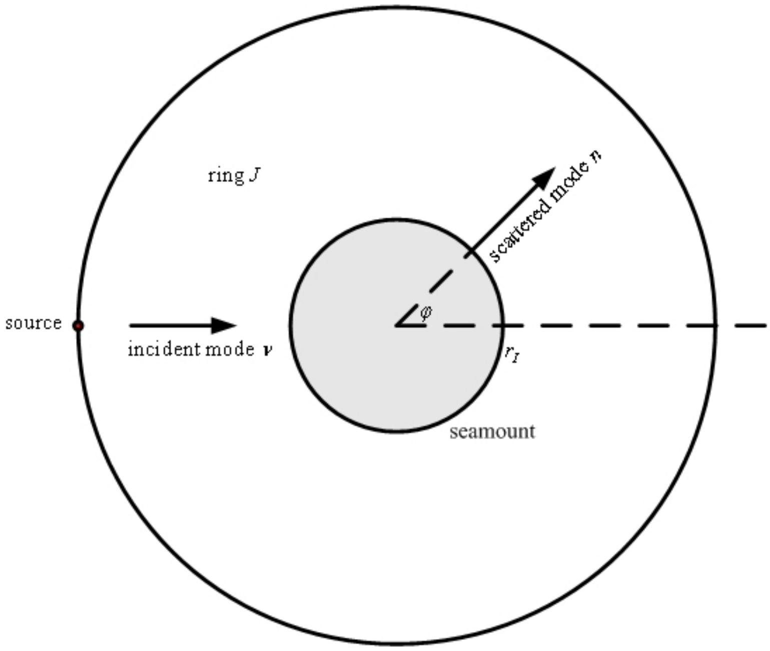

Figure 5-41: A single mode incident on a conical seamount.

With only one incident mode, denoted as mode ν, we have

$$b^J_{mn} = b^J_{mn}\delta_{n\nu}, \tag{5.19}$$

by substituting Eq. (5.19) into Eq. (5.18), we obtain the incident field with only one incident mode, mode ν,

$$p^{(\nu)}_{\text{inc}}(r, z, \phi) = \sum_{m=0}^{\infty} b^J_{m\nu}\hat{J}^J_{m\nu}(r)\Psi^J_\nu(z)\Phi_m(\phi), \tag{5.20}$$

where

$$b^J_{m\nu} = \frac{\pi}{2} i \frac{\Psi^J_\nu(z_s)}{\rho(z_s)}\Phi_m(\phi_s). \tag{5.21}$$

The scattered field is represented as

$$p_s(r, z, \phi) = \sum_{m=0}^{\infty}\sum_{n=1}^{\infty} a^J_{mn}\hat{H}1^J_{mn}(r)\Psi^J_n(z)\Phi_m(\phi). \tag{5.22}$$

At the interface $r = r_I$, we have

$$\hat{H}1^J_{mn}(r_I) = \frac{H^{(1)}_m(k^J_{rn} r_I)}{H^{(1)}_m(k^J_{rn} r_I)} \equiv 1, \tag{5.23}$$

thus at the interface $r = r_I$, the scattered field is

$$\begin{aligned} p_s(r_I, z, \phi) &= \sum_{m=0}^{\infty} \sum_{n=1}^{\infty} a^J_{mn} \Psi^J_n(z) \Phi_m(\phi) \\ &= \sum_{n=1}^{\infty} \left[\sum_{m=0}^{\infty} a^J_{mn} \Phi_m(\phi) \right] \Psi^J_n(z) \\ &= \sum_{n=1}^{\infty} A_n(\phi) \Psi^J_n(z), \end{aligned} \tag{5.24}$$

where

$$A_n(\phi) \triangleq \sum_{m=0}^{\infty} a^J_{mn} \Phi_m(\phi). \tag{5.25}$$

From the above we see that $|A_n(\phi)|$ is the amplitude of mode n at azimuthal angle ϕ in the scattered field.

If the oscillatory region in the mode shape of the incident mode is above the top of the seamount, or, the lower turning point of its eigenray is above the top of the seamount, then theoretically this mode will propagate past the seamount without exciting any other modes. Otherwise, there is interaction between the propagation of this incident mode and the seamount, which will excite other modes.

The above statement can be verified by case 3.

5.6.1 Mode Shapes of Mode 10 at 10 Hz and 20 Hz

The mode shapes of mode 10 for $f = 10$ Hz and $f = 20$ Hz are shown in Fig. 5-42(a) and 5-42(b), respectively. From Fig. 5-42 we see that at 10 Hz, the oscillatory region in the mode shape of mode 10 extends to a depth below the top of the seamount. At a higher frequency, $f = 20$ Hz, the oscillatory region in the mode shape of mode 10 extends to a depth above the top of the seamount.

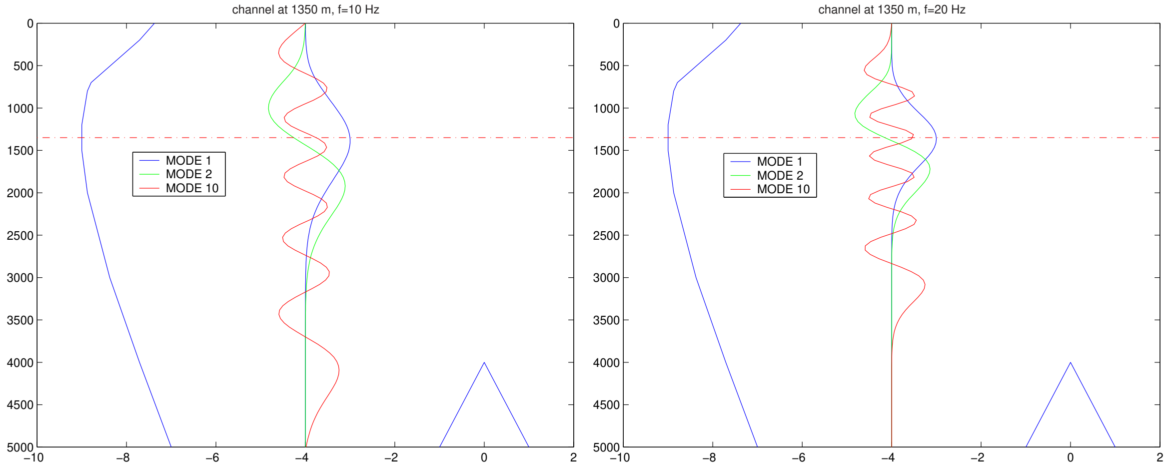

(a) (b)

Figure 5-42: Mode shapes of mode 10, (a) at 10 Hz, (b) at 20 Hz.

5.6.2 $|A_n(\phi)|$ with Mode 10 Incident at 10 Hz and 20 Hz

Fig. 5-43 shows $20\log_{10}|A_n(\phi)|$ at 10 Hz and 20 Hz. From Fig. 5-43 we can see that:

1) at 10 Hz, the propagation of mode 10 is affected by the seamount, thus some other modes are excited, and the scattered field is not zero; and

2) at 20 Hz, the propagation of mode 10 is not affected by the seamount, thus no other mode is excited, and the scattered field is zero.

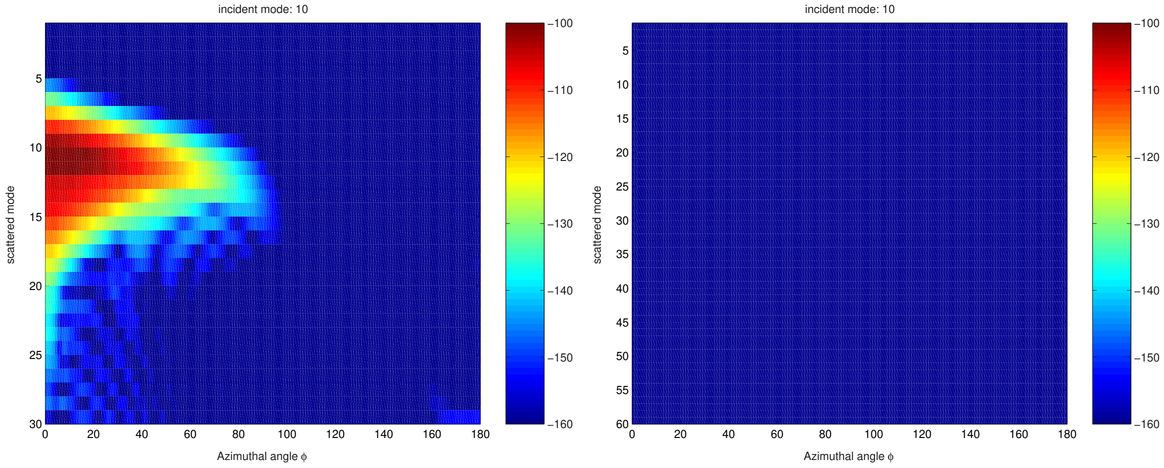

(a) (b)

Figure 5-43: $20\log_{10}|A_n(\phi)|$ with one single incident mode (mode 10), (a) at 10 Hz, other modes are excited and the scattered field is not zero; (b) at 20 Hz, no other modes are excited and the scattered field is approximately zero.

Chapter 6

Sound Propagation around Kermit-Roosevelt Seamount in 2004 BASSEX Experiment

In 2004, North Pacific Acoustic Laboratory (NPAL) was funded to conduct the SPICEX, LOAPEX, and BASSEX experiments. All these experiments coincided with each other and were ran between September and October of 2004. Among these experiments, we are interested in the Basin Acoustic Seamount Scattering Experiment (BASSEX), which was designed to measure the scattering effects of the Kermit-Roosevelt Seamount.

The Kermit-Roosevelt Seamount is one of the largest seamounts in the world. Its top reaches roughly 900 meters in a region where the average sea floor depth is about 5000 meters. To the south-east of Kermit Seamount is a smaller seamount (nicknamed "Elvis") with top depth around 1300 meters. The sizes of these two seamounts make them ideal to measure the three-dimensional sound propagation around a seamount.

6.1 Environment Data and Measured Energy around Kermit Seamount

6.1.1 Bathymetry of Kermit-Roosevelt Seamount

During the BASSEX experiment, multibeam bathymetry data was recorded to obtain an accurate measure of the size and shape of the seamounts. Fig.6-1 and Fig. 6-2 show the multibeam bathymetry gathered around the Kermit-Roosevelt Seamount Complex with a cubic interpolation applied to fill in regions where data was not available [10].

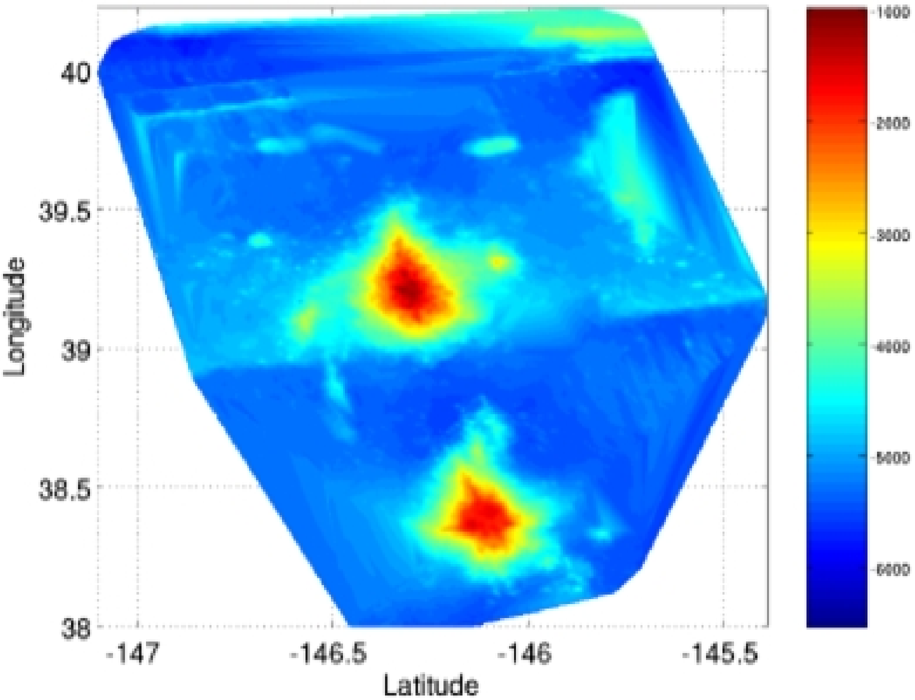

Figure 6-1: Multibeam bathymetry: top view (Courtesy of Joseph Sikora, Department of Electrical Engineering and Computer Science, MIT, "Sound propagation around underwater seamounts," 2005).

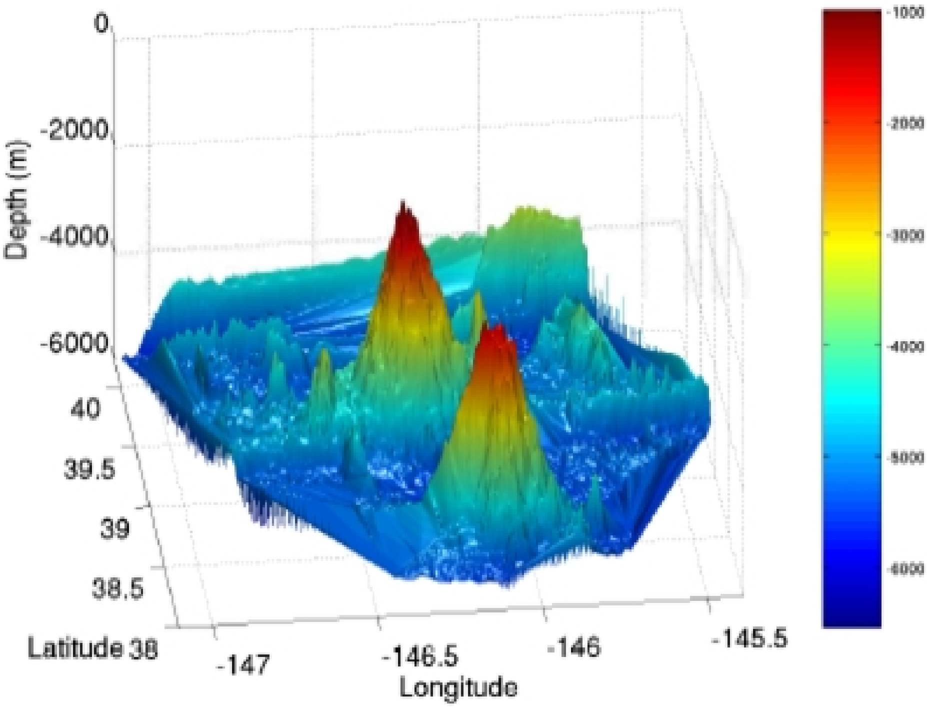

Figure 6-2: Multibeam bathymetry: isometric view. (Courtesy of Joseph Sikora, Department of Electrical Engineering and Computer Science, MIT, "Sound propagation around underwater seamounts," 2005).

6.1.2 Sources Used in Experiment

Figure 6-3 through 6-5 describe each of the sources used in the experiments. Fig. 6-6 shows the locations of these sources [10].

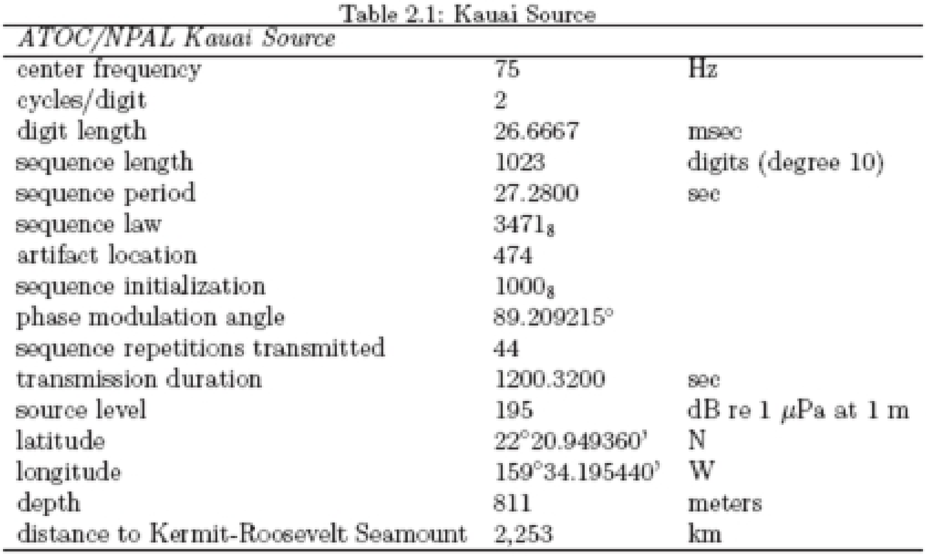

Table 2.1: Kauai Source

ATOC/NPAL Kauai Source		
center frequency	75	Hz
cycles/digit	2	
digit length	26.6667	msec
sequence length	1023	digits (degree 10)
sequence period	27.2800	sec
sequence law	3471_8	
artifact location	474	
sequence initialization	1000_8	
phase modulation angle	89.209215°	
sequence repetitions transmitted	44	
transmission duration	1200.3200	sec
source level	195	dB re 1 μPa at 1 m
latitude	22°20.949360'	N
longitude	159°34.195440'	W
depth	811	meters
distance to Kermit-Roosevelt Seamount	2,253	km

Figure 6-3: The Kauai Source. (Courtesy of Joseph Sikora, Department of Electrical Engineering and Computer Science, MIT, “Sound propagation around underwater seamounts,” 2005).

6.1.3 Sound Velocity Profiles Measured in Experiment

Sound Velocity Profiles (SVP) measured in the experiment in the flat region and at the axle of Kermit Seamount are shown in Fig. 6-7, with the sound-channel axis at depth 750 m.

6.1.4 Measured Acoustic Energy around Kermit-Roosevelt Seamount Complex in Experiment

Joseph Sikora processed the data from the cruise and obtained the measured acoustic energy around the Kermit-Roosevelt Seamount Complex. Fig. 6-8 and Fig. 6-9 show the acoustic energy measured from the SPICEX Source 1 (S1) and from the SPICEX Source 2 (S2) around the Kermit-Roosevelt Seamount Complex, respectively.

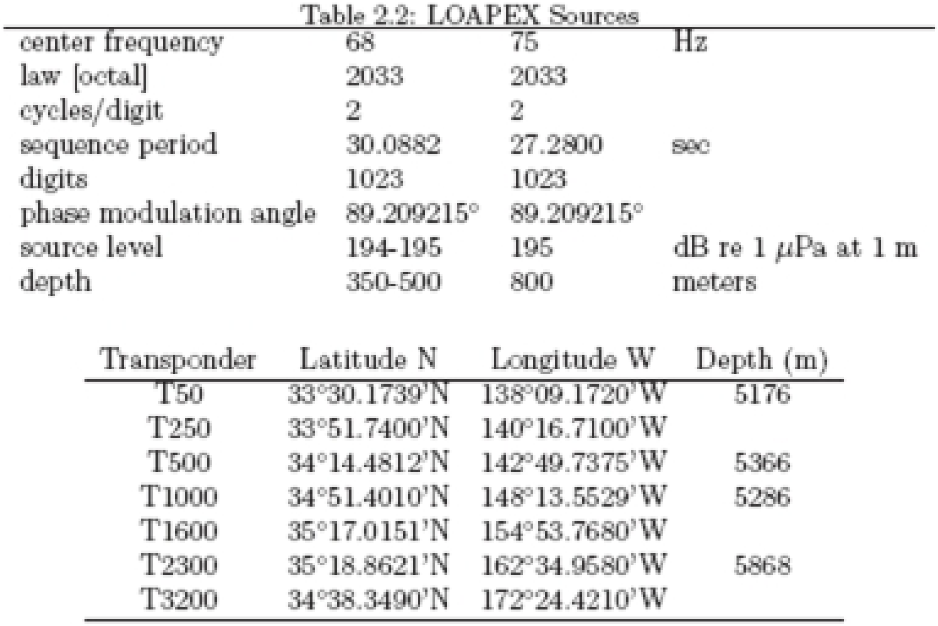

Table 2.2: LOAPEX Sources

center frequency	68	75	Hz
law [octal]	2033	2033	
cycles/digit	2	2	
sequence period	30.0882	27.2800	sec
digits	1023	1023	
phase modulation angle	89.209215°	89.209215°	
source level	194-195	195	dB re 1 μPa at 1 m
depth	350-500	800	meters

Transponder	Latitude N	Longitude W	Depth (m)
T50	33°30.1739'N	138°09.1720'W	5176
T250	33°51.7400'N	140°16.7100'W	
T500	34°14.4812'N	142°49.7375'W	5366
T1000	34°51.4010'N	148°13.5529'W	5286
T1600	35°17.0151'N	154°53.7680'W	
T2300	35°18.8621'N	162°34.9580'W	5868
T3200	34°38.3490'N	172°24.4210'W	

Figure 6-4: LOAPEX Sources. (Courtesy of Joseph Sikora, Department of Electrical Engineering and Computer Science, MIT, "Sound propagation around underwater seamounts," 2005).

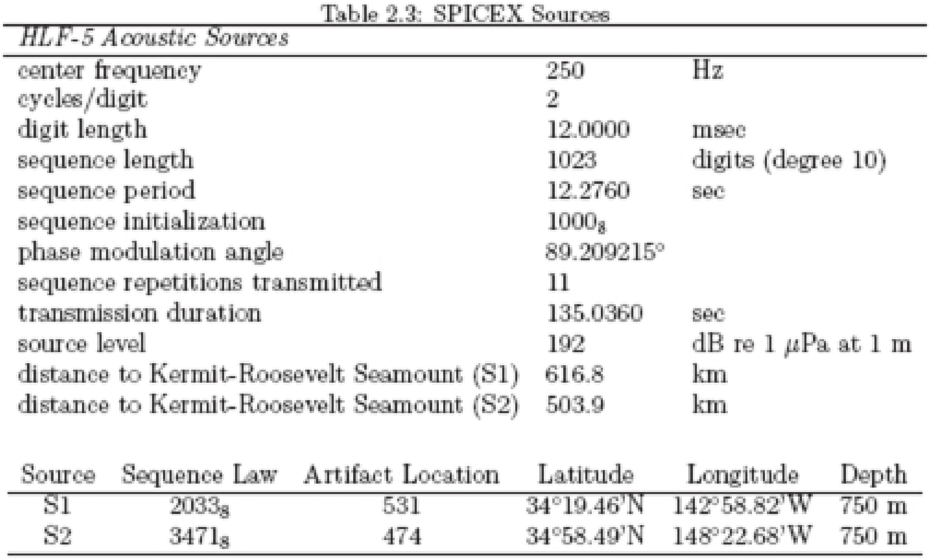

Table 2.3: SPICEX Sources

HLF-5 Acoustic Sources		
center frequency	250	Hz
cycles/digit	2	
digit length	12.0000	msec
sequence length	1023	digits (degree 10)
sequence period	12.2760	sec
sequence initialization	1000_8	
phase modulation angle	89.209215°	
sequence repetitions transmitted	11	
transmission duration	135.0360	sec
source level	192	dB re 1 μPa at 1 m
distance to Kermit-Roosevelt Seamount (S1)	616.8	km
distance to Kermit-Roosevelt Seamount (S2)	503.9	km

Source	Sequence Law	Artifact Location	Latitude	Longitude	Depth
S1	2033_8	531	34°19.46'N	142°58.82'W	750 m
S2	3471_8	474	34°58.49'N	148°22.68'W	750 m

Figure 6-5: SPICES Sources. (Courtesy of Joseph Sikora, Department of Electrical Engineering and Computer Science, MIT, "Sound propagation around underwater seamounts," 2005).

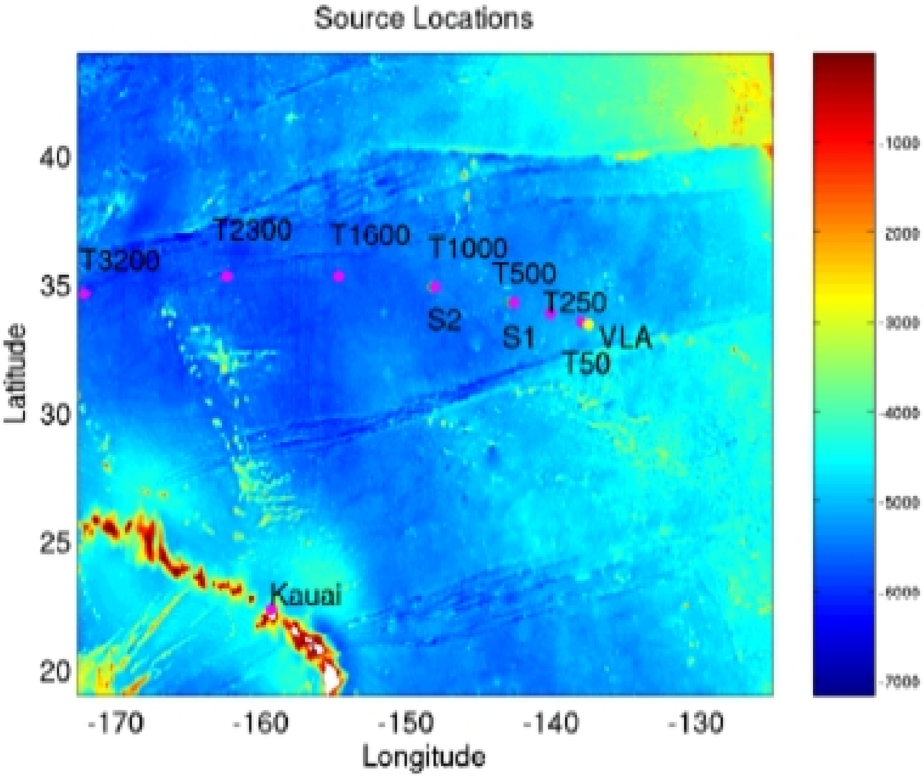

Figure 6-6: Source Positions: (S) SPICES moored source, (T) LOAPEX stations. (Courtesy of Joseph Sikora, Department of Electrical Engineering and Computer Science, MIT, "Sound propagation around underwater seamounts," 2005).

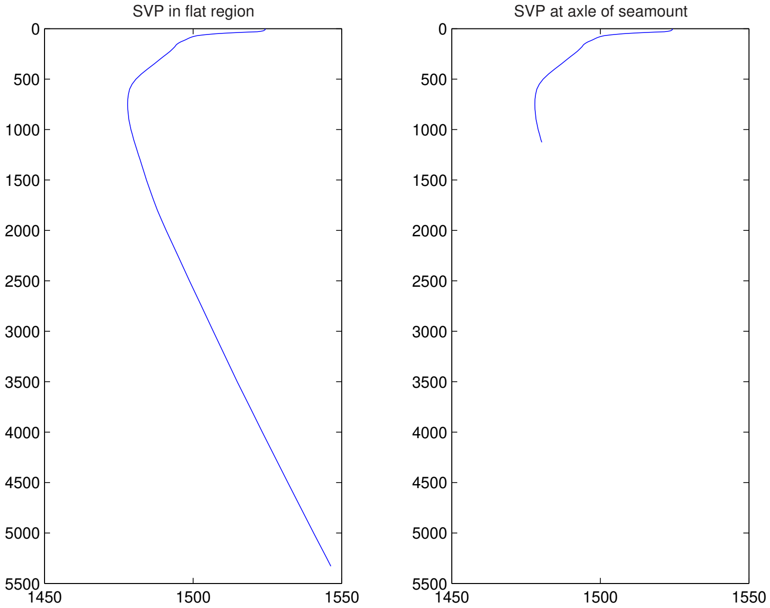

Figure 6-7: Sound velocity profiles in the flat region and at the axle of Kermit Seamount.

In these figures, each dot represents a location where an M-sequence was processed. The solid, maroon contour lines are on the two tallest seamounts in the complex, providing a reference. The arrow indicates the arrival direction of the signal from the source. A cubic interpolation algorithm was used in MATLAB to fill in regions of the chart where processed data was not available. From Fig. 6-8 and Fig. 6-9 we can see that the perturbation zone forms behind the seamount.

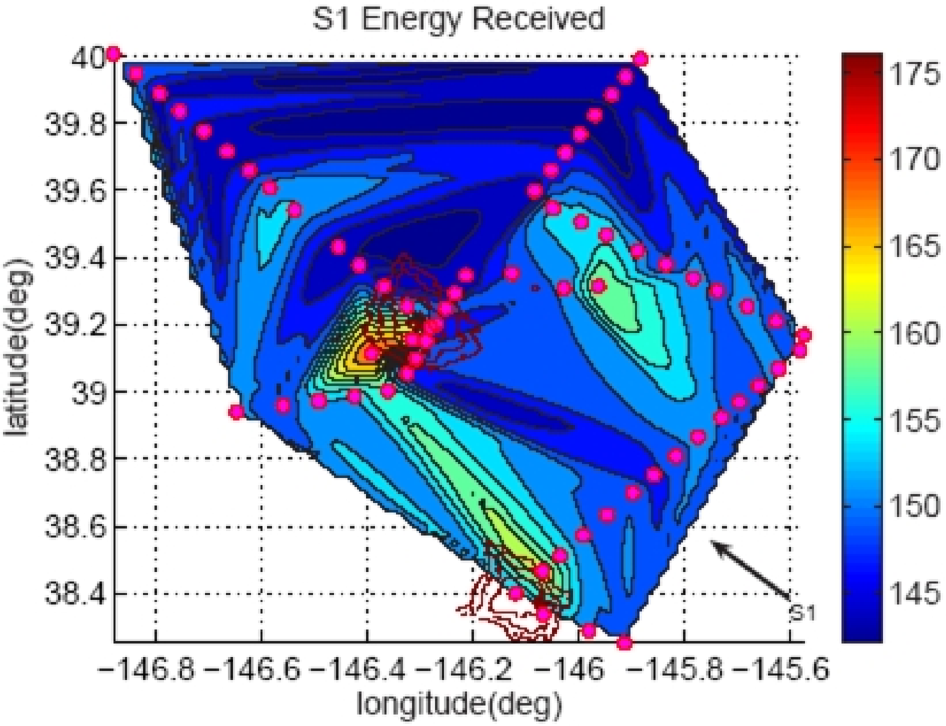

Figure 6-8: Received SPICEX Source 1 acoustic energy (dB). (Courtesy of Joseph Sikora, Department of Electrical Engineering and Computer Science, MIT, "Sound propagation around underwater seamounts," 2005).

6.1.5 The Environment Model of the Kermit Seamount Problem

To apply our three-dimensional spectral coupled mode model to the Kermit Seamount problem, we use a conic seamount of height 4201 m and the radius of the base as 26 km to approximate the Kermit Seamount. We use the SPICES Source 2 (S2) as the point source; however, at the current stage, we can not address our 3D model to deep

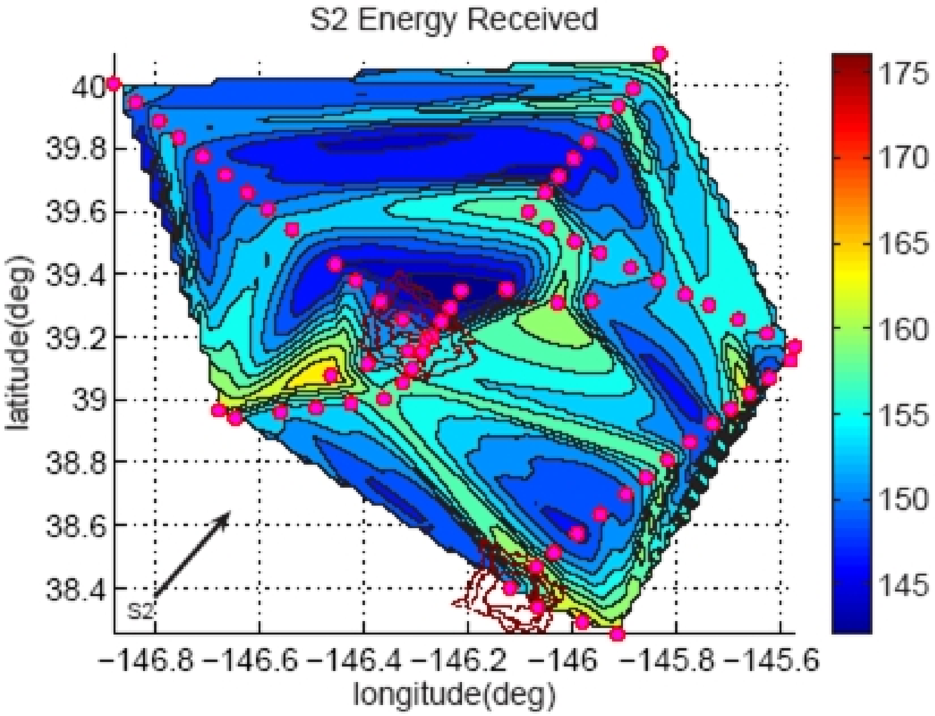

Figure 6-9: Received SPICEX Source 2 acoustic energy (dB). (Courtesy of Joseph Sikora, Department of Electrical Engineering and Computer Science, MIT, “Sound propagation around underwater seamounts,” 2005).

water propagation problems with a frequency as high as 250 Hz, so we use a lower source frequency of 75 Hz or 10 Hz instead. The schematic of the simplified Kermit Seamount problem is shown in Fig. 6-10.

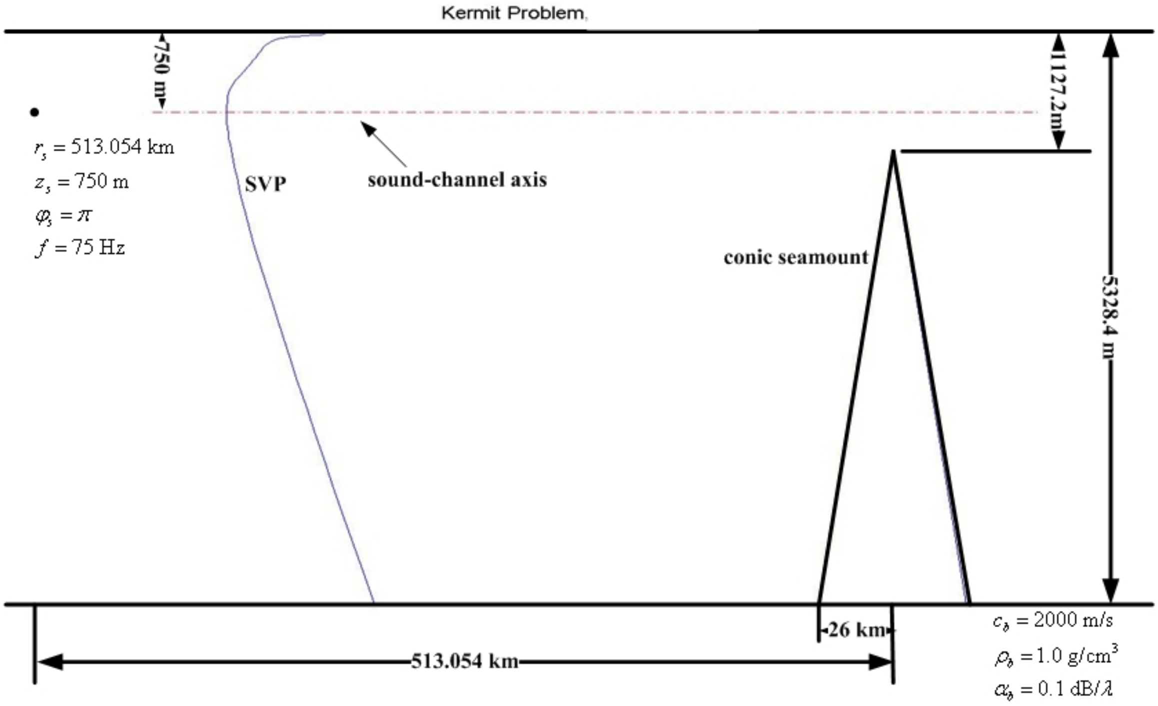

Figure 6-10: The schematic of the Kermit Seamount problem.

6.2 Results with the Source Frequency of 10 Hz

Before addressing the Kermit Seamount problem with the source frequency of 75 Hz, we apply our 3D model to that problem at a lower frequency, 10 Hz.

6.2.1 The Number of Normal Modes

We use different numbers of normal modes as the exciting modes and the propagating modes. Below we show how to determine these numbers by means of C-SNAP.

1) **The number of waterborne modes in the flat region**

Since

$$k_{rnc1} = \frac{\omega}{c_w(D)} = \frac{2\pi \times 10}{1546.36442} \approx 0.040632, \tag{6.1}$$

where $c_w(D)$ is the sound speed at the floor depth in the water column, together with the eigenvalues computed by C-SNAP, $k_{r15} = 0.040695 > k_{rnc1}$ and $k_{r16} = 0.040580 < k_{rnc1}$, we know that there are 15 waterborne modes in the flat region where water depth is 5328.48670 m.

2) **The number of propagating modes in the flat region**

We have

$$k_{rnc2} = \frac{\omega}{c_b(D)} = \frac{2\pi \times 10}{2000} \approx 0.031416, \tag{6.2}$$

where $c_b(D)$ is the sound speed at floor depth in seabed, together with the eigenvalue computed by C-SNAP, $k_{r47} = 0.031628 > k_{rnc2}$, we know that there are 47 propagating mode in the flat region where the water depth is 5328.48670 m. In fact, C-SNAP can compute only the propagating modes.

3) **The number of propagating modes on top of Kermit Seamount**

By running C-SNAP, we know there are 10 propagating modes on top of the seamount, where the water depth is 1127.23790 m.

In addition, the mode shapes of the first 4 modes in the flat region where the water depth is 5328.48670 m are shown in Fig. 6-11.

Inspired by [7], we use only the waterborne modes as the exciting modes, and use the propagating modes otherwise. In this case, we use the first 15 waterborne modes as the exciting modes, and use 47 propagating modes otherwise.

6.2.2 The Number of Rings and the Azimuthal Feature of Backscattering

From Section 5.3.3 we know that if we use uniform step-size rings not satisfying $\Delta r < \lambda/2$, where Δr is the step size and λ is the wavelength, to represent a smoothly varying seamount, then there will be artificial backscattering beams. By taking the

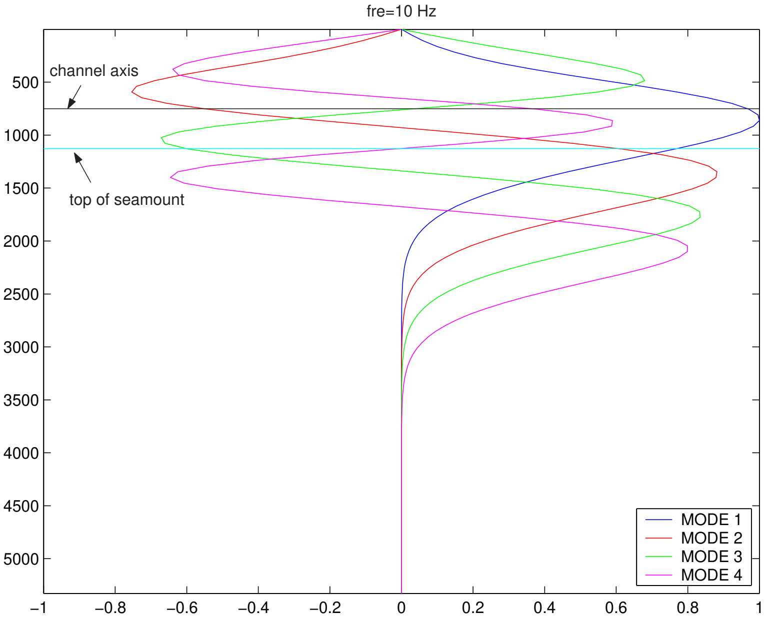

Figure 6-11: Mode shapes of the first 4 modes in the flat region where the water depth is 5328.48670 m.

random step-size technique, these artificial backscattering beams can be smeared out. In this section we will investigate the azimuthal feature of backscattering by means of analyzing $|A_n(\phi)|$, the amplitude of mode n at azimuthal angle ϕ, with a single mode incident (mode 10), at 10 Hz.

From Fig. 6-11 we see that the oscillatory region in the mode shape of mode 1 already extends to a depth below the top of the Kermit Seamount, and we know that the oscillatory region is larger for the higher-order modes, so the oscillatory region of mode 10 also extends to a depth below the top of Kermit Seamount. Therefore with mode 10 incident, the scattered field is nonzero.

128 Rings

With $f = 10$ Hz and mode 10 incident, by using 128 rings, $20\log_{10}|A_n(\phi)|$ is shown in Fig. 6-12(a), from which we can see that two strong backscattering beams are formed: one spans approximately from 80^o to 90^o and the other spans approximately from 120^o to 160^o. The two blue lines in Fig. 6-12(a) are the predicted locations of these two artificial backscattering beams by means of the method illustrated in Section 5.3.3, and they show good agreement with the computed results. The number of artificial backscattering beams is predicted by the following analysis (refer to Section 5.3.3).

With $f = 10$ Hz and 128 uniformly spaced rings, we have

$$\begin{aligned}
\lambda &= \frac{c}{f} \sim 150 \text{ m}, \\
\Delta r &= \frac{26 \times 1000}{128} \sim 203 \text{ m}, \\
1 \times \frac{\lambda}{\Delta r} - 1 &\sim \frac{150}{203} - 1 < 1, \\
2 \times \frac{\lambda}{\Delta r} - 1 &\sim 2 \times \frac{150}{203} - 1 < 1, \\
3 \times \frac{\lambda}{\Delta r} - 1 &\sim 3 \times \frac{150}{203} - 1 > 1,
\end{aligned}$$

from which we know that there are two artificial backscattering beams.

With the same number of rings, if we apply the random step-size technique, $20\log_{10}|A_n(\phi)|$ is shown in Fig. 6-12(b), from which we can see that both of these two artificial backscattering beams are smeared out.

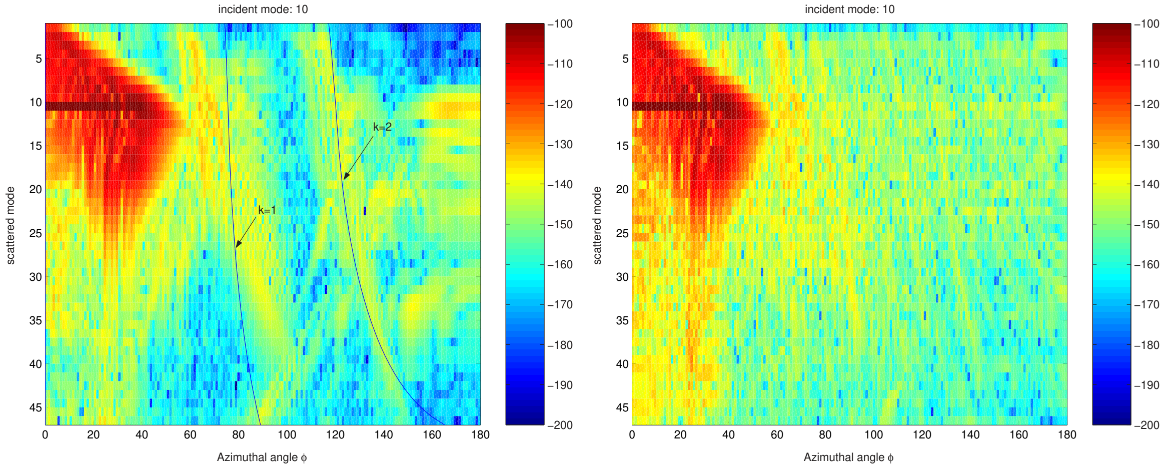

(a)

(b)

Figure 6-12: $20\log_{10}|A_n(\phi)|$ with mode 10 incident, 128 rings, (a) using a uniform step size, (b) using random step sizes. By using random step sizes, the artificial backscattering beams are smeared out.

256 Rings

With $f = 10$ Hz and mode 10 incident, by using 256 uniformly spaced rings, $20\log_{10}|A_n(\phi)|$ is shown in Fig. 6-13(a), from which we can see that one strong backscattering beam spans from 100^o to 150^o approximately. This phenomenon is physically meaningless for a smoothly varying seamount, and it is caused by the use of sparse rings to represent the seamount.

To predict the number of artificial backscattering beams, we follow the analysis as presented here. Now we have

$$\lambda = \frac{c}{f} \sim 150 \text{ m},$$
$$\Delta r = \frac{26 \times 1000}{256} \sim 102 \text{ m}.$$

Since

$$1 \times \frac{\lambda}{\Delta r} - 1 \sim \frac{150}{102} - 1 < 1,$$

and

$$2 \times \frac{\lambda}{\Delta r} - 1 \sim 2 \times \frac{150}{102} - 1 > 1,$$

we know there is one artificial backscattering beam in this case.

Next we predict the azimuthal angles of this artificial backscattering beam. From Section 5.3.3, for backscattered mode n, we have

$$\lambda_n = \frac{2\pi}{k_{rn}}, \tag{6.3}$$

thus with

$$\cos\phi_1' = \frac{\lambda_n}{\Delta r} - 1, \tag{6.4}$$

and $\phi = \pi - \phi'$, we can predict the azimuthal angles where this artificial backscattering beam forms for each mode, and the predicted result is shown by the blue line in Fig. 6-13(a). From Fig. 6-13(a) we can see that the predicted azimuthal angles of the artificial backscattering beam show good agreement with the computed result.

With the same number of rings, if we apply the random step-size technique, the result of $20\log_{10}|A_n(\phi)|$ is shown in Fig. 6-13(b), from which we can see that the artificial backscattering beam is smeared out to some extent.

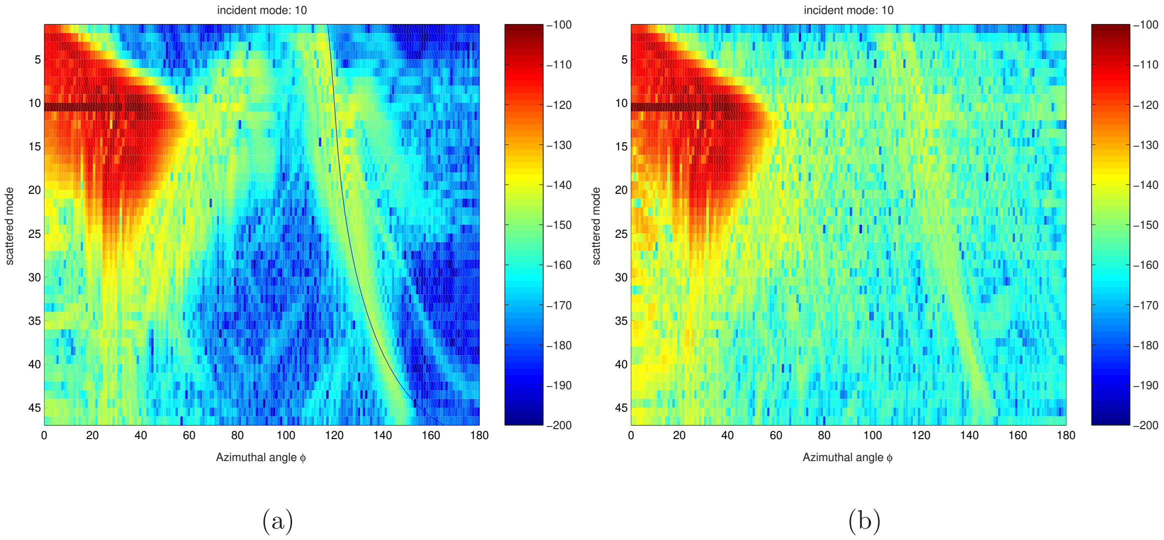

Figure 6-13: $20\log_{10}|A_n(\phi)|$ with mode 10 incident, 256 rings, (a) using a uniform step size, (b) using random step sizes. By using random step sizes, the artificial backscattering beam is smeared out to some extent.

512 Rings

With 512 rings, we have

$$\Delta r = \frac{26 \times 1000}{512} \sim 51 \text{ m} < \frac{\lambda}{2},$$

and from Section 5.3.3 we know that there is no artificial backscattering beams in this case. This can be verified by Fig. 6-14, from which we can see there is no strong artificial backscattering beams. Fig. 6-14(a) shows the result obtained by using a uniform step size, and Fig. 6-14(b) shows the result obtained by using random step sizes. From Fig. 6-14 we find that the backscattered field obtained by using random step sizes is stronger than that by using a uniform step size. This is because by using random step sizes, some step sizes are larger than the uniform step size, which is 51 m with 512 rings, thus creating some random roughness scattering.

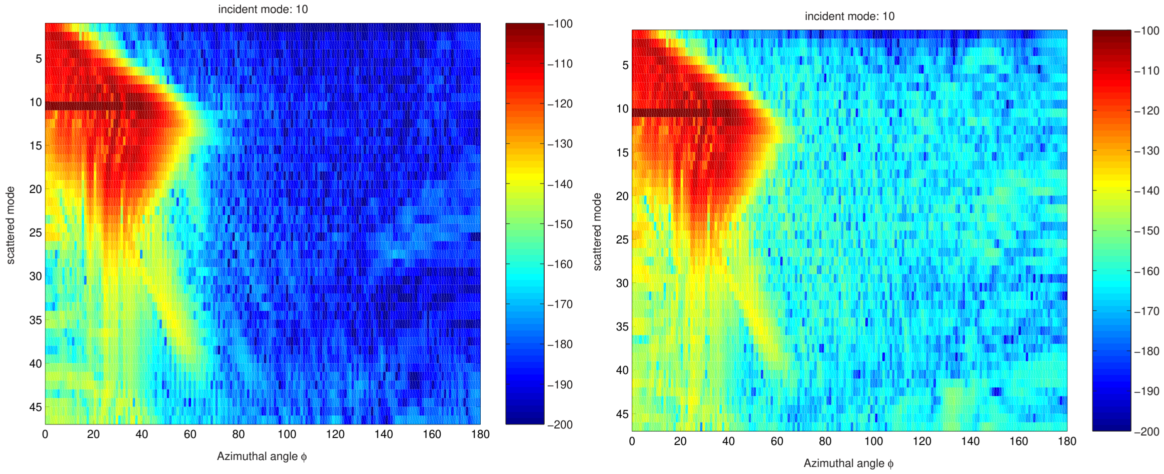

(a) (b)

Figure 6-14: $20\log_{10}|A_n(\phi)|$ with mode 10 incident, 512 rings, (a) using a uniform step size, (b) using random step sizes. In this case, the uniform step size is smaller than $\lambda/2$, so there is no artificial backscattering beam.

Conclusion

From the above results with $n = 7$, $n = 8$ and $n = 9$, we draw the conclusion that for a smoothly varying conical seamount, the existence of artificial backscattering beams in $|A_n(\phi)|$ is caused by numerical issues, and is not a physical phenomenon. In addition, with the same number of rings, the backscattered field obtained by using random step sizes is stronger than that by using a uniform step size, because by using random step sizes, some step sizes are larger than the uniform step size.

6.2.3 3D and $N\times$2D Results

From the analysis in the above sections, we use 15 waterborne modes as the exciting modes and 47 propagating modes otherwise. As to the number of rings, to satisfy $\Delta r < \lambda/4$, where $\lambda = 37.5$ m, at least $n = 10$, i.e. 1024 rings, should be used, which leads to $\Delta r = 26 \times 1000/1024 \approx 25.4$ m. However, from Fig. 6-12 and Fig. 6-13 we notice that the values of $20\log_{10}|A_n(\phi)|$ in the artificial backscattering beams, which are below -140 dB, are much smaller than the values in the forward scattering region. So, by using $n = 7$ (128 rings) or $n = 8$ (256 rings), the artificial backscattering beams will not contribute much to the total field. This can be verified by comparing the total field with $n = 7$ and $n = 10$, as shown in Fig. 6-16(b) and Fig. 6-17(d), respectively, from which we can see that there is little visible difference between them. Fig. 6-15 through Fig. 6-17 show the 3D results of the scattered field and the total field in the horizontal plane at depth 750 m with $n = 5$ (32 rings), $n = 6$ (64 rings), $n = 7$ (128 rings), $n = 8$ (256 rings), $n = 9$ (512 rings) and $n = 10$ (1024 rings), at $f = 10$ Hz. From these results we can see that the total field reaches convergence when $n = 7$. Fig. 6-18 shows the total field in the vertical plane at azimuthal angle $\phi' = 0$ with respect to the source, obtained by 3D and $N\times$2D models. From Fig. 6-18 we can see that above the top of Kermit Seamount, these two models give similar results, while below the top of Kermit Seamount, a stronger shadow zone appears behind the seamount by the 3D model than by the $N\times$2D model. The uniform step-size approach is used in obtaining these results.

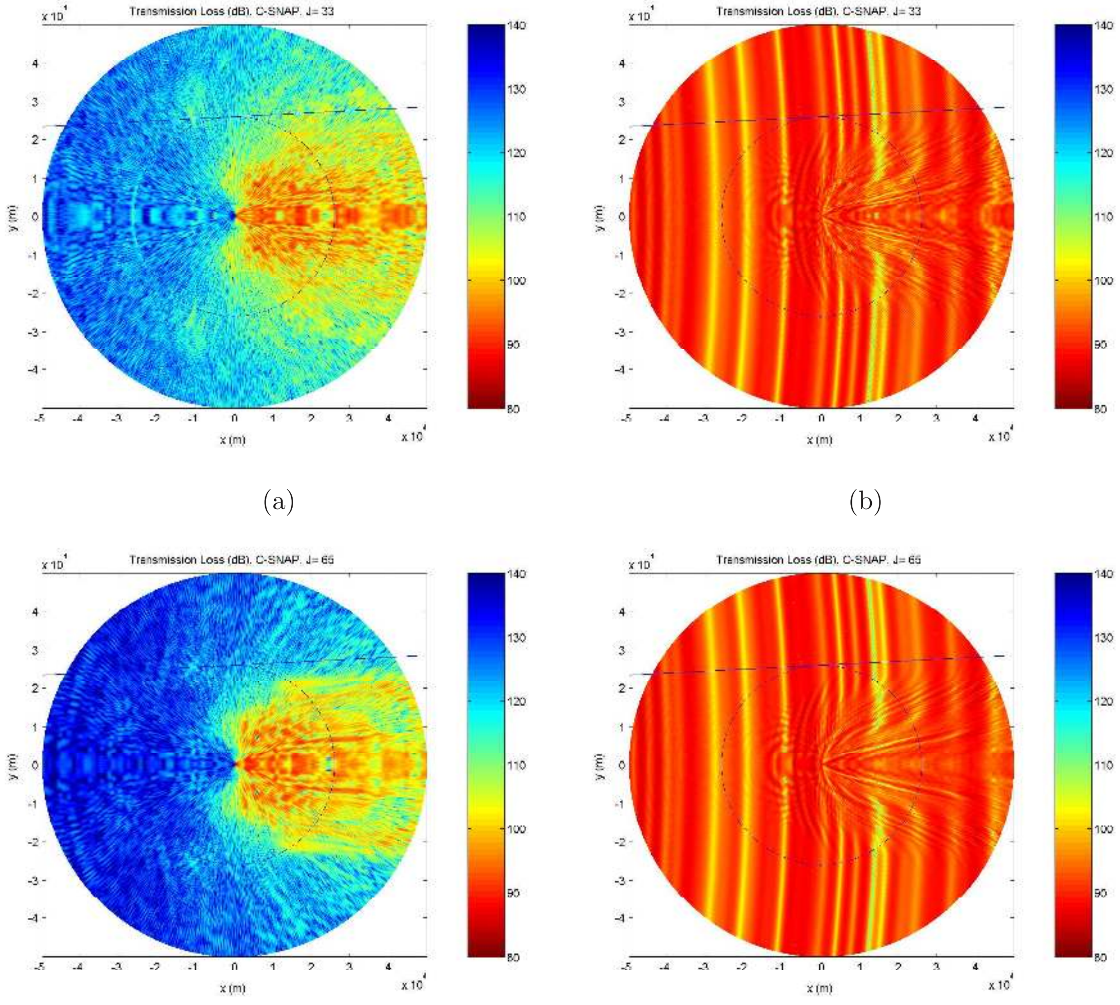

(a)

(b)

(c)

(d)

Figure 6-15: Scattered field and total field at 750 m, $f = 10$ Hz. (a) scattered field, $n = 5$, (b) total field, $n = 5$; (c) scattered field, $n = 6$, (d) total field, $n = 6$.

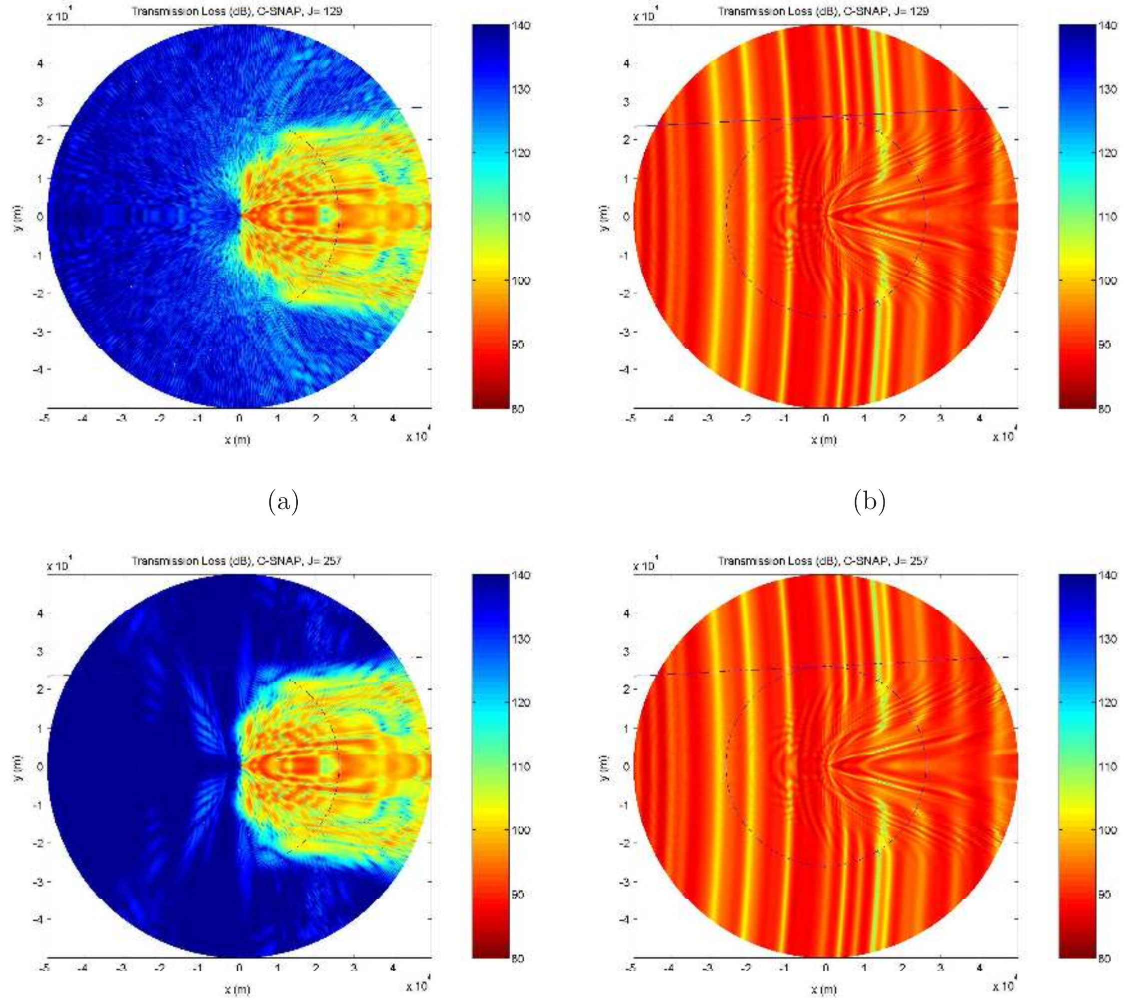

(a) (b)

(c) (d)

Figure 6-16: Scattered field and total field at 750 m, $f = 10$ Hz. (a) scattered field, $n = 7$, (b) total field, $n = 7$; (c) scattered field, $n = 8$, (d) total field, $n = 8$.

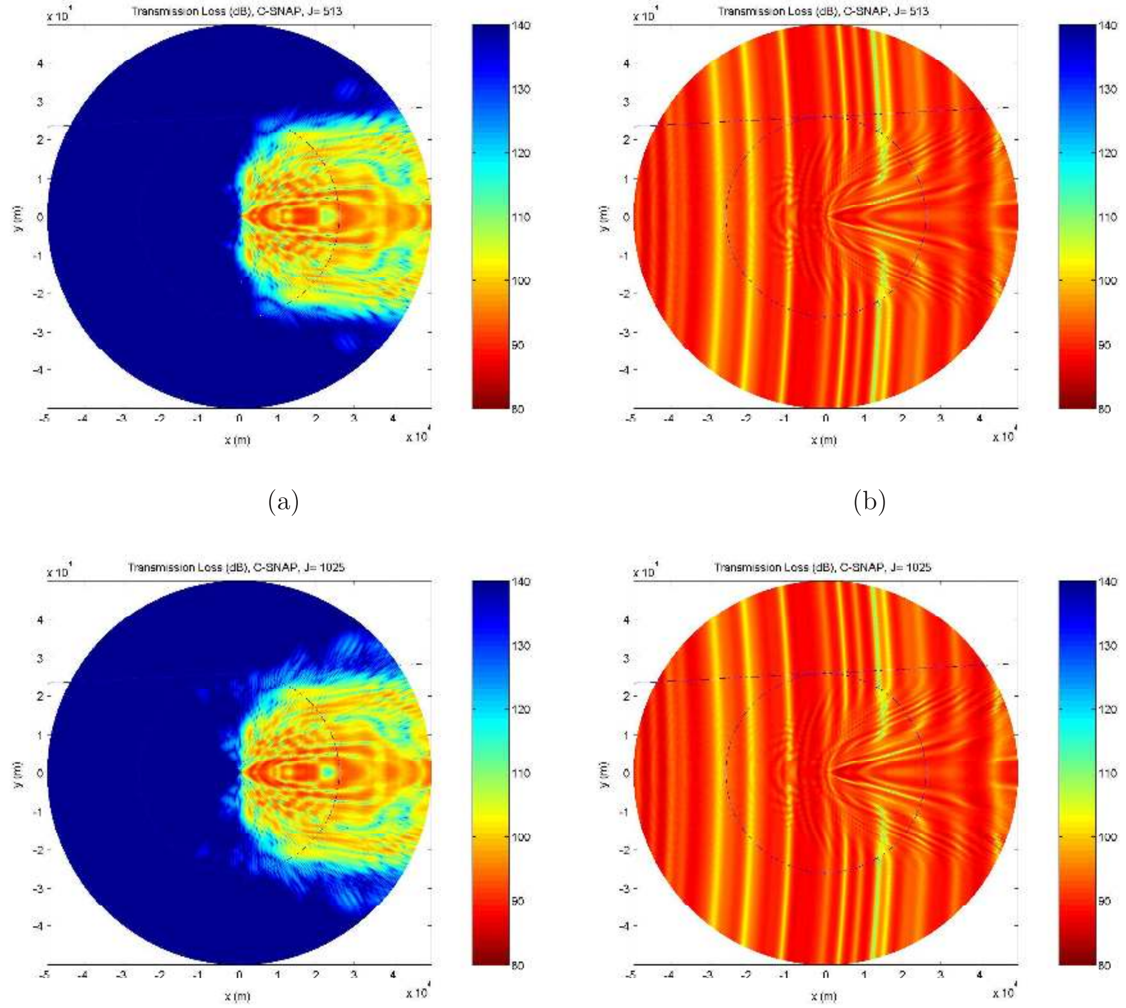

(a) (b)

(c) (d)

Figure 6-17: Scattered field and total field at 750 m, $f = 10$ Hz. (a) scattered field, $n = 9$, (b) total field, $n = 9$; (c) scattered field, $n = 10$, (d) total field, $n = 10$.

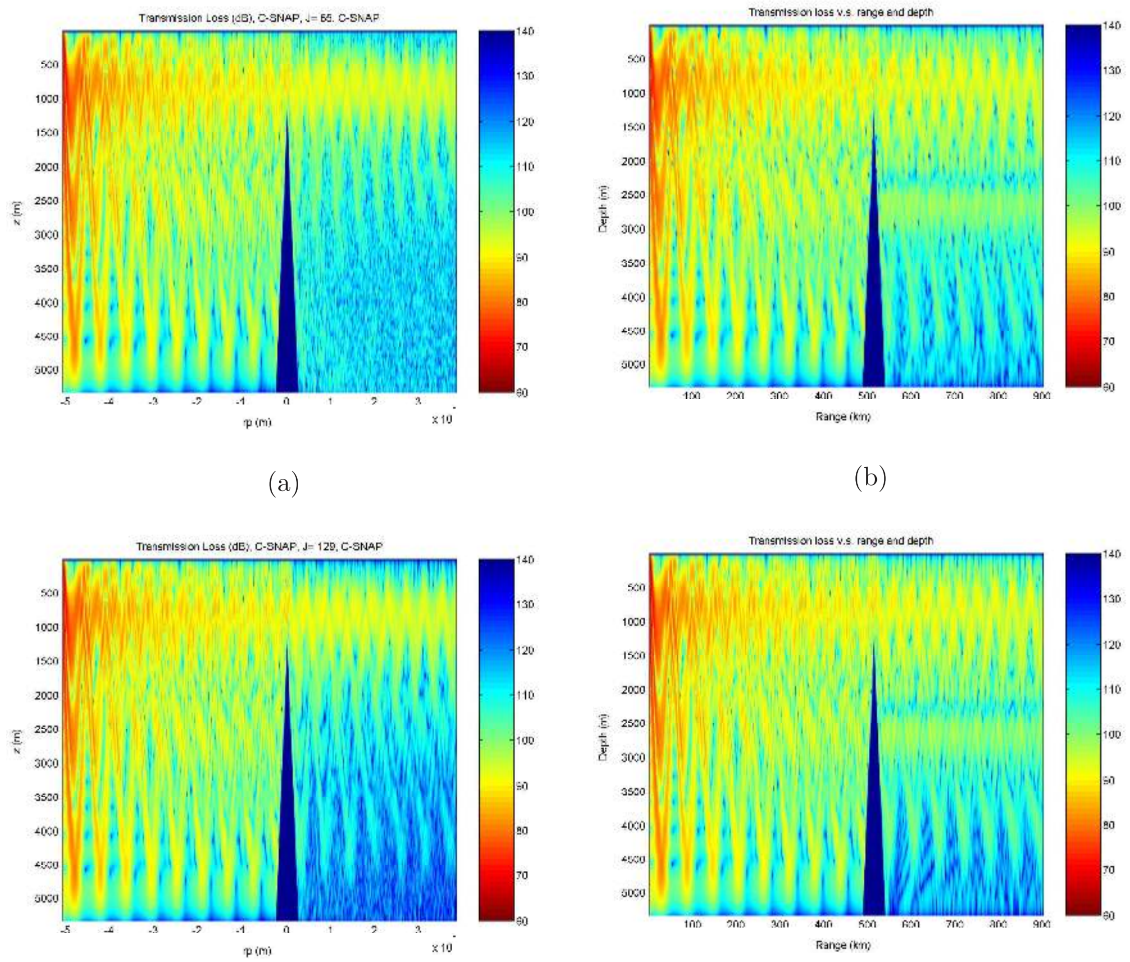

(a) (b)

(c) (d)

Figure 6-18: The total field in the vertical plane $\phi' = 0$ with respect to the source, $f = 10$ Hz, (a) by our 3D model, $n = 6$, not convergent, (b) by the $N\times 2$D model, $n = 6$, almost convergent; (c) by our 3D model, $n = 7$, convergent, (d) by the $N\times 2$D model, $n = 7$, convergent. There is great difference between the 3D result and the $N\times 2$D result behind the seamount, below the top of the seamount.

6.3 Results with the Source Frequency of 75 Hz

In Section 6.2 we address the Kermit Seamount problem with a source of frequency 10 Hz; in this section we will use a source of frequency 75 Hz, while keeping all the other parameters unchanged. Now we have 115 waterborne modes and 349 propagating modes in the flat region, and 76 propagating modes on top of Kermit Seamount. Due to the computational limit of our 3D model at the current stage, we use 115 waterborne modes as the exciting modes and 150 modes involved in mode coupling, as well as 256 rings ($n = 8$).

6.3.1 3D and $N\times$2D Results

Fig. 6-19 shows the field in the vertical plane $\phi' = 0$ with respect to the source, computed by our 3D model and by the $N\times$2D model, from which we can see that the fields above the top of Kermit Seamount obtained by these two models show good agreement, while below the top of Kermit Seamount, the fields behind the seamount by our 3D model and by the $N\times$2D model are different. Fig. 6-20 shows the field from 0 m to 500 m in depth and from 0 km to 200 km in range with respect to the axle of the Kermit Seamount, at azimuthal angle $\phi' = 0$ with respect to the source.

In the BASSEX experiment, a towed 162 element hydrophone array was used. The array was towed at approximately 3-4 knots at a depth of about 300 m throughout the experiment. From the acoustic energy measured from S2 around the Kermit Seamount, as shown in Fig. 6-9, we find that behind the Kermit Seamount, from 0 km to about 100 km in range, at azimuthal angle $\phi' = 0$ with respect to the source, the level difference is within 15 dB. From the results of our 3D and $N\times$2D models shown in Fig. 6-20, we find that at the depth of 300 m, from 0 km to 100 km in range, the level difference is also within 15 dB. However, there remains a difference in terms of the spatial extent of the maximum and minimum, which are significantly larger in the experiment than in the modeled results.

Fig. 6-21 shows the field in the horizontal plane at depth 250 m computed by the 3D model, from which we see that a shadow zone forms behind the Kermit Seamount.

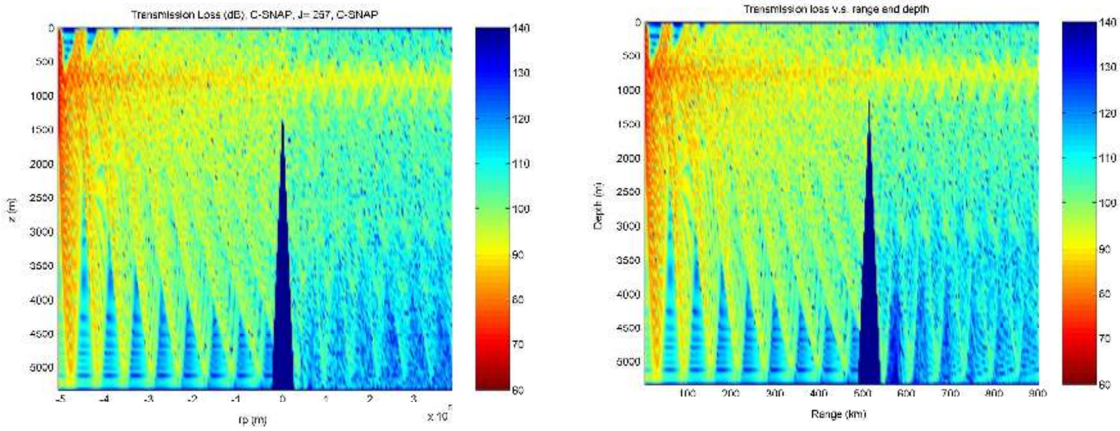

(a) (b)

Figure 6-19: Transmission loss in the vertical plane $\phi' = 0$ with respect to the source, with $f = 75$ Hz, $n = 8$ (256 rings), (a) by our 3D model, (b) by the $N\times$ 2D model. Difference appears behind the seamount, below the top of the seamount.

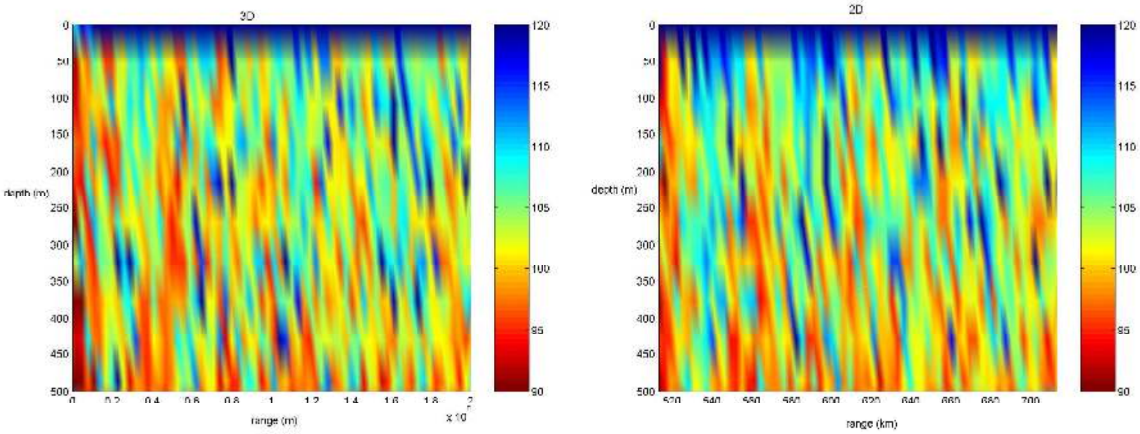

(a) (b)

Figure 6-20: Transmission loss in the vertical plane $\phi' = 0$ with respect to the source, with $f = 75$ Hz, $n = 8$ (256 rings), (a) by our 3D model, (b) by the $N\times$ 2D model. At the depth of 300 m, from 0 km to 100 km in range, the level difference is within 15 dB.

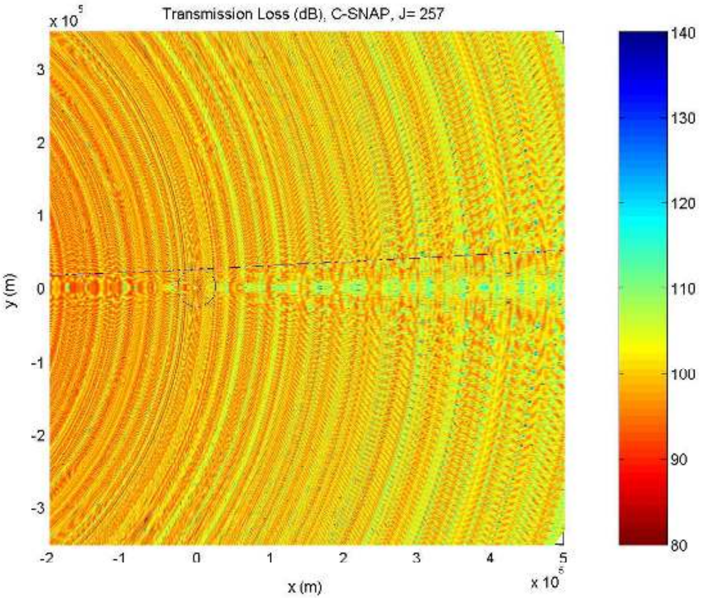

Figure 6-21: Transmission loss in the horizontal plane at depth 250 m, $f = 75$ Hz, by our 3D model. A perturbation zone forms behind the seamount.

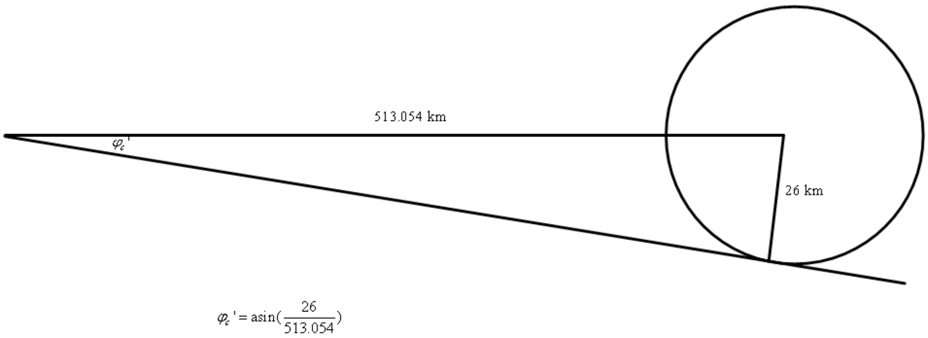

Figure 6-22: Tangent azimuthal angle in the Kermit Seamount problem.

By referring to Fig. 6-22, we compare the 3D results and the $N\times$2D results along 5 evenly spaced azimuthal angles, i.e., $\frac{0}{4}\phi'_c$, $\frac{1}{4}\phi'_c$, $\frac{2}{4}\phi'_c$, $\frac{3}{4}\phi'_c$, and $\frac{4}{4}\phi'_c$, with respect to the source, at depth 750 m. The results are shown in Fig. 6-23 through Fig. 6-25. From these results we can see that at depth 750 m, which is above the top of Kermit Seamount, the $N\times$2D model is a good approximation of our 3D model.

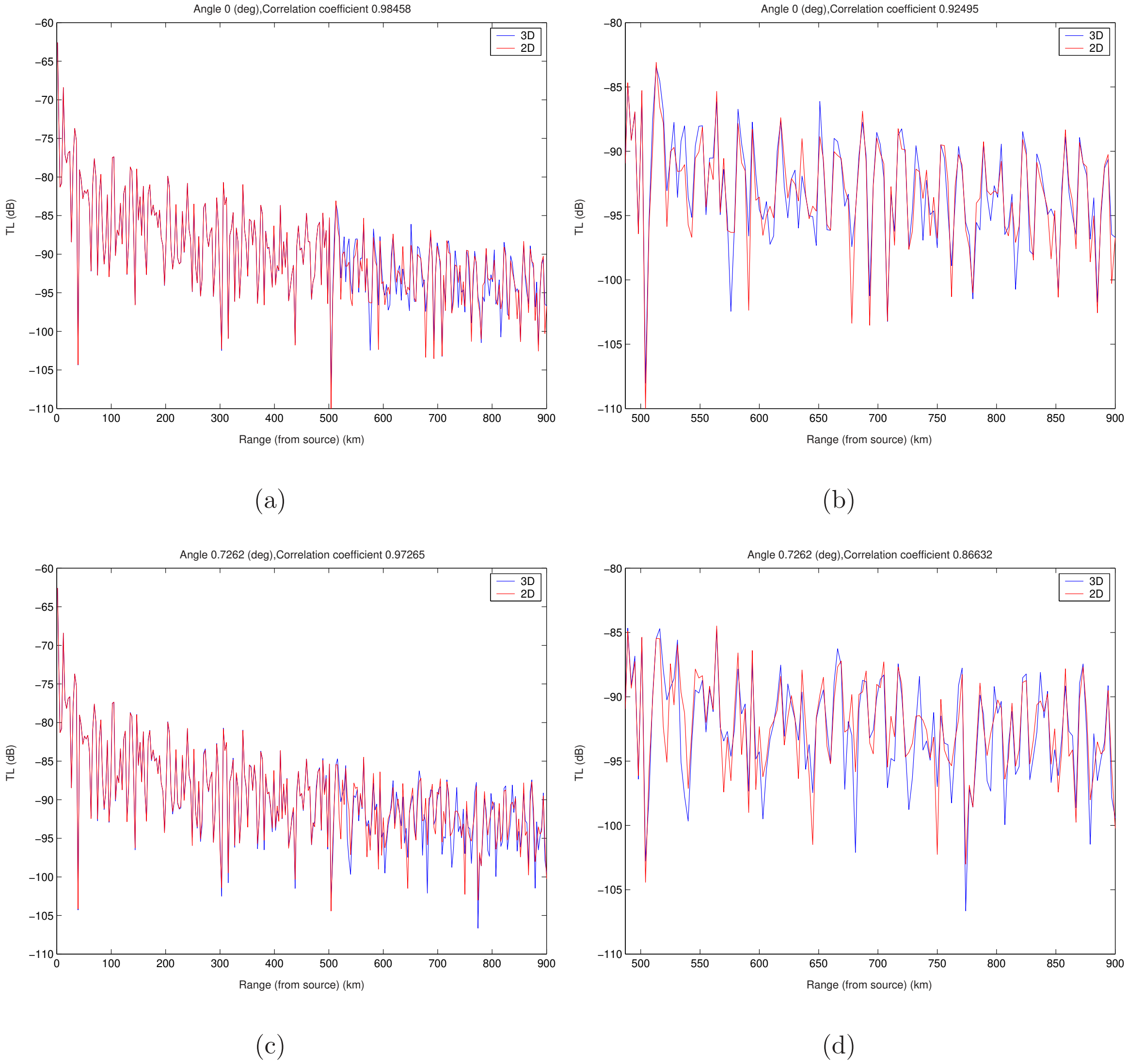

(a) (b)

(c) (d)

Figure 6-23: Transmission loss at depth 750 m, (a) along $\frac{0}{4}\phi'_c$, from the source, (b) along $\frac{0}{4}\phi'_c$, from the seamount; (c) along $\frac{1}{4}\phi'_c$, from the source, (d) along $\frac{1}{4}\phi'_c$, from the seamount. (The azimuthal angle is with respect to the source.)

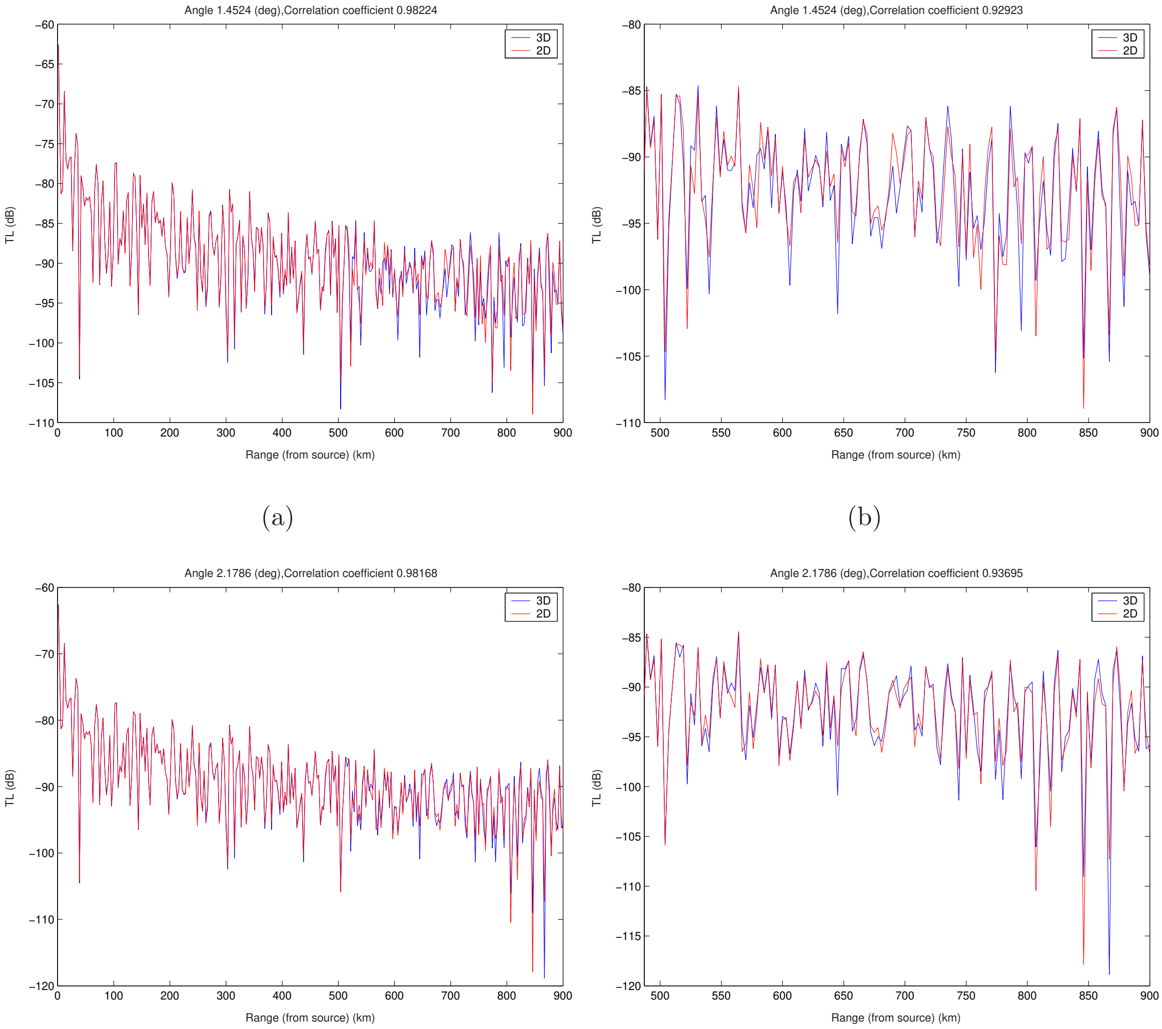

(a) (b)

(c) (d)

Figure 6-24: Transmission loss at depth 750 m, (a) along $\frac{2}{4}\phi'_c$, from the source, (b) along $\frac{2}{4}\phi'_c$, from the seamount; (c) along $\frac{3}{4}\phi'_c$, from the source, (d) along $\frac{3}{4}\phi'_c$, from the seamount. (The azimuthal angle is with respect to the source.)

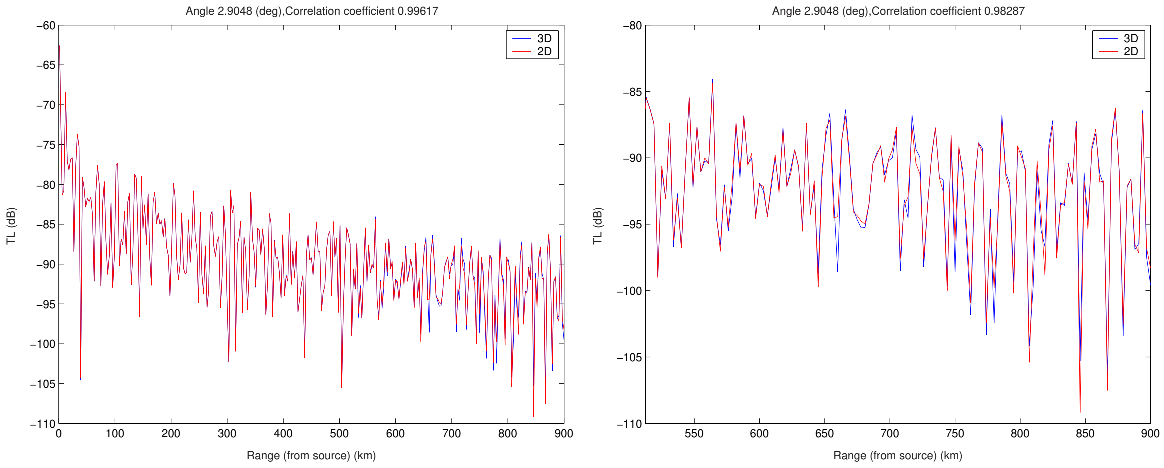

(a) (b)

Figure 6-25: Transmission loss at depth 750 m, (a) along $\frac{4}{4}\phi_c'$, from the source, (b) along $\frac{4}{4}\phi_c'$, from the seamount. (The azimuthal angle is with respect to the source.)

6.3.2 The Runtime of the 3D Model

For the Kermit Seamount problem with a source of frequency 75 Hz, with $n = 8$, i.e. 256 rings, and 150 modes involved in mode coupling, the runtime for computing the coupling coefficients is 203.4 hours, approximately 8.5 days, and the runtime for computing the field is 16.7 hours, approximately 0.7 days, on a single PC (1.7 GHz P4 with 256 MB memory).

6.4 Conclusions

From the results of our three-dimensional spectral coupled mode model, we come to the following conclusions:

1) A perturbation zone forms behind the Kermit Seamount.

2) Above the top of the Kermit Seamount, the results of the $N\times 2$D model and of our 3D model show good agreement.

Chapter 7

Conclusions and Future Work

7.1 Conclusions

Despite the great achievements obtained with the parabolic equation (PE) method, the coupled normal mode method remains a very efficient, simple and accurate method to solve range-dependent problems. The PE method is suitable only for treating the underwater acoustic propagation problems in cases where no significant backscattered field is expected. In addition, the PE method has inherent phase errors, which limit its applicability to a certain range of angles around the main propagation direction. Compared with the PE method, the normal mode method aims at solving the full-wave Helmholtz equation, so that it is applicable to cases where the backscattering is not negligible; in addition, it is free of angular limitations.

As we know, among functions $J_m(x)$, $Y_m(x)$, $H_m^{(1)}(x)$ and $H_m^{(2)}(x)$, the only pair of functions that preserves linear independence (numerically) is $J_m(x)$ and $H_m^{(1)}(x)$. In Eskenazi's approach [6], normalized Bessel and Hankel functions $\hat{J}_m(x)$ and $\hat{H}_m^{(1)}(x)$ are used as the two linearly independent solutions to the Bessel equation; however, no asymptotic forms of the normalized Bessel and Hankel functions are used in that approach. As shown in this thesis, asymptotic forms of normalized Bessel and Hankel functions for small and large arguments make the model applicable for relatively high frequencies and large-scale seamounts. From the convergence analysis of the azimuthal series, we know that the number of azimuthal modes (M) leading to convergence depends on the product of the wavenumber and the radius of the base of the seamount. When the frequency is high, or the radius of the base of the seamount is large, it is required to compute Bessel and Hankel functions of high orders. However, overflow and underflow problems arise when we compute high-order Bessel and Hankel functions. Appropriate normalization of these functions of high orders leads to finite values. For example, to compute Bessel and Hankel functions of order $m = 100$, together with the argument $x = 1$, MATLAB gives $J_m(x) \approx 8.431828789626675e-189$, $H_m^{(1)}(x) \approx 0-3.775287810110529e+185i$ and $J_m(x)H_m^{(1)}(x) \approx 0-0.00318325804464i$. The small argument approximation

$$J_m(x)H_m^{(1)}(x) \sim -\frac{i}{m\pi},\ m \gg |x|\,, \tag{7.1}$$

gives the approximate result $J_m(x)H_m^{(1)}(x) \approx 0 - 0.00318309886184i$. However, with the order $m = 1000$ and the argument $x = 1$, Mablab gives $J_m(x) = 0$, $H_m^{(1)}(x) = \text{Inf}$ and $J_m(x)H_m^{(1)}(x) = \text{NaN}$. In contrast, the small argument approximation (7.1) still gives a finite value for the product of $J_m(x)$ and $H_m^{(1)}(x)$, which is $J_m(x)H_m^{(1)}(x) \approx 0 - 3.183098861837907e - 004i$.

Superposition representation of the external field with respect to the seamount improves efficiency. In the previous works [6, 20], the number of azimuthal modes leading to convergence depends on the distances between the source and the axle of the conical seamount or cylindrical island. While in our approach as demonstrated in this thesis, that number depends on the radius of the base of the conical seamount or the cylindrical island. Thus, with all the other parameters the same, the farther the source is away from the conical seamount or the cylindrical island, the more computational effort is saved in our model. In other words, the larger the ratio r_s/r_I is, the more efficient our model is over the previous models [3, 6, 20].

Our three-dimensional spectral mode approach is applied to investigate the scattering from a cylindrical island. By using the superposition method, our approach is much more efficient than Athanassoulis and Propathopoulos's approach without sacrificing accuracy. By using normalized Bessel and Hankel functions as well as their asymptotic forms for large and small arguments, our approach eliminates the overflow and underflow problems which exist in Athanassoulis and Propathopoulos's approach. Thus, our approach is more stable than Athanassoulis and Propathopoulos's approach. Therefore, our approach is applicable to high-frequency and large-scale problems.

The $N\times 2\text{D}$ approach introduced first by Perkins and Baer [16] is efficient in solving three-dimensional propagation problems. However, as illustrated by numerical examples in this thesis, we find that the $N\times 2\text{D}$ approach is a good approximation of the true three-dimensional approach only under the condition that the three-dimensional effects are weak. The physical interpretation is that in the $N\times 2\text{D}$ model, only in-plane scattering is involved; however, in the true 3D model, both in-plane and out-of-plane scattering are involved. Therefore, when the azimuthal variation is weak, the in-plane scattering dominates and the out-of-plane scattering is negligible. As a result, the $N\times 2\text{D}$ model is a good approximation of the 3D model. Otherwise, if the three-dimensional effects are significant and the out-of-plane scattering is not negligible, the $N\times 2\text{D}$ model is not a good approximation of the 3D model. Factors such as bottom types and height of a seamount contribute to three-dimensional effects.

As illustrated in this thesis, the propagation of a mode is affected by the seamount only when the oscillatory region of the mode shape is above the top of the seamount, resulting in mode coupling and excitation. Otherwise, a mode will propagate past the seamount without being affected and no other modes will be excited due to the incidence of this mode.

As we know, in long-range, deep-water propagation problems, the acoustic field is not sensitive to the acoustic properties of the seabed. As a result, we may ignore the shear wave in the seamount in a deep-water waveguide. This statement is verified by a numerical example in this thesis.

It is shown in this thesis that the use of random step sizes in representing smoothly varying bathymetry can weaken the artificial backscattering beams. The use of uniform stair steps to represent smoothly varying bathymetry in ocean waveguides is common to most numerical solution techniques (parabolic equations, coupled modes, finite differences) employed today to solve range-dependent propagation and scattering problems. The disadvantage of this scheme is that it may introduce artificial beams in the backscattered field if the number of stairs/rings is not large enough. To solve this problem, we may either use more stairs/rings or use the technique of random step sizes in representing the bathymetry. As of today few published models apply the technique of random step sizes.

Our three-dimensional spectral coupled mode model is applied to the Kermit Seamount problem with bottom topography and sound velocity profiles obtained from the 2004 BASSEX experiment. From the results we see that a perturbation zone forms behind the Kermit Seamount. In addition, the results of the $N\times 2$D model and our 3D model agree well above the top of the Kermit Seamount.

7.2 Future Work

For the problem of three-dimensional propagation and scattering around a conical seamount, the solutions require not only precise mathematical representation, but also extensive computation. Although all the work in this thesis, including numerical examples and problems with realistic environment data, is done on a single PC (1.7 GHz P4 with 256 MB memory), it is impractical to address high-frequency, large-scale seamount problems because of the slow computation speed and limited memory at the current stage.

In addition to solving large-scale ocean acoustic problems on supercomputers, making improvements to the model is important. In the current model, the convergence rate concerning the number of the rings is too slow. Although the random step-size scheme helps to solve this problem to some extend, the improvement is far from satisfactory.

Appendix A

The Laplace Operator in Cartisian Coordinates, Cylindrical Polar Coordinates and Spherical Coordinates

The Laplace operator $\nabla^2 = \nabla \cdot \nabla$ takes different forms in Cartisian Coordinates, cylindrical polar coordinates and spherical coordinates.

A.1 The Laplace Operator in Cartisian Coordinates

In Cartisian coordinates (x, y, z), the form of the Laplace operator can be obtained by

$$\begin{aligned} \nabla^2 &= \nabla \cdot \nabla \\ &= \left(\frac{\partial}{\partial x}, \frac{\partial}{\partial y}, \frac{\partial}{\partial z}\right) \cdot \left(\frac{\partial}{\partial x}, \frac{\partial}{\partial y}, \frac{\partial}{\partial z}\right) \\ &= \frac{\partial^2}{\partial x^2} + \frac{\partial^2}{\partial y^2} + \frac{\partial^2}{\partial z^2}. \end{aligned} \tag{A.1}$$

A.2 The Laplace Operator in Cylindrical Polar Coordinates

In cylindrical polar coordinates (r, z, ϕ), we have [9, p. 1043]

$$\begin{aligned} \nabla &= \hat{e}_r \frac{\partial}{\partial r} + \hat{e}_z \frac{\partial}{\partial z} + \hat{e}_\phi \frac{1}{r} \frac{\partial}{\partial \phi} \\ &= \left(\frac{\partial}{\partial r}, \frac{\partial}{\partial z}, \frac{1}{r} \frac{\partial}{\partial \phi} \right), \end{aligned} \tag{A.2}$$

and the divergence of a vector $\vec{v} = (v_r, v_z, v_\phi)$ is [9, p. 1043]

$$\nabla \cdot \vec{v} = \frac{1}{r} \frac{\partial}{\partial r} (r v_r) + \frac{\partial v_z}{\partial z} + \frac{1}{r} \frac{\partial v_\phi}{\partial \phi}. \tag{A.3}$$

With Eqs. (A.2) and (A.3), we obtain the expression for the Laplace operator in cylindrical polar coordinates,

$$\begin{aligned} \nabla^2 &= \nabla \cdot \nabla \\ &= \nabla \cdot \left(\frac{\partial}{\partial r}, \frac{\partial}{\partial z}, \frac{1}{r} \frac{\partial}{\partial \phi} \right) \\ &= \frac{1}{r} \frac{\partial}{\partial r} \left(r \frac{\partial}{\partial r} \right) + \frac{\partial}{\partial z} \left(\frac{\partial}{\partial z} \right) + \frac{1}{r} \frac{\partial}{\partial \phi} \left(\frac{1}{r} \frac{\partial}{\partial \phi} \right) \\ &= \frac{1}{r} \frac{\partial}{\partial r} \left(r \frac{\partial}{\partial r} \right) + \frac{\partial^2}{\partial z^2} + \frac{1}{r^2} \frac{\partial^2}{\partial \phi^2} \qquad \text{(A.4)} \\ & \text{or further} \\ &= \frac{\partial^2}{\partial r^2} + \frac{1}{r} \frac{\partial}{\partial r} + \frac{\partial^2}{\partial z^2} + \frac{1}{r^2} \frac{\partial^2}{\partial \phi^2}. \qquad \text{(A.5)} \end{aligned}$$

A.3 The Laplace Operator in Spherical Coordinates

In spherical coordinates (r, θ, ϕ), we have [9, p. 1043]

$$\nabla = \hat{e}_r \frac{\partial}{\partial r} + \hat{e}_\theta \frac{1}{r} \frac{\partial}{\partial \theta} + \hat{e}_\phi \frac{1}{r \sin\theta} \frac{\partial}{\partial \phi}, \tag{A.6}$$

and the divergence of a vector $\vec{v} = (v_r, v_\theta, v_\phi)$ is [9, p. 1043]

$$\nabla \cdot \vec{v} = \frac{1}{r^2}\left[\frac{\partial}{\partial r}\left(r^2 v_r\right)\right] + \frac{1}{r\sin\theta}\left[\frac{\partial}{\partial\theta}\left(\sin\theta v_\theta\right)\right] + \frac{1}{r\sin\theta}\frac{\partial v_\phi}{\partial\phi}. \tag{A.7}$$

With Eqs. (A.6) and (A.7), we obtain the expression for the Laplace operator in spherical coordinates,

$$\begin{aligned}
\nabla^2 &= \nabla\cdot\nabla \\
&= \nabla\cdot\left(\frac{\partial}{\partial r}, \frac{1}{r}\frac{\partial}{\partial\theta}, \frac{1}{r\sin\theta}\frac{\partial}{\partial\phi}\right) \\
&= \frac{1}{r^2}\left[\frac{\partial}{\partial r}\left(r^2\frac{\partial}{\partial r}\right)\right] + \frac{1}{r\sin\theta}\left[\frac{\partial}{\partial\theta}\left(\sin\theta\frac{1}{r}\frac{\partial}{\partial\theta}\right)\right] + \frac{1}{r\sin\theta}\frac{\partial}{\partial\phi}\left(\frac{1}{r\sin\theta}\frac{\partial}{\partial\phi}\right) \\
&= \frac{1}{r^2}\frac{\partial}{\partial r}\left(r^2\frac{\partial}{\partial r}\right) + \frac{1}{r^2\sin\theta}\frac{\partial}{\partial\theta}\left(\sin\theta\frac{\partial}{\partial\theta}\right) + \frac{1}{r^2\sin^2\theta}\frac{\partial^2}{\partial\phi^2}.
\end{aligned} \tag{A.8}$$

Appendix B

The Normal Mode Solution to the Two-Dimensional Helmholtz Equation

In this section, solutions to the two-dimensional Helmholtz equation will be given, either for two-dimensional problems with a line source in plane geometry, or for two-dimensional problems with a point source in cylindrical geometry.

B.1 The Normal Mode Solution to the Two-Dimensional Helmholtz Equation with a Line Source in Plane Geometry [12]

From Section 2.1.1, the two-dimensional Helmholtz equation with a line source in plane geometry, in Cartisian coordinates (x, z), takes the form

$$\frac{\partial^2 p}{\partial x^2} + \rho(z)\frac{\partial}{\partial z}\left(\frac{1}{\rho(z)}\frac{\partial p}{\partial z}\right) + \frac{\omega^2}{c^2(z)}p = -\delta(x)\delta(z - z_0), \tag{B.1}$$

where $(x_0 = 0, z_0)$ is the location of the line source.

We seek a solution to Eq. (B.1) in the form

$$p(x,z)=\sum_{m=1}^{\infty}X_m(x)\Psi_m(z), \tag{B.2}$$

where $\Psi_m(z)$ are eigenfunctions of the depth-dependent equation

$$\rho(z)\frac{\mathrm{d}}{\mathrm{d}z}\left[\frac{1}{\rho(z)}\frac{\mathrm{d}\Psi_m(z)}{\mathrm{d}z}\right]+\left[\frac{\omega^2}{c^2(z)}-k_{xm}^2\right]\Psi_m(z)=0, \tag{B.3}$$

and k_{xm} are eigenvalues of Eq. (B.3). In addition, $\Psi_m(z)$ satisfy the orthonormal relation

$$\int_0^{\infty}\frac{1}{\rho(z)}\Psi_m(z)\Psi_n(z)\mathrm{d}z=\delta_{mn}. \tag{B.4}$$

Substitute Eq. (B.2) into Eq. (B.1), together with Eq. (B.3), we obtain

$$\sum_{m=1}^{\infty}\left(\frac{\mathrm{d}^2X_m}{\mathrm{d}x^2}\Psi_m+k_{xm}^2X_m\Psi_m\right)=-\delta(x)\delta(z-z_0), \tag{B.5}$$

by applying the operator $\int_0^{\infty}\frac{1}{\rho(z)}\Psi_n(z)\,(\cdot)\,\mathrm{d}z$ to Eq. (B.5), then we obtain the equation for $X_n(x)$,

$$\frac{\mathrm{d}^2X_n}{\mathrm{d}x^2}+k_{xn}^2X_n=-\delta(x)\frac{\Psi_n(z_0)}{\rho(z_0)}. \tag{B.6}$$

We may solve the ODE in Eq. (B.6) by means of the endpoint method (refer to Appendix C). Rewrite Eq. (B.6) in the following form,

$$\frac{\rho(z_0)}{\Psi_n(z_0)}\frac{\mathrm{d}^2X_n}{\mathrm{d}x^2}+\frac{\rho(z_0)}{\Psi_n(z_0)}k_{xn}^2X_n=-\delta(x), \tag{B.7}$$

thus we have

$$P_0(x)=\frac{\rho(z_0)}{\Psi_n(z_0)},\ P_1(x)=0,\ P_2(x)=\frac{\rho(z_0)}{\Psi_n(z_0)}k_{xn}^2,$$

$$x_0=0,$$

and

$$\begin{aligned}
&u_a(x) = e^{-ik_{xn}x},\ u_b(x) = e^{ik_{xn}x},\\
&W(x_0) = \begin{vmatrix} u_a(x_0) & u_b(x_0) \\ u_a'(x_0) & u_b'(x_0) \end{vmatrix} = \begin{vmatrix} 1 & 1 \\ -ik_{xn} & ik_{xn} \end{vmatrix} = 2ik_{xn},\\
&C = P_0(x_0)W(x_0) = \frac{\rho(z_0)}{\Psi_n(z_0)}2ik_{xn}.
\end{aligned}$$

So we obtain the solution to Eq. (B.6):

- for $x < 0$,

$$\begin{aligned}
X_n(x) &= -\frac{1}{C}u_a(x)u_b(x_0) \\
&= -\frac{\Psi_n(z_0)}{\rho(z_0)}\frac{1}{2ik_{xn}}e^{-ik_{xn}x};\ \text{and}
\end{aligned} \tag{B.8}$$

- for $x > 0$,

$$\begin{aligned}
X_n(x) &= -\frac{1}{C}u_a(x_0)u_b(x) \\
&= -\frac{\Psi_n(z_0)}{\rho(z_0)}\frac{1}{2ik_{xn}}e^{ik_{xn}x}.
\end{aligned} \tag{B.9}$$

We may rewrite solutions (B.8) and (B.9) into a uniform solution:

$$X_n(x) = \frac{i}{2\rho(z_0)}\Psi_n(z_0)\frac{e^{ik_{xn}|x|}}{k_{xn}}. \tag{B.10}$$

By substituting Eq. (B.10) into Eq. (B.2), we reach the solution to Eq. (B.1), i.e., the two-dimensional Helmholtz equation with a line source in plane geometry,

$$p(x,z) = \frac{i}{2\rho(z_0)}\sum_{m=1}^{\infty}\Psi_m(z_0)\Psi_m(z)\frac{e^{ik_{xm}|x|}}{k_{xm}}. \tag{B.11}$$

B.2 The Normal Mode Solution to the Two-Dimensional Helmholtz Equation with a Point Source in Cylindrical Geometry [12]

From Section 2.1.2, the two-dimensional Helmholtz equation with a point source in cylindrical geometry, in cylindrical coordinates (r, z), takes the form

$$\frac{1}{r}\frac{\partial}{\partial r}\left(r\frac{\partial p}{\partial r}\right) + \rho(z)\frac{\partial}{\partial z}\left(\frac{1}{\rho(z)}\frac{\partial p}{\partial z}\right) + \frac{\omega^2}{c^2(z)}p = -\frac{1}{2\pi}\frac{\delta(r)}{r}\delta(z - z_0), \tag{B.12}$$

where $(r_0 = 0, z_0)$ is the location of the point source.

We seek a solution to Eq. (B.12) in the form

$$p(r, z) = \sum_{m=1}^{\infty} R_m(r)\Psi_m(z), \tag{B.13}$$

where $\Psi_m(z)$ are eigenfunctions of the depth-dependent equation

$$\rho(z)\frac{\mathrm{d}}{\mathrm{d}z}\left[\frac{1}{\rho(z)}\frac{\mathrm{d}\Psi_m(z)}{\mathrm{d}z}\right] + \left[\frac{\omega^2}{c^2(z)} - k_{rm}^2\right]\Psi_m(z) = 0, \tag{B.14}$$

and k_{rm} are eigenvalues of Eq. (B.14).

By substituting Eq. (B.13) into Eq. (B.12), together with Eq. (B.14), we obtain

$$\sum_{m=1}^{\infty}\left[\frac{1}{r}\frac{\mathrm{d}}{\mathrm{d}r}\left(r\frac{\mathrm{d}R_m}{\mathrm{d}r}\right) + k_{rm}^2 R_m\right]\Psi_m = -\frac{1}{2\pi}\frac{\delta(r)}{r}\delta(z - z_0), \tag{B.15}$$

and by applying the operator $\int_0^{\infty} \frac{1}{\rho(z)}\Psi_n(z)\,(\cdot)\,\mathrm{d}z$ to Eq. (B.15), we obtain the equation for $R_n(r)$,

$$\frac{1}{r}\frac{\mathrm{d}}{\mathrm{d}r}\left(r\frac{\mathrm{d}R_n}{\mathrm{d}r}\right) + k_{rn}^2 R_n = -\frac{1}{2\pi}\frac{\delta(r)}{r}\frac{1}{\rho(z_0)}\Psi_n(z_0), \tag{B.16}$$

which is a 0th-order Bessel equation. We know that the solutions to an nth-order homogeneous Bessel equation

$$\frac{1}{r}\frac{\mathrm{d}}{\mathrm{d}r}\left(r\frac{\mathrm{d}R}{\mathrm{d}r}\right) + \left(k_r^2 - \frac{n^2}{r^2}\right)R = 0 \tag{B.17}$$

are any pair of $H_n^{(1)}(k_r r)$, $H_n^{(2)}(k_r r)$, $J_n(k_r r)$, and $Y_n(k_r r)$.

We may solve the inhomogeneous Bessel equation in Eq. (B.16) by means of the endpoint method (refer to Appendix C). Denote

$$A \equiv \frac{\Psi_n(z_0)}{2\pi\rho(z_0)}, \tag{B.18}$$

and rewrite Eq. (B.16) as

$$\frac{\mathrm{d}^2 R_n}{\mathrm{d}r^2} + \frac{1}{r}\frac{\mathrm{d}R_n}{\mathrm{d}r} + k_{rn}^2 R_n = -A\frac{\delta(r)}{r},$$

or,

$$\frac{r}{A}\frac{\mathrm{d}^2 R_n}{\mathrm{d}r^2} + \frac{1}{A}\frac{\mathrm{d}R_n}{\mathrm{d}r} + \frac{r}{A}k_{rn}^2 R_n = -\delta(r), \tag{B.19}$$

then we have

$$\begin{aligned}
&P_0(r) = \frac{r}{A},\ P_1(r) = \frac{1}{A},\ P_2(r) = \frac{r}{A}k_{rn}^2,\\
&r_0 = 0,
\end{aligned}$$

and

$$u_a(r) = J_0(k_{rn} r),\ u_b(r) = H_0^{(1)}(k_{rn} r).$$

Since

$$\begin{aligned}
W\left[J_n(z), H_n^{(1)}(z)\right] &= W\left[J_n(z), J_n(z) + iY_n(z)\right]\\
&= \cancelto{0}{W\left[J_n(z), J_n(z)\right]} + W\left[J_n(z), iY_n(z)\right]\\
&= iW\left[J_n(z), Y_n(z)\right]\\
&= i\frac{2}{\pi z},
\end{aligned}$$

we have

$$
\begin{aligned}
W\left[u_a(r_0), u_b(r_0)\right] &= \begin{vmatrix} J_0\left(k_{rn}r_0\right) & H_0^{(1)}\left(k_{rn}r_0\right) \\ \frac{\mathrm{d}J_0}{\mathrm{d}r}\left(k_{rn}r_0\right) & \frac{\mathrm{d}H_0^{(1)}}{\mathrm{d}r}\left(k_{rn}r_0\right) \end{vmatrix} \\
&= k_{rn} \begin{vmatrix} J_0\left(k_{rn}r_0\right) & H_0^{(1)}\left(k_{rn}r_0\right) \\ \frac{\mathrm{d}J_0}{\mathrm{d}(k_{rn}r)}\left(k_{rn}r_0\right) & \frac{\mathrm{d}H_0^{(1)}}{\mathrm{d}(k_{rn}r)}\left(k_{rn}r_0\right) \end{vmatrix} \\
&= k_{rn} W\left[J_0(k_{rn}r_0), H_0^{(1)}(k_{rn}r_0)\right] \\
&= \cancel{k_{rn}} i \frac{2}{\pi \cancel{k_{rn}} r_0} \\
&= \frac{2i}{\pi r_0},
\end{aligned}
$$

and thus

$$
C = P_0(r_0)W(r_0) = \frac{\cancel{r_0}}{A}\frac{2i}{\pi \cancel{r_0}} = \frac{1}{A}\frac{2i}{\pi}. \tag{B.20}
$$

So we obtain the solution to Eq. (B.16),

$$
\begin{aligned}
R_n(r) &= \Gamma_>(r, r_0) \\
&= -\frac{1}{C} u_a(r_0) u_b(r) \\
&= -A\frac{\pi}{2i}\cancelto{1}{J_0(0)} H_0^{(1)}(k_{rn}r) \\
&\quad \text{with Eq. (B.18)} \\
&= -\frac{\Psi_n(z_0)}{2\pi\rho(z_0)}\frac{\pi}{2i} H_0^{(1)}(k_{rn}r) \\
&= \frac{i}{4}\frac{\Psi_n(z_0)}{\rho(z_0)} H_0^{(1)}(k_{rn}r).
\end{aligned} \tag{B.21}
$$

By substituting Eq. (B.21) into Eq. (B.13), we reach the solution to Eq. (B.12), i.e., the two-dimensional Helmholtz equation with a point source in cylindrical geometry,

$$
p(r, z) = \frac{i}{4\rho(z_0)} \sum_{m=1}^{\infty} \Psi_m(z_0)\Psi_m(z) H_0^{(1)}(k_{rm}r). \tag{B.22}
$$

Appendix C

The Endpoint Method

The endpoint method [8, p. 83] is a powerful method to construct the one-dimensional Green's function $\Gamma(x, x_0)$ which satisfies

$$P_0(x)\frac{\mathrm{d}^2\Gamma(x,x_0)}{\mathrm{d}x^2} + P_1(x)\frac{\mathrm{d}\Gamma(x,x_0)}{\mathrm{d}x} + P_2(x)\Gamma(x,x_0) = -\delta(x-x_0), \tag{C.1}$$

on the interval $a \le x \le b$ and homogeneous boundary conditions or the Sommerfeld radiation condition at the two ends $x = a$ and $x = b$. The Green's function $\Gamma(x, x_0)$ is constructed from linearly independent solutions $u_a(x)$ and $u_b(x)$ of the homogeneous version of Eq. (C.1) which satisfy the boundary conditions at $x = a$ and $x = b$, respectively. The solution to Eq. (C.1) is

$$\Gamma(x,x_0) = \begin{cases} \Gamma_<(x,x_0) = -\frac{1}{C}u_a(x)u_b(x_0), & a \le x \le x_0; \text{ and} \\ \Gamma_>(x,x_0) = -\frac{1}{C}u_a(x_0)u_b(x), & x_0 \le x \le b, \end{cases} \tag{C.2}$$

where

$$C = P_0(x_0)W(x_0),$$

and the Wronskian is

$$W(x_0) = \begin{vmatrix} u_a(x_0) & u_b(x_0) \\ u_a'(x_0) & u_b'(x_0) \end{vmatrix} = u_a(x_0)u_b'(x_0) - u_a'(x_0)u_b(x_0).$$

Next, we will show briefly the derivation of Eq. (C.2).

We write the solution to Eq. (C.1) in the form

$$\Gamma(x,x_0)=\begin{cases} Au_a(x)u_b(x_0), & a\le x\le x_0;\ \text{and}\\ Au_a(x_0)u_b(x), & x_0\le x\le b.\end{cases} \tag{C.3}$$

$\Gamma(x,x_0)$ satisfies the boundary conditions at the two ends $x=a$ and $x=b$, and $\Gamma(x,x_0)$ is continuous at $x=x_0$.

Integrate Eq. (C.1) from $x_0-\epsilon$ to $x_0+\epsilon$, with $\epsilon>0$, and let $\epsilon\to 0$,

$$\begin{aligned}&\lim_{\epsilon\to 0}\int\limits_{x_0-\epsilon}^{x_0+\epsilon} P_0(x)\frac{\mathrm{d}^2\Gamma(x,x_0)}{\mathrm{d}x^2}\mathrm{d}x+\lim_{\epsilon\to 0}\int\limits_{x_0-\epsilon}^{x_0+\epsilon} P_1(x)\frac{\mathrm{d}\Gamma(x,x_0)}{\mathrm{d}x}\mathrm{d}x+\lim_{\epsilon\to 0}\int\limits_{x_0-\epsilon}^{x_0+\epsilon} P_2(x)\Gamma(x,x_0)\mathrm{d}x\\ =&-\lim_{\epsilon\to 0}\int\limits_{x_0-\epsilon}^{x_0+\epsilon}\delta(x-x_0)\mathrm{d}x.\end{aligned} \tag{C.4}$$

Because $\Gamma(x,x_0)$ is continuous at $x=x_0$, so both the second term and the third term on the left hand side of Eq. (C.4) are zero[1], and

$$\begin{aligned}\lim_{\epsilon\to 0}\int\limits_{x_0-\epsilon}^{x_0+\epsilon} P_0(x)\frac{\mathrm{d}^2\Gamma(x,x_0)}{\mathrm{d}x^2}\mathrm{d}x =&P_0(x_0)\lim_{\epsilon\to 0}\left[\frac{\mathrm{d}\Gamma}{\mathrm{d}x}(x_0+\epsilon,x_0)-\frac{\mathrm{d}\Gamma}{\mathrm{d}x}(x_0-\epsilon,x_0)\right]\\ &\text{with Eq. (C.3)}\\ =&P_0(x_0)\lim_{\epsilon\to 0}\left[Au_a(x_0)u_b'(x_0+\epsilon)-Au_a'(x_0-\epsilon)u_b(x_0)\right]\\ =&P_0(x_0)\left[Au_a(x_0)u_b'(x_0)-Au_a'(x_0)u_b(x_0)\right].\\ =&P_0(x_0)AW(x_0),\end{aligned}$$

where

$$W(x_0)=\begin{vmatrix} u_a(x_0) & u_b(x_0)\\ u_a'(x_0) & u_b'(x_0)\end{vmatrix}. \tag{C.5}$$

---

[1] $\lim_{\epsilon\to 0}\int_{x_0-\epsilon}^{x_0+\epsilon} P_1(x)\frac{\mathrm{d}\Gamma(x,x_0)}{\mathrm{d}x}\mathrm{d}x=P_1(x_0)\lim_{\epsilon\to 0}\left[\Gamma(x_0+\epsilon,x_0)-\Gamma(x_0-\epsilon,x_0)\right]=0$, and $\lim_{\epsilon\to 0}\int_{x_0-\epsilon}^{x_0+\epsilon} P_2(x)\Gamma(x,x_0)\mathrm{d}x=P_2(x_0)\lim_{\epsilon\to 0}\int_{x_0-\epsilon}^{x_0+\epsilon}\Gamma(x,x_0)=0$.

So, Eq. (C.4) yields

$$P_0(x_0)AW(x_0) = -1,$$

from which we obtain

$$A = -\frac{1}{P_0(x_0)W(x_0)}. \tag{C.6}$$

By substituting Eq. (C.6) into Eq. (C.3), we obtain the Green's function as expressed in Eq. (C.2).

Appendix D

Properties of Bessel Functions

Bessel functions are solutions to Bessel equations. In this section we will give a brief review of the properties of Bessel functions [21].

D.1 The Bessel Equation and Solutions

The standard form of a Bessel equation of order ν is [9, p. 900]

$$\frac{\mathrm{d}^2 y}{\mathrm{d}x^2} + \frac{1}{x}\frac{\mathrm{d}y}{\mathrm{d}x} + \left(1 - \frac{\nu^2}{x^2}\right) y = 0, \tag{D.1}$$

and its solutions are Bessel functions of the first and second kind, $J_\nu(x)$ and $Y_\nu(x)$ (Y_ν is also called the Neuman function); and Hankel functions of the first and second kind, $H_\nu^{(1)}(x)$ and $H_\nu^{(2)}(x)$.

In Acoustics, a more frequently used form of an nth-order Bessel equation is

$$\frac{\mathrm{d}^2 R}{\mathrm{d}r^2} + \frac{1}{r}\frac{\mathrm{d}R}{\mathrm{d}r} + \left(k_r^2 - \frac{n^2}{r^2}\right) R = 0. \tag{D.2}$$

Eq. (D.2) can be easily transformed into the form in Eq. (D.1). Let $z = k_r r$, then Eq. (D.2) becomes

$$k_r^2 \frac{\mathrm{d}^2 R}{\mathrm{d}z^2} + k_r \frac{1}{z} k_r \frac{\mathrm{d}R}{\mathrm{d}z} + \left(k_r^2 - k_r^2 \frac{n^2}{z^2}\right) R = 0, \tag{D.3}$$

or,

$$\frac{\mathrm{d}^2R}{\mathrm{d}z^2}+\frac{1}{z}\frac{\mathrm{d}R}{\mathrm{d}z}+\left(1-\frac{n^2}{z^2}\right)R=0. \tag{D.4}$$

From the above, we see that Eq. (D.2) is indeed an nth-order Bessel equation with argument $z=k_rr$, thus the solutions to Eq. (D.2) are $J_n(k_rr)$, $Y_n(k_rr)$, $H_n^{(1)}(k_rr)$ and $H_n^{(2)}(k_rr)$. The general solution to Eq. (D.2) is composed of two linearly independent functions with arbitrary constants C_1 and C_2, such as

$$R(r)=C_1H_n^{(1)}(k_rr)+C_2H_n^{(2)}(k_rr). \tag{D.5}$$

D.2 Asymptotic Forms of Bessel Functions

D.2.1 Large Arguments

Bessel functions of the first and second kind, $J_n(k_rr)$ and $Y_n(k_rr)$, are called the standing wave solutions of Eq. (D.2), because their asymptotic behaviors (as $x\to\infty$) are given by [21, p. 118]

$$J_n(x)\sim\sqrt{\frac{2}{\pi x}}\cos\left(x-n\frac{\pi}{2}-\frac{\pi}{4}\right), \tag{D.6}$$

and

$$Y_n(x)\sim\sqrt{\frac{2}{\pi x}}\sin\left(x-n\frac{\pi}{2}-\frac{\pi}{4}\right). \tag{D.7}$$

In addition, the asymptotic forms of their derivatives, i.e. $J_n'(x)$ and $Y_n'(x)$, are as below:

$$J_n'(x)\sim-\sqrt{\frac{2}{\pi x}}\sin\left(x-n\frac{\pi}{2}-\frac{\pi}{4}\right), \tag{D.8}$$

and

$$Y_n'(x)\sim\sqrt{\frac{2}{\pi x}}\cos\left(x-n\frac{\pi}{2}-\frac{\pi}{4}\right). \tag{D.9}$$

Hankel functions of the first and second kind, $H_n^{(1)}(k_rr)$ and $H_n^{(2)}(k_rr)$, are called traveling wave solutions of Eq. (D.2), because their asymptotic behaviors (as $x\to\infty$)

are given by[21, p. 118]

$$H_n^{(1)}(x) \sim \sqrt{\frac{2}{\pi x}} e^{i\left(x - n\frac{\pi}{2} - \frac{\pi}{4}\right)}, \tag{D.10}$$

and

$$H_n^{(2)}(x) \sim \sqrt{\frac{2}{\pi x}} e^{-i\left(x - n\frac{\pi}{2} - \frac{\pi}{4}\right)}. \tag{D.11}$$

In addition, the asymptotic forms of their derivatives are as below:

$$H_n^{(1)\prime}(x) \sim i\sqrt{\frac{2}{\pi x}} e^{i\left(x - n\frac{\pi}{2} - \frac{\pi}{4}\right)} = iH_n^{(1)}(x), \tag{D.12}$$

and

$$H_n^{(2)\prime}(x) \sim -i\sqrt{\frac{2}{\pi x}} e^{-i\left(x - n\frac{\pi}{2} - \frac{\pi}{4}\right)} = -iH_n^{(2)}(x). \tag{D.13}$$

D.2.2 Small Arguments

$J_n(x)$

The series representation of $J_n(z)$ is [21, p. 118]

$$J_n(z) = \left(\frac{z}{2}\right)^n \sum_{k=0}^{\infty} \frac{(-1)^k}{k!(n+k)!} \left(\frac{z}{2}\right)^{2k}, \quad |\arg z| < \pi. \tag{D.14}$$

From this series representation we can see that for small arguments, we have

$$\begin{aligned} J_n(x) &= \left(\frac{x}{2}\right)^n \left[\frac{1}{n!} - \frac{1}{(n+1)!}\left(\frac{x}{2}\right)^2 + \cdots\right] \\ &= \frac{1}{n!}\left(\frac{x}{2}\right)^n + O(x^{n+2}), \end{aligned} \tag{D.15}$$

from which we obtain

$$J_n(x) \sim \frac{1}{n!}\left(\frac{x}{2}\right)^n, \text{ for } |x| \to 0, \tag{D.16}$$

or, as $|x| \to 0$:

- $n = 0$,

$$J_0(x) \sim 1, \tag{D.17}$$

and

$$J_0'(x) \sim 0. \tag{D.18}$$

- $n \neq 0$,

$$J_n(x) \sim \frac{1}{n!}\left(\frac{x}{2}\right)^n, \tag{D.19}$$

and

$$\begin{aligned} J_n'(x) &\sim \frac{1}{n!}\frac{1}{2^n} n x^{n-1} \\ &= \frac{1}{2(n-1)!}\left(\frac{x}{2}\right)^{n-1}. \end{aligned} \tag{D.20}$$

Fig. D-1 shows the shapes of $J_n(x)$ for n=0, 1, 5, and 10, from which we can see that as $x \to 0$, $J_0(x) \to 1$ and $J_n(x) \to 0$ as $n \neq 0$.

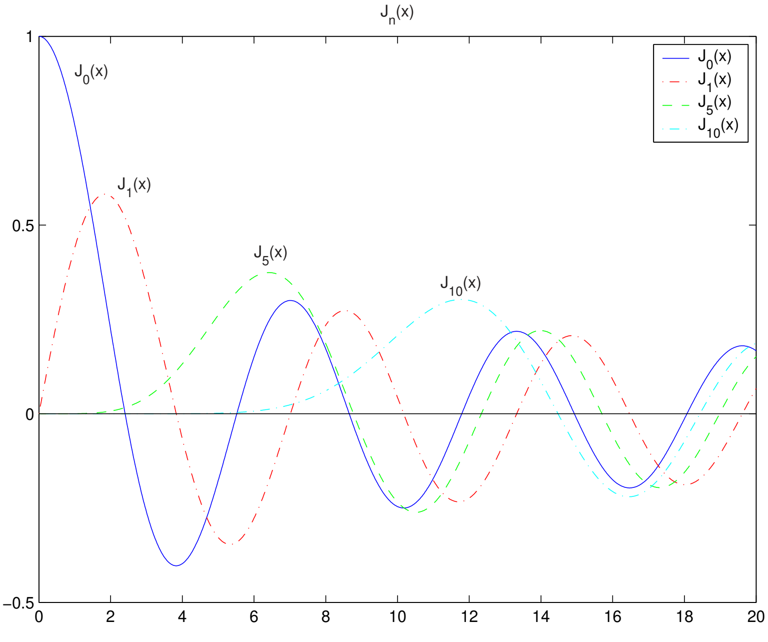

Figure D-1: Bessel functions of the first kind of orders 0, 1, 5 and 10. As $x \to 0$, $J_0(x) \to 1$ and $J_n(x) \to 0$ as $n \neq 0$.

$\boldsymbol{Y_n(x)}$

The small argument approximations of $Y_n(x)$ are [21, p.119]

$$\begin{aligned} Y_0(x) &\sim \frac{2}{\pi}\left[\ln\frac{x}{2}+\gamma\right], && \text{(D.21)}\\ Y_n(x) &\sim -\frac{(n-1)!}{\pi}\left(\frac{2}{x}\right)^n,\ n\neq 0, && \text{(D.22)} \end{aligned}$$

and the small argument approximations of their derivatives are

$$\begin{aligned} Y_0'(x) &\sim \frac{2}{\pi}\frac{2}{x}\frac{1}{2}=\frac{1}{\pi}\frac{2}{x}, && \text{(D.23)}\\ Y_n'(x) &\sim -\frac{(n-1)!}{\pi}n\left(\frac{2}{x}\right)^{n-1}2\left(-\frac{1}{x^2}\right) \\ &= \frac{n!}{\pi}\frac{2^n}{x^{n+1}} \\ &= \frac{n!}{2\pi}\left(\frac{2}{x}\right)^{n+1}. && \text{(D.24)} \end{aligned}$$

In Eq. (D.21), $\gamma = 0.57721\cdots$ is Euler's constant. From Eqs. (D.21) and (D.22) we can see that $x = 0$ is a singular point of $Y_n(x)$. The shapes of $Y_n(x)$ for n=0, 1, 5 and 10 are shown in Fig. D-2, from which we can see that as $x \to 0$, $Y_n(x) \to -\infty$.

$\boldsymbol{H_n^{(1)}(x)}$

For small arguments, we have:

- if $n \neq 0$,

$$\begin{aligned} H_n^{(1)}(x) &= J_n(x)+iY_n(x) \\ &\sim iY_n(x) \\ &\sim -i\frac{(n-1)!}{\pi}\left(\frac{2}{x}\right)^n,\ n\neq 0, && \text{(D.25)} \end{aligned}$$

and

$$H_n^{(1)\prime}(x)\sim iY_n'(x)=\frac{in!}{2\pi}\left(\frac{2}{x}\right)^{n+1},\ n\neq 0. \qquad \text{(D.26)}$$

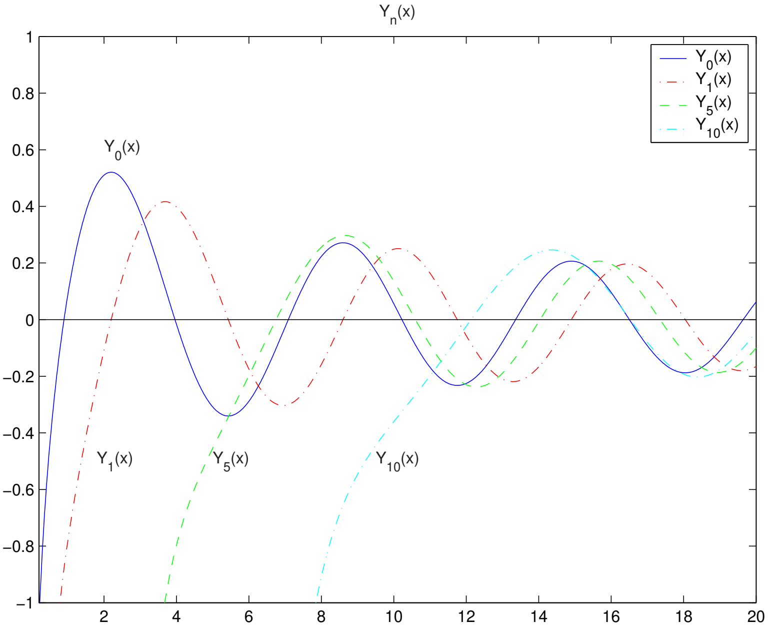

Figure D-2: Bessel functions of the second kind of orders 0, 1, 5 and 10. As $x \to 0$, $Y_n(x) \to -\infty$.

- if $n = 0$,

$$\begin{aligned} H_0^{(1)}(x) &= J_0(x) + iY_0(x) \\ &\sim 1 + iY_0(x) \\ &\sim 1 + i\frac{2}{\pi}\left[\ln\frac{x}{2} + \gamma\right], \end{aligned} \tag{D.27}$$

  and

$$H_0^{(1)\prime}(x) \sim iY_0'(x) = \frac{i}{\pi}\frac{2}{x}. \tag{D.28}$$

$H_n^{(2)}(x)$

For small arguments, we have:

- if $n \neq 0$,

$$\begin{aligned} H_n^{(2)}(x) &= J_n(x) - iY_n(x) \\ &\sim -iY_n(x) \\ &\sim i\frac{(n-1)!}{\pi}\left(\frac{2}{x}\right)^n, \; n \neq 0, \end{aligned} \tag{D.29}$$

and

$$H_n^{(2)\prime}(x) \sim -\frac{i}{2}\frac{n!}{\pi}\left(\frac{2}{x}\right)^{n+1}. \tag{D.30}$$

- if $n = 0$,

$$\begin{aligned} H_0^{(2)}(x) &= J_0(x) - iY_0(x) \\ &\sim 1 - iY_0(x) \\ &\sim 1 - i\frac{2}{\pi}\left[\ln\frac{x}{2} + \gamma\right], \end{aligned} \tag{D.31}$$

and

$$H_0^{(2)\prime}(x) \sim -\frac{i}{\pi}\frac{2}{x}. \tag{D.32}$$

D.3 Negative Orders

The following formulas are useful [21, p. 119],

$$J_{-n}(x) = (-1)^n J_n(x), \tag{D.33}$$

and

$$Y_{-n}(x) = (-1)^n Y_n(x). \tag{D.34}$$

D.4 Recursion Relations for Bessel Functions

Some recursion relations for Bessel functions are [21, p. 121]

$$Z_{n-1}(z) + Z_{n+1}(z) = \frac{2n}{z} Z_n(z), \tag{D.35}$$

$$Z_{n-1}(z) - Z_{n+1}(z) = 2\frac{\mathrm{d}Z_n(z)}{\mathrm{d}z}, \tag{D.36}$$

where Z denotes J, Y, $H^{(1)}$ or $H^{(2)}$.

Another useful recursion relation is

$$Z_{n-1}(z) - \frac{n}{z} Z_n(z) = \frac{\mathrm{d}Z_n(z)}{\mathrm{d}z}, \tag{D.37}$$

which is easily obtained by adding Eqs. (D.35) and (D.36).

D.5 Wronskian Relations for Bessel Functions

Some useful Wronskian relations for Bessel functions are [21, p. 121]

$$W\left[J_n(z), Y_n(z)\right] = \frac{2}{\pi z}, \tag{D.38}$$

$$W\left[H_n^{(1)}(z), H_n^{(2)}(z)\right] = -\frac{4i}{\pi z}, \tag{D.39}$$

where the Wronskian of functions $f(z)$ and $g(z)$ is defined as

$$W\left[f(z), g(z)\right] \equiv \begin{vmatrix} f(z) & g(z) \\ f'(z) & g'(z) \end{vmatrix} = f(z)g'(z) - f'(z)g(z). \tag{D.40}$$

Notes:

1) We notice that the Wronskian of $J_n(z)$ and $Y_n(z)$, or that of $H_n^{(1)}(z)$ and $H_n^{(2)}(z)$, are independent of the order n.

2) It is easy to derive Eq. (D.39) from Eq. (D.38), as shown below,

$$\begin{aligned}W\left[H_n^{(1)}(z), H_n^{(2)}(z)\right] &= \begin{vmatrix} H_n^{(1)} & H_n^{(2)} \\ H_n^{(1)'} & H_n^{(2)'} \end{vmatrix} \\ &= \begin{vmatrix} J_n + iY_n & J_n - iY_n \\ J_n' + iY_n' & J_n' - iY_n' \end{vmatrix} \\ &= 2i\left(J_n' Y_n - J_n Y_n'\right) \\ &= -2iW\left[J_n, Y_n\right] \\ &= -\frac{4i}{\pi z}.\end{aligned}$$

3) Eq. (D.38) is the basic Wronskian relation and may be used to derive other Wronskian relations for $J_n(z)$, $Y_n(z)$, $H_n^{(1)}(z)$ and $H_n^{(2)}(z)$. For example, we may obtain $W\left[J_n(z), H_n^{(1)}(z)\right]$ as below,

$$\begin{aligned}W\left[J_n(z), H_n^{(1)}(z)\right] &= W\left[J_n(z), J_n(z) + iY_n(z)\right] \\ &= W\left[J_n(z), J_n(z)\right] + W\left[J_n(z), iY_n(z)\right] \\ &= iW\left[J_n(z), Y_n(z)\right] \\ &= \frac{2i}{\pi z}. \qquad \text{(D.41)}\end{aligned}$$

4) We can check Eq. (D.39) with asymptotic forms of $H_n^{(1)}(z)$ and $H_n^{(2)}(z)$. For $|z| \to \infty$, we have

$$H_n^{(1)}(z) \sim \sqrt{\frac{2}{\pi z}} e^{i\left(z - n\frac{\pi}{2} - \frac{\pi}{4}\right)}, \qquad \text{(D.42)}$$

$$H_n^{(2)}(z) \sim \sqrt{\frac{2}{\pi z}} e^{-i\left(z - n\frac{\pi}{2} - \frac{\pi}{4}\right)}, \qquad \text{(D.43)}$$

and

$$\frac{\mathrm{d}H_n^{(p)}(z)}{\mathrm{d}z} = H_{n-1}^{(p)}(z) - \frac{n}{z} H_n^{(p)}(z), \; p = 1, 2. \qquad \text{(D.44)}$$

Thus the Wronskian of $H_n^{(1)}(z)$ and $H_n^{(2)}(z)$ for $|z| \to \infty$ is

$$\begin{aligned}
W\left[H_n^{(1)}(z), H_n^{(2)}(z)\right] =& H_n^{(1)}(z)\frac{\mathrm{d}H_n^{(2)}(z)}{\mathrm{d}z} - \frac{\mathrm{d}H_n^{(1)}(z)}{\mathrm{d}z}H_n^{(2)}(z) \\
=& H_n^{(1)}(z)\left[H_{n-1}^{(2)}(z) - \frac{n}{z}H_n^{(2)}(z)\right] - \left[H_{n-1}^{(1)}(z) - \frac{n}{z}H_n^{(1)}(z)\right]H_n^{(2)}(z) \\
=& H_n^{(1)}(z)H_{n-1}^{(2)}(z) - H_{n-1}^{(1)}(z)H_n^{(2)}(z) \\
=& \sqrt{\frac{2}{\pi z}}e^{i\left(z-n\frac{\pi}{2}-\frac{\pi}{4}\right)}\sqrt{\frac{2}{\pi z}}e^{-i\left[z-(n-1)\frac{\pi}{2}-\frac{\pi}{4}\right]} \\
& - \sqrt{\frac{2}{\pi z}}e^{i\left[z-(n-1)\frac{\pi}{2}-\frac{\pi}{4}\right]}\sqrt{\frac{2}{\pi z}}e^{-i\left(z-n\frac{\pi}{2}-\frac{\pi}{4}\right)} \\
=& \frac{2}{\pi z}e^{-i\frac{\pi}{2}} - \frac{2}{\pi z}e^{i\frac{\pi}{2}} \\
=& -\frac{4i}{\pi z}. \qquad \text{(D.45)}
\end{aligned}$$

In the above derivation, we used some properties of the Wronskian. The relations below are useful about the Wronskian. For functions $f_1(x)$, $f_2(x)$ and $f_3(x)$,

- $W\left[f_1(x), f_1(x)\right] = 0$.
- $W\left[f_1(x), f_2(x) + f_3(x)\right] = W\left[f_1(x), f_2(x)\right] + W\left[f_1(x), f_3(x)\right]$.
- $W\left[f_1(x), Cf_2(x)\right] = CW\left[f_1(x), f_2(x)\right]$, where C is a constant.
- $W\left[f_2(x), f_1(x)\right] = -W\left[f_1(x), f_2(x)\right]$.

Appendix E

Linearly Independent Solutions of Bessel Equations for Both Large and Small Arguments

The Bessel equation of order ν takes the form [9, p. 900]

$$\frac{\mathrm{d}^2 y}{\mathrm{d}x^2} + \frac{1}{x}\frac{\mathrm{d}y}{\mathrm{d}x} + \left(1 - \frac{\nu^2}{x^2}\right) y = 0. \tag{E.1}$$

Theoretically, solutions to the Bessel equation in Eq. (E.1) can be any pair of two of the functions $H_\nu^{(1)}(x)$, $H_\nu^{(2)}(x)$, $J_\nu(x)$ and $Y_\nu(x)$. However, as shown below, only one pair can be chosen to remain independence for both large and small arguments [17].

E.1 Linearly Independent Solutions for Large Arguments

Below we will seek linearly independent solutions for large arguments, i.e., for $|x| \gg \nu$ or, $|x| \to \infty$ with ν fixed. Denote $x = a + ib$ ($b > 0$) and assume $b \to \infty$, then we have the asymptotic forms of Hankel functions as

$$\begin{aligned} H_\nu^{(1)}(x) &\sim \sqrt{\frac{2}{\pi x}} e^{i\left(x-\nu\frac{\pi}{2}-\frac{\pi}{4}\right)} \\ &= \sqrt{\frac{2}{\pi x}} e^{i\left(a+ib-\nu\frac{\pi}{2}-\frac{\pi}{4}\right)} \\ &= \sqrt{\frac{2}{\pi x}} e^{i\left(a-\nu\frac{\pi}{2}-\frac{\pi}{4}\right)} e^{-b} \\ &\to 0, \text{ as } b \to \infty, \end{aligned} \tag{E.2}$$

and

$$\begin{aligned} H_\nu^{(2)}(x) &\sim \sqrt{\frac{2}{\pi x}} e^{-i\left(x-\nu\frac{\pi}{2}-\frac{\pi}{4}\right)} \\ &= \sqrt{\frac{2}{\pi x}} e^{-i\left(a-\nu\frac{\pi}{2}-\frac{\pi}{4}\right)} e^{b} \\ &\to \infty, \text{ as } b \to \infty. \end{aligned} \tag{E.3}$$

In wave theory, $H_\nu^{(1)}(x) \to 0$ means an outgoing wave decays exponentially with range, and $H_\nu^{(2)}(x) \to \infty$ means an incoming wave increases exponentially with range. With Eqs. (E.2) and (E.3), we have (assume Im(x) > 0)

$$\begin{aligned} J_\nu(x) &= \frac{1}{2}\left[H_\nu^{(1)}(x) + H_\nu^{(2)}(x)\right] \\ &\sim \frac{1}{2} H_\nu^{(2)}(x), \text{ as } \mathrm{Im}(x) \to \infty, \end{aligned} \tag{E.4}$$

and

$$\begin{aligned} Y_\nu(x) &= \frac{1}{2}\left[H_\nu^{(1)}(x) - H_\nu^{(2)}(x)\right] \\ &\sim -\frac{1}{2} H_\nu^{(2)}(x), \text{ as } \mathrm{Im}(x) \to \infty. \end{aligned} \tag{E.5}$$

Thus for $|x| \gg \nu$,

$$H_\nu^{(1)}(x) \sim \sqrt{\frac{2}{\pi x}} e^{i\left(x-\nu\frac{\pi}{2}-\frac{\pi}{4}\right)}, \tag{E.6}$$

$$H_\nu^{(2)}(x) \sim 2J_\nu(x) \sim -2Y_\nu(x) \sim \sqrt{\frac{2}{\pi x}} e^{-i\left(x-\nu\frac{\pi}{2}-\frac{\pi}{4}\right)}. \tag{E.7}$$

So we come to the conclusion for $|x| \gg \nu$: when $|x| \gg \nu$, $H_\nu^{(2)}(x)$, $J_\nu(x)$ and $Y_\nu(x)$ are linearly dependent, all of them are linearly independent of $H_\nu^{(1)}(x)$.

We may see the conclusion above clearly from Fig. E-1, where $\log_{10}|J_\nu(x)|$, $\log_{10}|Y_\nu(x)|$, $\log_{10}\left|H_\nu^{(1)}(x)\right|$ and $\log_{10}\left|H_\nu^{(2)}(x)\right|$ are plotted with $\nu = 1$, $x = a + ib = a + ia$ (let $b = a > 0$).

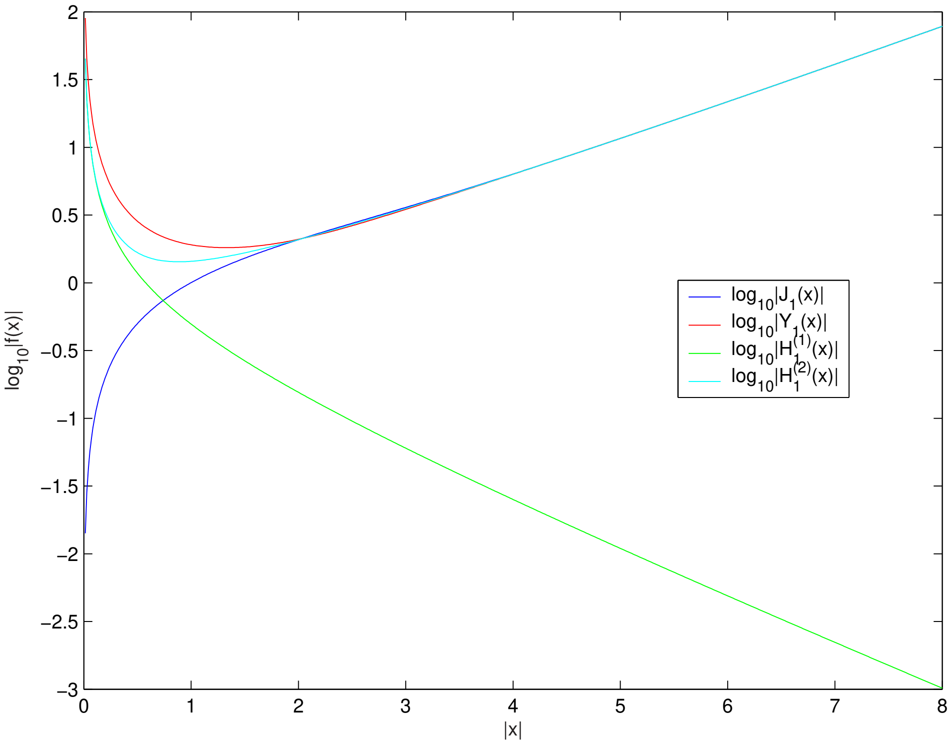

Figure E-1: Bessel and Hankel functions of order $\nu = 1$. As $|x| \gg \nu$, $H_\nu^{(2)}(x)$, $J_\nu(x)$ and $Y_\nu(x)$ are linearly dependent, all of them are linearly independent of $H_\nu^{(1)}(x)$; as $|x| \ll \nu$, $H_\nu^{(1)}(x)$, $H_\nu^{(2)}(x)$ and $Y_\nu(x)$ are linearly dependent, all of them are linearly independent of $J_\nu(x)$.

E.2 Linearly Independent Solutions for Small Arguments

Below we will seek linearly independent solutions for small arguments, i.e., $|x| \ll \nu$ or, $|x| \to 0$ with ν fixed. Since as $|x| \to 0$, $J_\nu(x)$ approaches a finite value, which is either 1 (when $\nu = 0$) or 0 (when $\nu \neq 0$), while $Y_\nu(x) \to -\infty$, we have

$$\begin{aligned} H_\nu^{(1)}(x) &= J_\nu(x) + iY_\nu(x) \\ &\sim iY_\nu(x), \qquad \text{(E.8)} \\ H_\nu^{(2)}(x) &= J_\nu(x) - iY_\nu(x) \\ &\sim -iY_\nu(x). \qquad \text{(E.9)} \end{aligned}$$

From the above, we come to the conclusion for $|x| \ll \nu$: when $|x| \ll \nu$, $H_\nu^{(1)}(x)$, $H_\nu^{(2)}(x)$ and $Y_\nu(x)$ are linearly dependent, all of them are linearly independent of $J_\nu(x)$. This conclusion can also be seen clearly in Fig. E-1.

E.3 Linearly Independent Solutions for Both Large and Small Arguments

As shown in Table E.1, we reach the conclusion: The only pair of functions that preserves linear independence for both large arguments, i.e. $|x| \gg \nu$, and small arguments, i.e. $|x| \ll \nu$, is $H_\nu^{(1)}(x)$ and $J_\nu(x)$.

condition	independent solution set 1	independent solution set 2
$\lvert x\rvert \gg \nu$	$H_\nu^{(1)}(x)$	$H_\nu^{(2)}(x)$, $J_\nu(x)$, $Y_\nu(x)$
$\lvert x\rvert \ll \nu$	$H_\nu^{(1)}(x)$, $H_\nu^{(2)}(x)$, $Y_\nu(x)$	$J_\nu(x)$

Table E.1: Linearly independent solutions of the Bessel equation in Eq. (E.1).

Appendix F

Asymptotic Forms of Normalized Bessel and Hankel Functions of High Orders with Debye Asymptotic Expansion

Below we will give the asymptotic forms of normalized Bessel and Hankel functions of high orders by applying the Debye asymptotic expansion [1, 5].

F.1 Debye Asymptotic Expansion

If α is fixed and positive and ν is large and positive, then (Eqs. 9.3.7 and 9.3.8 in [1])

$$
\begin{aligned}
J_\nu(\nu \mathrm{sech}\alpha) &\sim \frac{e^{\nu(\tanh\alpha-\alpha)}}{\sqrt{2\pi\nu\tanh\alpha}}\left\{1+\sum_{k=1}^{\infty}\frac{u_k(\coth\alpha)}{\nu^k}\right\},\\
Y_\nu(\nu \mathrm{sech}\alpha) &\sim -\frac{e^{\nu(\alpha-\tanh\alpha)}}{\sqrt{\frac{1}{2}\pi\nu\tanh\alpha}}\left\{1+\sum_{k=1}^{\infty}(-1)^k\frac{u_k(\coth\alpha)}{\nu^k}\right\},
\end{aligned}
$$

where

$$
\begin{aligned}
&u_0(t) = 1, \\
&u_1(t) = (3t - 5t^3)/24, \\
&u_2(t) = (81t^2 - 462t^4 + 385t^6)/1152, \\
&\text{etc.}
\end{aligned}
$$

When the order m is large (when the value of Y_m drops below -10^{10}), we use the Debye asymptotic expansion with the first three terms, and evaluate the normalized Bessel and Hankel functions as shown in the following sections.

F.2 The Asymptotic Form of $\hat{J}_m(x_1) = J_m(x_1)H_m^{(1)}(x_2)$ of High Orders

First, let

$$x_1 = m\text{sech}\alpha_1 \Longrightarrow \alpha_1 = \text{asech}(\frac{x_1}{m}), \tag{F.1}$$

$$x_2 = m\text{sech}\alpha_2 \Longrightarrow \alpha_2 = \text{asech}(\frac{x_2}{m}), \tag{F.2}$$

and then evaluate

$$
\begin{aligned}
J_m(x_1)H_m^{(1)}(x_2) =& J_m(x_1)[J_m(x_2) + iY_m(x_2)] \\
=& J_m(x_1)J_m(x_2) + iJ_m(x_1)Y_m(x_2),
\end{aligned} \tag{F.3}
$$

where

$$
\begin{aligned}
J_m(x_1)J_m(x_2) =& \frac{e^{m(\tanh\alpha_1 - \alpha_1 + \tanh\alpha_2 - \alpha_2)}}{2\pi m\sqrt{\tanh\alpha_1 \tanh\alpha_2}} \\
&\times \left\{1 + \frac{u_1(\coth\alpha_1)}{m} + \frac{u_2(\coth\alpha_1)}{m^2}\right\} \left\{1 + \frac{u_1(\coth\alpha_2)}{m} + \frac{u_2(\coth\alpha_2)}{m^2}\right\},
\end{aligned} \tag{F.4}
$$

$$J_m(x_1)Y_m(x_2) = -\frac{e^{m(\tanh\alpha_1-\alpha_1+\alpha_2-\tanh\alpha_2)}}{\pi m\sqrt{\tanh\alpha_1\tanh\alpha_2}} \times \left\{1+\frac{u_1(\coth\alpha_1)}{m}+\frac{u_2(\coth\alpha_1)}{m^2}\right\}\left\{1-\frac{u_1(\coth\alpha_2)}{m}+\frac{u_2(\coth\alpha_2)}{m^2}\right\}. \tag{F.5}$$

F.3 The Asymptotic Form of $\hat{J}'_m(x_1) = J'_m(x_1)H_m^{(1)}(x_2)$ of High Orders

Evaluate $\hat{J}'_m(x_1)$ by

$$\begin{aligned}\hat{J}'_m(x_1) =& J'_m(x_1)H_m^{(1)}(x_2)\\ =& \left[J_{m-1}(x_1)-\frac{m}{x_1}J_m(x_1)\right]H_m^{(1)}(x_2)\\ =& J_{m-1}(x_1)H_m^{(1)}(x_2)-\frac{m}{x_1}J_m(x_1)H_m^{(1)}(x_2),\end{aligned} \tag{F.6}$$

where $J_m(x_1)H_m^{(1)}(x_2)$ is evaluated by Eqs. (F.3), (F.4), and (F.5), and $J_{m-1}(x_1)H_m^{(1)}(x_2)$ is evaluated as below:

First, let

$$x_1 = (m-1)\mathrm{sech}\alpha_1 \Longrightarrow \alpha_1 = \mathrm{asech}(\frac{x_1}{m-1}), \tag{F.7}$$

$$x_2 = m\mathrm{sech}\alpha_2 \Longrightarrow \alpha_2 = \mathrm{asech}(\frac{x_2}{m}), \tag{F.8}$$

and then evaluate

$$\begin{aligned}J_{m-1}(x_1)H_m^{(1)}(x_2) =& J_{m-1}(x_1)[J_m(x_2)+iY_m(x_2)]\\ =& J_{m-1}(x_1)J_m(x_2)+iJ_{m-1}(x_1)Y_m(x_2),\end{aligned} \tag{F.9}$$

where

$$J_{m-1}(x_1)J_m(x_2) = \frac{e^{m(\tanh\alpha_1-\alpha_1+\tanh\alpha_2-\alpha_2)}e^{\alpha_1-\tanh\alpha 1}}{2\pi\sqrt{m(m-1)}\sqrt{\tanh\alpha_1\tanh\alpha_2}} \times\left\{1+\frac{u_1(\coth\alpha_1)}{m-1}+\frac{u_2(\coth\alpha_1)}{(m-1)^2}\right\}\left\{1+\frac{u_1(\coth\alpha_2)}{m}+\frac{u_2(\coth\alpha_2)}{m^2}\right\}, \tag{F.10}$$

$$J_{m-1}(x_1)Y_m(x_2) = -\frac{e^{m(\tanh\alpha_1-\alpha_1+\alpha_2-\tanh\alpha_2)}e^{\alpha_1-\tanh\alpha_1}}{\pi\sqrt{m(m-1)}\sqrt{\tanh\alpha_1\tanh\alpha_2}} \times\left\{1+\frac{u_1(\coth\alpha_1)}{m-1}+\frac{u_2(\coth\alpha_1)}{(m-1)^2}\right\}\left\{1-\frac{u_1(\coth\alpha_2)}{m}+\frac{u_2(\coth\alpha_2)}{m^2}\right\}. \tag{F.11}$$

F.4 The Asymptotic Form of $\hat{H}_m^{(1)}(x_1) = H_m^{(1)}(x_1)/H_m^{(1)}(x_2)$ of High Orders

We evaluate $\hat{H}_m^{(1)}(x_1) = H_m^{(1)}(x_1)/H_m^{(1)}(x_2)$ as below:

$$\begin{aligned}\hat{H}_m^{(1)}(x_1) =& \frac{H_m^{(1)}(x_1)}{H_m^{(1)}(x_2)}\\ =& \frac{J_m(x_2)H_m^{(1)}(x_1)}{J_m(x_2)H_m^{(1)}(x_2)},\end{aligned} \tag{F.12}$$

where $J_m(x_2)H_m^{(1)}(x_1)$ and $J_m(x_2)H_m^{(1)}(x_2)$ are evaluated by Eqs. (F.3), (F.4) and (F.5).

F.5 The Asymptotic Form of $\hat{H}_m^{(1)'}(x_1) = H_m^{(1)'}(x_1)/H_m^{(1)}(x_2)$ of High Orders

We evaluate $\hat{H}_m^{(1)'}(x_1) = \frac{H_m^{(1)'}(x_1)}{H_m^{(1)}(x_2)}$ as below:

$$\begin{aligned}
\frac{H_m^{(1)'}(x_1)}{H_m^{(1)}(x_2)} =& \frac{H_{m-1}^{(1)}(x_1) - \frac{m}{x_1}H_m^{(1)}(x_1)}{H_m^{(1)}(x_2)} \\
=& \frac{H_{m-1}^{(1)}(x_1)}{H_m^{(1)}(x_2)} - \frac{m}{x_1}\frac{H_m^{(1)}(x_1)}{H_m^{(1)}(x_2)},
\end{aligned} \tag{F.13}$$

where $\frac{H_m^{(1)}(x_1)}{H_m^{(1)}(x_2)}$ is evaluated by Eq. (F.12) and $\frac{H_{m-1}^{(1)}(x_1)}{H_m^{(1)}(x_2)}$ is evaluated as below:

$$\frac{H_{m-1}^{(1)}(x_1)}{H_m^{(1)}(x_2)} = \frac{J_m(x_2)H_{m-1}^{(1)}(x_1)}{J_m(x_2)H_m^{(1)}(x_2)}, \tag{F.14}$$

in which $J_m(x_2)H_m^{(1)}(x_2)$ is evaluated by Eqs. (F.3), (F.4) and (F.5), and $J_m(x_2)H_{m-1}^{(1)}(x_1)$ is evaluated as below:

First, let

$$x_2 = m\text{sech}\alpha_2 \Longrightarrow \alpha_2 = \text{asech}(\frac{x_2}{m}), \tag{F.15}$$

$$x_1 = (m-1)\text{sech}\alpha_1 \Longrightarrow \alpha_1 = \text{asech}(\frac{x_1}{m-1}), \tag{F.16}$$

and then evaluate $J_m(x_2)H_{m-1}^{(1)}(x_1)$ as below,

$$\begin{aligned}
J_m(x_2)H_{m-1}^{(1)}(x_1) =& J_m(x_2)[J_{m-1}(x_1) + iY_{m-1}(x_1)] \\
=& J_m(x_2)J_{m-1}(x_1) + iJ_m(x_2)Y_{m-1}(x_1),
\end{aligned} \tag{F.17}$$

where

$$\begin{aligned} J_m(x_2)J_{m-1}(x_1) =& \frac{e^{m(\tanh\alpha_2-\alpha_2+\tanh\alpha_1-\alpha_1)}e^{\alpha 1-\tanh\alpha 1}}{2\pi\sqrt{m(m-1)}\sqrt{\tanh\alpha_1\tanh\alpha_2}} \\ &\times\left\{1+\frac{u_1(\coth\alpha_2)}{m}+\frac{u_2(\coth\alpha_2)}{m^2}\right\}\left\{1+\frac{u_1(\coth\alpha_1)}{m-1}+\frac{u_2(\coth\alpha_1)}{(m-1)^2}\right\}, \end{aligned} \tag{F.18}$$

$$\begin{aligned} J_m(x_2)Y_{m-1}(x_1) =& -\frac{e^{m(\tanh\alpha_2-\alpha_2+\alpha_1-\tanh\alpha_1)}e^{\tanh\alpha 1-\alpha 1}}{\pi\sqrt{m(m-1)}\sqrt{\tanh\alpha_1\tanh\alpha_2}} \\ &\times\left\{1+\frac{u_1(\coth\alpha_2)}{m}+\frac{u_2(\coth\alpha_2)}{m^2}\right\}\left\{1-\frac{u_1(\coth\alpha_1)}{m-1}+\frac{u_2(\coth\alpha_1)}{(m-1)^2}\right\}. \end{aligned} \tag{F.19}$$

Appendix G

Derivation of Coupling Coefficients b^J_{mn} and c_{mn}

In Section 2.2.3 we derived the coupling coefficients B_{mn} and C_{mn} with source conditions, where unnormalized Hankel functions are used as solutions to the Bessel equation. Below we will derive the coupling coefficients b^J_{mn} and c_{mn} with normalized Bessel and Hankel functions as solutions to the Bessel equation.

From Section 2.2.3 we have two equations for b^J_{mn} and c_{mn},

$$b^J_{mn} J_m(k^J_{rn} r_s) H^{(1)}_m(k^J_{rn} r_s) - c_{mn} = -a^J_{mn} \frac{H^{(1)}_m(k^J_{rn} r_s)}{H^{(1)}_m(k^J_{rn} r^{J-1})}, \tag{G.1}$$

$$b^J_{mn} \frac{\mathrm{d}J_m}{\mathrm{d}r}(k^J_{rn} r_s) H^{(1)}_m(k^J_{rn} r_s) - c_{mn} \frac{\frac{\mathrm{d}H^{(1)}_m}{\mathrm{d}r}(k^J_{rn} r_s)}{H^{(1)}_m(k^J_{rn} r_s)} = -a^J_{mn} \frac{\frac{\mathrm{d}H^{(1)}_m}{\mathrm{d}r}(k^J_{rn} r_s)}{H^{(1)}_m(k^J_{rn} r^{J-1})} + \frac{1}{r_s} \frac{\Psi^J_n(z_s)}{\rho(z_s)} \Phi_m(\phi_s), \tag{G.2}$$

To use Cramer's rule to obtain b^J_{mn}, first we find the determinants

$$\begin{aligned}
D &= \begin{vmatrix} J_m(k^J_{rn} r_s) H^{(1)}_m(k^J_{rn} r_s) & -1 \\ \frac{\mathrm{d}J_m}{\mathrm{d}r}(k^J_{rn} r_s) H^{(1)}_m(k^J_{rn} r_s) & -\frac{\frac{\mathrm{d}H^{(1)}_m}{\mathrm{d}r}(k^J_{rn} r_s)}{H^{(1)}_m(k^J_{rn} r_s)} \end{vmatrix} \\
&= -J_m(k^J_{rn} r_s)\frac{\mathrm{d}H^{(1)}_m}{\mathrm{d}r}(k^J_{rn} r_s) + \frac{\mathrm{d}J_m}{\mathrm{d}r}(k^J_{rn} r_s) H^{(1)}_m(k^J_{rn} r_s) \\
&= H^{(1)}_m(k^J_{rn} r_s) k^J_{rn} \frac{\mathrm{d}J_m}{\mathrm{d}(k^J_{rn} r)}(k^J_{rn} r_s) - k^J_{rn}\frac{\mathrm{d}H^{(1)}_m}{\mathrm{d}(k^J_{rn} r)}(k^J_{rn} r_s) J_m(k^J_{rn} r_s) \\
&= k^J_{rn} W\left[H^{(1)}_m(k^J_{rn} r_s), J_m(k^J_{rn} r_s)\right] \\
&= -ik^J_{rn} W\left[J_m(k^J_{rn} r_s), Y_m(k^J_{rn} r_s)\right] \\
&= -ik^J_{rn}\frac{2}{\pi k^J_{rn} r_s} \\
&= -\frac{2i}{\pi r_s}, \qquad \text{(G.3)}
\end{aligned}$$

and

$$\begin{aligned}
N_b &= \begin{vmatrix} -a^J_{mn}\frac{H^{(1)}_m(k^J_{rn} r_s)}{H^{(1)}_m(k^J_{rn} r^{J-1})} & -1 \\ -a^J_{mn}\frac{\frac{\mathrm{d}H^{(1)}_m}{\mathrm{d}r}(k^J_{rn} r_s)}{H^{(1)}_m(k^J_{rn} r^{J-1})} + \frac{1}{r_s}\frac{\Psi^J_n(z)}{\rho(z_s)}\Phi_m(\phi_s) & -\frac{\frac{\mathrm{d}H^{(1)}_m}{\mathrm{d}r}(k^J_{rn} r_s)}{H^{(1)}_m(k^J_{rn} r_s)} \end{vmatrix} \\
&= a^J_{mn}\cancel{\frac{1}{H^{(1)}_m(k^J_{rn} r^{J-1})}\frac{\mathrm{d}H^{(1)}_m}{\mathrm{d}r}}(k^J_{rn} r_s) - a^J_{mn}\cancel{\frac{\mathrm{d}H^{(1)}_m}{\mathrm{d}r}(k^J_{rn} r_s)\frac{1}{H^{(1)}_m(k^J_{rn} r^{J-1})}} + \frac{1}{r_s}\frac{\Psi^J_n(z_s)}{\rho(z_s)}\Phi_m(\phi_s) \\
&= \frac{1}{r_s}\frac{\Psi^J_n(z_s)}{\rho(z_s)}\Phi_m(\phi_s), \qquad \text{(G.4)}
\end{aligned}$$

thus we obtain

$$\begin{aligned}
b^J_{mn} &= \frac{N_b}{D} \\
&= \frac{\frac{1}{r_s}\frac{\Psi^J_n(z_s)}{\rho(z_s)}\Phi_m(\phi_s)}{-\frac{2i}{\pi r_s}} \\
&= \frac{i}{2}\pi\frac{\Psi^J_n(z_s)}{\rho(z_s)}\Phi_m(\phi_s). \qquad \text{(G.5)}
\end{aligned}$$

By substituting Eq. (G.5) into Eq. (G.1), we obtain c_{mn},

$$c_{mn} = \frac{i}{2}\pi \frac{\Psi_n^J(z_s)}{\rho(z_s)} \Phi_m(\phi_s) J_m(k_{rn}^J r_s) H_m^{(1)}(k_{rn}^J r_s) + a_{mn}^J \frac{H_m^{(1)}(k_{rn}^J r_s)}{H_m^{(1)}(k_{rn}^J r^{J-1})}. \tag{G.6}$$

Appendix H

Derivation of Formulas in Outward Marching

In Section 4.3.2, we list the formulas in the outward marching. Below we will give the derivation of those formulas.

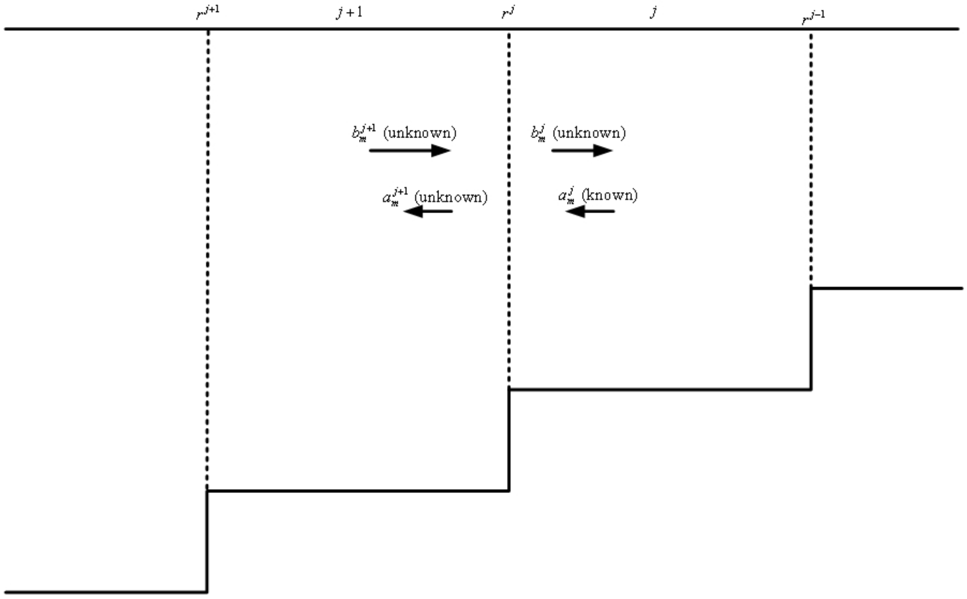

Figure H-1: Coupling between two neighboring rings in outward marching.

Refer to Fig. H-1, we have the following boundary conditions:

1) **Continuity of pressure at $r = r^j$.**

The boundary condition

$$p^{j+1}(r^j, z, \phi) = p^j(r^j, z, \phi), \tag{H.1}$$

as well as Eq. (4.19), gives rise to (for azimuthal mode m)

$$\sum_{n=1}^{\infty} \left[a_{mn}^{j+1} \hat{H}1_{mn}^{j+1}(r^j) + b_{mn}^{j+1} \hat{J}_{mn}^{j+1}(r^j) \right] \Psi_n^{j+1}(z) = \sum_{n=1}^{\infty} \left[a_{mn}^{j} \hat{H}1_{mn}^{j}(r^j) + b_{mn}^{j} \hat{J}_{mn}^{j}(r^j) \right] \Psi_n^{j}(z). \tag{H.2}$$

By applying $\int_0^\infty \frac{1}{\rho^{j+1}(z)} \Psi_\nu^{j+1}(z)(\cdot)\mathrm{d}z$ to Eq. (H.2), we obtain

$$a_{m\nu}^{j+1} \hat{H}1_{m\nu}^{j+1} + b_{m\nu}^{j+1} \hat{J}_{m\nu}^{j+1} = \sum_{n=1}^{\infty} \left[a_{mn}^{j} \hat{H}1_{mn}^{j} + b_{mn}^{j} \hat{J}_{mn}^{j} \right] \int_0^\infty \frac{1}{\rho^{j+1}(z)} \Psi_\nu^{j+1}(z) \Psi_n^j(z) \mathrm{d}z. \tag{H.3}$$

With notation

$$(C_c)_{\nu n}^j \triangleq \int_0^\infty \frac{1}{\rho^{j+1}(z)} \Psi_\nu^{j+1}(z) \Psi_n^j(z) \mathrm{d}z, \tag{H.4}$$

we may rewrite Eq. (H.3) in the matrix form,

$$\boldsymbol{\hat{H}1}_m^{j+1} \boldsymbol{a}_m^{j+1} + \boldsymbol{\hat{J}}_m^{j+1} \boldsymbol{b}_m^{j+1} = \boldsymbol{C_c^j} [\boldsymbol{\hat{H}1}_m^{j} \boldsymbol{a}_m^{j} + \boldsymbol{\hat{J}}_m^{j} \boldsymbol{b}_m^{j}], \tag{H.5}$$

where $\boldsymbol{\hat{H}1}_m^j$, $\boldsymbol{\hat{J}}_m^j$, $\boldsymbol{\hat{H}1}_m^{j+1}$, and $\boldsymbol{\hat{J}}_m^{j+1}$ are diagonal matrixes and $\boldsymbol{a}_m^j$, $\boldsymbol{b}_m^j$, $\boldsymbol{a}_m^{j+1}$ and $\boldsymbol{b}_m^{j+1}$ are column vectors. Note that $\boldsymbol{C_c^j}$ does not depend on the azimuthal mode m.

2) Continuity of normal particle velocity at $\boldsymbol{r = r^j}$.

The boundary condition

$$\frac{1}{\rho^{j+1}(z)} \frac{\partial p^{j+1}}{\partial r}(r^j, z, \phi) = \frac{1}{\rho^{j}(z)} \frac{\partial p^{j}}{\partial r}(r^j, z, \phi), \tag{H.6}$$

with notations

$$D\hat{H}1_{mn}^j(r) \triangleq \frac{\frac{\mathrm{d}H_m^{(1)}(k_{rn}^j r)}{\mathrm{d}(k_{rn}^j r)}}{H_m^{(1)}(k_{rn}^j r^{j-1})}, \; D\hat{J}_{mn}^j(r) \triangleq \frac{\mathrm{d}J_m(k_{rn}^j r)}{\mathrm{d}(k_{rn}^j r)} H_m^{(1)}(k_{rn}^j r^j), \tag{H.7}$$

as well as Eq. (4.19), leads to (for azimuthal mode m)

$$\begin{aligned}&\frac{1}{\rho^{j+1}(z)}\sum_{n=1}^{\infty}\left[a_{mn}^{j+1}k_{rn}^{j+1}D\hat{H}1_{mn}^{j+1}(r^j)+b_{mn}^{j+1}k_{rn}^{j+1}D\hat{J}_{mn}^{j+1}(r^j)\right]\Psi_n^{j+1}(z)\\ =&\frac{1}{\rho^{j}(z)}\sum_{n=1}^{\infty}\left[a_{mn}^{j}k_{rn}^{j}D\hat{H}1_{mn}^{j}(r^j)+b_{mn}^{j}k_{rn}^{j}D\hat{J}_{mn}^{j}(r^j)\right]\Psi_n^{j}(z).\end{aligned} \tag{H.8}$$

Apply $\int_0^\infty \Psi_\nu^{j+1}(z)(\cdot)\mathrm{d}z$ to Eq. (H.8), and we obtain

$$\begin{aligned}&a_{m\nu}^{j+1}k_{r\nu}^{j+1}D\hat{H}1_{m\nu}^{j+1}(r^j)+b_{m\nu}^{j+1}k_{r\nu}^{j+1}D\hat{J}_{m\nu}^{j+1}(r^j)\\ =&\sum_{n=1}^{\infty}\left[a_{mn}^{j}k_{rn}^{j}D\hat{H}1_{mn}^{j}(r^j)+b_{mn}^{j}k_{rn}^{j}D\hat{J}_{mn}^{j}(r^j)\right]\int_0^\infty\frac{1}{\rho^j(z)}\Psi_\nu^{j+1}(z)\Psi_n^j(z)\mathrm{d}z.\end{aligned} \tag{H.9}$$

With notation

$$(C_d)_{\nu n}^j \triangleq \frac{k_{rn}^j}{k_{r\nu}^{j+1}}\int_0^\infty\frac{1}{\rho^j(z)}\Psi_\nu^{j+1}(z)\Psi_n^j(z)\mathrm{d}z, \tag{H.10}$$

we may rewrite Eq. (H.9) in the matrix form,

$$\boldsymbol{D\hat{H}1}_m^{j+1}\boldsymbol{a}_m^{j+1}+\boldsymbol{D\hat{J}}_m^{j+1}\boldsymbol{b}_m^{j+1}=\boldsymbol{C}_{\boldsymbol{d}}^j[\boldsymbol{D\hat{H}1}_m^j\boldsymbol{a}_m^j+\boldsymbol{D\hat{J}}_m^j\boldsymbol{b}_m^j]. \tag{H.11}$$

Now we have Eq. (H.5) and Eq. (H.11),

$$\begin{aligned}\boldsymbol{\hat{H}1}_m^{j+1}\boldsymbol{a}_m^{j+1}+\boldsymbol{\hat{J}}_m^{j+1}\boldsymbol{b}_m^{j+1} &= \boldsymbol{C}_{\boldsymbol{c}}^j[\boldsymbol{\hat{H}1}_m^j\boldsymbol{a}_m^j+\boldsymbol{\hat{J}}_m^j\boldsymbol{b}_m^j], && \text{(H.12a)}\\ \boldsymbol{D\hat{H}1}_m^{j+1}\boldsymbol{a}_m^{j+1}+\boldsymbol{D\hat{J}}_m^{j+1}\boldsymbol{b}_m^{j+1} &= \boldsymbol{C}_{\boldsymbol{d}}^j[\boldsymbol{D\hat{H}1}_m^j\boldsymbol{a}_m^j+\boldsymbol{D\hat{J}}_m^j\boldsymbol{b}_m^j]. && \text{(H.12b)}\end{aligned}$$

To solve $\boldsymbol{a}_m^{j+1}$, we first solve it from Eq. (H.12) and then apply the one-way approximation, i.e., $\boldsymbol{b}_m^{j+1}=0$, $\boldsymbol{b}_m^j=0$, instead of first imposing $\boldsymbol{b}_m^{j+1}=0$, $\boldsymbol{b}_m^j=0$, and then solving $\boldsymbol{a}_m^{j+1}$ from the simplified Eq. (H.12).

Apply $\boldsymbol{D\hat{J}}_m^{j+1}$ × Eq. (H.12a) − $\boldsymbol{\hat{J}}_m^{j+1}$ × Eq. (H.12b), and notice that since $\boldsymbol{\hat{J}}_m^{j+1}$, $\boldsymbol{D\hat{J}}_m^{j+1}$ are both diagonal matrixes, thus $\boldsymbol{D\hat{J}}_m^{j+1}\times\boldsymbol{\hat{J}}_m^{j+1}=\boldsymbol{\hat{J}}_m^{j+1}\times\boldsymbol{D\hat{J}}_m^{j+1}$, then we obtain

$$\begin{aligned}&[\boldsymbol{D}\hat{\boldsymbol{J}}_m^{j+1}\hat{\boldsymbol{H}}\boldsymbol{1}_m^{j+1}-\hat{\boldsymbol{J}}_m^{j+1}\boldsymbol{D}\hat{\boldsymbol{H}}\boldsymbol{1}_m^{j+1}]\boldsymbol{a}_m^{j+1}\\ =&[\boldsymbol{D}\hat{\boldsymbol{J}}_m^{j+1}\boldsymbol{C}_{\boldsymbol{c}}^j\hat{\boldsymbol{H}}\boldsymbol{1}_m^j-\hat{\boldsymbol{J}}_m^{j+1}\boldsymbol{C}_{\boldsymbol{d}}^j\boldsymbol{D}\hat{\boldsymbol{H}}\boldsymbol{1}_m^j]\boldsymbol{a}_m^j+[\boldsymbol{D}\hat{\boldsymbol{J}}_m^{j+1}\boldsymbol{C}_{\boldsymbol{c}}^j\hat{\boldsymbol{J}}_m^j-\hat{\boldsymbol{J}}_m^{j+1}\boldsymbol{C}_{\boldsymbol{d}}^j\boldsymbol{D}\hat{\boldsymbol{J}}_m^j]\boldsymbol{b}_m^j.\end{aligned} \tag{H.13}$$

Now impose the one-way approximation $\boldsymbol{b}_m^j=0$, then Eq. (H.13) leads to

$$[\boldsymbol{D}\hat{\boldsymbol{J}}_m^{j+1}\hat{\boldsymbol{H}}\boldsymbol{1}_m^{j+1}-\hat{\boldsymbol{J}}_m^{j+1}\boldsymbol{D}\hat{\boldsymbol{H}}\boldsymbol{1}_m^{j+1}]\boldsymbol{a}_m^{j+1}=[\boldsymbol{D}\hat{\boldsymbol{J}}_m^{j+1}\boldsymbol{C}_{\boldsymbol{c}}^j\hat{\boldsymbol{H}}\boldsymbol{1}_m^j-\hat{\boldsymbol{J}}_m^{j+1}\boldsymbol{C}_{\boldsymbol{d}}^j\boldsymbol{D}\hat{\boldsymbol{H}}\boldsymbol{1}_m^j]\boldsymbol{a}_m^j. \tag{H.14}$$

The factor of $\boldsymbol{a}_m^{j+1}$ can be simplified as below,

$$\begin{aligned}&D\hat{J}_{mn}^{j+1}\hat{H}1_{mn}^{j+1}-\hat{J}_{mn}^{j+1}D\hat{H}1_{mn}^{j+1}\\ =&\frac{\mathrm{d}J_m(k_{rn}^{j+1}r^j)}{\mathrm{d}(k_{rn}^{j+1}r)}H_m^{(1)}(k_{rn}^{j+1}r^{j+1})\frac{H_m^{(1)}(k_{rn}^{j+1}r^j)}{H_m^{(1)}(k_{rn}^{j+1}r^j)}-J_m(k_{rn}^{j+1}r^j)H_m^{(1)}(k_{rn}^{j+1}r^{j+1})\frac{\frac{\mathrm{d}H_m^{(1)}(k_{rn}^{j+1}r^j)}{\mathrm{d}(k_{rn}^{j+1}r)}}{H_m^{(1)}(k_{rn}^{j+1}r^j)}\\ =&\frac{H_m^{(1)}(k_{rn}^{j+1}r^{j+1})}{H_m^{(1)}(k_{rn}^{j+1}r^j)}\left[\frac{\mathrm{d}J_m}{\mathrm{d}(k_{rn}^{j+1}r)}(k_{rn}^{j+1}r^j)H_m^{(1)}(k_{rn}^{j+1}r^j)-J_m(k_{rn}^{j+1}r^j)\frac{\mathrm{d}H_m^{(1)}}{\mathrm{d}(k_{rn}^{j+1}r)}(k_{rn}^{j+1}r^j)\right]\\ =&\frac{H_m^{(1)}(k_{rn}^{j+1}r^{j+1})}{H_m^{(1)}(k_{rn}^{j+1}r^j)}\underbrace{W[H_m^{(1)},J_m](k_{rn}^{j+1}r^j)}_{-\frac{2i}{\pi k_{rn}^{j+1}r^j}}\\ =&-\frac{2i}{\pi r^j}\frac{1}{k_{rn}^{j+1}}\frac{H_m^{(1)}(k_{rn}^{j+1}r^{j+1})}{H_m^{(1)}(k_{rn}^{j+1}r^j)},\end{aligned} \tag{H.15}$$

so we obtain

$$\begin{aligned}\boldsymbol{D}\hat{\boldsymbol{J}}_m^{j+1}\hat{\boldsymbol{H}}\boldsymbol{1}_m^{j+1}-\hat{\boldsymbol{J}}_m^{j+1}\boldsymbol{D}\hat{\boldsymbol{H}}\boldsymbol{1}_m^{j+1}=&-\frac{2i}{\pi r^j}\mathrm{diag}\left(\frac{1}{k_{rn}^{j+1}}\frac{H_m^{(1)}(k_{rn}^{j+1}r^{j+1})}{H_m^{(1)}(k_{rn}^{j+1}r^j)}\right),\ n=1,\cdots,N\\ \triangleq&\boldsymbol{G}_{\boldsymbol{a}}^{j+1},\end{aligned} \tag{H.16}$$

and therefore

$$(\boldsymbol{G}_{\boldsymbol{a}}^{\boldsymbol{j+1}})^{-1}=i\frac{\pi r^j}{2}\mathrm{diag}\left(k_{rn}^{j+1}\frac{H_m^{(1)}(k_{rn}^{j+1}r^j)}{H_m^{(1)}(k_{rn}^{j+1}r^{j+1})}\right),\ n=1,\ldots,N. \tag{H.17}$$

Thus, from Eq. (H.14) we obtain

$$\begin{aligned}\boldsymbol{a}_m^{j+1} =&(\boldsymbol{G}_{\boldsymbol{a}}^{j+1})^{-1}\left[\boldsymbol{D}\hat{\boldsymbol{J}}_m^{j+1}\boldsymbol{C}_{\boldsymbol{c}}^j\hat{\boldsymbol{H}}\mathbf{1}_m^j - \hat{\boldsymbol{J}}_m^{j+1}\boldsymbol{C}_{\boldsymbol{d}}^j\boldsymbol{D}\hat{\boldsymbol{H}}\mathbf{1}_m^j\right]\boldsymbol{a}_m^j \\ =&\boldsymbol{S}_{m1}^j\boldsymbol{a}_m^j,\end{aligned} \tag{H.18}$$

where

$$\boldsymbol{S}_{m1}^j \triangleq (\boldsymbol{G}_{\boldsymbol{a}}^{j+1})^{-1}[\boldsymbol{D}\hat{\boldsymbol{J}}_m^{j+1}\boldsymbol{C}_{\boldsymbol{c}}^j\hat{\boldsymbol{H}}\mathbf{1}_m^j - \hat{\boldsymbol{J}}_m^{j+1}\boldsymbol{C}_{\boldsymbol{d}}^j\boldsymbol{D}\hat{\boldsymbol{H}}\mathbf{1}_m^j]. \tag{H.19}$$

Appendix I

The Spectral Coupled Mode Solution to a Range-Independent Waveguide Problem

Below we will show that our three-dimensional spectral coupled mode solution will reduce to the two-dimensional normal mode solution for range-independent problems. We only focus on the field in the region inside the source range, i.e. $r \leq r_s$; the discussion about the field outside the source range is similar and thus is omitted. A detailed discussion about the equivalence of the spectral normal mode solution and the two-dimensional normal mode solution for range-independent problems can be found in Section 2.2.4.

As illustrated in Fig. I-1, for a range-independent problem, we have $k_{rn}^{j} = k_{rn}^{j+1} = k_{rn}$. Now Eq. (4.65) becomes

$$\left(\boldsymbol{F_b^j}\right)^{-1} = \frac{\pi r^j}{2i} \mathrm{diag}\left(k_{rn} \frac{H_m^{(1)}(k_{rn} r^{j-1})}{H_m^{(1)}(k_{rn} r^j)} \right), \ n = 1, 2, \ldots, N. \tag{I.1}$$

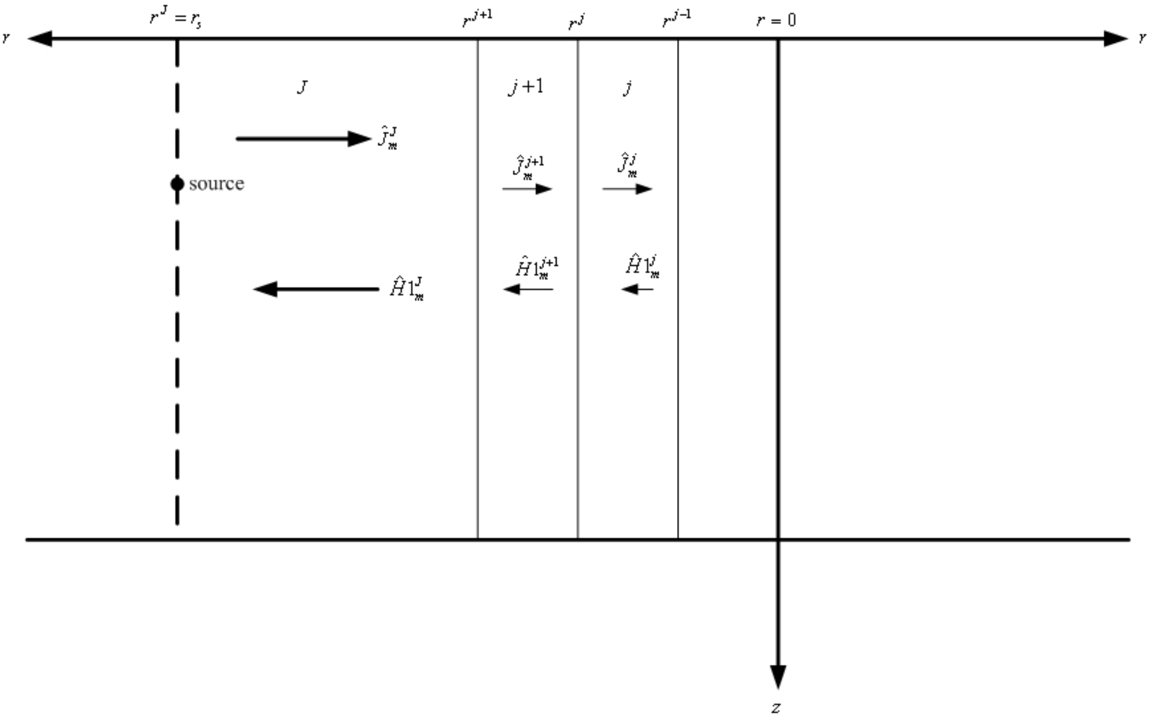

Figure I-1: To apply the spectral coupled mode method to a range-independent problem.

Since now $\boldsymbol{C}_{\boldsymbol{a}}^{j+1} = \boldsymbol{C}_{\boldsymbol{b}}^{j+1} = \boldsymbol{I}$, we have

$$\begin{aligned}
&\boldsymbol{D}\hat{\boldsymbol{J}}_m^j \boldsymbol{C}_{\boldsymbol{a}}^{j+1} \hat{\boldsymbol{J}}_m^{j+1} - \hat{\boldsymbol{J}}_m^j \boldsymbol{C}_{\boldsymbol{b}}^{j+1} \boldsymbol{D}\hat{\boldsymbol{J}}_m^{j+1} \\
=&\boldsymbol{D}\hat{\boldsymbol{J}}_m^j \hat{\boldsymbol{J}}_m^{j+1} - \hat{\boldsymbol{J}}_m^j \boldsymbol{D}\hat{\boldsymbol{J}}_m^{j+1} \\
=&\text{diag}\left(J_m'(k_{rn}r^j) H_m^{(1)}(k_{rn}r^j) J_m(k_{rn}r^j) H_m^{(1)}(k_{rn}r^{j+1})\right. \\
&\left. -J_m(k_{rn}r^j) H_m^{(1)}(k_{rn}r^j) J_m'(k_{rn}r^j) H_m^{(1)}(k_{rn}r^{j+1})\right)_{n=1,2,\ldots,N} \\
=&\boldsymbol{0},
\end{aligned} \tag{I.2}$$

thus Eq. (4.62) becomes

$$\boldsymbol{R}_{m2}^{j+1} = -\left(\boldsymbol{F}_{\boldsymbol{b}}^j\right)^{-1} \left(\boldsymbol{D}\hat{\boldsymbol{J}}_m^j \boldsymbol{C}_{\boldsymbol{a}}^{j+1} \hat{\boldsymbol{J}}_m^{j+1} - \hat{\boldsymbol{J}}_m^j \boldsymbol{C}_{\boldsymbol{b}}^{j+1} \boldsymbol{D}\hat{\boldsymbol{J}}_m^{j+1}\right) = \boldsymbol{0}, \tag{I.3}$$

and then Eq. (4.67) leads to

$$\boldsymbol{a}_m^{j+1} = -\left(\boldsymbol{R}_{m1}^{j+1}\right)^{-1} \boldsymbol{R}_{m2}^{j+1} \boldsymbol{b}_m^{j+1} = \boldsymbol{0}, \tag{I.4}$$

so we have

$$\boldsymbol{a}_m^j = \mathbf{0},\ j = 1, 2, \ldots, J. \tag{I.5}$$

By substituting Eq. (I.4) into Eq. (4.68) we obtain

$$\boldsymbol{b}_m^j = \boldsymbol{R}_{m4}^{j+1}\boldsymbol{b}_m^{j+1} + \boldsymbol{R}_{m3}^{j+1}\boldsymbol{a}_m^{j+1} = \boldsymbol{R}_{m4}^{j+1}\boldsymbol{b}_m^{j+1}. \tag{I.6}$$

Since

$$\begin{aligned}
&\boldsymbol{D}\hat{\boldsymbol{H}}\mathbf{1}_m^j\boldsymbol{C}_{\boldsymbol{a}}^{j+1}\hat{\boldsymbol{J}}_m^{j+1} - \hat{\boldsymbol{H}}\mathbf{1}_m^j\boldsymbol{C}_{\boldsymbol{b}}^{j+1}\boldsymbol{D}\hat{\boldsymbol{J}}_m^{j+1}\\
=&\boldsymbol{D}\hat{\boldsymbol{H}}\mathbf{1}_m^j\hat{\boldsymbol{J}}_m^{j+1} - \hat{\boldsymbol{H}}\mathbf{1}_m^j\boldsymbol{D}\hat{\boldsymbol{J}}_m^{j+1}\\
=&\mathrm{diag}\left(\frac{H_m^{(1)\prime}(k_{rn}r^j)}{H_m^{(1)}(k_{rn}r^{j-1})}J_m(k_{rn}r^j)H_m^{(1)}(k_{rn}r^{j+1})\right.\\
&\left.-\frac{H_m^{(1)}(k_{rn}r^j)}{H_m^{(1)}(k_{rn}r^{j-1})}J_m'(k_{rn}r^j)H_m^{(1)}(k_{rn}r^{j+1})\right)_{n=1,2,\ldots,N}\\
=&\mathrm{diag}\left(\frac{H_m^{(1)}(k_{rn}r^{j+1})}{H_m^{(1)}(k_{rn}r^{j-1})}W\left[J_m(k_{rn}r^j), H_m^{(1)}(k_{rn}r^j)\right]\right)_{n=1,2,\ldots,N}\\
=&\frac{2i}{\pi r^j}\mathrm{diag}\left(\frac{1}{k_{rn}}\frac{H_m^{(1)}(k_{rn}r^{j+1})}{H_m^{(1)}(k_{rn}r^{j-1})}\right)_{n=1,2,\ldots,N},
\end{aligned} \tag{I.7}$$

from Eq. (4.64), as well as Eq. (I.1) and Eq. (I.7), $\boldsymbol{R}_{m4}^{j+1}$ reduces to

$$\begin{aligned}
\boldsymbol{R}_{m4}^{j+1} &= \left(\boldsymbol{F}_b^j\right)^{-1}\left(\boldsymbol{D}\hat{\boldsymbol{H}}\mathbf{1}_m^j\boldsymbol{C}_{\boldsymbol{a}}^{j+1}\hat{\boldsymbol{J}}_m^{j+1} - \hat{\boldsymbol{H}}\mathbf{1}_m^j\boldsymbol{C}_{\boldsymbol{b}}^{j+1}\boldsymbol{D}\hat{\boldsymbol{J}}_m^{j+1}\right)\\
&= \frac{\pi r^j}{2i}\mathrm{diag}\left(k_{rn}\frac{H_m^{(1)}(k_{rn}r^{j-1})}{H_m^{(1)}(k_{rn}r^j)}\right)_{n=1,2,\ldots,N}\frac{2i}{\pi r^j}\mathrm{diag}\left(\frac{1}{k_{rn}}\frac{H_m^{(1)}(k_{rn}r^{j+1})}{H_m^{(1)}(k_{rn}r^{j-1})}\right)_{n=1,2,\ldots,N}\\
&= \mathrm{diag}\left(\frac{H_m^{(1)}(k_{rn}r^{j+1})}{H_m^{(1)}(k_{rn}r^j)}\right)_{n=1,2,\ldots,N}.
\end{aligned} \tag{I.8}$$

By substituting Eq. (I.8) into Eq. (I.6), we obtain

$$\begin{aligned}
\boldsymbol{b}^j_m &= \boldsymbol{R}^{j+1}_{m4}\boldsymbol{b}^{j+1}_m \\
&= \operatorname{diag}\left(\frac{H^{(1)}_m(k_{rn}r^{j+1})}{H^{(1)}_m(k_{rn}r^j)}\right)_{n=1,2,\ldots,N}\boldsymbol{b}^{j+1}_m \\
&= \left[\frac{H^{(1)}_m(k_{rn}r^{j+1})}{H^{(1)}_m(k_{rn}r^j)}b^{j+1}_{mn}\right]_{n=1,2,\ldots,N},
\end{aligned} \tag{I.9}$$

which leads to

$$\begin{aligned}
b^j_{mn} &= \frac{H^{(1)}_m(k_{rn}r^{j+1})}{H^{(1)}_m(k_{rn}r^j)}b^{j+1}_{mn} \\
&= \frac{H^{(1)}_m(k_{rn}r^{j+1})}{H^{(1)}_m(k_{rn}r^j)}\frac{H^{(1)}_m(k_{rn}r^{j+2})}{H^{(1)}_m(k_{rn}r^{j+1})}\cdots\frac{H^{(1)}_m(k_{rn}r^J)}{H^{(1)}_m(k_{rn}r^{J-1})}b^J_{mn} \\
& \quad r^J = r_s \\
&= \frac{H^{(1)}_m(k_{rn}r_s)}{H^{(1)}_m(k_{rn}r^j)}b^J_{mn}.
\end{aligned} \tag{I.10}$$

With Eqs. (I.5) and (I.10), for a range-independent problem, our three-dimensional spectral coupled mode solution reduces to

$$\begin{aligned}
p^j(r,z,\phi) &= \sum_{m=0}^{\infty}\sum_{n=1}^{\infty}\left[\cancelto{0}{a^j_{mn}}\hat{H}1^j_{mn}(r) + b^j_{mn}\hat{J}^j_{mn}(r)\right]\Psi^j_n(z)\Phi_m(\phi) \\
&= \sum_{m=0}^{\infty}\sum_{n=1}^{\infty}\frac{H^{(1)}_m(k_{rn}r_s)}{H^{(1)}_m(k_{rn}r^j)}b^J_{mn}J_m(k_{rn}r)H^{(1)}_m(k_{rn}r^j)\Psi^j_n(z)\Phi_m(\phi) \\
&= \sum_{m=0}^{\infty}\sum_{n=1}^{\infty}H^{(1)}_m(k_{rn}r_s)J_m(k_{rn}r)\frac{i}{2}\pi\frac{\Psi_n(z_s)}{\rho(z_s)}\Phi_m(\phi_s)\Psi_n(z)\Phi_m(\phi) \\
&= \frac{i}{2}\frac{\pi}{\rho(z_s)}\sum_{m=0}^{\infty}\sum_{n=1}^{\infty}H^{(1)}_m(k_{rn}r_s)J_m(k_{rn}r)\Psi_n(z_s)\Psi_n(z)\Phi_m(\phi_s)\Phi_m(\phi) \\
&= \frac{i}{4\rho(z_s)}\sum_{n=1}^{\infty}\Psi_n(z_s)\Psi_n(z)H^{(1)}_0(k_{rn}r'),
\end{aligned} \tag{I.11}$$

where

$$r' = \sqrt{r^2 + r_s^2 - 2rr_s\cos(\phi_s - \phi)}. \tag{I.12}$$

From the above we can see that for a range-independent problem, our three-dimensional spectral coupled mode solution reduces to the spectral normal mode solution, or the two-dimensional normal mode solution (refer to Section 2.2.4).

Appendix J

Input Files for Case 1, Case 2a, Case 2b and Case 3

J.1 The Input Files for Case 1

J.1.1 Input Files for the Three-Dimensional Seamount Model

C-SNAP.DAT

```
3D SEAMOUNT Model
1
40.
1   20 20
100, 0
250.  0.   0.    0.                     1       ! REG   1
  0.  1500.
250.  1500.
8000. 1.0E10  0.
  0.  1.0E5
8000. 1.0E5
1.0E10 0.     1.0E5
0.  0.
```

```
 250.0   0.  0.     0.35                 0       !  REG  2
   0.    1500.
 250.   1500.
 8000. 1.0E10  0.
   0.  1.0E5
 8000. 1.0E5
 1.0E10  0.     1.0E5
 0.  0.
MATCH 4
NMESH 4
!PLANE
!OPTMZ
TLRAN,COH,PLT
0.  2.  0.005
100.  100.
```

SMINPUT.DAT

```
C-SNAP
0
1 20
800.000000 3.14159265358979 100.000000
100
100.
1000.000000 5.000000
0.0050000
```

J.1.2 The Input File for the Two-Dimensional C-SNAP Model

```
 2D C-SNAP Model
 1
 40.
 1   20 20
 100, 0
 250.  0.   0.    0.                     0       ! REG   1
   0.  1500.
 250.  1500.
 8000. 1.0E10  0.
   0.  1.0E5
 8000. 1.0E5
 1.0E10 0.     1.0E5
 0.  0.
MATCH 3
NMESH 4
!PLANE
!OPTMZ
TLRAN,COH,PLT
0.  2.  0.005
100.  100.
```

J.2 Input Files for Case 2a

C-SNAP.DAT

```
 SEAMOUNT
 1
 40.
 1   20 20
 100, 0
 250.  0.   0.    0.                    6       ! REG   1
   0.  1500.
 250.  1500.
 8000. 1.0E10  0.
   0.  1.0E5
 8000. 1.0E5
 1.0E10 0.     1.0E5
 0.  0.
 150.0   0.  0.     0.35                0       !  REG  2
   0.   1500.
 150.   1500.
 8100. 1.0E10  0.
   0.  1.0E5
 8100. 1.0E5
 1.0E10  0.     1.0E5
 0.  0.
MATCH 4
NMESH 4
!PLANE
!OPTMZ
TLRAN,COH,PLT
0.  2.  0.005
```

```
100.  100.
```

SMINPUT.DAT

```
C-SNAP
0
1 20
800.000000 3.14159265358979 100.000000
100
100.
1000.000000 5.000000
0.0050000
```

J.3 Input Files for Case 2b

J.3.1 Input Files for the Three-Dimensional Seamount Model

<u>**C-SNAP.DAT**</u>

```
 SEAMOUNT waveguide ! FOR 3D MODEL
 1
 40.
 1   120  120
 100, 0
 250.  0.   0.    0.                     6       ! REG   1
   0.  1500.
 250.  1500.
 4000. 2.0  0.1
   0.  1800.
 4000. 1800.
 2.0 0.1     1.0E10
 0.  0.
 150.0   0.  0.     0.35                 0       !  REG  2
   0.   1500.
 150.   1500.
 4100. 2.0  0.1
   0.  1800.
 4100. 1800.
 2.0  0.1     1.0E10
 0.  0.
MATCH 4
NMESH 4
TLRAN,COH,PLT
0.  2.  0.005
100.  100.
```

SMINPUT.DAT

```
C-SNAP
0
1 120
800.000000 3.14159265358979 100.000000
100
100.
2000.000000 10.000000
0.0050000
```

J.3.2 The Input File for the Two-Dimensional C-SNAP Model (at Azimuthal Angle $\phi = 0$ with respect to the Source)

C-SNAP.DAT

```
 SEAMOUNT waveguide ! FOR 2D MODEL
 1
 40.
 1   120  120
 100, 0
 250.  0.   0.     0.0                     -1       ! REG   1
   0.  1500.
 250.  1500.
 4000. 2.0  0.1
   0.  1800.
 4000. 1800.
 2.0 0.1     1.0E10
 0.  0.
 250.  0.   0.     0.45                     7       ! REG   1
   0.  1500.
 250.  1500.
```

```
 4000. 2.0  0.1
   0.  1800.
 4000. 1800.
 2.0 0.1     1.0E10
 0.  0.
 150.0   0.  0.     0.80                 7       !  REG  2
   0.   1500.
 150.   1500.
 4100. 2.0  0.1
   0.  1800.
 4100. 1800.
 2.0  0.1     1.0E10
 0.  0.
 250.  0.   0.    1.15                     0       ! REG   1
   0.  1500.
 250.  1500.
 4000. 2.0  0.1
   0.  1800.
 4000. 1800.
 2.0 0.1     1.0E10
 0.  0.
MATCH 3
NMESH 4
!PLANE
!OPTMZ
TLRAN,COH,PLT
0.  2.  0.01
100. 100.
```

J.4 Input Files for Case 3

J.4.1 Input Files for the Three-Dimensional Seamount Model

C-SNAP.DAT

```
 DEEP
 1
 10
 1  43  43
 100  0
5000.0  0.0   0.0                   0            7     ! Profile  1
    0.0, 1536.00
  200.0, 1528.00
  700.0, 1502.00
  800.0, 1500.00
 1200.0, 1497.00
 1500.0, 1497.00
 2000.0, 1500.00
 3000.0, 1512.00
 4000.0, 1528.00
 5000.0, 1545.00
    0.
1.0, 0.1, 2000.0
0.0   0.0
1200.0  0.0   0.0                  20            0     ! Profile  2
    0.0, 1536.00
  200.0, 1528.00
  700.0, 1502.00
  800.0, 1500.00
 1200.0, 1497.00
    0.
```

```
1.0, 0.1, 2000.0
0.0   0.0
!LARGE
MATCH    4
NMESH    1
!OPTMZ
TLRAN,COH,PLT
0   200  0.1
100.  4500.
```

SMINPUT.DAT

```
C-SNAP
0
1 12
100000.000000 3.14159265358979 100.000000
50
300.
250000.000000 2000.000000
0.002
```

J.4.2 The Input File for the Two-Dimensional C-SNAP Model (at Azimuthal Angle $\phi = 0$ with respect to the Source)

C-SNAP.DAT

```
 DEEP
 1
 10
 1  12  43
 100  0
5000.0  0.0   0.0                   0            -1     ! Profile  1
```

```
    0.0, 1536.00
  200.0, 1528.00
  700.0, 1502.00
  800.0, 1500.00
 1200.0, 1497.00
 1500.0, 1497.00
 2000.0, 1500.00
 3000.0, 1512.00
 4000.0, 1528.00
 5000.0, 1545.00
    0.
1.0, 0.1, 2000.0
0.0   0.0
5000.0  0.0   0.0                    80            5     ! Profile  2
    0.0, 1536.00
  200.0, 1528.00
  700.0, 1502.00
  800.0, 1500.00
 1200.0, 1497.00
 1500.0, 1497.00
 2000.0, 1500.00
 3000.0, 1512.00
 4000.0, 1528.00
 5000.0, 1545.00
    0.
1.0, 0.1, 2000.0
0.0   0.0
1200.0  0.0   0.0                    100            5     ! Profile  3
    0.0, 1536.00
  200.0, 1528.00
```

```
  700.0, 1502.00
  800.0, 1500.00
 1200.0, 1497.00
    0.
1.0, 0.1, 2000.0
0.0   0.0
5000.0  0.0   0.0                   120            0     ! Profile  4
    0.0, 1536.00
  200.0, 1528.00
  700.0, 1502.00
  800.0, 1500.00
 1200.0, 1497.00
 1500.0, 1497.00
 2000.0, 1500.00
 3000.0, 1512.00
 4000.0, 1528.00
 5000.0, 1545.00
    0.
1.0, 0.1, 2000.0
0.0   0.0
!LARGE
MATCH    3
NMESH    1
!OPTMZ
TLRAN,COH,PLT
0   200  0.1
100.  4500.
```

Appendix K

Formulas for the Use of Random Stair-step Sizes to Approximate Bathymetry Changes

Below we will give the formulas used in our three-dimensional spectral coupled mode model for approximating the bathymetry change by using random stair-step sizes.

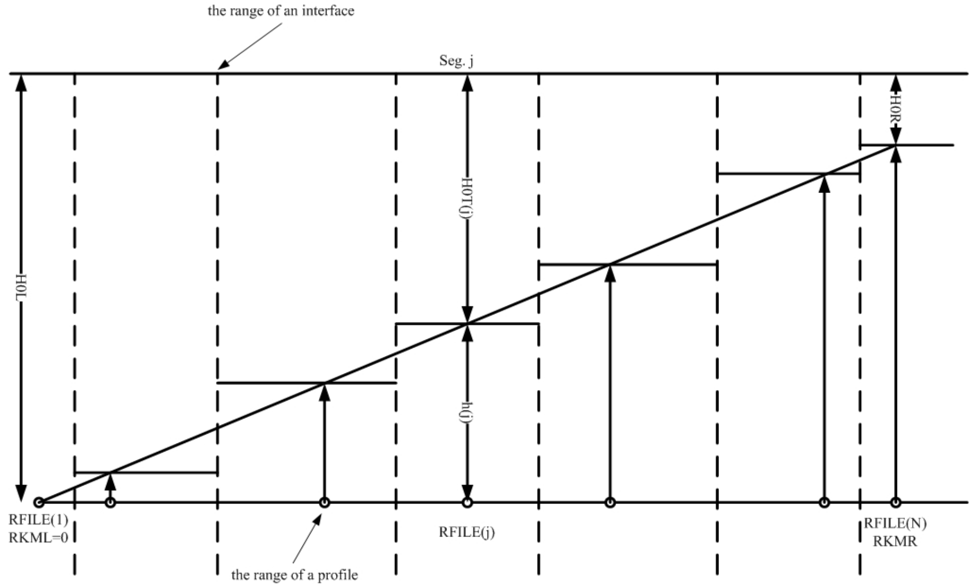

Figure K-1: Use of random stair-step sizes to approximate bathymetry changes.

As illustrated in Fig. K-1, we have two known sound velocity profiles located at RFILE(1) and RFILE(N). In the formulas below, N is the number of segments, RFILE is the range of a SVP, RCOUPL is the range of an interface, Δx is the uniform step size, α is a random number from -0.3 to 0.3, H0T(j) is the water depth in segment j.

$$RKML = RFILE(1),\ RKMR = RFILE(N), \tag{K.1}$$

$$\Delta x = \frac{RKMR - RKML}{N-1}, \tag{K.2}$$

$$RFILE0(j) = RFILE0(j-1) + \Delta x,\ j = 2, \ldots, N-1, \tag{K.3}$$

$$RFILE(j) = RFILE0(j) + \alpha\Delta x,\ j = 2, \ldots, N-1, \tag{K.4}$$

$$RCOUPL(j) = \frac{1}{2}\left[RFILE(j-1) + RFILE(j)\right],\ j = 2, \ldots, N,$$

$$RATIOX(j) = \frac{h(j)}{H0L - H0R} = \frac{RFILE(j) - RKML}{RKMR - RKML},\ j = 2, \ldots, N-1, \tag{K.5}$$

$$h(j) = RATIOX(j) \times (H0L - H0R),\ j = 2, \ldots, N-1, \tag{K.6}$$

$$H0T(j) = H0L - h(j) = H0L + RATIOX(j) \times (H0R - H0L),\ j = 2, \ldots, N-1. \tag{K.7}$$

Bibliography

[1] M. Abramowitz and I. A. Stegun. *Handbook of Mathematical Functions with Formulas, Graphs and Mathematical Tables.* Appl. Math. Ser. No. 55. National Bureau of Standards, Washington, DC, 1972.

[2] E. Anderson, Z. Bai, C. Bischof, L. S. Blackford, J. Demmel, J. Dongarra, J. Du Croz, A. Greenbaum, S. Hammarling, A. Mckenney, and D. Sorensen. *LAPACK User's Guide.* Society for Industrial and Applied Mathematics, Philadelphia, PA, 1999.

[3] Gerassimos A. Athanassoulis and Aristides M. Propathopoulos. Three-dimensional acoustic scattering of a source-generated field from a cylindrical island. *J. Acoust. Soc. Am.*, 100(1), July 1996.

[4] G. Botseas, D. Lee, and D. King. For3d: A computer model for solving the lss three-dimensional, wide angle wave equation. *NUSC TR*, 7943, 1987.

[5] M.J. Buckingham and A. Tolstoy. An analytical solution for benchmark problem 1: The "ideal" wedge. *J. Acoust. Soc. Am*, 87:1511–1513, 1990.

[6] Jérémie Eskenazi. A computer model for sound propagation around conical seamounts. Master's thesis, MIT, 2001.

[7] C.M. Ferla, M.B. Porter, and F.B. Jensen. *C-SNAP: Coupled SACLANTCEN normal mode poopagation loss model.* Underwater Research Division.

[8] George V. Frisk. *Ocean and seabed acoustics.* Prentice-Hall Inc., 1994.

[9] I.S. Gradshteyn and I.M. Ryzhik. *Table of Integrals, Series, and Products.* Academic Press, 2000.

[10] Joseph J. Sikora III. Sound propagation around underwater seamounts. Master's thesis, MIT, 2005.

[11] Finn B. Jensen. On the use of stair steps to approximate bathymetry changes in ocean waveguides. *Theoretical and Computational Acoustics*, 1996.

[12] Finn B. Jensen, William A. Kuperman, Michael B. Porter, and Henrik Schmidt. *Computational Ocean Acoustics.* AIP Press, 1994.

[13] D. Lee, M. Schultz, and Y. Saad. A three-dimensional wide angle wave equation with vertical density variations. *Computational Acoustics*, 1, 1990.

[14] Wenyu Luo. A three-dimensional coupled modes solution for range-dependent waveguides. Master's thesis, MIT, 2005.

[15] S. T. McDaniel. Propagation of normal mode in the parabolic approximation. *J. Acoust. Soc. Am.*, 57, 1975.

[16] J. S. Perkins and R. N. Baer. An approximation to the three-dimensional parabolic-equation method for acoustic propagation. *J. Acoust. Soc. Am.*, 72(2), August 1982.

[17] David C. Ricks. Elastodynamic modeling of fluid-loaded cylindrical shells with multiple layers and internal attachments. Master's thesis, MIT, 1994.

[18] David C. Ricks and Henrik Schmidt. A numerically stable global matrix method for cylinderlly layered shells excited by ring forces. *J. Acoust. Soc. Am.*, 95(6), June 1994.

[19] W. Siegmann, D. Lee, and G. Botseas. Analytic solutions for testing accuracy and azimuthal coupling in three-dimensional acoustic propagation. *Computational Acoustics*, 1, 1990.

[20] Michael I. Taroudarkis. A coupled-mode formaulaton for the solution in the pressence of a conical sea-mount. *Journal of Computational Acoustics*, 4(1), 1996.

[21] Earl G. Williams. *Fourier Acoustics.* Academic Press, 1999.